AN INTEGRATED STUDY OF LOW-RESISTIVITY HYDROCARBON PAY ZONES: A study of two “dual resistivity” gas reservoirs, onshore Mozambique Basin

Thesis

by

VINCENT MASHABA (MSc)

Submitted in partial fulfilment of the requirements for the degree

PHILOSOPHIAE DOCTOR (GEOLOGY)

In the Faculty of Natural & Agricultural Sciences

University of Pretoria

Final Submission: September 2014

Major Subject: **Petrophysics**

I, **Vincent Mashaba,** declare that the thesis/dissertation, which I hereby submit for the degree PhD (Geology) at the University of Pretoria, is my own work and has not previously been submitted by me for a degree at this or any other tertiary institution.

SIGNATURE……..

DATE:…….....

ABSTRACT

The overall demand for gas in Mozambique is projected to grow from 3.5 PJ/a to approximately 35PJ/a by 2025, as a result of growing extractive industries such as petroleum exploration and mining as well as non-extractive industries such as agriculture. The potential for gas to supplement the national energy supply and to drive economic development in the country is large. With growing energy demand and conversion of gas to electricity, integrated reservoir studies to optimise recovery of gas are becoming increasingly important. This study presents an integrated reservoir study of the low-resistivity sandstone gas reservoirs in the Mozambique Basin. The two investigated reservoir formations are the J-Reservoir and K-Reservoir of the Lower Grudja Formation of Maastrichtian age, which host two separate gas accumulations.

Conventional water saturation (S_w) calculations such as Archie's equation fail to give accurate results that are consistent with the production figures and well test results. The results of the water saturation calculated using this method are also inconsistent with the water saturation calculated using Nuclear Magnetic Resonance (NMR), the only tool that gives accurate calculation of the water saturation (S_w) in the low-resistivity reservoirs. The primary objective of the research was to understand the cause of the low-resistivity phenomena by evaluating the reservoir characteristics such as textural fabric, mineralogy and clay content of the J- and K-Reservoirs. The presence of clay-bound water and the conductive minerals in the reservoir formation are known to be some of the main causes of low-resistivity phenomena in sedimentary basins around the world.

The clay volume in the two reservoirs was evaluated using the gamma ray (GR) log and the results were compared well to clay calculated from core data using X-ray Diffraction (XRD) and Laser Grain Size Analysis (LGSA). The study showed that the clay volumes ranged from 6% to 30% from the top towards the bottom of the J-Reservoir and 2.4% to 18% from the top towards the bottom of the K-Reservoir. The calculated silt volumes for the J-and K-Reservoirs ranged 0-70% with a general increase in silt volume towards the bottom of the reservoirs.

Petrology studies established that conductive minerals within the J-and K-Reservoirs play an insignificant role, if any, on the overall conductivity of the reservoir, due to their presence in very low quantities. Pyrite in particular, a well-known conductive mineral, occurs in small amounts from trace level to up to 2 weight %, based on X-Ray Diffraction (XRD) analysis of the J- and the K-Reservoirs.

The water saturation (S_w) in the J-and K-Reservoirs was calculated using the Archie and Simandoux equations and the results were compared to NMR-calculated water saturation.

The author developed a new algorithm to improve and accurately calculate water saturation (S_w) in the J-Reservoir and the K-Reservoirs. This new algorithm, which takes into account the contribution the clay and silt bound water on the overall resistivity of the reservoir, is given by the following equation:

$$S_w = \{[-(V_{cl}*C_{cl} + V_{silt}*C_{silt}) \pm ((V_{cl}*C_{cl} + V_{silt}*C_{silt})^2 - 4*(C_w * PHIE^m)*(-C_{total}))^{1/2}]/ (2*C_w \times PHIE^m)\} + F_{corr}$$

Where
S_w: Water saturation
V_{cl}: Volume of clay
C_{cl}: Conductivity of the clay bound water
V_{silt}: Volume of silt
C_{silt}: Conductivity of the silt bound water
C_{total}: Total conductivity of the reservoir system
PHIE: Effective porosity
F_{corr}: Correction factor to account for using a constant n=2. This factor shift the saturation curve up or down by a constant match the NMR-calculated water saturation.

The Simandoux equation and the new algorithm developed by the author yielded significant improvement in water saturation results, when compared to water saturation calculated using Archie's equation. In one of the wells, A21, the water saturation calculated using the new algorithm matched the NMR-calculated water saturation.

DEDICATION

This work is dedicated to my entire family and most importantly to my late brother Ernest Mashaba. This is for you.

ACKNOWLEDGEMENTS

I would like to acknowledge my supervisor Prof. Dr. Dr. Habil. Wladyslaw Altermann, Kumba-Exxaro Chair in Geodynamics, for accepting my proposal and for his support throughout my research and the Head of the Department of Geology at the University of Pretoria, Prof. Patrick G. Eriksson, for giving me the opportunity to contribute positively to the scientific fraternity of South Africa.

I would also like to pass my sincere gratitude to Dr Adegboyega Elegbede for his valuable advice and in-depth knowledge of the Petrophysics subject, Dr Watfa Mohammed for the course material on Advanced Petrophysics. Lastly, I would like to thank Sasol Petroleum International (SPI) and Instituto Nacional de Petroleo (INP) for granting permission and access to the data used in this study.

GLOSSARY OF ACRONYMS AND ABBREVIATIONS

(a): a constant in Archie's saturation equation often assumed to be 1

API: The unit of radioactivity used for natural gamma ray (GR) logs

Bscf: Billion standard cubic feet

BVM: Bulk volume movable fluids

BVI: Bulk volume irreducible water

CBW: Clay-bound water

CEC: Cation exchange capacity

CMR: Combinable magnetic resonance

C_p: Velocity compaction factor

DSDP: Deep Sea drilling project

DST: Drill stem test. A procedure for isolating and testing pressure and productive capacity of a reservoir

DT: Sonic transit time

ECL: Oil and gas service company based in the UK (now RPS)

Electro-facies: Author's definition of different electrical response in the reservoir based on changes in the reservoir facies

ENH: Empressa Nacional de Hidrocarbonetos- Mozambique's National Enterprise of Hydrocarbons

FF: Formation factor in Archie's saturation equation also = $R_o/R_w = a / \varphi^m = F$

GDT: An acronym to describe a gas content that extends to the lower part of the reservoir also referred to as "gas down to"

GR: Gamma ray

GWC: Gas water contact

I_{GR}: Gamma ray index

ILD: Deep induction log

INP: Instituto Nacional de Petroleo (National Petroleum Institute of Mozambique)

K: Potassium, a chemical element

LGSA: Laser grain size analysis

LLD: Deep induction measurement (Laterolog)

LLS: Shallow induction measurement (Laterolog)

(m): Cementation factor used in Archie's water saturation equation

MD: Measured depth

Mbmsl: Metres below mean sea level

MMscf: Million standard cubic feet

(n): Saturation exponent in Archie's saturation equation

NMR: Nuclear magnetic resonance

NTG: Net-to-Gross
OMNI: Core Laboratory based in Houston Texas, USA
P_e: Photo-Electric effect

PHIE: Effective porosity

PHIT: Total porosity

RCA: Routine core analysis

RF: Radio frequency

R_m: Resistivity of the matrix

R_{mf}: Resistivity of the mud filtrate

R_{min} and Rmax: Regional best estimates for two lithologies in any log response

R_o: Resistivity of brine

R_t: Observed bulk resistivity

R_w: Formation water resistivity

SCAL: Special core analysis

SEM: Scanning electron microscope

S_w: Water saturation

S_{wirr}: Irreducible water saturation

T: Temperature (^oC)

Tcf: Trillion cubic feet

$T_{f:}$ Sonic interval transit time of the pore fluid
Th: Thorium, a naturally occurring radioactive chemical element
T_{log}: Sonic interval transit time
T_{ma}: Sonic interval time in the matrix

TOC: Total organic content

TVD: Total vertical depth

T_2: NMR relaxation time
V_{log}: Un-normalized log curve
V_{norm}: Normalized values of the log curve
V_p: Compressional velocity
VRT: Velocity-resistivity transform
$V_{sh:}$ Volume of shale
V_{shale}: Volume of shale
W_{max}: Value of a different lithology in each well in the well normalization equation
W_{min}: Value of specific lithology in each well in the well normalization equation
XRD: X-Ray diffraction
Φt: Total porosity
ρ_{ma}: Density of the matrix
$\rho_{b:}$ Bulk density
ρ_f: Fluid density

TABLE OF CONTENTS

LIST OF FIGURES

LIST OF TABLES

APPENDIX CONTENTS

CHAPTER 1: INTRODUCTION

1.1 Background: Gas Demand in Mozambique and South Africa

Mozambique (Fig. 1) is ending its post-war recovery period and the country is on the brink of industrial revolution. The country's economic growth is largely dependent on the development of the energy sector such as building of gas to electricity power stations, to meet the growing demand of the industry, such as mining and agriculture, as well as the regional demand for electricity in the neighbouring countries such as South Africa. The overall local demand for gas in Mozambique is projected to grow from 3.5 Petra Joules per annum (PJ/a) to approximately 35PJ/a by 2025, according to the IESE Study, (2012). With the population in Mozambique expected to double in 2030 from the current 29 million, and since the country is ranked bottom of the United Nations Human Development Index (UNDP, 2013), access to modern energy forms will be pivotal to lift the population out of poverty (IESE, 2012). The gas based power generation has been identified as the main driver for Mozambique industrialisation in the proposed Mozambique Gas Master Plan commissioned by the International Finance Corporation (IFC, 2012).

South Africa is also dependent to some extent on the gas supply from Mozambique, to meet the growing demand for electricity. The peak electricity demand in South Africa is projected to grow by 2.8% per annum from 38.9 to 67.8 Giga Watts (GW) by 2030 (South African Department of Energy, 2011) and South Africa's power utility company Eskom, has been under a lot of pressure recently to meet the country's growing electricity demand and other gas usage. One of the options to meet the growing electricity demand both in Mozambique and South Africa, is to build gas to power facilities; therefore Mozambique will have to optimise the extraction and development of its natural gas resources. This can only be achieved by having an in-depth understanding of the reservoirs from which the gas is being produced. Currently, the only gas producing fields are the two gas fields discussed herein, whose producing reservoirs are classified as low-resistivity pays and pose a challenge in estimating the water that is likely to be encountered as a by-product of gas production.

Most hydrocarbon (gas) bearing clastic reservoir formations in sedimentary basins around the world are characterised by an increase in electric resistivity contrast between the hydrocarbon-bearing part of the reservoir and the water-bearing zone. The resistivity of hydrocarbons (oil and gas) is generally higher than the resistivity of formation water, since dissolved solutes in the formation water provide an effective pathway for electrical current to flow. However, in Mozambique basin, hydrocarbon-bearing reservoir formations are known to exhibit low-resistivity response and conventional wire-line log analysis give inaccurate

water saturation (S_w) results. The problem of identifying low-resistivity pay has been recognised and studied for over three decades in other sedimentary basins in Europe, Gulf of Mexico, South America and North Africa (Worthington, 1997).

The calculated water saturation using conventional log analysis for the J- and K- Reservoirs discussed in this thesis, contradicts water saturation calculated using the Nuclear Magnetic Resonance (NMR) tool which gives accurate water saturation (S_w) results in low-resistivity pay reservoirs. The conventionally calculated water saturations also contradict the Drill Stem Test (DST) data, which is a test done on a well to determine the flow of hydrocarbons and water before the reservoirs can be set to a full field gas development and production.

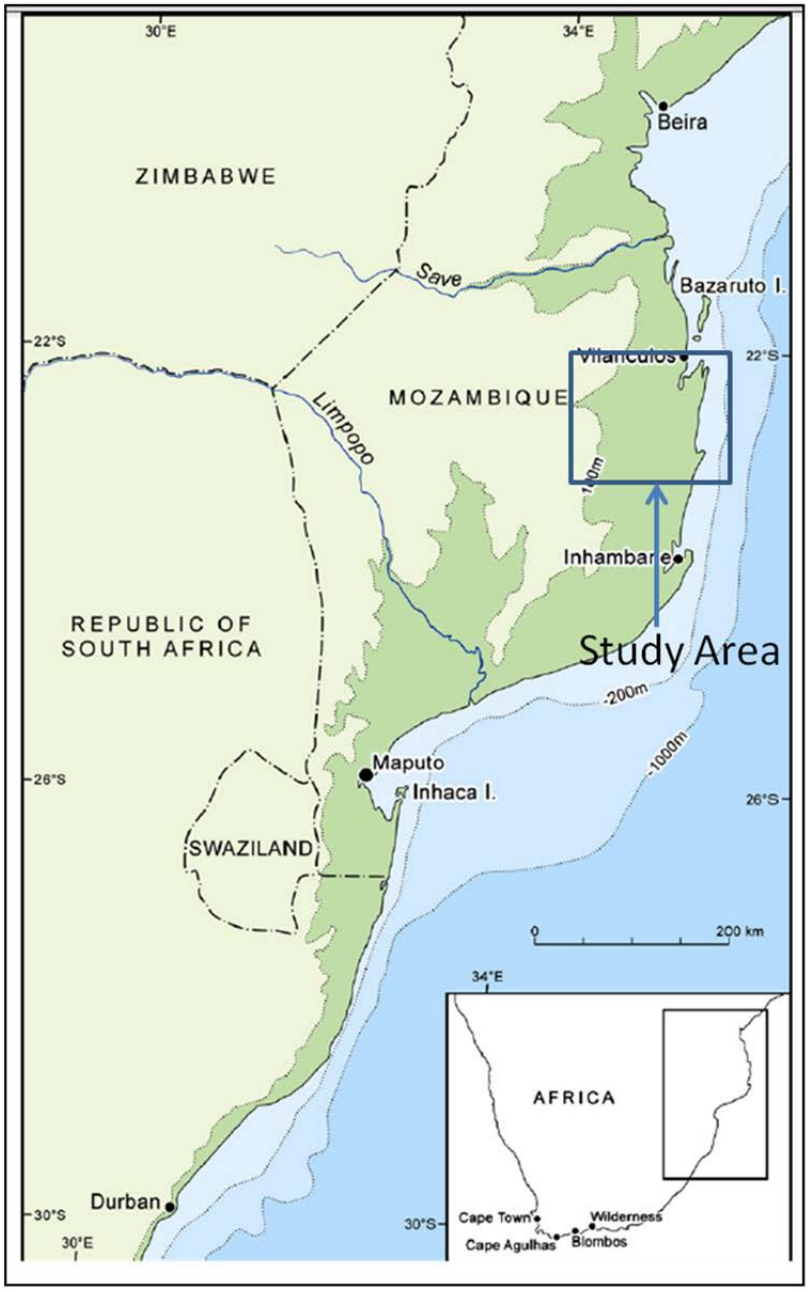

Figure 1: Locality map of the Mozambique Basin (modified from Armitage et al., 2006). The general study area is shown as a blue rectangle.

1.2 Exploration History – Mozambique Basin

Exploration for hydrocarbons contributed immensely to the current understanding of the Mozambique Basin, with five Deep Sea Drilling Project (DSDP) wells drilled in this area (Flores, 1973). The Deep Sea Drilling Project was an ocean-drilling project, which also included coring of the deep wells in the Atlantic, Pacific and Indian Oceans to better understand the stratigraphy of the East African margin. Integration of gravity and magnetic data with the DSDP and surface geology, e.g. outcrops, complemented most of the shallow exploratory wells drilled in the 1900's, which mainly targeted the hydrocarbon seeps observed on surface. The first exploratory well to discover hydrocarbons resulted in a blow out, in the early 1950s (ENH-ECL, 2000). Hydrocarbons from this well flowed for a short period of time and this event proved the existence of a working petroleum system in the Mozambique basin. This subsequently led to the formal awarding of exploration concessions. Exploration began in 1961 when Gulf Mozambique formed a partnership with Arco, later AMOCO, subsequently acquired by BP (ENH-ECL, 2000).

Gas was discovered in the onshore area, south of the North Save river mouth (Field A) by Gulf Oil in 1961, which was followed by another discovery in 1962, in the Buzi area near Beira (ENH-ECL, 2000). Another gas discovery was made in Field B in 1967 (Flores, 1973). Recently, the first discovery of liquid hydrocarbons was made near the town of Inhassoro. If commercially developed, this field will provide the very first liquid hydrocarbons (oil) from the onshore Mozambique basin (www.sasol.com).

The development of Field A and Field B into commercial gas producers did not happen until 2003, probably due to lack of market to commercialise the discovered gas, political instability and lack of proper infrastructure to transport the gas to the market. Civil war and civil unrest resulted in destruction of infrastructure and lack of development in the country for at least two decades. For instance, the only gas processing facility in the town of Inhassoro, Mozambique, was completed by Sasol in 2004 and this facilitated the 865km pipeline to Secunda, South Africa, to supply customers via a supply network of approximately 2500km (www.sasol.com). It is however also likely; that the low-resistivity pay zones were mistaken for water bearing zones due to high apparent water saturations calculated using conventional well log analysis, which prevented further development. The recent big gas discoveries in the northern most part of Mozambique (Rovuma Basin), where hundreds of trillions of cubic feet (Tcf) of gas have been discovered, have re-ignited interest from major oil companies for hydrocarbon exploration in this region of East Africa.

All the future investment decisions on mega-projects such as pipelines and gas processing facilities depend on whether potential gas developments are properly scoped out and the potential gas reserves are accurately calculated. One of the key input parameters in calculating hydrocarbon reserves are the resistivity log data which record high resistivity values, when encountering hydrocarbon accumulation. However, in Mozambique basin, the hydrocarbon-bearing zones exhibit low-resistivity phenomena, which make it challenging to accurately calculate the amount of hydrocarbons in the reservoir.

In the past, some assumptions have been made about the cause of low-resistivity pay reservoirs in Mozambique but no integrated study has been undertaken to understand the cause for these low-resistivity pay zones. The author postulates herein, that one of the reasons that some of the gas discoveries onshore Mozambique were abandoned by the earlier exploration companies, were the inaccurate water saturation calculations resulting from the low-resistivity phenomena described above.

1.3 Research Objectives

The objectives of this study were to comprehensively investigate the cause of the low-resistivity phenomena in the J- and K-Reservoirs and to use different methodologies such as the Archie and Simandoux equation, and to develop a new equation to calculate the water saturation (S_w) within these reservoirs. New approaches based on the modified Archie's equation were also used to test their efficiency in calculating the water saturation in these low-resistivity reservoirs. The water saturation calculated from these methods is compared to:

I. Water saturation (S_w) calculated using the Nuclear Magnetic Resonance (NMR) data. The water saturation (S_w) calculated using NMR data will be used as a benchmark to evaluate the efficiency of the water saturation methods mentioned above, due to its ability to calculate bound, irreducible water and movable water within the reservoir.
II. Dynamic data, which comprised mainly well-test data, to validate the results of water saturation (S_w) calculations from these methods.

The available data to test the hypotheses in the study, comprise both, the static (seismic, wireline logs and core) and dynamic data (well tests). Although permission was granted by Sasol and the Instituto Nacional de Petroleo (INP) of Mozambique to use data from the two gas fields, there was a limitation on the amount of data that the author was allowed to use

due to confidentiality reasons. The well names and reservoir names have also been changed and publication policy was restricted.

CHAPTER 2: GEOLOGICAL HISTORY OF THE MOZAMBIQUE BASIN

2.1 Break-up and Rifting in East African Margin

The formation and evolution of the sedimentary basins along the East African margin is mainly attributed to the break-up of the Gondwana supercontinent which took place during the Permian to Triassic (Fig. 2). Rifting in the Karoo times (Permian to Early Jurassic) was followed by two phases of continental separation in the mid-Jurassic and continued through mid-Cretaceous (Coster et al., 1989). The exact reconstruction of the fit of continents prior to break up of Gondwana is still an unresolved problem (Leinweber and Jokat, 2011) and little is known about the movement of continents soon after the initial break up (Leinweber and Jokat, 2012), however, the continental fit in the Cenozoic period is well constrained, according to Bernard et al. (2005). The age of the break up unconformity is another issue, still under debate in the academic world. Several authors suggest different time estimates for the break. For example Duncan et al. (1997) and Martin (2007), place the break up at between 190-175 Ma; Reeves and De Wit (2000) place the break up at 170 Ma, which is closer to Coster et al., 1989, who placed the break up at 165 million years ago. Other authors such as Salman and Abdula (1995) as well as Konig and Jokat (2006), place the break up at 157 Ma and 167.2 Ma, respectively.

Two major rift phases were identified, the first rift phase started in the Early Jurassic with an anticlockwise (north- eastern) movement of Antarctica, along the reactivated Pebane shear zone relative to Africa (Mahanjane, 2012). This was followed by the final north-south rifting at around 170 Ma (Reeves and De Wit, 2000) and the early drifting of east Antarctica together with Madagascar from Africa, which occurred between 160Ma and 170Ma, according to Konig and Jokat (2006). However, Konig and Jokat (2010) revised their earlier hypothesis of the timing of the drifting by using the age of the oldest magnetic anomalies, M24 and M26, that indicate that drifting started around 155 Ma and 55.3 Ma, respectively (Jokat, 2010). Other authors such as Simpson et al., (1979) and Bergh (1977), used the M21 and M24 magnetic anomalies to deduce the age of the rifting. Another attempt at a continental break

up, took place in the Late Cretaceous to Early Tertiary, which resulted in the formation of the East African Rift System (Coster et al., 1989).

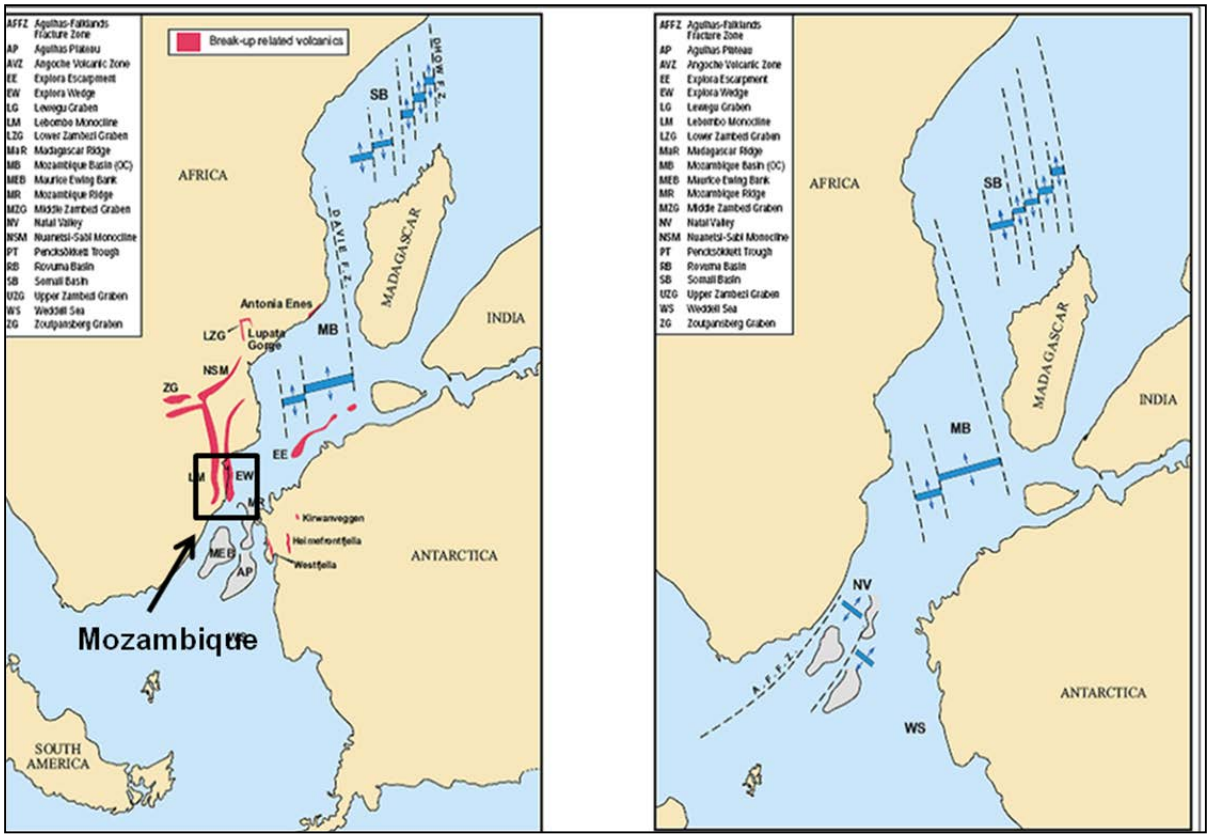

Figure 2: Break-up of Gondwana (after ENH-ECL, 2000). The breakup of Gondwana supercontinent and the rifting and drifting resulted in the formation of the Mozambique Basin. The general study area is shown on the left map (black square), which depicts the time of Early Jurassic, at c. 190 Ma. In the right picture the situation during Early Cretaceous (120 Ma) is shown.

2.2 The Development of Mozambique Basins

The break-up of Gondwana and the subsequent north-south rifting and drifting of Antarctica relative to Africa facilitated the opening of the Indian Ocean (Flores et al., 1973). Subsequently these movements led to the formation of the Riiser-Laser Sea in Antarctica (Mahanjane, 2012) and the formation of the Mozambique Basin and the Somali Basin, in the western Indian Ocean (Reeves et al., 2000; Reeves et al., 2002; Konig and Jokat, 2006), and their conjugates in Antarctica (Matthews et al., 2001). Figure 3 below is the regional magnetic expression of the rifting of Antarctica relative to Africa and the formation of the Riiser-Laser Sea in Antarctica. Several models have since been put forward using the reconstruction of the Gondwana super-continent to study the evolution of Mozambique

Basin, especially the northern fit between the East African Basins with their conjugate basins in Dronning Maud Land or Antarctica (Mahanjane, 2012).

The age of the oldest oceanic crust between Mozambique and Antarctica is also a subject of current debate. Lawver et al., (1991) place the age of the oldest oceanic crust at 170 Ma, which is in line with the rifting age of between 170 Ma and 160 Ma (Konig and Jokat., 2006). This postulate is further supported by Courtillot et al. (1999), who stated that sea floor spreading started at around 170 Ma and the placement of dykes parallel to the Zambezi coast also occurred around 170 Ma (Mahanjane, 2012). The geological similarities between south-east Africa and Antarctica have been studied and also documented by earlier South African workers such as Alex du Toit (1937) or Grantham et al. (1988).

During the rifting period, structures in the form of graben features and faults resulted in the formation of a broad platform depression in the Mozambique basin. These depressions were subsequently filled with clastic and carbonate formations, which according to Salman and Abdula (1973), can be correlated with the formations of the Karoo Supergroup. The last rifting phase in the mid-Miocene resulted in the Urema Graben feature in Figure 7 (ENH-ECL, 2000).

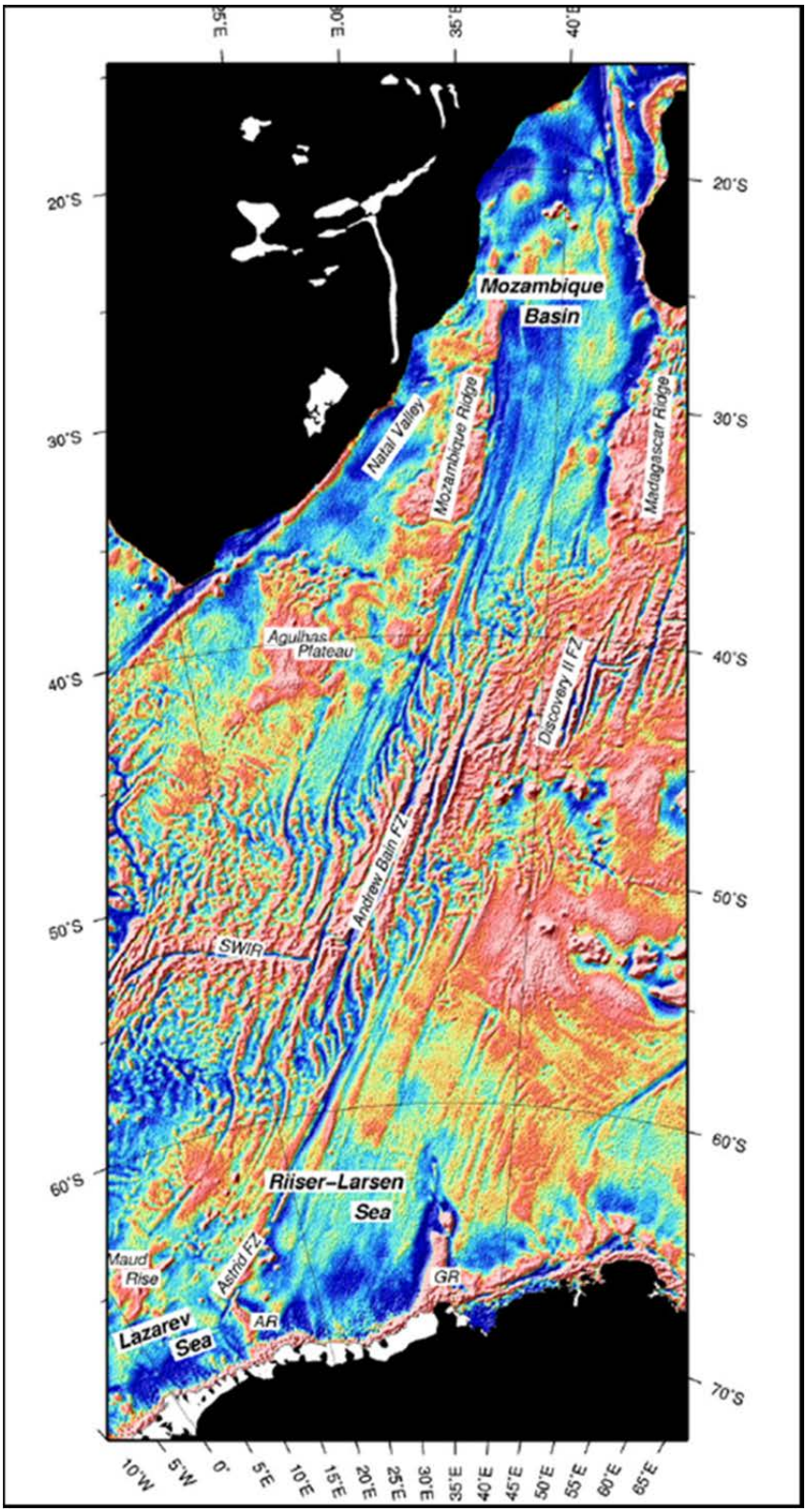

Figure 3: Regional magnetic expression of the rifting of Antarctica relative to Africa, (Jokat et al., 2012).

In Figure 4 below, two distinct magnetic anomalies labelled “Magnetic 1” and “Magnetic 2” are the magnetic expressions of the Zimbabwe and Kaapvaal Archean cratons, respectively. The two cratons, which form the continental nucleus of southern Africa, were consolidated in late Archean times, according to James et al., (2003).

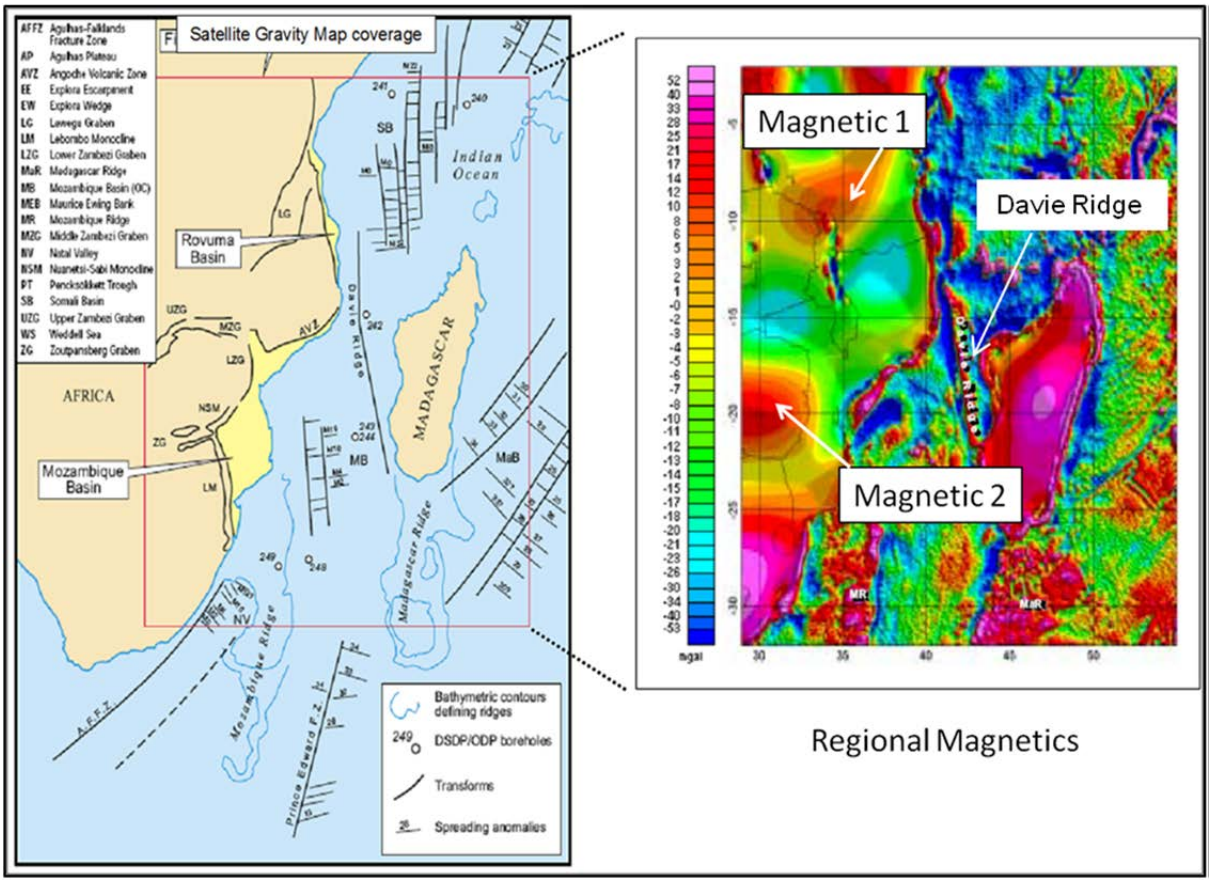

Figure 4: Gravity and magnetic expressions of the rifting; magnetic 1 and magnetic 2 are the anomalies of the Zimbabwe and Kaapvaal cratons, respectively (modified from ENH-ECL, 2000).

The two cratons have been subjected to high-grade metamorphism and high degree of deformation that resulted in the formation of gneisses and granulites (Gwavava et al., 1992). The magnetic low in between the two cratons is an expression of the 600 km long and 250 km wide Limpopo mobile belt, which can be further divided into three zones, the Northern Marginal Zone, the Central Zone and the Southern Marginal Zone (James et al., 2003). Another prominent magnetic feature in Figure 4 is the Davie Ridge, which according to Coster et al. (1989), is an expression of a continent-ocean transform. The Limpopo River that lies within the Limpopo Belt, which is shown as a magnetic low in Figure 4, is one of the major rivers responsible for sediment transport into the Mozambique Basin (Fig. 8).

- **Volcanic activity**

The mid-Jurassic was characterised by the reactivation of strike slip faults accompanied by volcanic activity in the Karoo and the conjugate Ferrar provinces, between 190 and 170 Ma (Mahanjane, 2012). This postulate is further supported by Cox et al. (1992), who place the volcanic activity between 190 and 185 million years. Fitch and Miller (1984), postulate that the earliest phase of Karoo volcanic activity peaked at around 200-190 Ma. According to the model by Cox (1992), which is based on the analysis of the Karoo volcanism, there is a 20 Ma gap between the onset of volcanism and the formation of the first oceanic crust. Courtillot et al. (1999), placed the seafloor spreading at around 170 Ma. The expressions of the volcanism and related lava flows can be seen along the present day south eastern margin of the basin, the Lebombo monocline (Fig. 7) which according to Fitch et al. (1984), is dated between 198 and 173 Ma, and to the north-west, by the Nuanetsi-Sabi monocline. The lava eruptions occurred through fissures along weakness zones of the crust (Cox et al., 1970) and are dated from 160 to 200 Ma (Hales, 1960). The volcanic activity has continued through the Cretaceous and the Tertiary times and the evidence for this is in the form of abundant igneous plugs, dykes, sills and lava flows, seen on seismic data and outcrops in the Mozambique basin. These episodes of volcanic activity are the reason why the Mozambique basin is classified as a volcanic margin rather than as a typical passive margin basin (ENH-ECL, 2000).

The Mozambique basins can be generally divided into two classes: the marginal and the interior rift basins (Coster et al., 1989). The former includes the coastal Mozambique and the Rovuma Basins (Salman et al., 1995) and the latter includes the Maniamba, Lake Nyassa and the Middle Zambezi basins (Fig. 5). These five basins can be further classified according to their basin formation episodes, relative to the break-up of the Gondwana, as pre-break-up, syn-break-up and post-break-up basins.

2.2.1 Pre-Break–Up Basins

The pre-break-up basins include the northern Mozambique basins of Maniamba and the Middle Zambezi (Fig. 5). Both basins are part of the Karoo rift system, filled with late Karoo age (Permian) sedimentary rocks (Coster et al., 1989). According to Johnson et al. (1996), the middle Zambezi Graben (Fig. 5) is filled with the late Carboniferous to Permian in the lower Karoo, where lower Jurassic basalts overlie the upper section of the Triassic sedimentary rocks. This section belongs to the Upper Karoo, which was formed as a result of a pull-apart rifting, as a response to Gondwanide collision in the south, in the Cape Fold Belt (Daly et al., 1991).

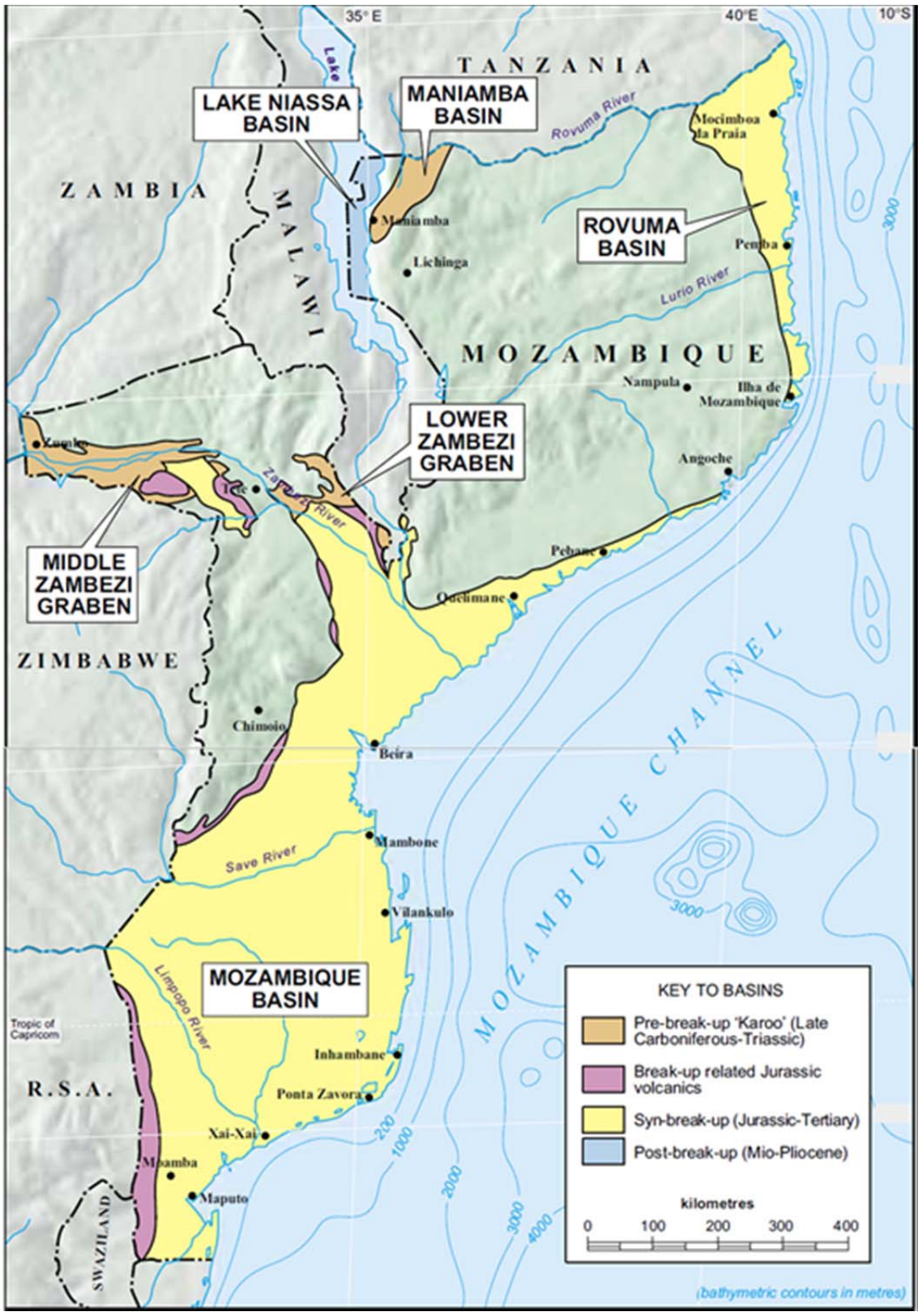

Figure 5: Mozambique sedimentary basins and present-day river systems. Two major coastal basins are recognised, the Mozambique and Rovuma basins.

2.2.2 Syn-Break-Up Basins

The coastal basins of Mozambique, namely the Mozambique and the Rovuma basins, are classified as the syn-break-up basins (ENH-ECL, 2000). The Mozambique basin (Fig. 7) is an asymmetric depression, which is bound to the north by the Mozambique metamorphic belt (Coster et al., 1989) and to the north west and south west by the Nuanetsi-Sabi monocline and the Lebombo monocline, respectively (Gwavava et al., 1992). The Rovuma basin, on the other hand, occupies the coastal section of northern Mozambique, along the Rovuma River and extends offshore to the bathymetric feature known as the Davie Ridge (Figs. 4 and 5), which is a continent-ocean transform fault, where most of the early movement during the continental separation took place (Heirtzler et al., 1971). The two coastal basins are separated by the Precambrian and Palaeozoic basement and the main difference between them is related to the changing sedimentary environment in the period of the Gondwana break up, during the Jurassic and Early Cretaceous times, when the drift of Madagascar and the sea floor spreading took place (ENH-ECL, 2000).

2.2.3 Post-Break-Up Basins

The only post-break up basin in Mozambique is the Lake Niassa basin shown in Figure 5. This is a rift basin, formed mainly during the Miocene and it represents the southern continuation of the East African Rift System (EARS), which is currently considered one of the most prolific hydrocarbon provinces in East Africa (KPMG Report, 2013). The propagation of the East African Rift System to the south resulted in the formation of local depressions, which were occupied by lakes in the past. As a result, large alluvial fans also developed due to loss of flow within these depressions caused by disruptions of the drainage of the river system (Haddon et al., 2005). Although basins in the EARS are considered to be the most prolific hydrocarbon provinces, the significant uplift of the Karoo Supergroup that took place in the Pliocene and exposed the Karoo Supergroup sedimentary rocks to erosion, might have destroyed some of the hydrocarbon-bearing traps (Haddon et al., 2005). The sedimentary section in this basin is composed of Miocene to Pliocene lacustrine and fluviatile sediments (ENH-ECL, 2000).

2.3 Mozambique Basin

The onshore Mozambique Basin, the subject of this study, covers an area of 275000 km^2 (Matthews et al., 2001), the remaining offshore part covers 105000 km^2 (Coster et al., 1989). The onshore lower Zambezi, the inner-graben and the offshore Zambezi delta also form part of the Mozambique Basin (Fig. 5). As previously stated, the basin is defined as an asymmetric depression which is bound to the south west by the Lebombo monocline where Karoo basalts dip eastwards, below the Cretaceous sediments of the basin (Fig. 7). To the north-west, the basin is bounded by another monocline, called the Nuanetsi-Sabi monocline, so the western margin of the basin is bound by outcropping Karoo igneous rocks characterised by the short- wavelength positive gravity anomaly (Gwavava et al., 1992). Cox and Bristow (1984), suggested that the Karoo volcanics young from north to south, but this is disputed by the current radiometric dating suggesting the opposite, according to ENH-ECL, 2000.

According to Matthews et al. (2001), the basin formed almost entirely on the proto-oceanic crust but Gwavava et al. (1992), argued, based on gravity modelling, that the basin could be underlain by a highly stretched continental crust. The sedimentary fill of the Mozambique basin is composed of Early Jurassic, Cretaceous and Tertiary sedimentary deposits reaching in thickness up to 12000 meters in the Zambezi Delta depression (Coster et al., 1989). The total sedimentary cover from the Jurassic to the Quaternary is thickest in the west and thins to the east, as it approaches the continental shelf.

In the northern part of Mozambique Basin, both onshore and offshore, the Zambezi Delta has been formed in an area of depressed crust (Zambezi Delta Depression), where sediment loading began in the Late Oligocene to Early Miocene (Watford et al., 2005). Further off the east of the Zambezi Delta, at the water depths of between 1000m and 2500m (Mahanjane, 2012), the Beira high is situated (Fig. 7). According to Mahanjane (2012), the origin of the Beira high could be of oceanic or continental Magmatism, or even sedimentary, with an over-print of compressional forces. However, the more plausible model is that by Koning and Jokat (2012), who postulate the existence of smaller remnant continental blocks within the northern Mozambique. In this scenario, the Beira high could be one of the remnants of the continental masses displaced during the drifting between Africa and Antarctica (Konig and Jokat, 2010). This model is also supported by a 2D flexural back stripping and gravity-magnetic modelling done by Watts (2000), using the NW-SE magnetic profile over the Beira high. This author concluded that the gravity anomaly associated with the Beira high was due to the “edge effect” which is normally caused by a continental crust

over a thin oceanic crust. The Beira high is 280 km long and 100 km wide and overlain by Mesozoic and Cenozoic sediments (Mahanjane, 2012). Sediments within the Zambezi depression onlap onto the Beira high and the sedimentary onlap is one of the under-explored play types in the offshore Mozambique Basin (ENH-ECL, 2000).

A generalized stratigraphic column for the Mozambique Basin is shown in Figure 6 (Walford et al., 2005). It is based mainly on outcrops and some of the deeper Deep Sea Drilling Program wells (DSDP), since most of the wells in the basin only targeted the shallower formations, where most of the hydrocarbon discoveries have been made. The J- and K-Reservoirs are located within the Late Cretaceous, Maastrichtian age Lower Grudja Formation. There is a missing stratigraphic section in the Early Oligocene, but in areas where the sediments exist, they are mainly of the continental detrital facies and are overlain by the Miocene Inharrime anhydrites (Walford et al., 2005).

2.3.1 Structural Framework of the Basin

According to a regional study done by Filbrandt et al., (1990), as part of their exploration effort for hydrocarbons, the structural setting of the basin occurred as a result of two main processes. The first process was the gradual platform subsidence, which is also referred to by Salman and Abdula (1973), as a broad platform depression. The results of this process can be seen in the southern part of the basin as the inner graben system represented by extensive faulting, shown in Figure 7. The other process that caused large-scale structural features, was the formation of pull-apart basins associated with strike or oblique slip on nearby major transform faults such as the Davie and the Comoro ridges as Antarctica moved away from Africa (Coster et al., 1989). Some of these structural features can also be seen in Figure7 as narrow, heavily faulted, steep sided, N-S trending basins comprising the Xai-Xai Graben complex to the south of the Inner-Graben system. These basins are 20 to 40km wide and can be clearly seen in some of the long offset 2D seismic lines in this part of the Mozambique Basin (Filbrandt et al., (1990).

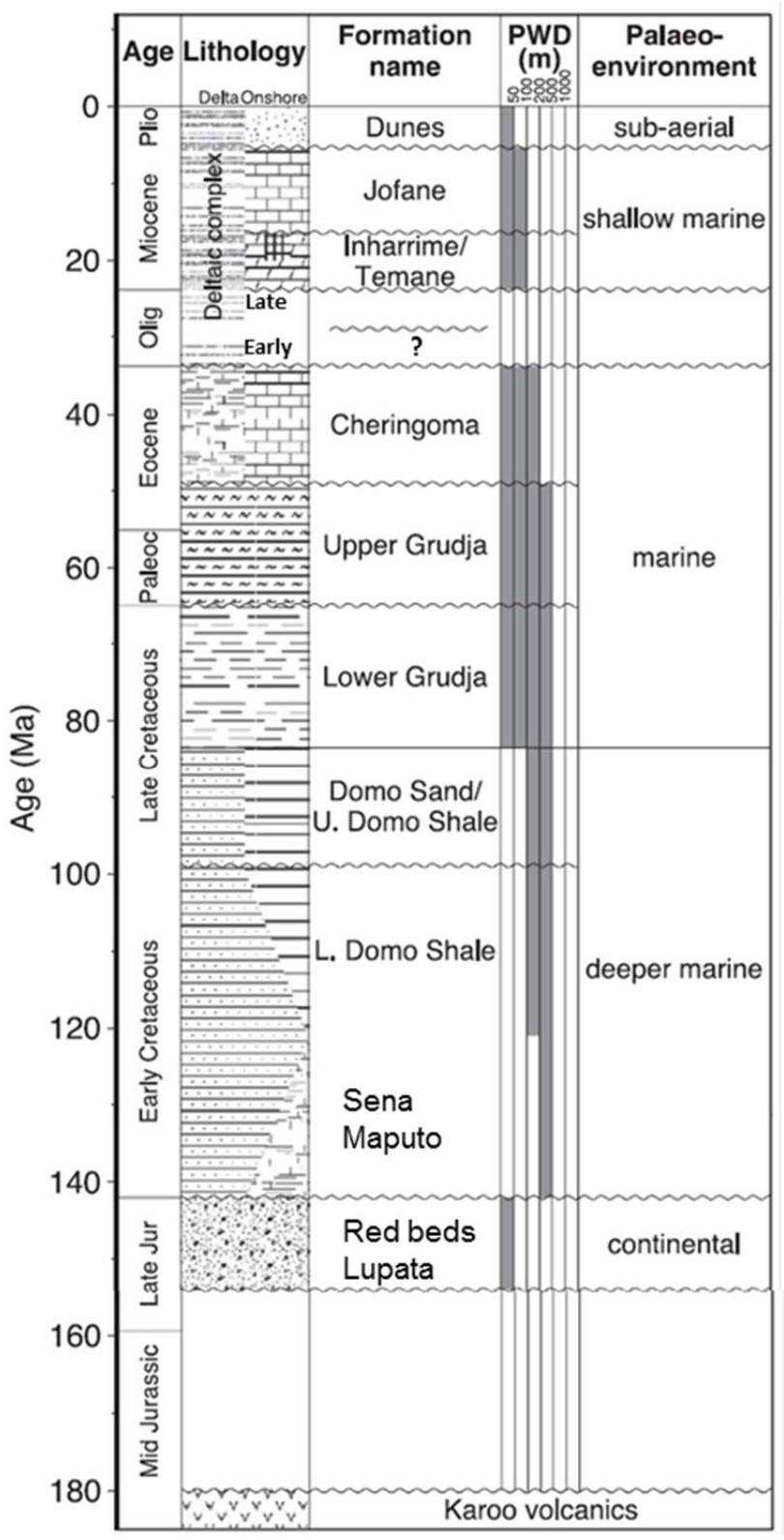

Figure 6: Generalised stratigraphic column for the Mozambique Basin (modified from Walford et al., 2005). Most oil and gas discoveries in the basin were made in the Late Cretaceous, Lower Grudja Formation.

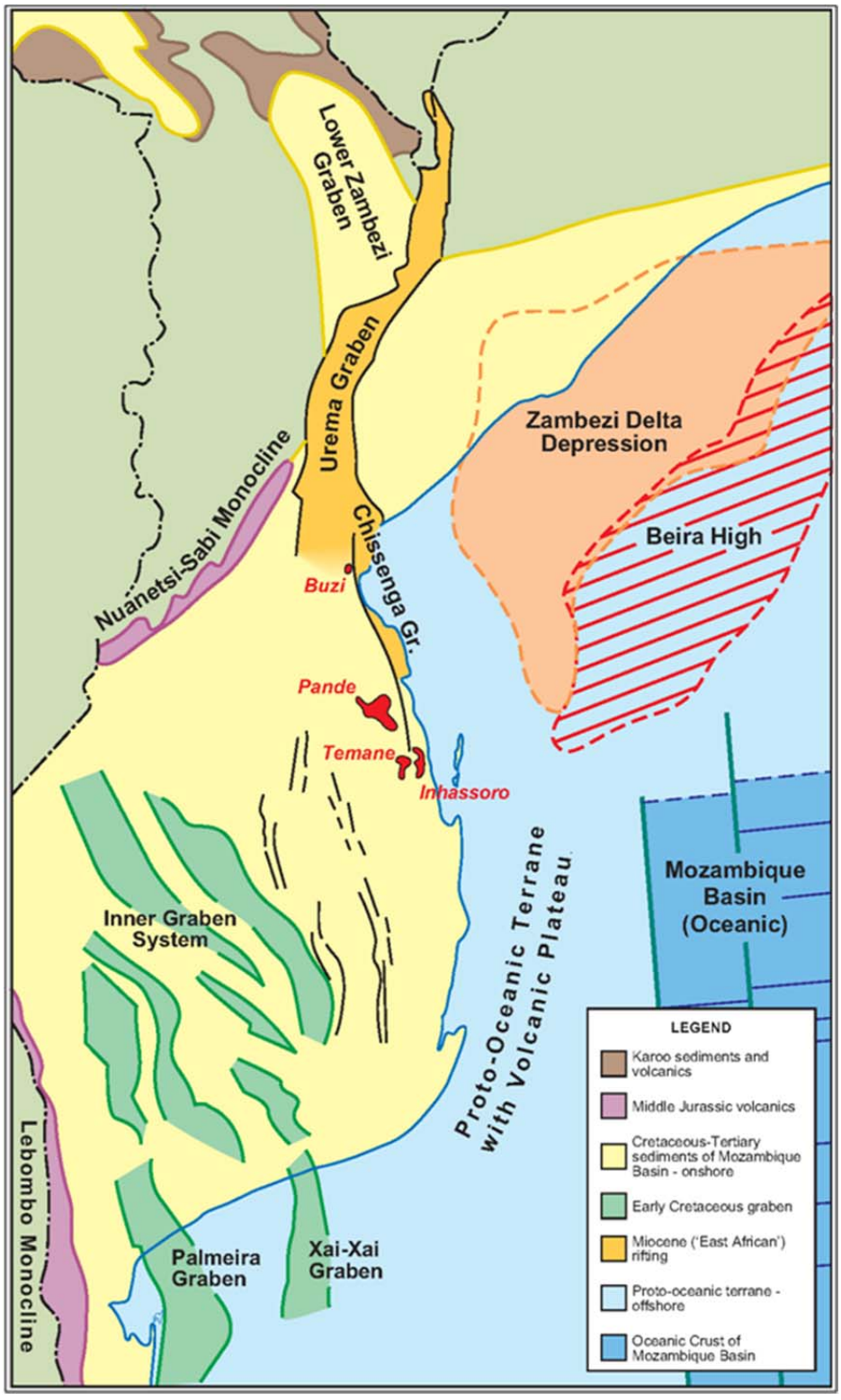

Figure 7: The structural framework of the Mozambique Basin (Matthews et al., 2001). The Mozambique Basin is essentially bounded by the Lebombo and Nuanetsi-Sabi monoclines to the south-west and north-west of the basin, respectively.

Another significant feature of the structural setting of the Mozambique Basin is the Miocene East African Rift System (EARS) in the northern part of the basin. The continuation of this

system from Eastern-Central Africa can be seen in the Lake Niassa rift to the north and in the southerly extensions of the Chire-Urema and Chissenga grabens (Fig. 7). This is a north – south trending graben system that cuts across the Lower Zambezi Graben and extends into the central onshore - offshore part of the Mozambique Basin (Matthews et al., 2001). As the depression developed, thick piles of sediments from the adjacent highlands were deposited.

2.3.2 Sedimentation - Paleo-river Systems

An unconformity dated at 150 Ma marks the beginning of the drift which was followed by the transgressive sedimentary cycle which quickly became regressive as sediment supply outpaced accommodation space (Coster et al., 1989). Depositional sequences corresponding to these phase are the Late Jurassic continental red-beds, the Early Cretaceous Sena Formation, deltaic Lupata Formation and the transitional to Marine Maputo Formation (Coster et al., 1989) as shown in Figure 6. The Late Cretaceous comprises the marine Lower Grudja Formation. The Mesozoic and Cenozoic sediments are predominantly deltaic and marine in origin (Salman and Abdula, 1995) and consist of predominantly reworked, clastic deposits in a deltaic environment (Walford et al., 2005). The Cretaceous sediments, which comprise both the continental and the marine sediments, directly overlie the Karoo paleo-surface and represent a transgressive surface (Flores, 1973). The main conduits for transportation of sediments in Mozambique Basins are the paleo-river systems (Fig. 8), which include inter-alia, the paleo-Zambezi river that is considered to be the largest eastward draining river in Africa (Wellington, 1955). One of the main sediment depo-centres in the Mozambique Basin according to Moore et al. (2001), is in the area around the North Save River mouth (Fig.5) but some of the sediments could have been sourced from the north, around the Beira area, based on the geometry of the basin.

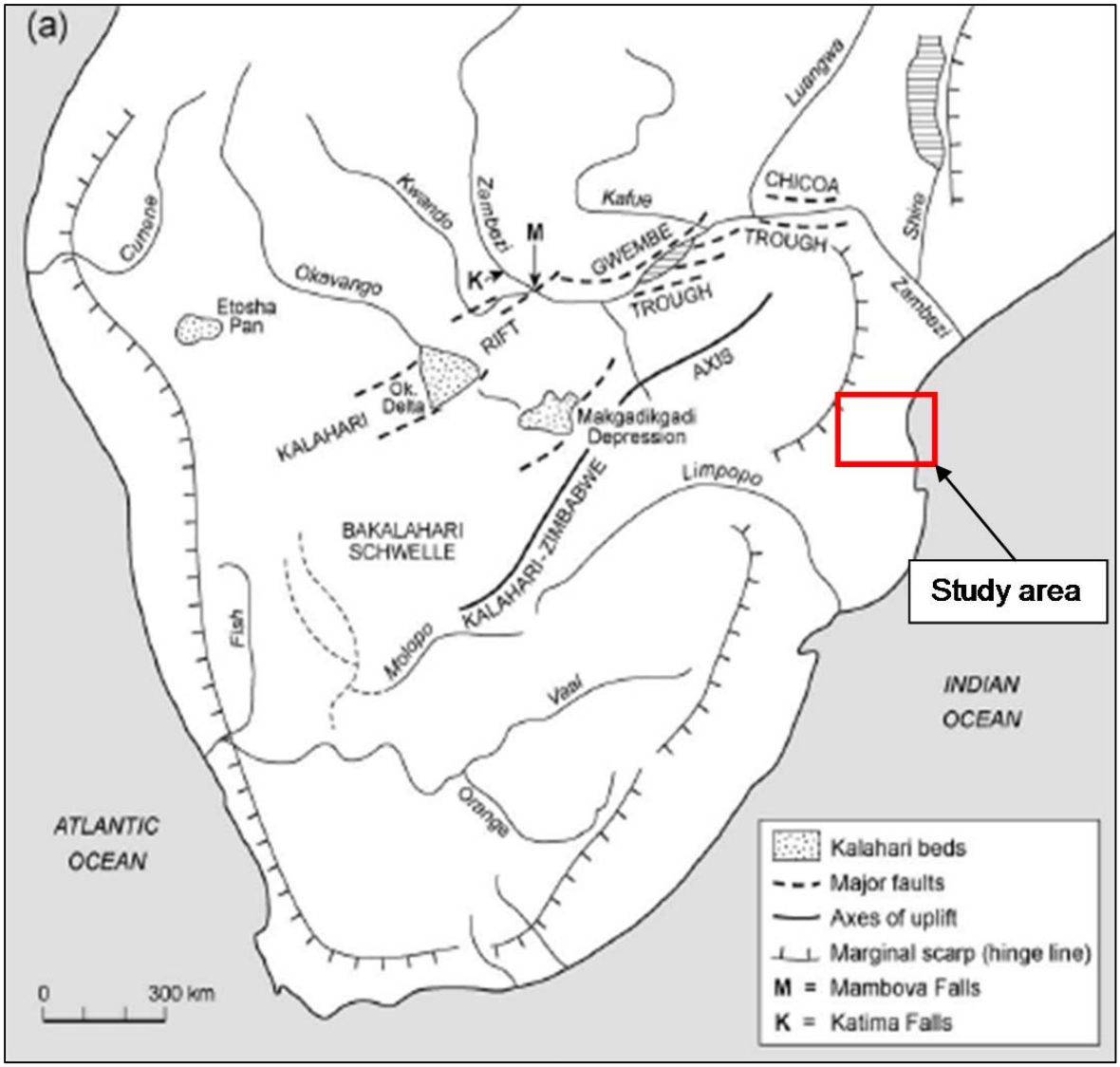

Figure 8: Drainage system in southern Africa (Goudie, 2004 and Thomas et al., 1991). The main conduits for transportation of sediments in Mozambique Basins are the paleo-river systems, which include inter-alia, the paleo-Zambezi river which is considered to be the largest eastward draining river in Africa

2.3.2.1 Continental Sediments

The sandstones and conglomerates of the Sena Formation were deposited during the upper Cretaceous and according to Moore et al. (2001), these are continental facies deposited at the inner margin of the coastal plain, whereas the marine sediments such as the offshore equivalent of the Sena Formation, known as Maputo Formation (Flores, 1973 and Coster et al., 1989), were deposited mostly at the outer margin.

2.3.2.2 Marine Sediments

The marine sediments were deposited during widespread marine conditions that prevailed during the Senonian times up to the Palaeocene. The Grudja Formation that hosts the J- and K-Reservoirs as well as the younger, algal, oolitic Cheringoma limestone of Eocene age (Flores, 1973), forms part of these marine deposits. The Grudja Formation consists of the shaly Upper Grudja and the Lower Grudja, which comprises clay with inter-beds of glauconitic and marly sandstone (Walford et al., 2005). The Palaeocene was also a time of water depth becoming shallower (Walford et al., 2005) and marking the beginning of a regression, that continued in the upper Eocene (Flores et al., 1973).

2.3.3 Depositional Systems

Different depositional systems exist in the Mozambique Basin, ranging from deltaic to marine or near shore-face depositional environments (Fig. 9). Several core data were analysed in the past by consultant companies to better understand the depositional environment of the two main gas producing reservoirs in Mozambique Basin, the J- and K-Reservoirs. Analysis of the core samples collected from both reservoirs was used to characterise the reservoir texture and mineralogy. The core analysis indicates that the J- and the K-Reservoirs are generally characterised by a variety of burrows and a high degree of bioturbation. This is indicative of a shallow-marine, low-energy depositional environment (Howard et al., 1981).

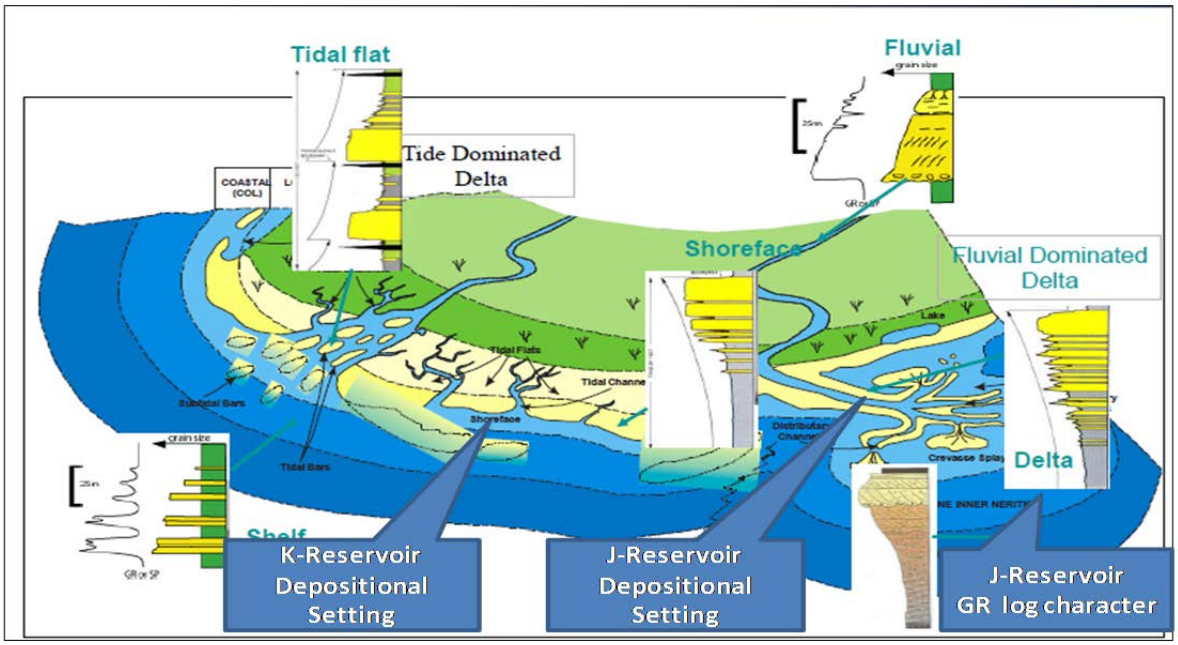

Figure 9: Various depositional systems within the Mozambique Basin. The J- and the K-Reservoir fall within the fluvial delta and shore-face depositional environment, respectively. Diagram after Watfa, (2012).

2.3.3.1 Depositional System: J-Reservoir

The core images in Figure 10 and Figure 11 show the reservoir section of the J-Reservoir at well A15, where it represents a fine to medium-grained sandstone. Lamination seen in Figure 10 is an indication of near-shore facies as described by Howard et al. (1981). Dwelling burrows are more abundant than feeding burrows and this is indicative of a high-energy environment (Pemberton, 2001). The J-Reservoir represents mainly a deltaic facies input from a paleo-river systems, mainly the Paleo-Zambezi and Paleo-Limpopo rivers (Fig. 8). This is consistent with Gwavava et al. (1992), who asserted that this part of the Mozambique Basin consists of at least 6km thick sediments that represent the paleo-deltaic environment, based on gravity modelling.

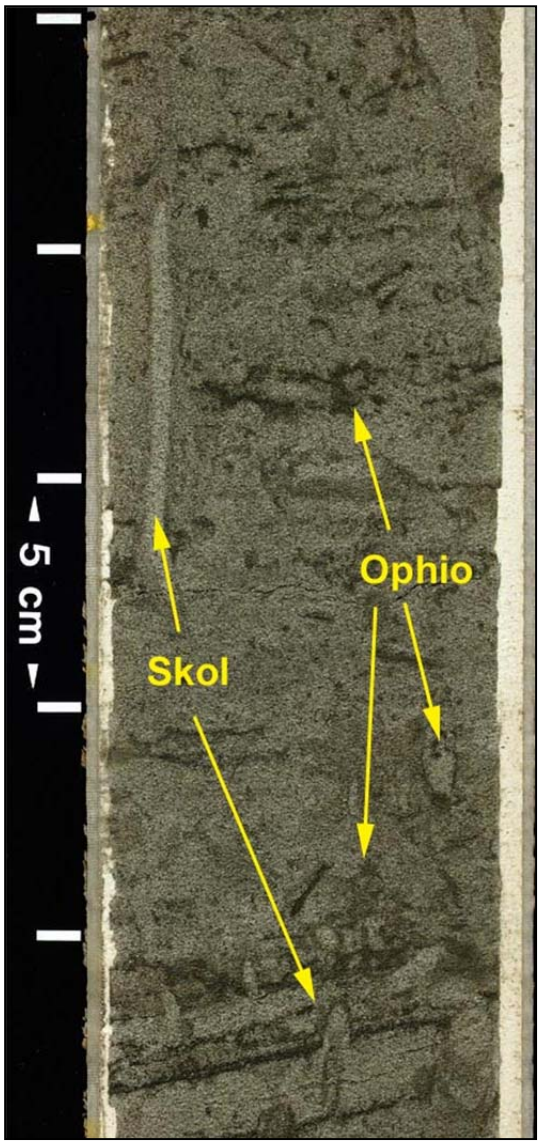

Figure 10: Core Image I: J-Reservoir, well A15 at depth 1157 m. Dwelling burrows of Ophiomorpha and Skolithos were identified in this core image as shown above.

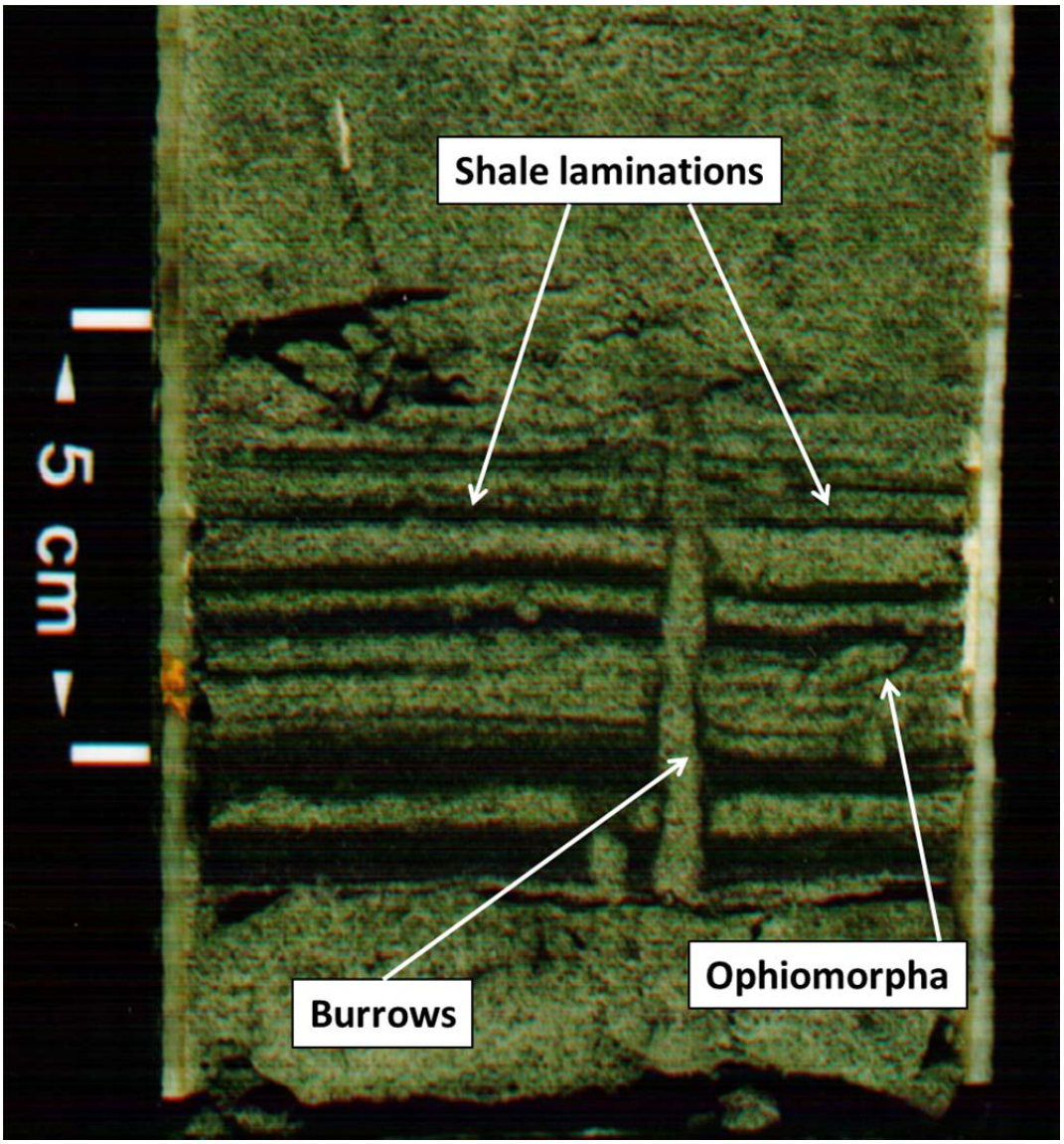

Figure 11: Core Image II: J-Reservoir at depth 1160.75 m, well A15. Shale lamination and escape burrows were observed in the core. Dwelling burrows are also present, as seen in the core image (Ophiomorpha).

2.3.3.2 Depositional System: K-Reservoir

The K-Reservoir can be divided into three lithological sub-units, based on the log character and some paleontological evidence from core data samples retrieved from the reservoir section. However, the focus of this study will be the upper most section of the K-Reservoir, which is the main gas producer reservoir in Field B. The oyster shell fragments, which appear to have been transported from their initial place of origin, can be seen in the core image of the K-Reservoir (Fig. 12). This is evidence of a near shore to coastal, marine depositional environment and the absence of bioturbation or encrusting of the fragments is

indicative of low-energy environment and very short exposure (if any) before being buried. Some evidence of sub-aerial exposure such as linear mottling (roots) can however, be seen in some cores, as well as dwelling burrows such as Ophiomorpha and Skolithos (Gerard et al., 2008). More shell and oyster fragments can be seen in the B12 core in Figure 13.

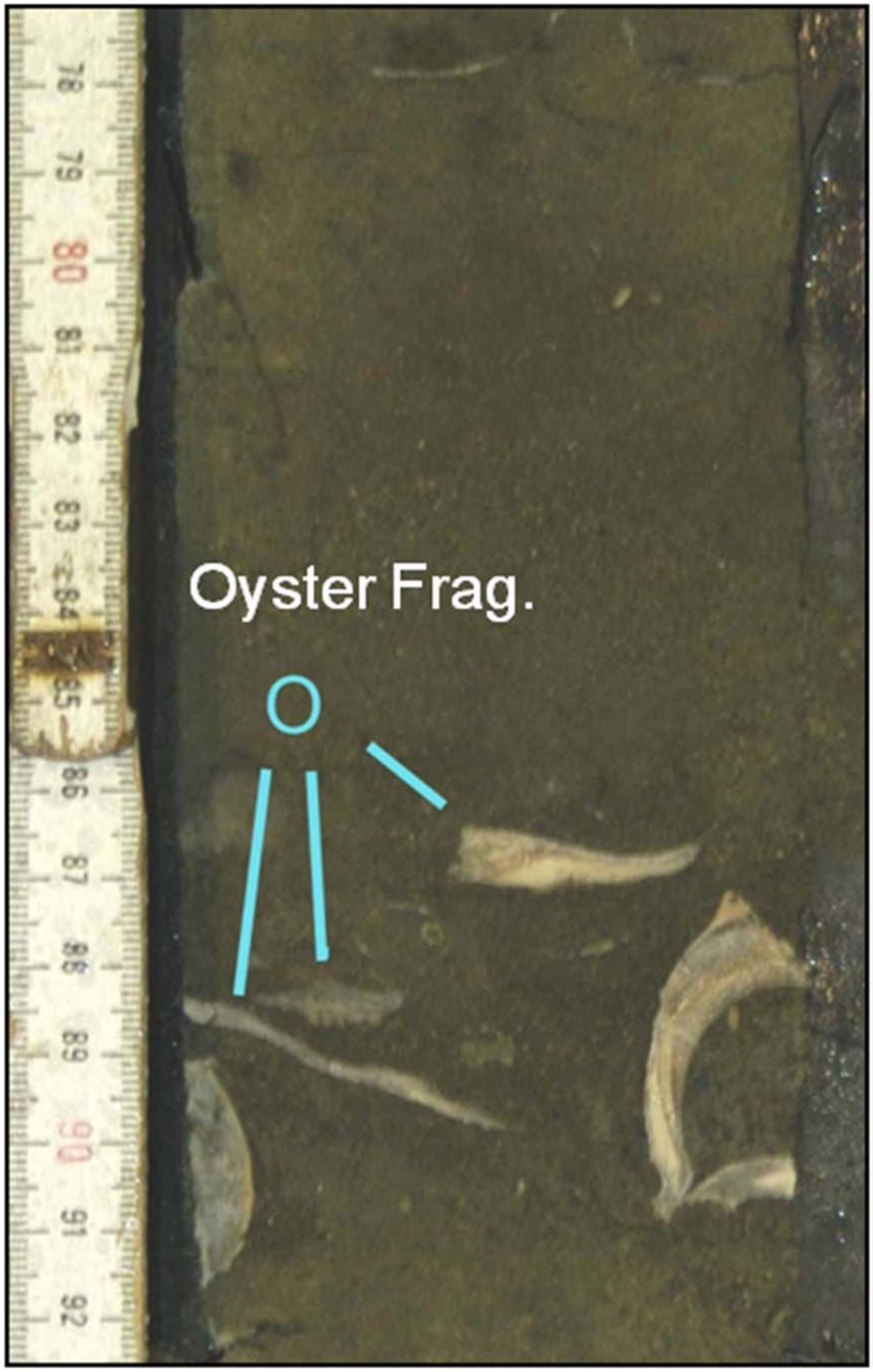

Figure 12: Core Image III: K-Reservoir, well B13. Oyster shell fragments can be seen in the core image. The low level of mechanical damage of the shell fragments by wave action indicates a short re-deposition distance and rapid burial and also low-energy depositional environment (Howard et al., 1981). Oyster banks are often situated in high energy rocky

environments and must have been swept from there into a low-energy depositional area, as evidenced by the fine grained matrix.

Based on the core evidence described above, the depositional environment for the K-Reservoir can be generally described as marine, inter-bar, shelf mudstone and shelf bar margin (OMNI, 2007).

Figure 13: Core Image IV: K-Reservoir at depth 1299.25 m, well B12. Fragments of shell, probably oyster or any marine fossil such as pelecypods (Gerard et al., 2008) can be seen in this core image.

2.4 Facies Analysis

Several reservoir and non-reservoir facies have been identified over the years in the Mozambique Basin and they can be broadly classified into continental and marine facies, depending on the conditions that prevailed at the time of deposition (Coster et al., 1989).

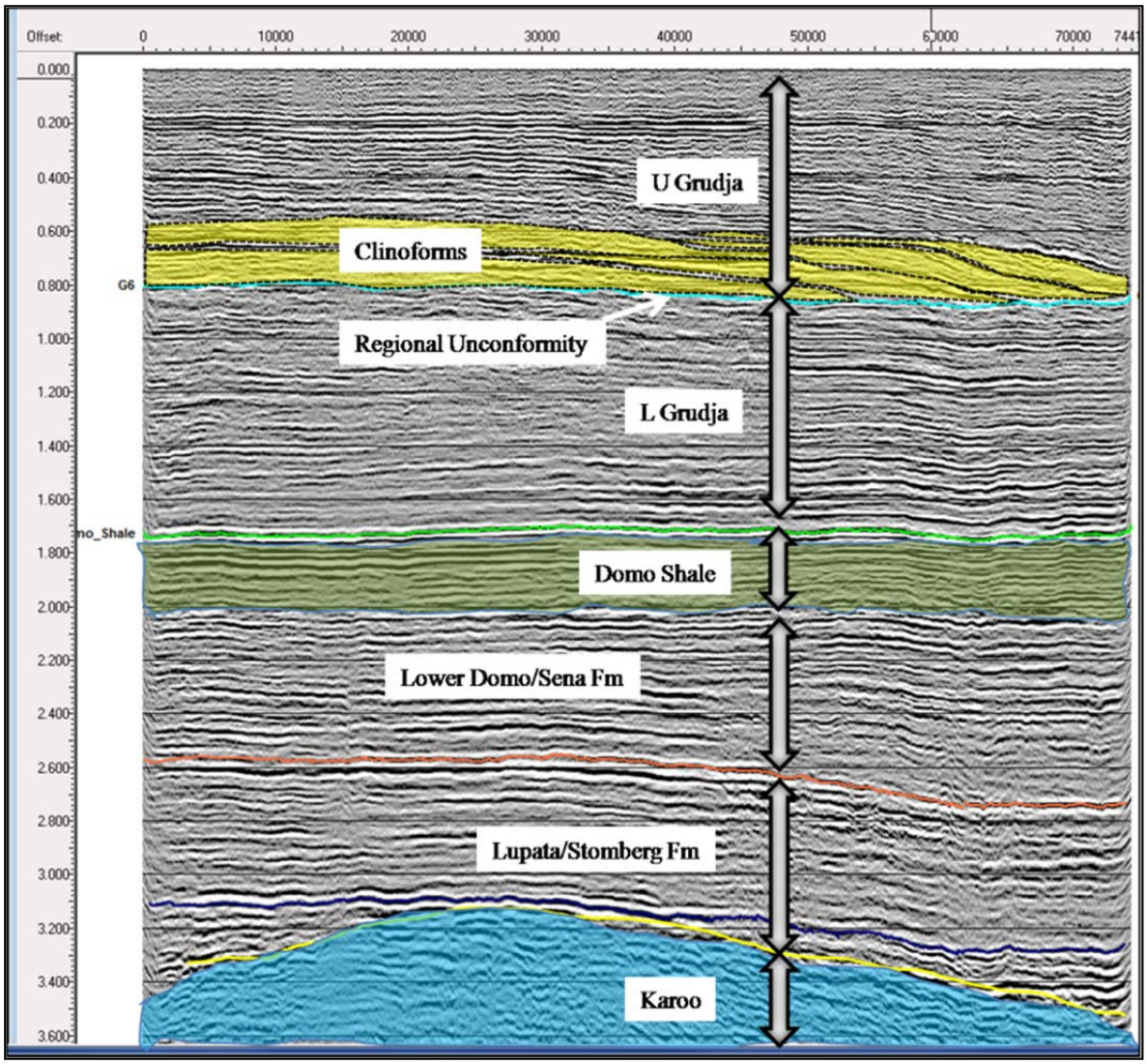

Figure 14: Regional unconformity as shown as the base of the clinoforms (yellow) on the 2D seismic section. This unconformity separates the Upper Grudja Formation from the Lower Grudja Formation.

The Grudja Formation, which hosts the J- and K-Reservoirs, can be further sub-divided into the Upper and the Lower Grudja sections. The two sub-divisions are separated by a regional Maastrichtian unconformity, visible as a strong seismic reflector on a seismic cross section in Figure 14. The Late Cretaceous J- and K-Reservoirs are part of the Lower Grudja Formation (Flores, 1973). Laterally, the transition between continental and marine facies is relatively unknown, but Figure 15, which is modified from the regional study commissioned by

Filbrandt et al., (1990), shows roughly the transition between the two facies. The continental facies, as shown in the stratigraphic column in Figure 6, are expected to be in the deeper section towards the Late Jurassic (Walford et al., 2005) and grade eastwards into the Cretaceous, Eocene and Late Oligocene marine beds (Flores, 1970).

2.4.1 Continental Facies

Precambrian, crystalline and metamorphic rocks form the common basement for Mozambique Basins (Salman et al., 1973) as shown in the generalised stratigraphy in Figure 6. The continental facies grade eastwards and upwards into the Upper Cretaceous, Eocene and Late Oligocene marine beds (Flores, 1970). These continental facies are characterised by arkosic, poorly sorted sandstones, siltstones and conglomerates that are inter-bedded with red and grey shales (Filbrandt et al., 1990).

During the Upper Jurassic, following the period of intra-cratonic rifting that gave rise to the break-up of Gondwanaland, arid conditions led to the deposition of red claystones and silts along the eastern margin of the basin. These are commonly known as red-beds and contain minor amounts of anhydrite (Filbrandt et al., 1990). The Cretaceous coastal plain, possibly dominated by paralic or lagoonal deposits, was relatively wide and formed a boundary to a low angle continental shelf in the south.

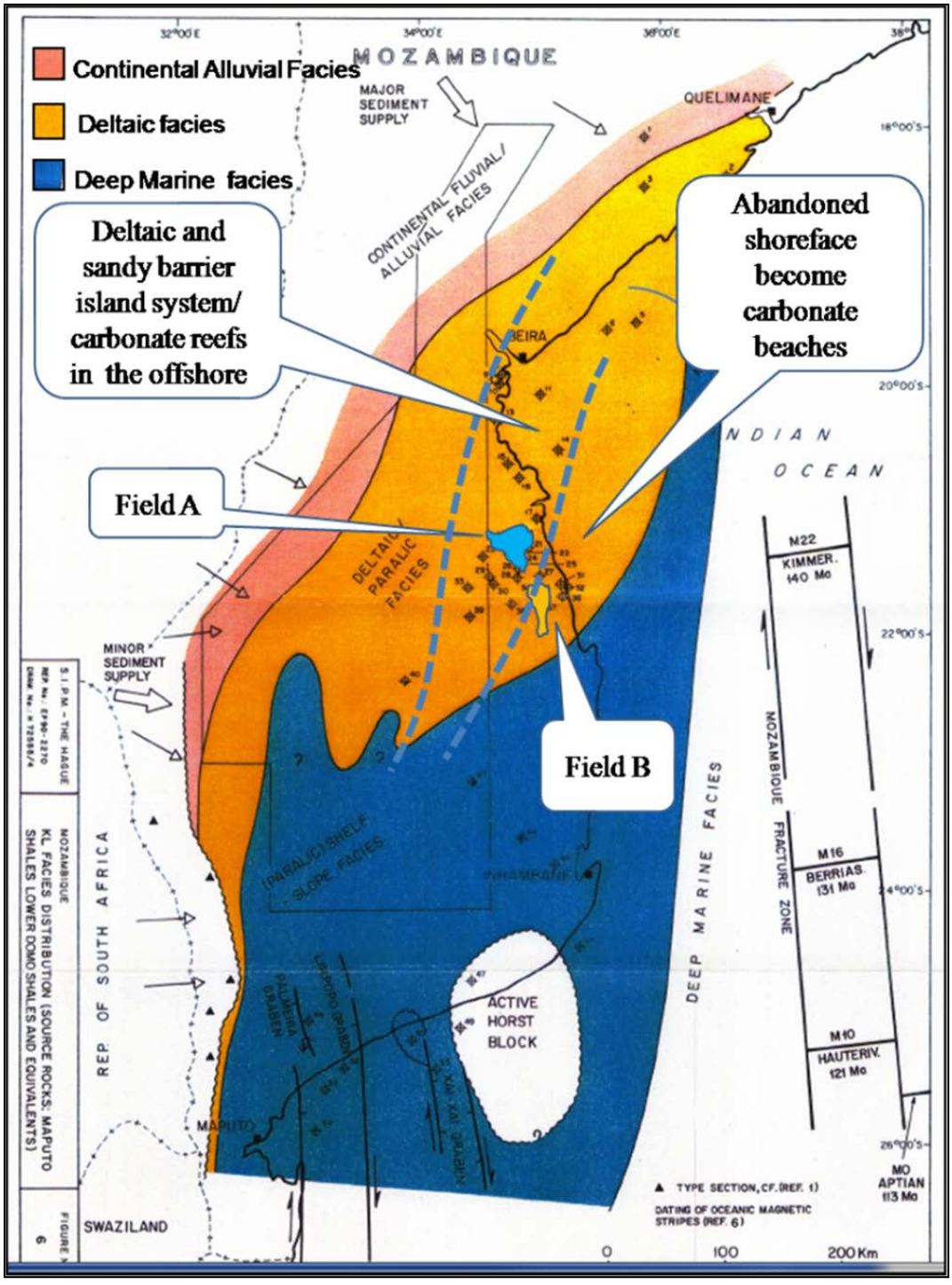

Figure 15: Facies boundary map (modified from Filbrandt et al., (1990). Continental, deltaic and marine facies delineated according to regional facies distribution. The J- and K-Reservoirs fall within the deltaic environment.

2.4.2. Marine Facies

Marine conditions were developed as a result of the Antarctica's and Madagascar's southwards drift relative to Africa (section 2.2). These conditions are represented by the

transgressive Maputo Formation, which is interpreted as slope deposits (Coster et al., 1989). Marine facies also exist above the Lower Grudja Formation (younger sequence known as the Upper Grudja Formation) and these are known to occur within the central part of the Mozambique Basin, where the Upper Grudja Formation is represented by a section of algal and oolitic limestone of the Cheringoma Formation, of Eocene age. This formation extends eastwards into the subsurface of the coastal area (Flores, 1970).

The Lower Grudja Formation is underlain by another marine facies deposited during the Late Cretaceous rise of sea level, the shale facies of the Upper Domo Shale Formation. Directly underneath the Upper Domo Shales are the sandstone facies of the Late Cretaceous Domo Sandstone Formation which overlay the Early Cretaceous Lower Domo Shale Formation. The deposition of the shales of the Lower Domo Shale Formation is attributed to the conditions associated with the rifting phase (deepening of the basin) and according to Flores, (1970), has very little sand intercalations.

2.5 Source Rock and Thermal Maturity

None of the wells drilled in Mozambique Basin have penetrated a source rock but several wells drilled in the south of the Mozambique Basin proved poor to moderate organic rich shales in the Domo Shale section. The Domo Shales have in the past been considered to be one of the source rocks in the Mozambique Basin, next to the Karoo sedimentary rocks (Filbrandt et al., 1990) The shales were deposited when Madagascar was drifting southwards, in the Kimmeridgian until the Barremian. Ocean crust was generated in the offshore part of Mozambique Basin and fully marine conditions, provided a unique environment for the development of anoxia and the formation of possible oil and gas prone source rocks. These fully marine conditions are first represented by the transgressive Maputo Formation, which is classified as slope deposits (Coster et al., 1989). However, the regional low geothermal gradient of approximately 2^{o}C /100m implies that the required depth for peak source rock maturity greatly restricts the potential charge capacity in the basin. The geothermal gradient is supported by the results of the Deep Sea Drilling Project (DSDP) wells drilled to the south of Mozambique, South Africa and on the Falklands Plateau, which also penetrated the Jurassic to Cretaceous black shales with high total organic carbon (TOC) content (Filbrandt et al., 1990). The shales closer to the continental margin owe their high TOC content to the presence of lignite, i.e. coal prone source rocks (Filbrandt et al., 1990). Even though the Lower Domo Shale Formation has traditionally been considered to be the main source rock in both fields, maturity considerations suggest that there is also

another deeper, pre–Tertiary source rock, possibly in the syn-rift section (Filbrandt et al., 1990).

CHAPTER 3: Case Study (J- and K-Reservoirs)

The outline of the J-Reservoir (Field A) and K-Reservoir (Field B) are shown in Figure 16. The gas fields are geographically located about 50km from each other and closer to the present day Mozambique coastline. The geometry of the fields is based purely on the extracted seismic amplitude anomaly and well control. The two reservoir formations exhibit low-resistivity phenomena, as described in section 3.2.

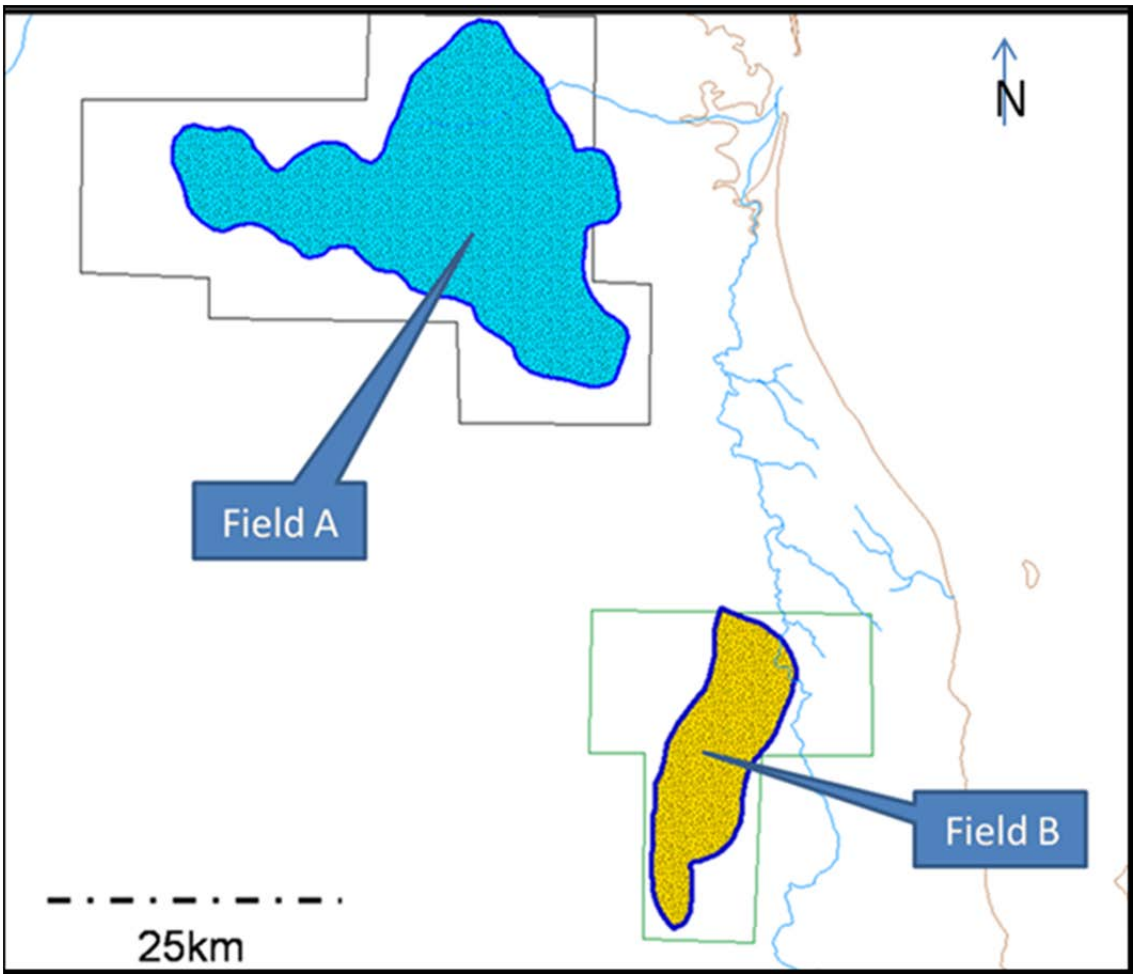

Figure 16: The outline of Field A and Field B, as defined by mapping and amplitude extraction on 2D seismic lines.

3.1 Reservoir Architecture

- **Architecture of the J- Reservoir**

The seismic amplitude map of the J-Reservoir is shown in Figure 17. The map also represents the lateral extent of the gas accumulation in the J-Reservoir. The 600 km^2 field represents deltaic deposits.

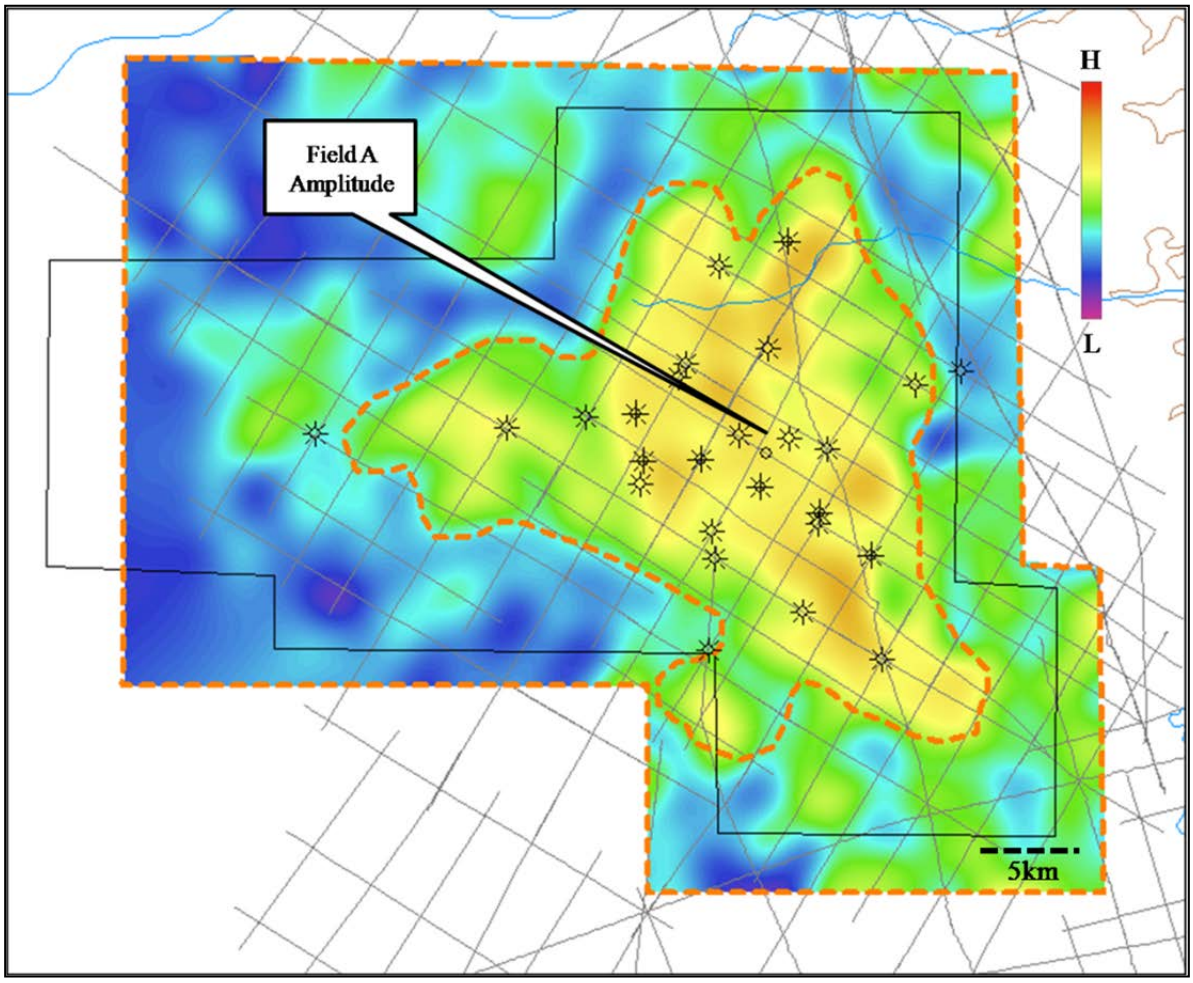

Figure 17: The seismic amplitude map generated from the top of the J-Reservoir horizon. The extent of the reservoir is also defined by well control.

The high seismic amplitude (orange to yellow colour) represents a “soft” acoustic impedance response caused by the presence of gas in the reservoir. The strong amplitude dies out towards the edges of the reservoir which represents a stratigraphic, lateral trapping mechanism for the gas within the reservoir. In addition to the stratigraphic trapping, the depth structure and isopach maps indicate that there is a structural trapping component to the J-Reservoir, i.e., there exists a structural closure to the north of the J-Reservoir. Two cross-sections were generated by the author across the reservoir using well-to-well gamma-

ray log correlation to explain its geometry and to demonstrate the extent of the reservoir in the E-W and N-S directions (Fig.18 and Fig.19).

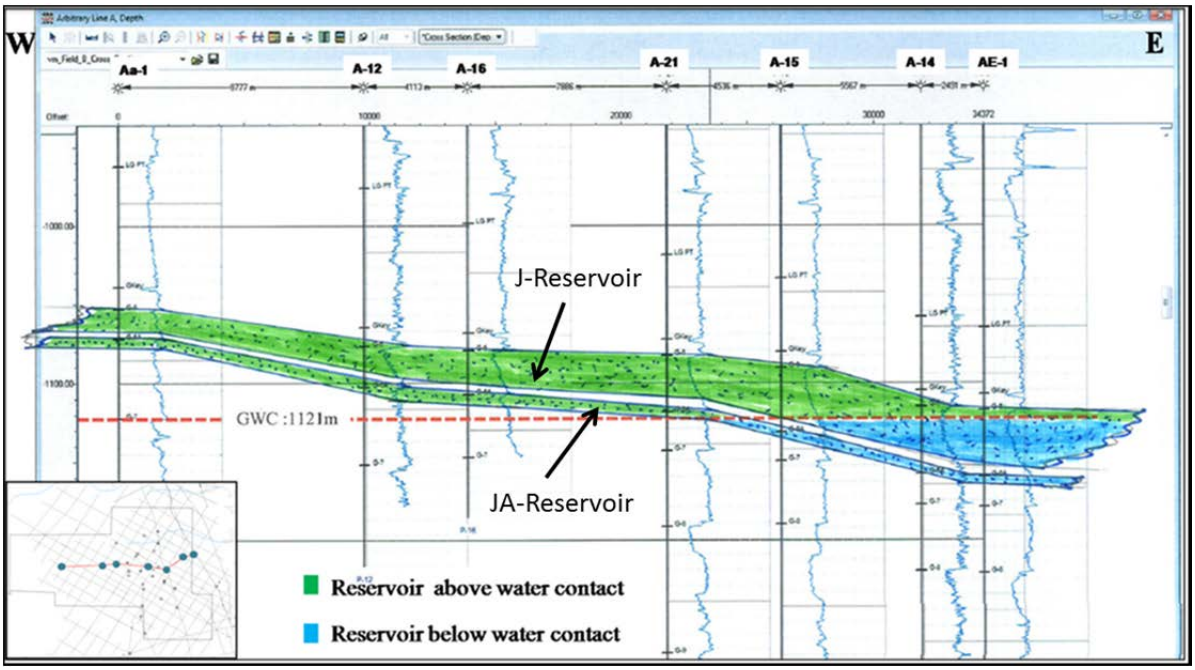

Figure 18: The east-west cross-section through the J-Reservoir, Field A shows a shallow dip (4^{o}) to the East. The gas water contact (GWC) is also shown as a red dashed line at 1121 m TVD. Insert: Basemap shows the location of this E-W section.

A shallow dip of approximately 4^{o} to the east was measured for the J-Reservoir, which is a slightly shallower dipping angle (but in the same direction), than the dip angle measured in the K-Reservoir of Field B, which, was measured to be 7^{o} to the east. The gas-water contact (GWC) at 1121 m of total vertical depth (TVD) shown in Figure 18 and Figure 19 is supported by both petrophysical evaluation and the reservoir pressure data (Appendix 12). The J-Reservoir thickens to the east, which is indicative of the ocean-ward progradation of a delta. A thin discontinuous reservoir (JA-reservoir) exists below the main J-Reservoir with a constant thickness across the Field A and a pinch out to the south. This is a separate, thin and non-productive reservoir in Field A. The N-S section in Figure19 shows a relatively flatter reservoir profile with a structural high around Well A21, which supports the existence of a structural trapping component on the J-Reservoir.

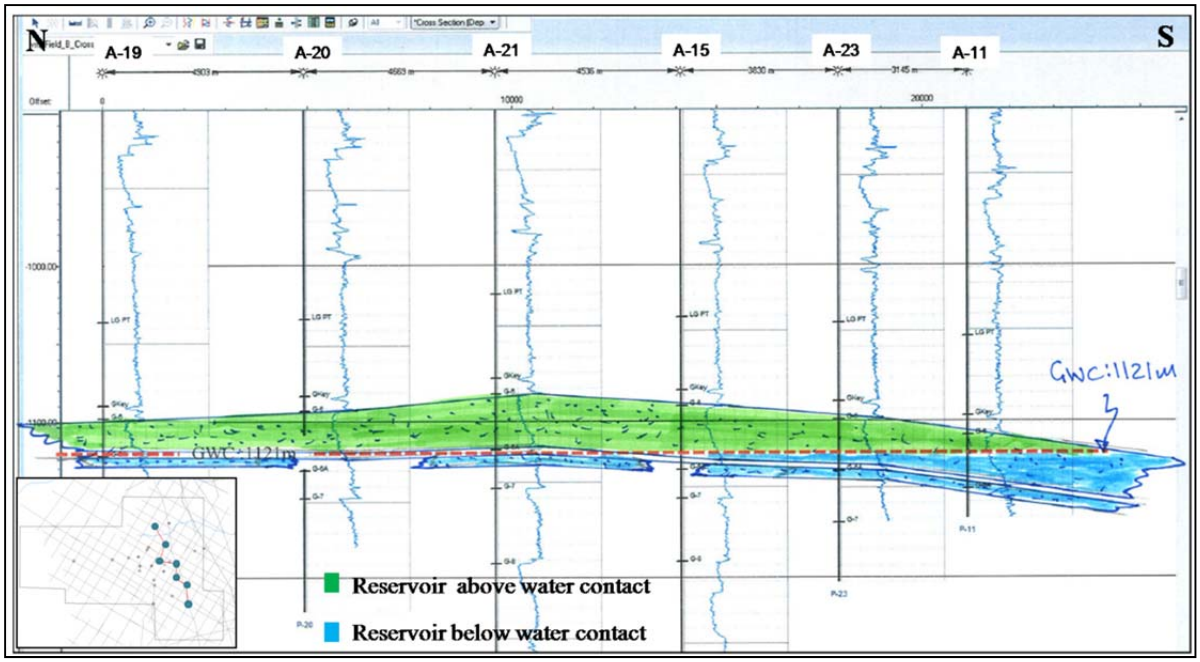

Figure 19: The north-south cross section through the J-Reservoir shows a shallow dipping to the south. Insert: Basemap shows the location of this N-S section.

- **Architecture of the K- Reservoir**

The K-Reservoir is divided into three lithological sub-units, the sub-division of these units denoted K-Reservoir, KB-Reservoir and KC-Reservoir, is based on the gamma ray (GR) log response and the bio-fossils assemblages. The seismic amplitude map shown in Figure 20 was extracted from the top of the upper most, main reservoir, the K-Reservoir. Due to the inability of the seismic data to resolve the three lithological sub-units of the K-Reservoir, the amplitude anomaly is representative of all three sub-units mentioned above.

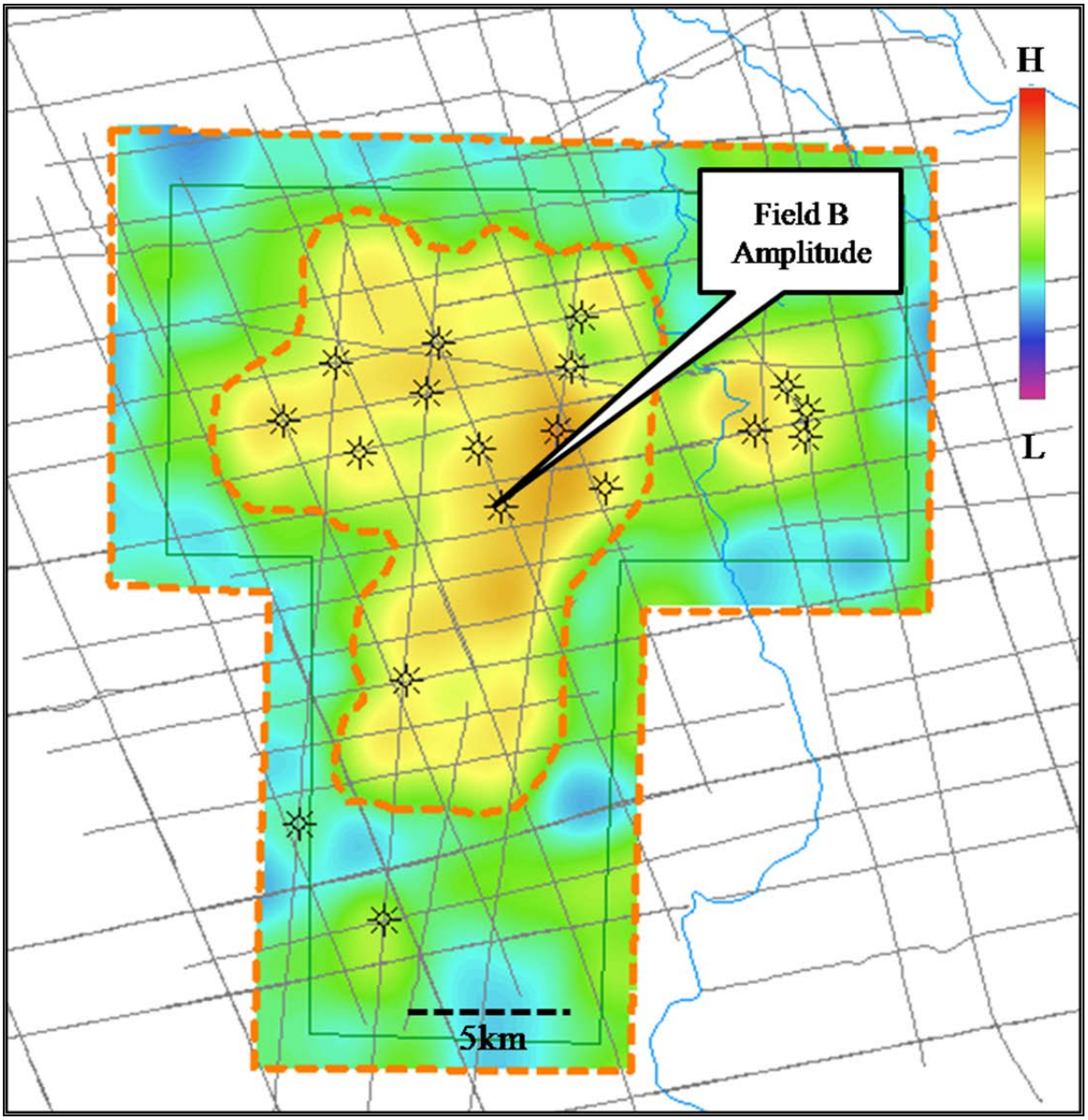

Figure 20: The outline of Field B as defined by an amplitude map generated from the top of the K-Reservoir horizon. The extent of the reservoir is also defined by well control.

The K-Reservoir can also be classified as a combination of both stratigraphic and structural trap. The east-west, well to well correlation of the gamma ray (GR) log is shown in Fig. 21. The profile indicates an almost flat structural profile to the west of the reservoir and dip changes halfway through the reservoir to an eastward dip of about 7^{o}. A small displacement or fault can also be inferred to the western most part of the reservoir, and has been confirmed on the seismic section in the proximity of the B6 and B11 wells. The N-S profile shown in Figure 22 shows a generally flat profile with a slight dip to the south close to well B17.

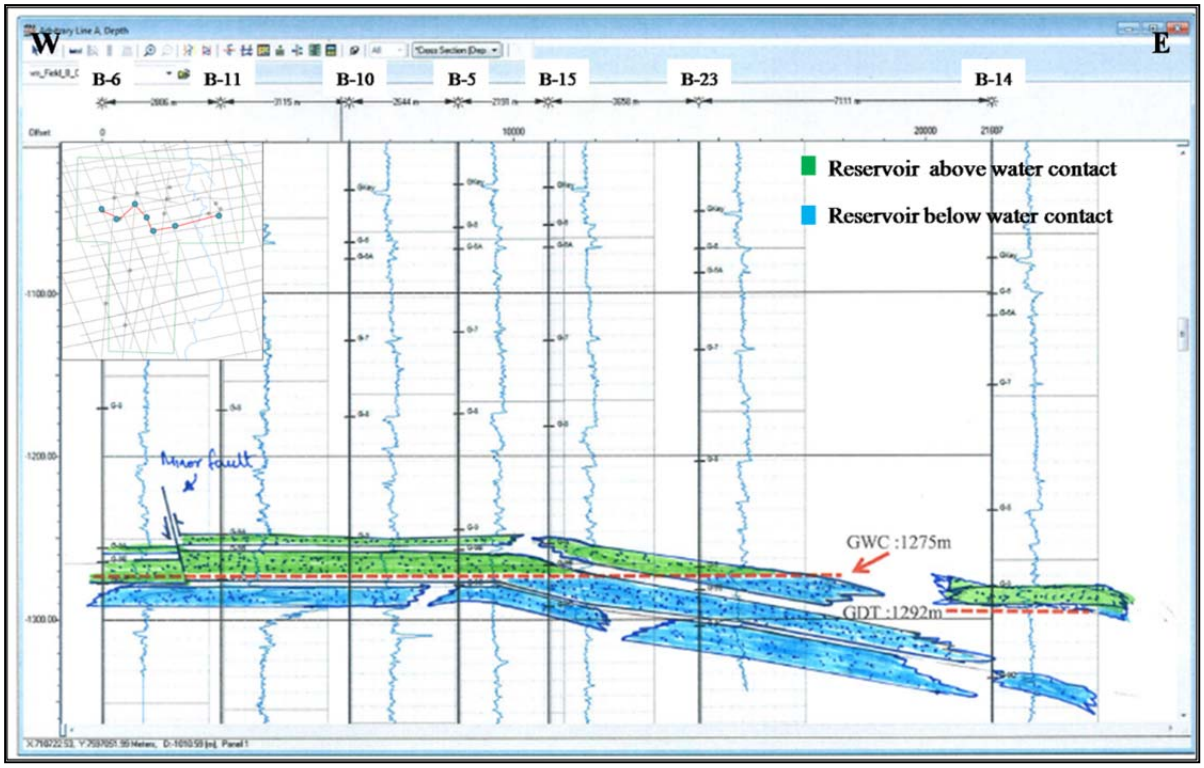

Figure 21: The east-west cross section through the K-Reservoir shows two gas water contacts (GWC) area also shown as red dotted lines. The reservoir is slightly dipping to the East. Insert: Basemap shows the location of this E-W section.

Based on core description, the K-Reservoir is not a continuous reservoir but a series of discontinuous sand bodies, typical of a deltaic depositional setting. Two gas water contacts (GWC) were identified based on the seismic and pressure data. The western part of the reservoir (from well B6 to well B23) has a gas water contact (GWC) at 1275 m TVD and the eastern part (around B14) has a gas water contact at 1292 m TVD. Based on these differences in pressure as well as the geochemical differences between the gas accumulations to the east and the west, Field B can be divided into two separated accumulations but this study will refer to both fields collectively as Field B.

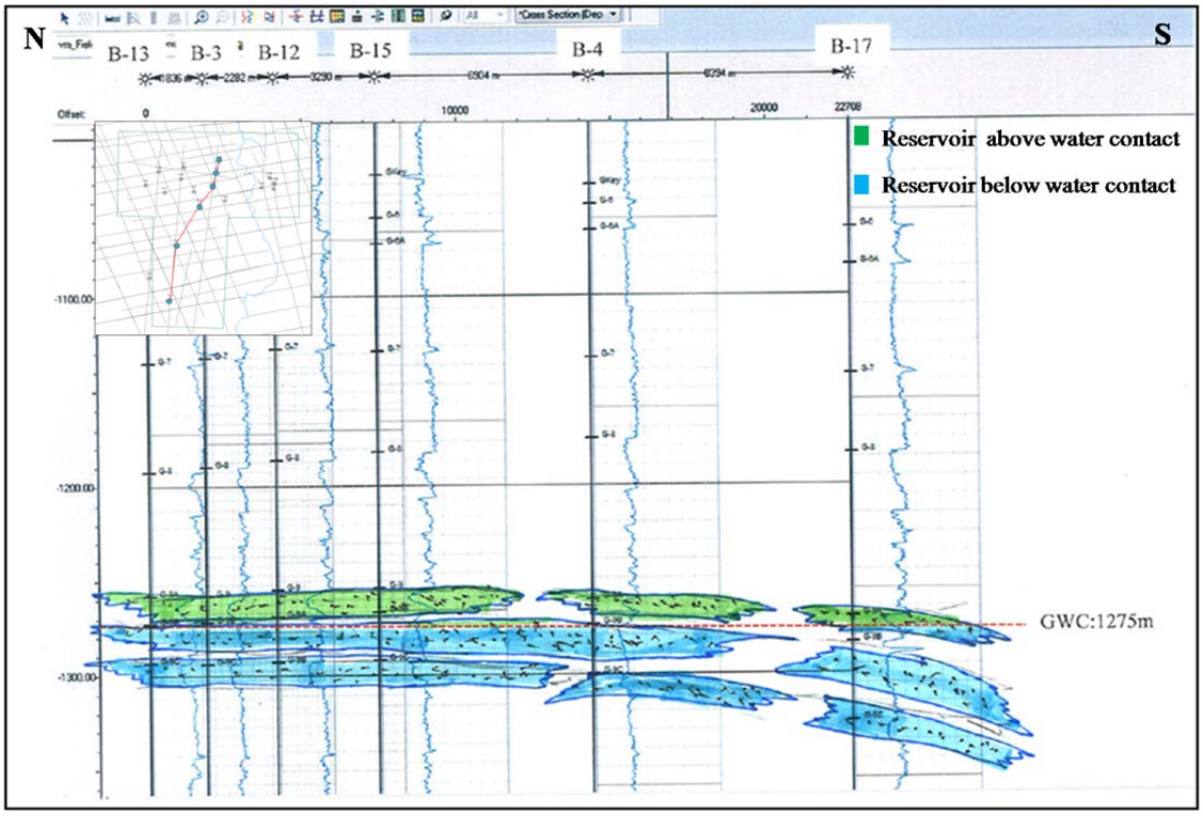

Figure 22: The north-south cross section through the K-Reservoir shows a generally flat with a slight dip to the south close to B17. Insert: Basemap shows the location of this N-S cross-section.

3.2 Definition: Low-resistivity Pay

Low-resistivity pay zones can be defined as zones of low-resistivity contrast between a brine-water-bearing section of the reservoir and the hydrocarbon-bearing (oil or gas) part of the reservoir, rather than the absolute low-resistivity of the formation (Worthington, 2000). According to Worthington (2000), various causes for the low-resistivity pay zones have been documented in the past four decades and Hamada et al. (2000) sub-divided the cause of low-resistivity pay zones into two main categories:

I. The first category refers to reservoirs where the actual water saturation is high but water-free hydrocarbons are produced. This, according to Hamada et al., (2000), is mainly caused by micro-porosity (see section 4.5).

II. The second category refers to cases where the calculated water saturation is higher than the water that is produced during hydrocarbon production. This is often caused by the presence of conductive minerals such as pyrite, metal sulphides and graphite in the reservoir. This situation can lead to a sub-economic exploitation of the reservoir.

The inability to accurately calculate the water saturation in a hydrocarbon-bearing reservoir due to the low-resistivity phenomena has an impact on hydrocarbon exploration, field appraisal and field development. In conventional oil and gas wells, water is brought to the surface as a by-product of oil and gas production, this water plays a significant role in the profitability of oil and gas production. It is therefore important to accurately predict the water production associated with the production of hydrocarbons so that better water handling facilities such as water disposal wells can be optimally designed.

During the exploration phase, a combination of conventional logs such as resistivity, density and neutron logs are used to evaluate hydrocarbon pay zones in normal resistivity reservoirs. However, due to the failure of conventional log analysis to accurately determine the petrophysical properties in low-resistivity pay, potential hydrocarbon pay zones may be overlooked and mistaken for water bearing zones. A discovery of hydrocarbon accumulation is normally followed by an appraisal phase in which delineation wells are drilled to ascertain the areal extent of the accumulation. Inaccurate water saturation calculations may lead to an underestimation of the potential size of the discovery and the hydrocarbon accumulation may ultimately be deemed to be non-commercial.

3.3 Problem Statement

The probable causes of low-resistivity pay zones have been documented in various parts of the world. These causes are directed at specific reservoirs or particular depositional environment and therefore, may not be directly applicable to other reservoirs, where conditions initially appear to be similar (Worthington, 2000). It is therefore necessary to study and better understand the specific causes of low-resistivity pay zones in Mozambique in order to improve future exploration and exploitation of hydrocarbons in the basin. The two main problems that this study seeks to address are:

I. The cause of the low-resistivity phenomena associated with the J- and K- Reservoirs of the Mozambique Basin.
II. To recommend an algorithm and a workflow that can improve the accuracy of calculation of water saturation in these reservoirs.

3.4 Research Approach

In order to address the main two problems outlined above, the below delineated research approach was followed:

I. Petrological analysis of core data from the J-Reservoir and the K-Reservoir to characterize the fabric, texture and the framework of the grain mineralogy of the reservoirs. These factors as well as the type and patterns of cementation, control the volume of bound water in the reservoir and therefore contribute to the low-resistivity phenomena.
II. An integrated analysis of wireline log data such as density, resistivity, neutron and gamma ray logs to characterise the gas bearing reservoir based on the well log response. Calculation of water saturation based on the newly designed workflow that improves the accuracy such calculation in these reservoirs, based on Archie's and Simandoux equations and the modified versions of these equations.
III. Develop a new algorithm to calculate the water saturation in the J- and K-Reservoirs.
IV. NMR and well test data were used to validate the results in (II & III).

3.5 Hypotheses

The main hypothesis for the cause of the low-resistivity pay in Mozambique basin is the high irreducible bound water, which is caused by the presence of clay and silt bound water in the J- and K- Reservoirs. When water is introduced to the clay, the cations from the clay are released into the water and as a result, the conductivity of the water is increased (Boyd et al., 1995). Additionally, several other hypotheses will be tested based on Worthington (2000), who suggested that the general cause of the low-resistivity phenomena can take the cause of coupled elements as listed below:

I. Bimodal particle size distribution due to differential grain size sorting.
II. Matrix microporosity - this refers to microporosity that is not caused by diagenetic clays blocking the pore spaces but exists within the rock matrix.
III. Superficial microporosity – when diagenetic clay coats the grains and reduces the porosity.
IV. Presence of glauconite - iron rich clay-like mineral, often found in marine sandstones and limestones. Due to its high Cation Exchange Capacity (CEC), the presence of glauconite in the formation may have an effect on the resistivity log (Bahr et al., 1993).

V. Presence of conductive minerals such as pyrite and magnetite, which can lower the intrinsic conductivity contrast between pay and formation water in the reservoir.

VI. The effect of bed lamination on the resistivity of the reservoir, where the resolution of logging tools cannot resolve the resistivity caused by hydrocarbons in the thin bedded sandstone. The overall results are the high resistivity from the thin beds being masked by the low-resistivity of the formation water between the thin beds.

VII. Very low-salinity formation waters in the reservoir, which reduces the resistivity contrasts between pay zone and the formation water. The low salinity formation water results in high resistivity. Since hydrocarbons are also characterised by high resistivity, the resistivity contrast between the hydrocarbon-bearing formations and water-bearing formations is reduced.

The contribution of these factors to the low-resistivity pay is explained in detail in section 4.5 and will be evaluated in the study to investigate their contribution to the low-resistivity phenomena of the J- and K-Reservoirs formations.

3.6 Available Data

- **Well and Core Data**

The wells used in the analysis are listed in Table 1, which also indicates whether core data were available or acquired in the well. Since not all the wells have a complete suite of logs relevant to this study, the criteria used for selecting the key wells were mainly the availability of the standard log suite, which includes gamma ray, neutron, resistivity and density logs, as well as core and NMR data. NMR data were however, available only from few wells.

Well Name	Field Name	Reservoir Unit	Core Data
A11	Field A	J-Reservoir	Available
A12	Field A	J-Reservoir	Available
A13	Field A	J-Reservoir	
A14	Field A	J-Reservoir	
A15	Field A	J-Reservoir	Available
A16	Field A	J-Reservoir	
A17	Field A	J-Reservoir	
A21	Field A	J-Reservoir	Available
A22	Field A	J-Reservoir	Available
A23	Field A	J-Reservoir	Available
B9	Field B	K-Reservoir	Available
B10	Field B	K-Reservoir	Available
B11	Field B	K-Reservoir	
B12	Field B	K-Reservoir	Available
B13	Field B	K-Reservoir	Available
B16	Field B	K-Reservoir	Available
B17	Field B	K-Reservoir	
B18	Field B	K-Reservoir	
B21	Field B	K-Reservoir	Available
B22	Field B	K-Reservoir	Available

Table 1: List of wells used in the study, wells with a prefix "A" and "B" are from Field A and Field B, respectively.

- **2D Seismic Data**

2D seismic data with average spacing of 6k m exists in the study area (Fig. 23). These lines were used to map and define the areal extent of the J- and the K-Reservoirs. The sparse spacing between the 2D lines presented some difficulties in defining subtle changes in geology between the seismic lines but the overall general architecture of the reservoirs was successfully defined based on the reservoir limits defined by the wells that drilled into the J- and K-Reservoirs.

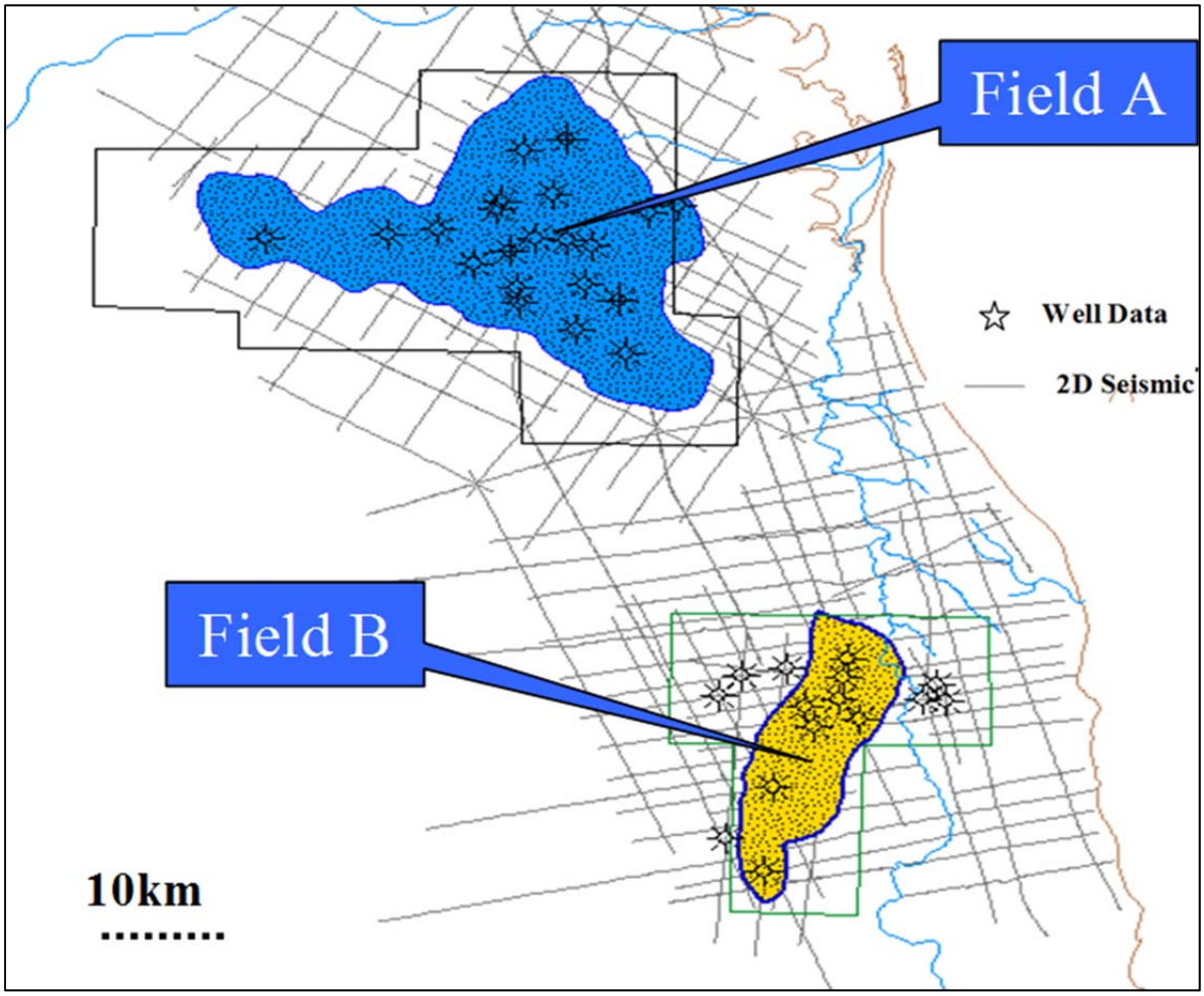

Figure 23: Data coverage in the study area. 2D seismic lines are sparsely spaced in the study area while the well data area mainly clustered around the two fields.

CHAPTER 4: LITERATURE REVIEW

The purpose of this literature review is to summarise and explain the key logging tools used in this study and the research on the work already done thus far pertaining to the study

subject. The main sources of the literature review are the published papers, course materials, various websites and reports compiled by companies that studied the Mozambique Basin in the past as part of their effort to explore for hydrocarbons. The following subjects will form part of the literature review:

I. The logging tools will be explained for the readers unfamiliar with geophysical borehole tools.
II. The theory and the development of the water saturation algorithm by Archie (1942).
III. The background on the Simandoux equation (1963).
IV. The theory and development of the relationship between resistivity and velocity (Faust Equation).
V. The possible causes of low resistivity pay reservoirs in Mozambique. A review of causes of low resistivity pays in other basins.

4.1 Review of Logging Tools

In this section, the sonic, density and neutron logs, collectively known as porosity logs, as well as electrical logs such as resistivity or induction and the photoelectric factor (PEF) logs will be reviewed. A modern tool called Nuclear Magnetic Resonance or NMR will also be reviewed for its importance in accurately predicting the reservoir properties such as porosity and, particularly, the ability to differentiate between bound (irreducible) water saturation (S_w) in low-resistivity pay zones. One of the key components of any logging tool is its ability to detect and to resolve the bed thickness and the ability of the log to calculate the true parametric value of that bed (resolution) according to Worthington (2000). The low-resistivity phenomena are partly a function of the characteristics of logging tools, where the limits on the logging tool's resolution may manifest as low-resistivity pay (Worthington et al., 2000). Figure 24 is a summary of the tools' resolutions and their depth of penetration into the formation.

The vertical resolution of the logging tools shown in Figure 24 is between 1 to 100 inches while the depth of penetration from the borehole wall into the rock (radial investigation) also falls within a similar range.

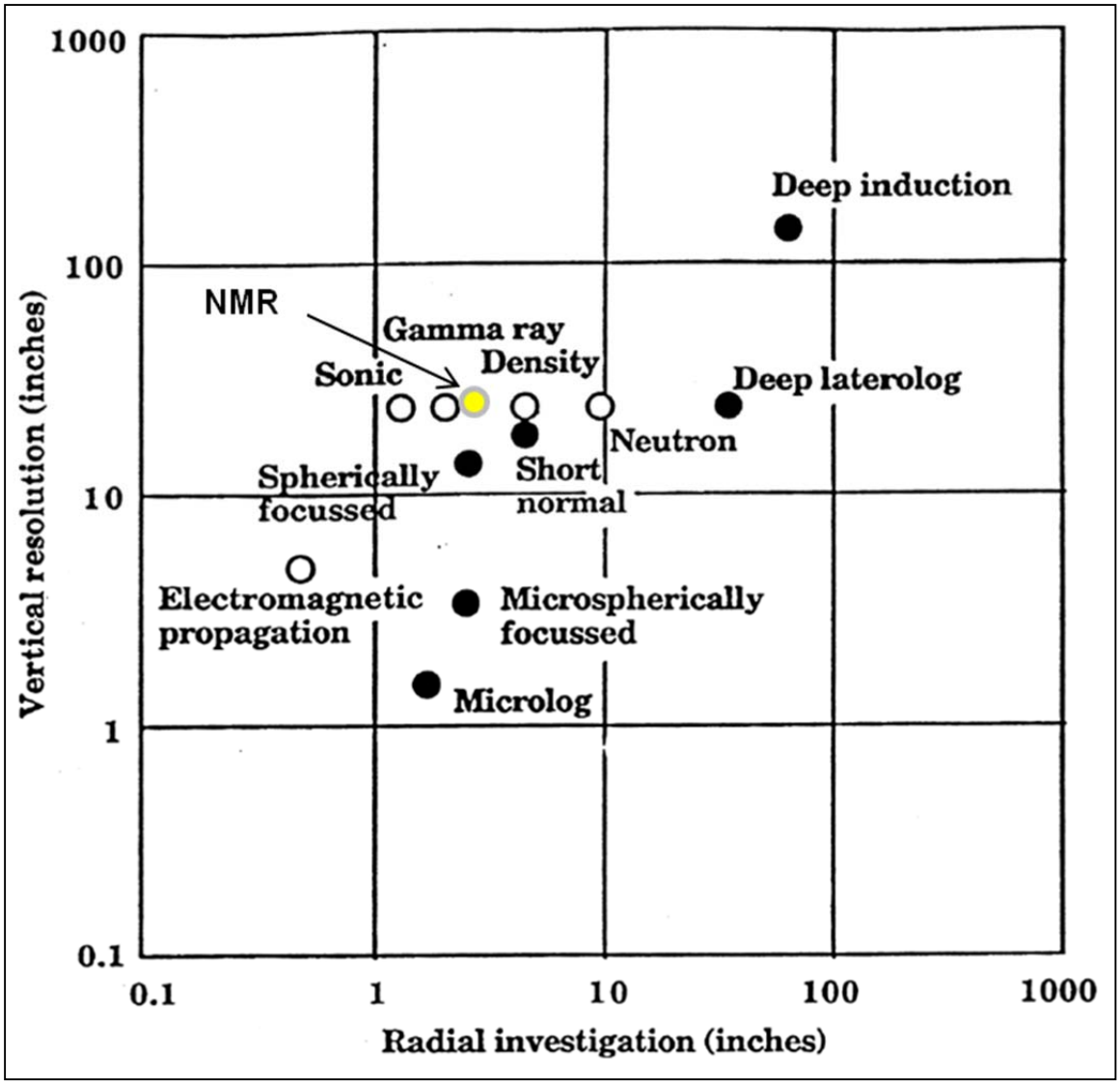

Figure 24: The radial and vertical resolution of various logging tools (Taha, 2010) shows the range of between 1inch to approximately 100 inches in vertical resolution and from 0.8 inches to approximately 100 inches in radial investigation.

4.1.1 The Porosity Logs (density, neutron and sonic)

Porosity is defined as the ratio of the volume of all pores to the bulk volume of the rock and is one of the important input parameters in calculating the volume hydrocarbon in the reservoir ($1-S_w$). The most important logs used to calculate total and effective porosity are the sonic, density and neutron logs hence these three logs are collectively known as the porosity logs. When all three logs are available, then total and effective porosity of the rock formation which is defined as the ratio of all the interconnected pores to the bulk volume of the rock can be determined. In addition to porosity calculation, other information such as clay

content and the presence of hydrocarbons can be also be determined using the porosity logs (Tixier et al., 1968).

4.1.1.1 The Sonic Log

The sonic logging tool shown in Figure 25 measures the wave travel-time in the formation between the transmitter and the receiver. The transmitters (upper and lower) emit a pulse of elastic wave, which travels through the formation, and arrives at the receiver at different transit times, which are measured in microseconds/foot (μs/ft). The wave propagation is normally in the form of a compressional wave (P-wave) but the more advanced version of the tool can measure other waveforms such as the secondary S-wave (Schlumberger, 1991). The transit time between the transmitter and the receiver is dependent upon the acoustic properties of the medium it traverses. In highly consolidated sandstones, the travel time will be faster than in un-consolidated sandstones, since velocity is a function of rock density. The acoustic property of the formation is also a function of both fluids and formation matrix, therefore, porosity can be estimated from sonic wave travel time if the composition of the formation is known (Schlumberger, 1991) using Wyllie's time – average equation (Wyllie et al., 1956) shown below (equation 4.1).

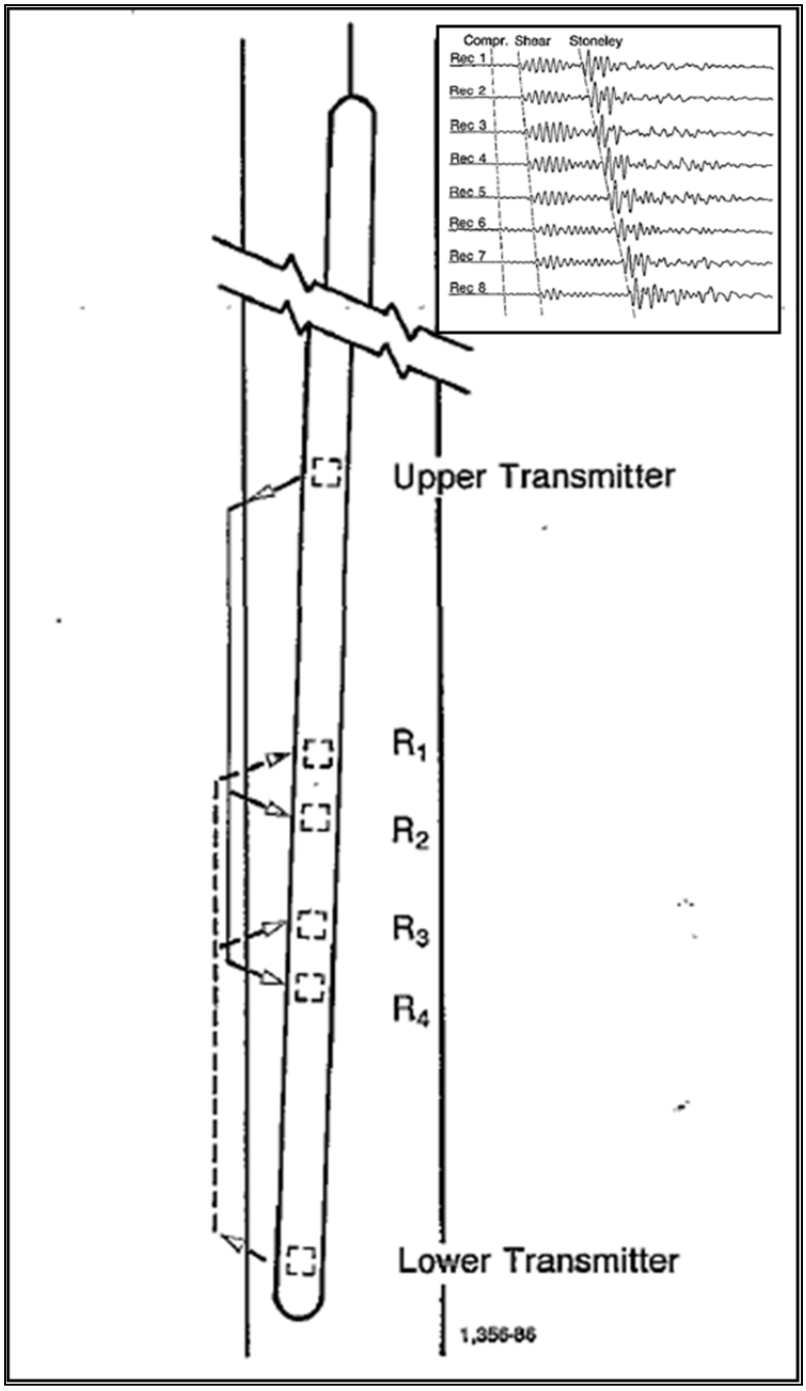

Figure 25: The sonic logging tool (modified from Schlumberger, 2001) consists of two transmitters, the upper and the lower transmitter and of several receivers placed between the transmitters. The sonic wave paths closer to the borehole wall are illustrated in the Figure above.

Wyllie's equation is defined as:

$$\varphi = (T_{log} - T_{ma}) / (T_f - T_{ma}) \quad \text{..... (4.1)}$$

Where,

$T_{log:}$ sonic interval transit time as measured from the log

$T_{ma:}$ sonic interval time within the rock matrix

$T_{f:}$ sonic interval transit time of the saturating pore fluid.

Equation 4.1 gives more reliable porosity values in clean, compacted sands saturated with water (Tixier et al., 1968). In poorly consolidated sands, a factor ($1/C_p$) is applied to equation 4.1, to give:

$$\varphi = \{(T_{log} - T_{ma}) / (Tf - T_{ma})\}.1/C_p \quad \text{..... (4.2)}$$

Where,

C_p: the compaction factor

An underlying shale zone can be used to estimate the compaction in the unconsolidated sand since the compaction range for shale is empirically known to be between 0.8 and 1.3 i.e. $0.8 < C_p < 1.3$ (Bassiouni, 1994). The minimum value of the compaction factor, C_p, should be 1 in consolidated sands (Tixier et al., 1968).

4.1.1.2 The Density Log

The density-logging tool (Fig. 26) measures the density of the formation, which in turn is indicative of the porosity of that formation. The tool emits gamma ray particles into the formation and when the emitted particles collide with electrons in the formation's matrix, they lose some of their energy to the electrons and continue to propagate at a much lower energy. The density of the formation is then estimated from the number (density) of gamma rays that reaches the detector or scintillation counter (Schlumberger, 1991). The high number of electrons in the formation implies a denser formation and this in turn causes a higher number of gamma rays particles to be scattered back to the receiver. This is the basic principle of how the density is estimated (Schlumberger, 1991). In this study the density log will be primarily used to estimate the porosity of the formation using equation 4.3.

Porosity can be derived from density log as follows:

$$\Phi_{total} = (\rho_{ma} - \rho_b) / (\rho_{ma} - \rho_f) \quad \text{..... (4.3)}$$

Where:

Φ_{total} = Total porosity

ρ_{ma} = is the density of the matrix

ρ_b = is the bulk density measured from the log

ρ_f = is the fluid density (gm/cc). Densities of water =1, oil =0.8 and gas =0.2

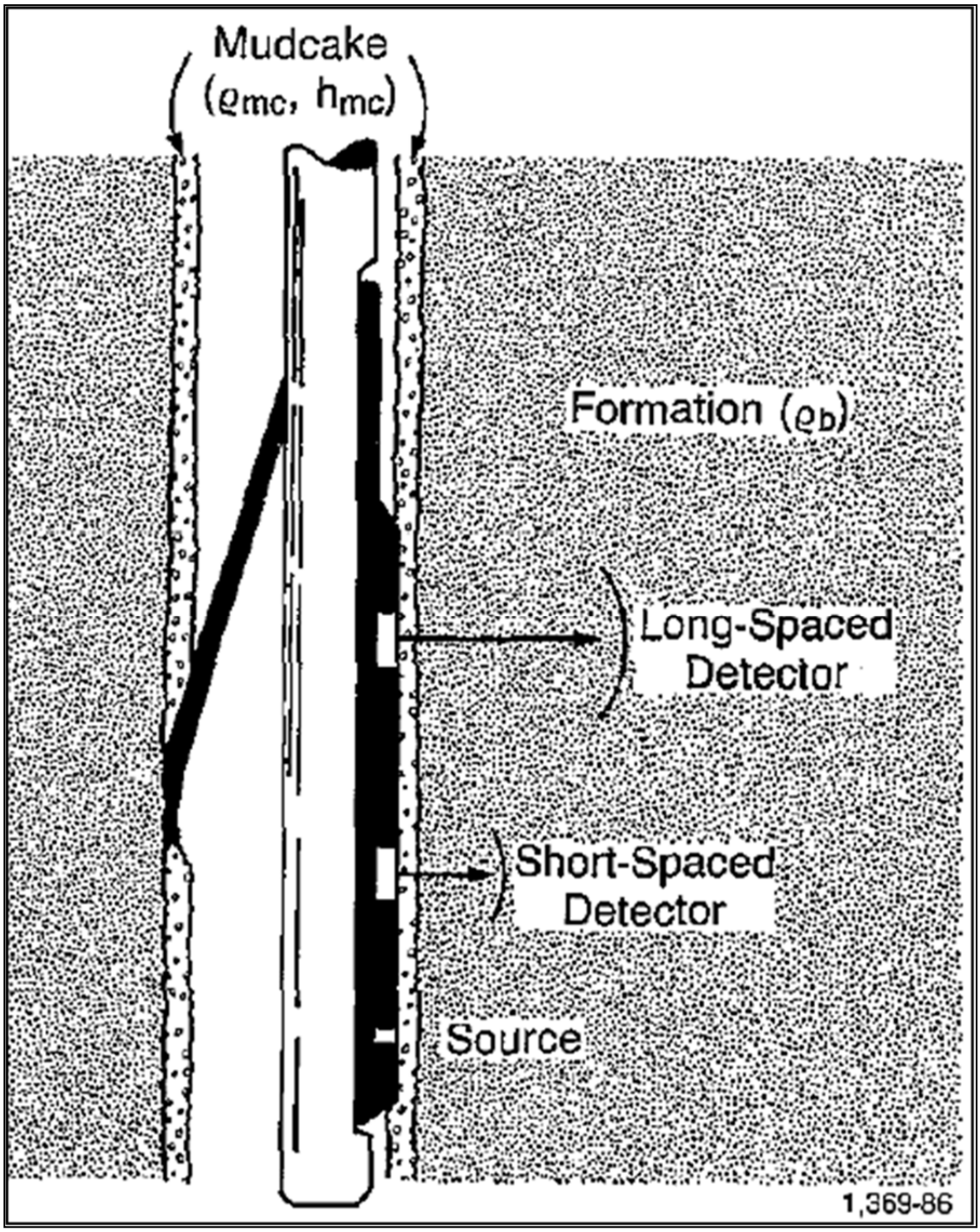

Figure 26: The density logging tool (Schlumberger, 1991). Radioactive elements from the formation are measured on the scintillation counter in the density tool.

The porosity of any porous sedimentary rock is generally lower than 50% (Tiab et al., 2004). The two most commonly used tools are the Compensated Density Tool and the Spectral Density Tool and the main difference between the two is the gamma ray scattering mode. The former uses the Compton scattering mode while the latter uses the Photoelectric (P_e) effect mode. Water and hydrocarbons give a low Photoelectric effect (P_e) on the Spectral Density Tool (Schlumberger, 1991) and therefore can be used together with other logging tools, to identify hydrocarbon-bearing formations. In gas-bearing reservoirs, porosity calculated using equation 4.3 tend to over-estimate the calculated porosity due to the low density of gas (ρ_f) which lowers the denominator.

4.1.1.3 The Neutron Log

A neutron logging tool shown in Figure 27 measures the amount of the hydrogen element in the formation's pore spaces and since the pore spaces are filled with fluids with variable number of hydrogen bound molecules, the measured amount of hydrogen is indicative of the porosity of that formation. Water and hydrocarbons comprise of hydrogen as part of their chemical composition and therefore the tool essentially measures the pore volume filled by water and or hydrocarbons (Taha, 2010). The latest neutron tool is the Compensated Neutron Tool (CNT) and consists of a chemical source, AmBe241, which releases the high-energy neutrons in the energy range of 1-10MeV into the formation (Weatherford, 2011). When these neutrons collide with formation nuclei, particularly the hydrogen atom because it is close in size to the neutron, they undergo scattering, losing energy and therefore slow down. This is also called an elastic neutron scattering (Watfa, 2012).

The thermal detectors of the neutron tool in Figure 27 measures the neutron population in the thermal (slow) region and this in turn is a measure of hydrogen index in the formation. Another form of scattering is called an inelastic scattering where the neutron bounces off the nucleus which then gets excited and emits an inelastic gamma ray. The measurement of the spectrum of emitted gamma ray (counts) is proportional to the porosity of the formation (Watfa, 2012). In gas-bearing reservoirs, the porosity calculated using the neutron log underestimate the true porosity since hydrogen elements are further apart in gas than other fluids such as oil and water. Since neutron calculated porosity is always lower than the density calculated porosity in gas bearing reservoirs, the cross-over between the two measurements (see Figures 42 and 43) can be used to identify gas-bearing formation.

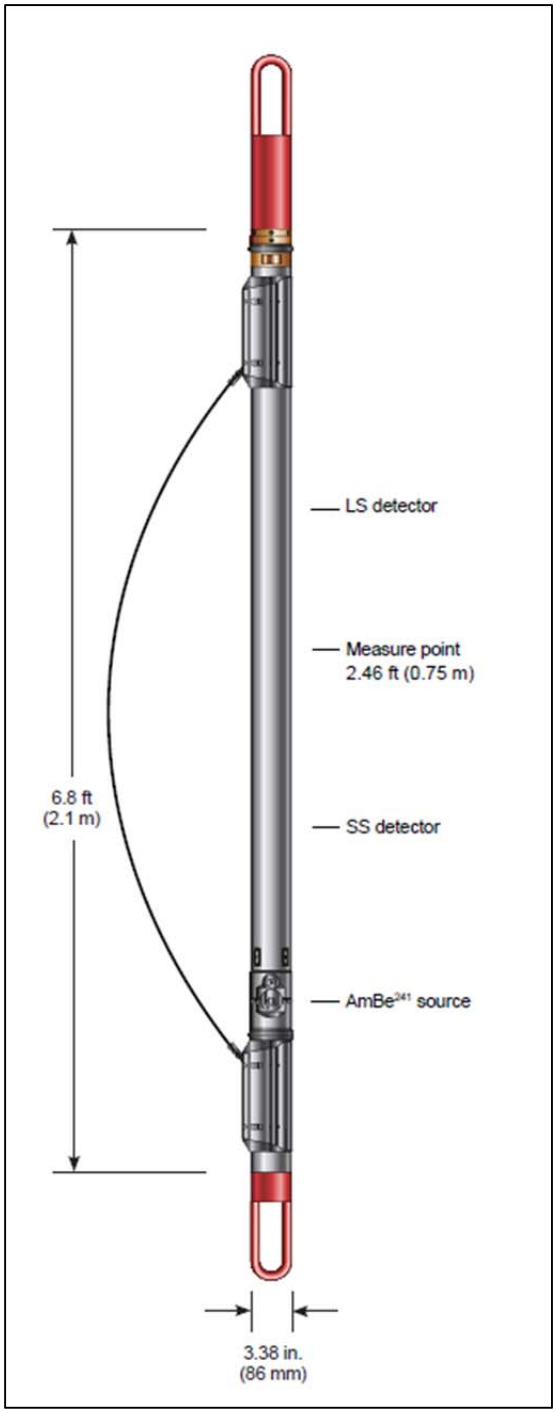

Figure 27: The neutron logging tool (Weatherford, 2011) showing the radioactive source and the detectors (thermal and epithermal).

4.1.2 The Electrical Logs (Induction and Laterologs)

The resistivity log was in the past used qualitatively to correlate lithology between wells and also as a tool to identify potential pay zones in hydrocarbons exploration (Archie, 1942). Resistivity can be described as the ability to impede the current to flow through the formation

and is measured in ohm-m. The current is primarily conducted through water in the formation whereas the rock matrix and hydrocarbons are non-conductive. The resistivity therefore depends on the resistivity of the formation water (R_w), the amount of fluids (water) present in the pore space and the pore structure and the (Watfa, 2012). In turn, the ability of the water to conduct electricity depends on its salinity and temperature. The presence of hydrocarbons in the formation reduces the volume of conducting water and so reduces the conductive capability of the formation (ECL, 2003).

Resistivity tools are designed to read at different depth of investigation with the deepest reading the un-invaded zone (R_t) as shown in Figure 28. The resistivity readings in the flushed zone (R_{xo}) and the resistivity of the mud-filtrate (R_{mf}) are also shown in the borehole profile (Fig. 28). Total resistivity (R_t) is the most important parameter used in calculating the water saturation.

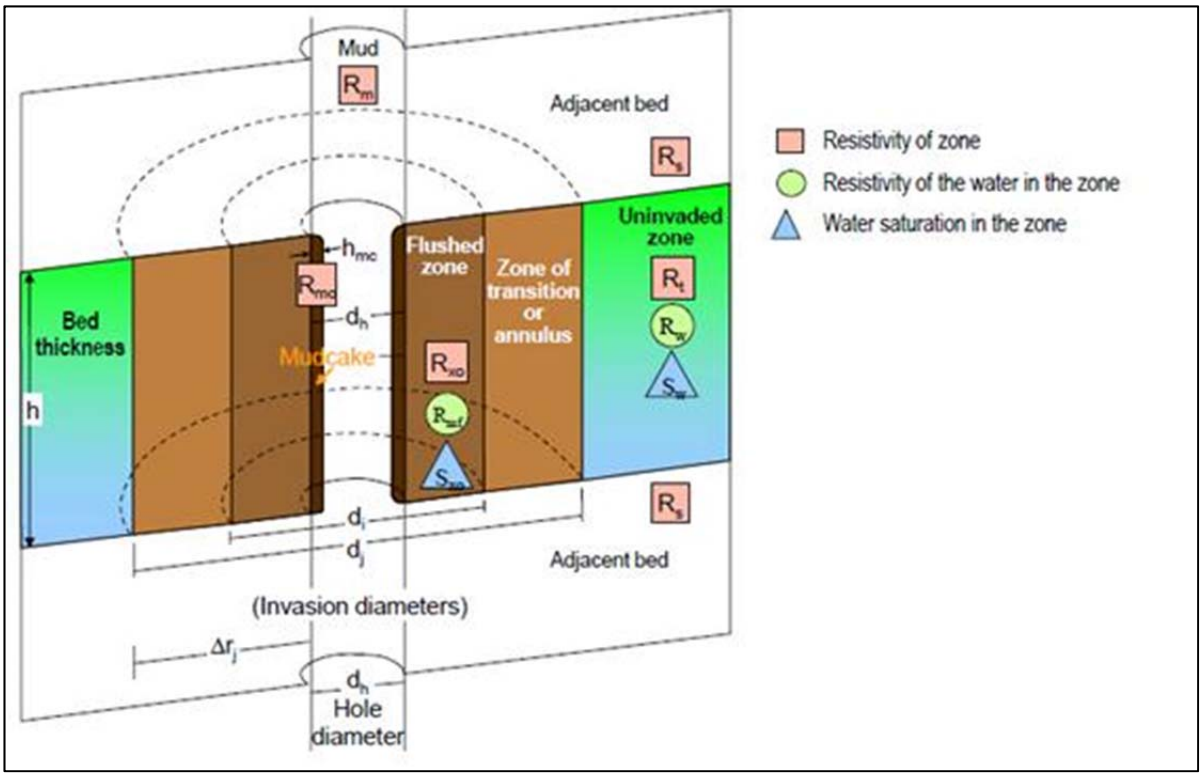

Figure 28: The borehole environment showing resistivity measurements in the flushed zone, zone of transition and un-invaded zone (Watfa, 2012).

Different mud systems are used during drilling operations for lubrication and to reduce the temperature caused by friction on the drill bit. The mud system design can be water based or oil based depending on the objectives of the drilling and since the mud can either transmit or impede the flow of current in to the formation, its resistivity should be known and corrected

for in the log analysis. The resistivity of the drilling mud (R_m) is not directly measured during logging but determined in the laboratory before any drilling activities.

Resistivity tools are also designed for different mud systems. The Laterolog Tools (Fig. 29) are designed for saline water based mud system whereas the Induction Logging Tools (Fig. 30) are designed for oil or fresh water based mud. The Dual Laterolog as shown in Figure 29 measure the deep and shallow resistivity. The tool uses electrodes to transmit an electric current that flows through mud into formation and the strength of the current is measured by receiving electrodes in the tool (ECL, 2003).

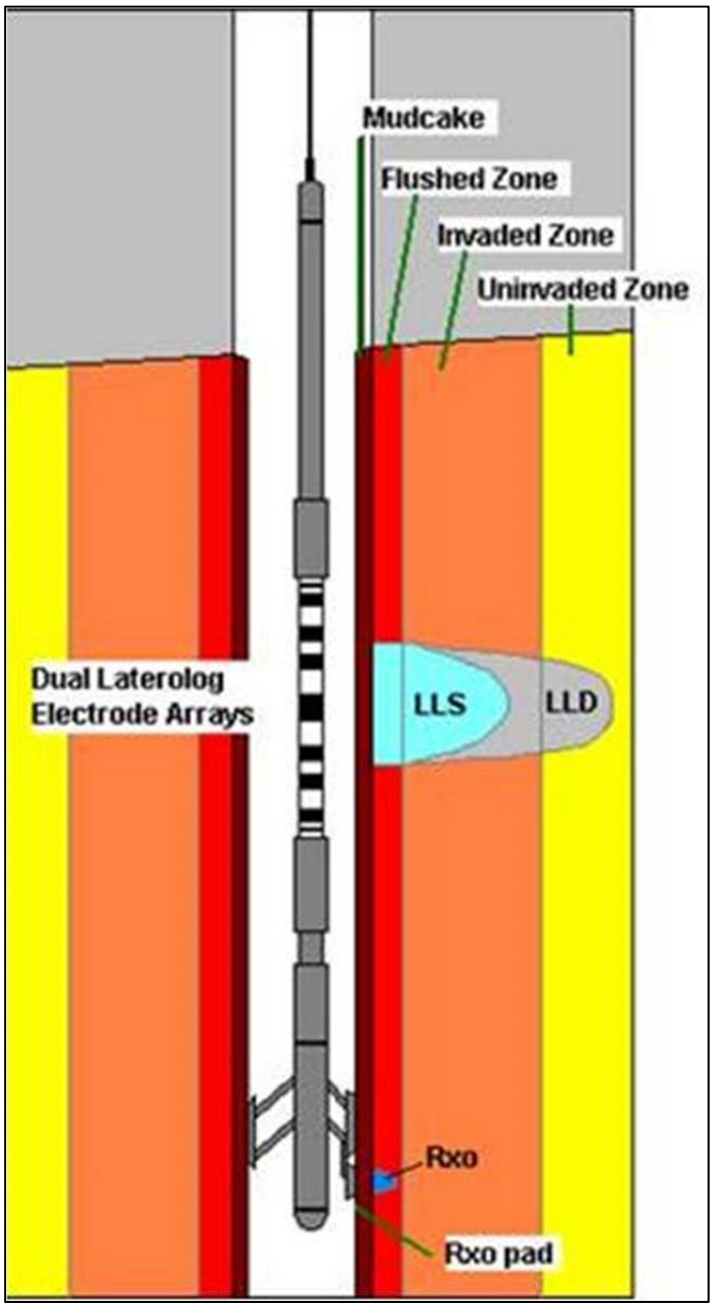

Figure 29: A Laterolog logging measures the deep (LLD) and shallow (LLS) reading resistivity. Tool transmits an electric current that flows through the mud into the formation.

In the Induction tool (Fig. 30), a high frequency alternating current is sent through the transmitter coil, which creates an alternating magnetic field. The magnetic field induces secondary current in the formation and the receiver coils measure the strength of the current in the formation i.e. the conductivity within the formation. Dual Induction Tools measure the deep (ILD) and medium (ILM) reading resistivities. In summary, the Laterolog Tool measures the electrical resistivity whereas the induction log measures the electrical conductivity (Taha, 2010).

One of the challenges in resistivity measurement is the presence and detection of electrical anisotropy which may be caused by (1) variations in water saturation in the reservoir (2) the variations in grain size and pore space geometry and (3) the variable electrical conductivity contrast between the grains and the pore space in which the conductivity in the direction perpendicular to the stratigraphic set is less than the conductivity in the plane to the set especially in cross bedded sequences (Klein et al., 1997). Electrical anisotropy can also arise due to thin interbeds of sediments with different electrical properties and according to Klein et al.(1997), the high-conductivity contrast between shales and sands can give rise to anisotropy in these shaly sand sequences. Porosity variation is another potential source of electrical anisotropy in uniformly water-saturated sands (Schon et al., 2000). Electrical anisotropy has long been considered to be the main source of error in traditional Induction log analysis (Klein, 1993). The new generation induction tools such as the High Definition Induction Logging Tool (HDIL) can accurately measure resistivities in thinly laminated reservoirs by using seven receiver array and eight operating frequencies to provide a detailed evaluation of the resistivity within these thin beds (Baker Hughes, 2012).

4.1.3 The Lithology Logs

Two lithology logs will be reviewed in this section and these are the gamma ray (GR) and the photoelectric effect (PEF) logs. The gamma ray log (GR) was used in this study to define the lithology, sand and shale and to calculate the amount of clay in the reservoir formation. The clay volume is an important parameter in determining the amount of clay-bound water in the reservoir. The PEF log was not used in the study but worth describing it as one of the lithology logs.

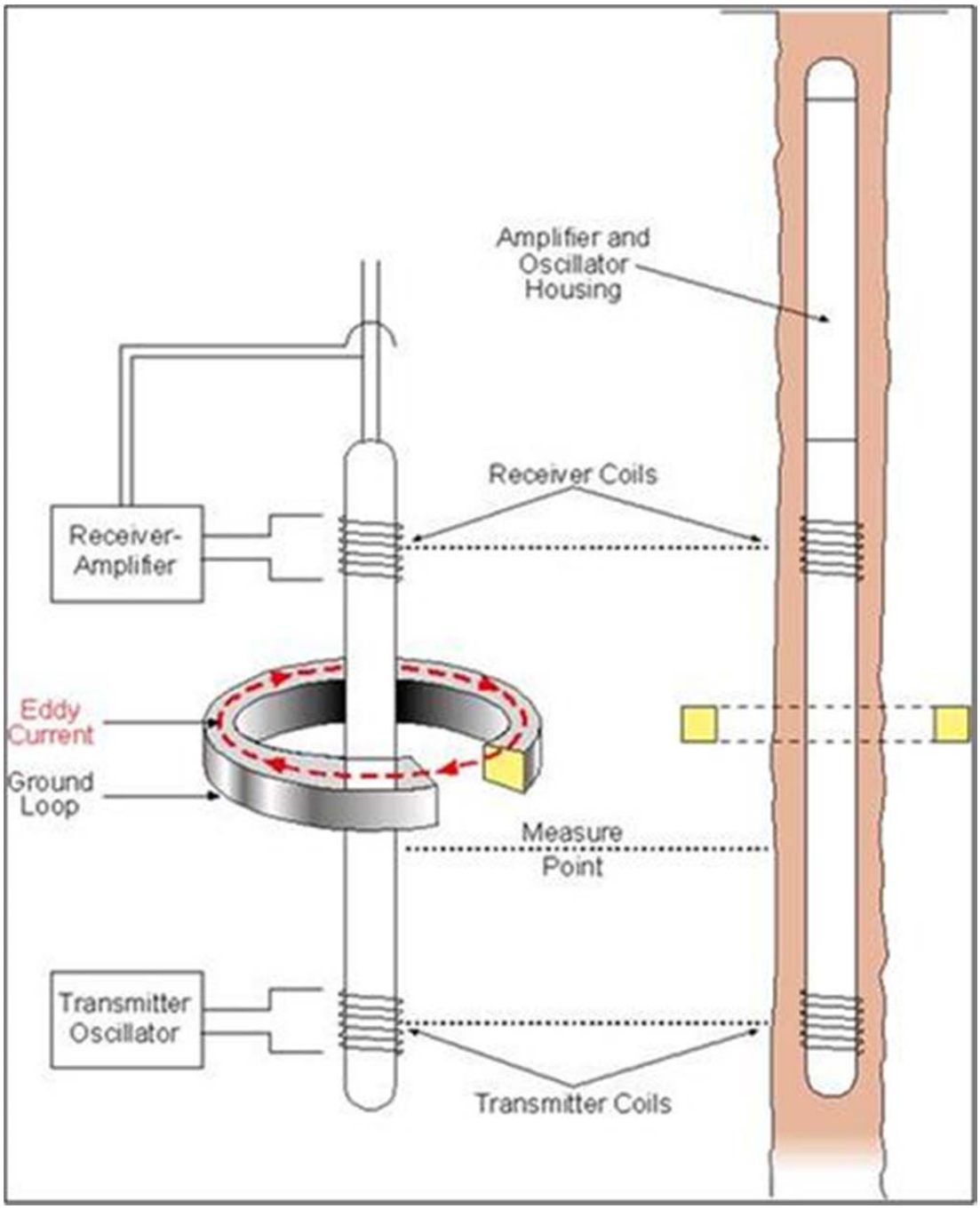

Figure 30: An Induction logging tool contains transmitting electromagnets that induce a current to flow in the formation around the borehole (ECL, 2003).

4.1.3.1 The Photo Electric Factor (PEF)

The photoelectric factor (PEF) log is a good matrix indicator and the measurement is also slightly influenced by the formation porosity. The log measures the photoelectric absorption index (P_e) of the formation (Schlumberger, 1981). The PE index is related to the atomic

number of the elements that make a particular formation. Pore fluids normally have a low P_e compared to the matrix and therefore as mentioned above, the tool is more of a lithology indicator than a fluid indicator. In Figure 31 below, the variation in the spectrum for formation with constant density but different atomic number Z (Schlumberger, 1981) is demonstrated. The tool is normally used with other lithology logs such as gamma ray and density log, to generate cross-plots that can assist in the identification of gas in the formation.

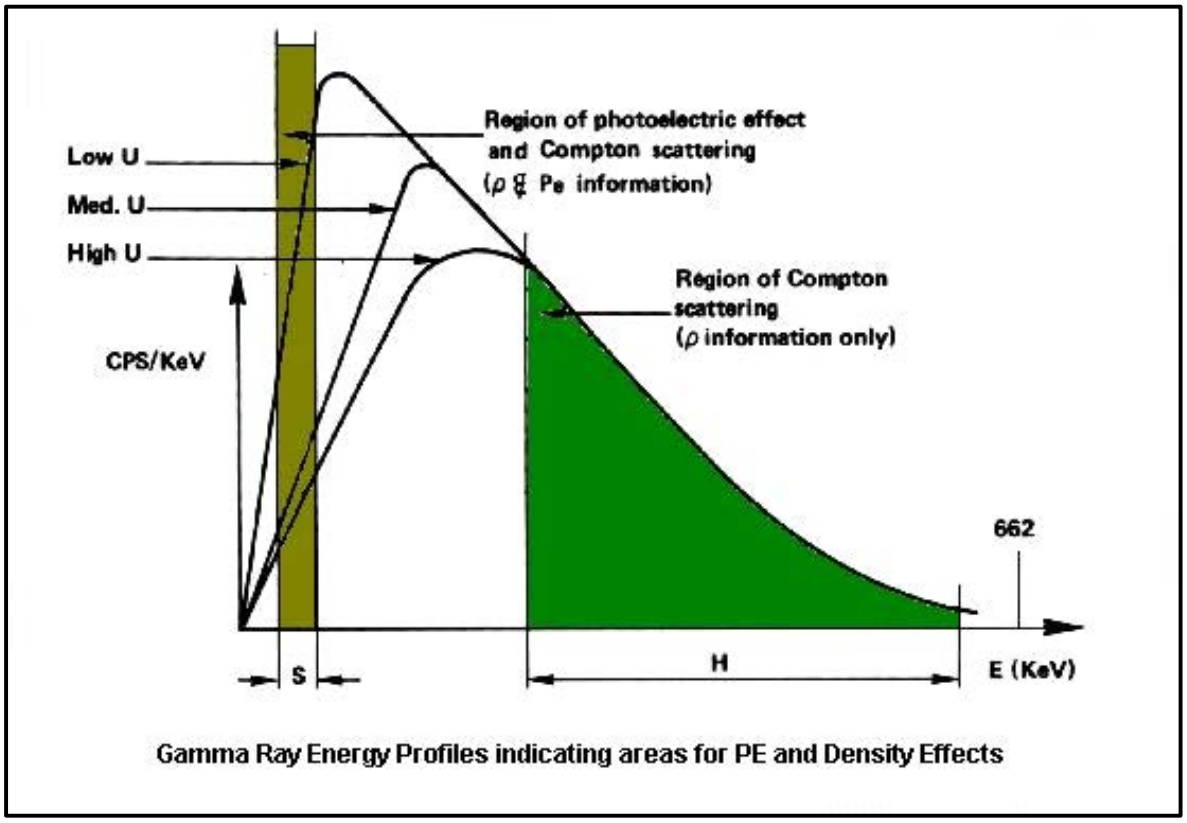

Gamma Ray Energy Profiles indicating areas for PE and Density Effects

Figure 31: Photo-electric (PEF) (Schlumberger, 1991). The Figure above shows variations in the spectrum for formation with constant density but different atomic number Z.

4.1.3.2 The Gamma Ray Log (GR)

The gamma ray (GR) tool measures the natural radioactivity from the most common radioactive elements such as potassium (K), thorium (Th) and uranium (U) in the formation closer to the borehole wall (Hyde, 2001). The tool contains a measuring instrument equipped with a scintillation counter that measures the average levels of radioactivity over a certain period of time (Fig. 32). The electrons in the formation impede the travel path of the gamma ray and therefore, the denser the formation is, the more reduced are the levels of measured gamma ray (Ditzhuijzen, 1994). Potassium is most common in the clay minerals and feldspars and hence the tool can be used as a clay/shale or arkoses indicator and therefore

as a guide for well-to-well correlations. Uranium and thorium are also abundant in some heavy minerals and thus, can also assist in well-to-well correlations. It is worth noting that other minerals such as K-feldspar, zircon, mica and glauconite (see section 4.5) and uranium salts will have an effect of the gamma ray response.

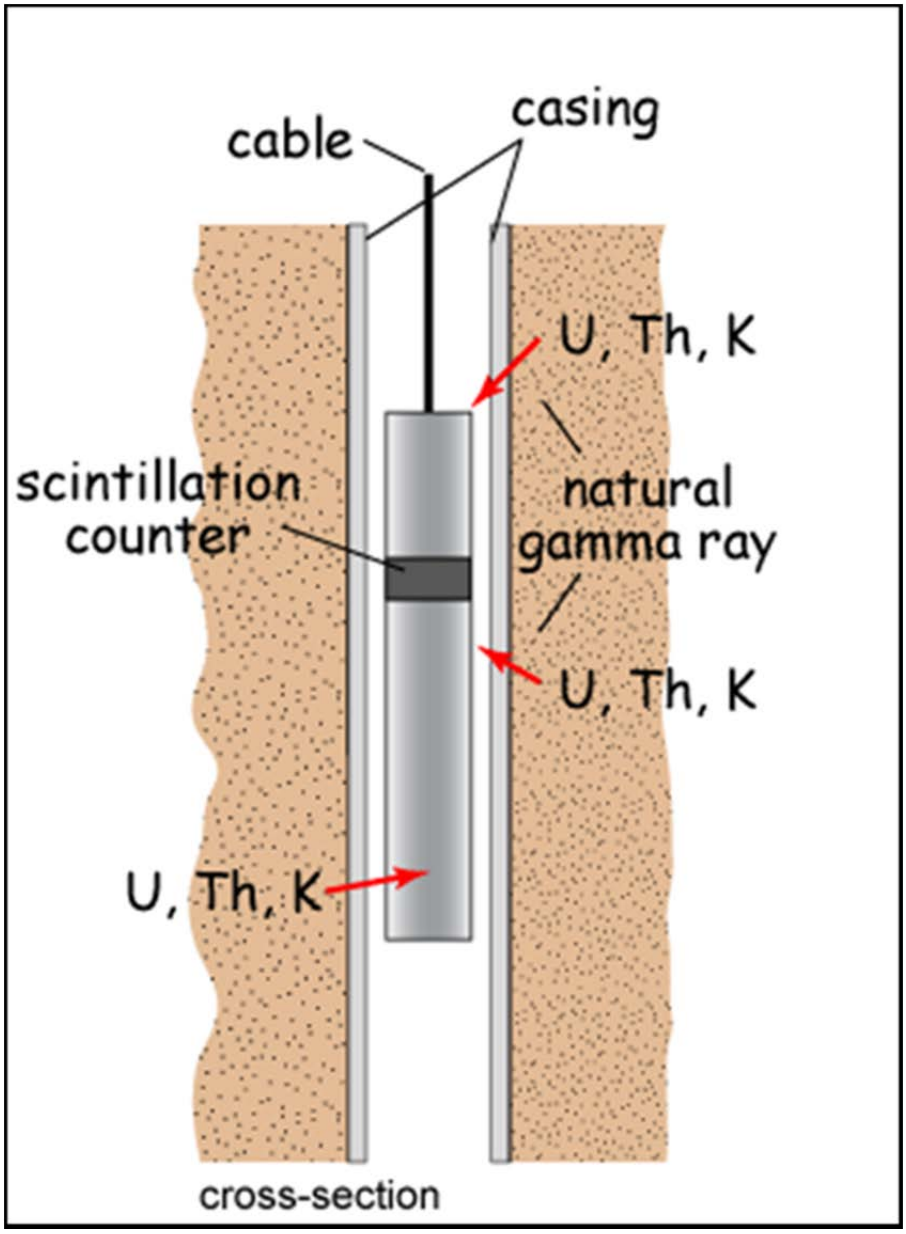

Figure 32: Gamma ray tool (after www.gg.uwyo.edu). The tool contains a measuring instrument equipped with a scintillation counter that measures the average levels of radioactivity over a certain period of time.

The conventional gamma ray (GR) tool measures the total formation gamma ray response but the spectral gamma ray (SGR) tool can separate the response from K, Th and Uranium (Ditzhuijzen, 1994).

4.1.4 Nuclear Magnetic Resonance (NMR)

The Nuclear Magnetic Resonance (NMR) tool is used to measure and calculate porosity and water saturation in reservoir formations. Figure 33 shows the basic configuration on the NMR tool, called MRIL after Halliburton. In the low-resistivity reservoirs of Mozambique, NMR is the only tool that gives reliable water saturation (S_w) results. The principle of NMR involves hydrogen nuclei-protons, which are exposed to a static magnetic field until all the nuclei are aligned (magnetized) in the direction of the magnetic field. When the radio frequency (RF) pulse of a particular magnitude and frequency is introduced for certain time duration, the magnetic direction of the nuclei-proton can be rotated by 90 degrees (Boyd et al., 1995).

When the RF pulse is removed, the proton will rotate back to the direction of the magnetic field, and emits the RF pulse, the strength of which is proportional to the number of mobile protons. This is in turn, gives information about the type of fluid in the formation. The time it takes for the proton to return to its original state, called relaxation time (T_2), gives information about the pore size and the type of fluid in the formation. This is the basis to separate the movable from the immovable water in the formation. Figure 34 shows the separation of different fluids based on the relaxation times T_2. The modern NMR tool is a pad-mounted device with permanent magnets to provide the static field described above. This is called the Combinable Magnetic Resonance or CMR (Baker Hughes, 2007).

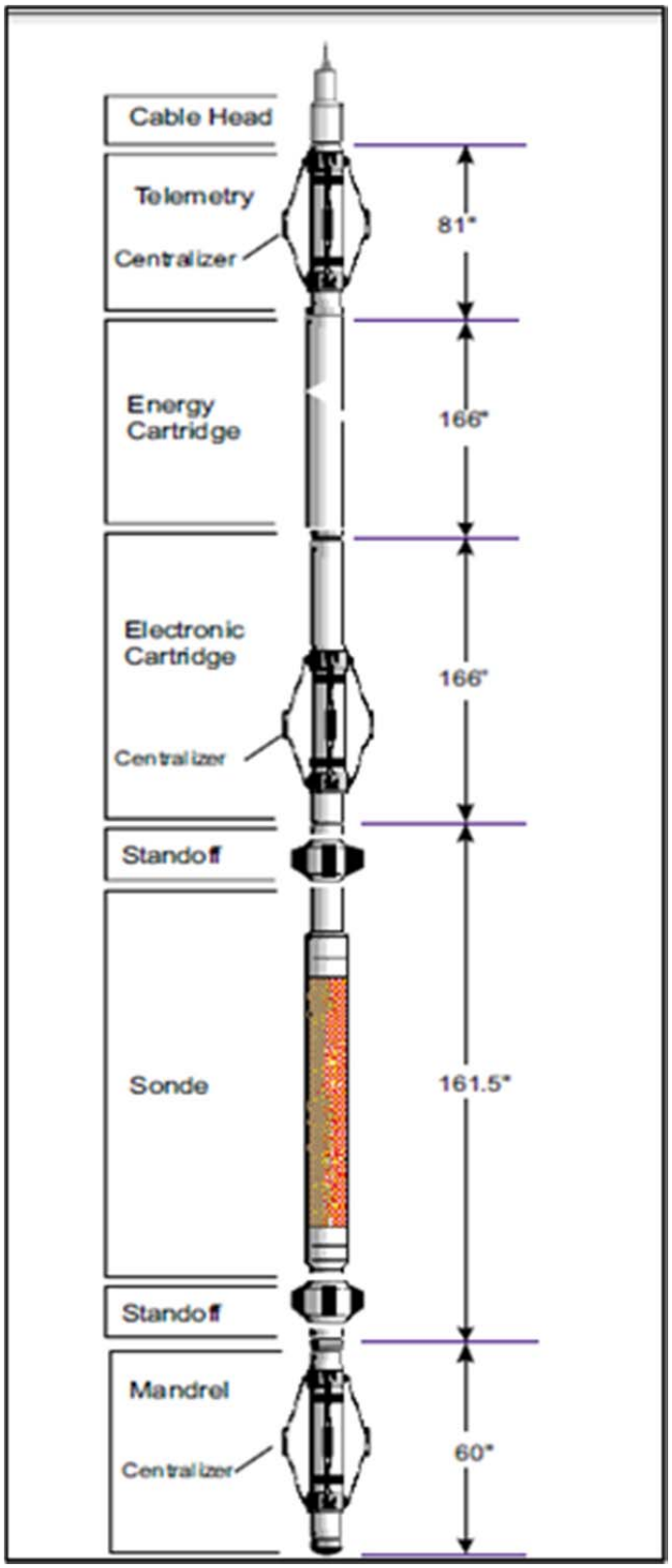

Figure 33: The basic configuration on the NMR tool, called MRIL after Halliburton. The tool consists of a magnetic mandrel, an electronics cartridge and several energy storage cartridges (Coates et al., 1999).

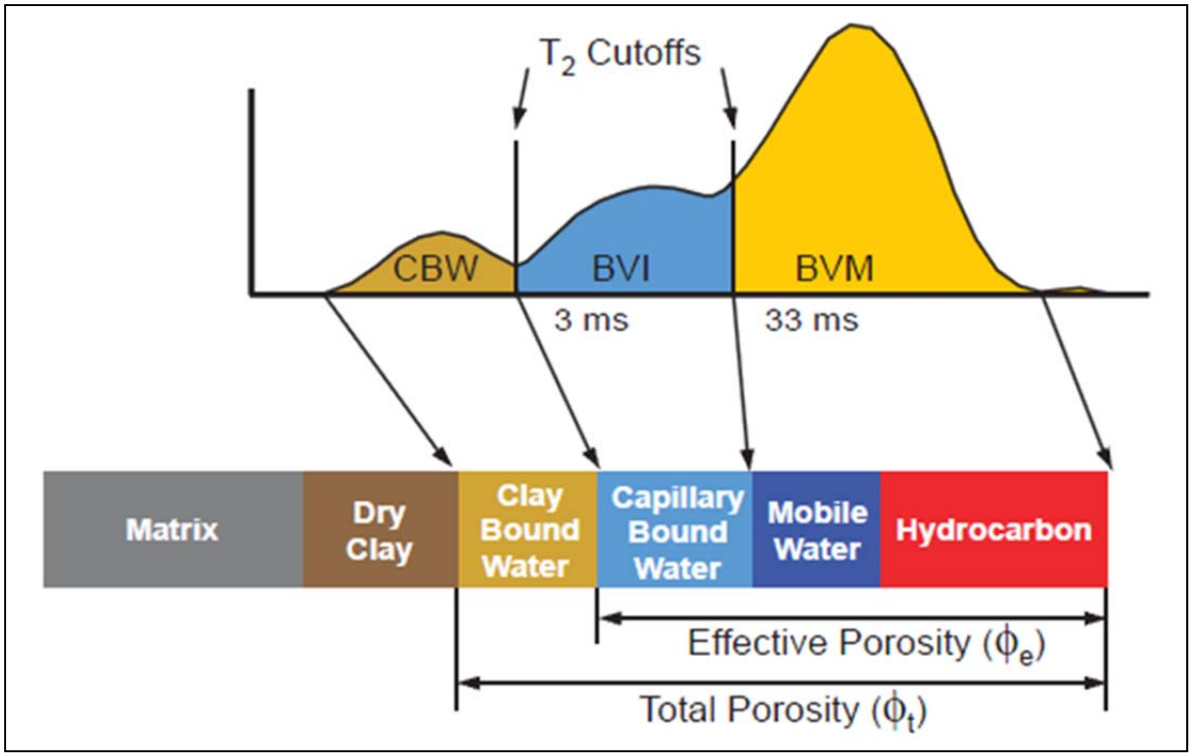

Figure 34: NMR relaxation times (Baker Hughes, 2007). The T_2 spectrum represents the distribution of T_2 decay rates that are directly related to the pore size in the formation. Typical T_2 cut offs are 3ms for clay-bound water (CBW), 33ms for irreducible water BVI and movable fluids (BVM).

4.1.5 Borehole and Environmental Correction

In order to improve the signal to noise ratio on the log data, borehole environmental corrections have to be applied on the logging tools. The most important tools to correct are the gamma ray, density, neutron and resistivity tools (www.petrophysics.net). Table 2 summarises some of the corrections required to different logging tools to compensate for the borehole effects such as borehole size, mud properties used during drilling operations and mud invasion (ECL, 2003). In most instances, the poor log data are attributed to enlarged borehole size due to washouts which result in poor coupling between the tool and the borehole wall.

Log Type	Environmental Corrections
Gamma Ray	Hole size and mud weight
Density	Hole size and mud weight
Neutron	Hole size, mud thickness, mud salinity, mud weight, temperature, formation salinity
Deep/Shallow Restivity	Hole size, mud resistivity
Micro-Restivity	Mud cake resistivity and thickness
SP	Bed thickness

Table 2: A summary of environmental corrections for various well logs, the most important tools to correct for are the gamma ray, density, neutron and resistivity tools

The mud properties such as the density, salinity, radioactivity and resistivity may also affect the log readings and have to be accurately measured and corrected, for instance for the mud invasion which involves the displacement of formation fluids may change the bulk formation properties close to the borehole. The logging service companies often provide environmentally corrected log data as part of the agreed scope of work. Table 2 below show a list of logs and common environmental correction done on them.

4.2 Archie's Water Saturation (S_w) Equation

4.2.1 Theory and Background

Archie's saturation equation is commonly used in estimating the water saturation (S_w) in the reservoir formations. In the past, the electrical log was used qualitatively to correlate (well-to-well) between different lithologies drilled during oil and gas exploration and to determine some electrical properties of theses formation. In 1941, Gustav Archie presented a paper on how to quantitatively estimate water saturation (S_w) in the reservoir, using the electrical logs.

Archie suggested an empirical relationship between the resistivity and reservoir properties for brine filled formations and for formations that are partially filled with hydrocarbons, using core data from the Gulf of Mexico. The resistivity of the brine filled formation (R_o) was found to depend on the resistivity of the brine (R_w) and the formation factor (FF). The following empirical relationship between the FF and R_o as formulated:

$R_o = FFR_w$ …….. (4.4)

To investigate the relationship between the resistivity of the formation, its permeability and porosity, cross-plots were generated as shown in Figure 35.

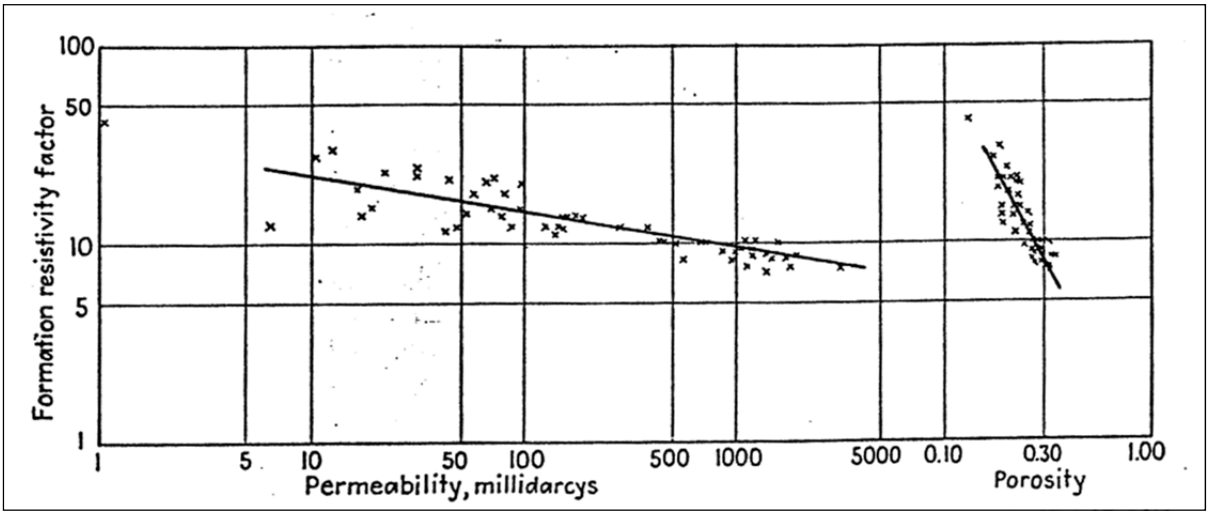

Figure 35: Resistivity versus permeability and porosity plot (after Archie, 1942). The empirical relationship between formation resistivity factor and porosity is more pronounced than the relationship between formation resistivity factor and permeability. Data came from the Gulf of Mexico core.

It was concluded from the cross-plots that the relationship between resistivity and porosity was more robust than the relationship between resistivity and permeability.
Based on the relationship between the porosity (φ) and the resistivity of brine (R_w) in Figure 35, the following empirical relationship exists:

$R_w = \varphi^{-m}$ …….. (4.5)

Where 'm' is the slope on the graph and is sometimes called the cementation factor. This value ranges from 1.8 to 2.0 for consolidated sandstone and 1.3 for unconsolidated sand. Combining Eq. 4.4 and 4.5 yields the following relationship:

$R_o = F\,\varphi^{-m}$ …….. (4.6)

4.2.2 Water and Hydrocarbon Saturation Calculation

The effect of hydrocarbon saturation when pores are partially filled with hydrocarbons, on the resistivity log, was investigated by displacing some of the brine filled pores with non-conducting hydrocarbons.

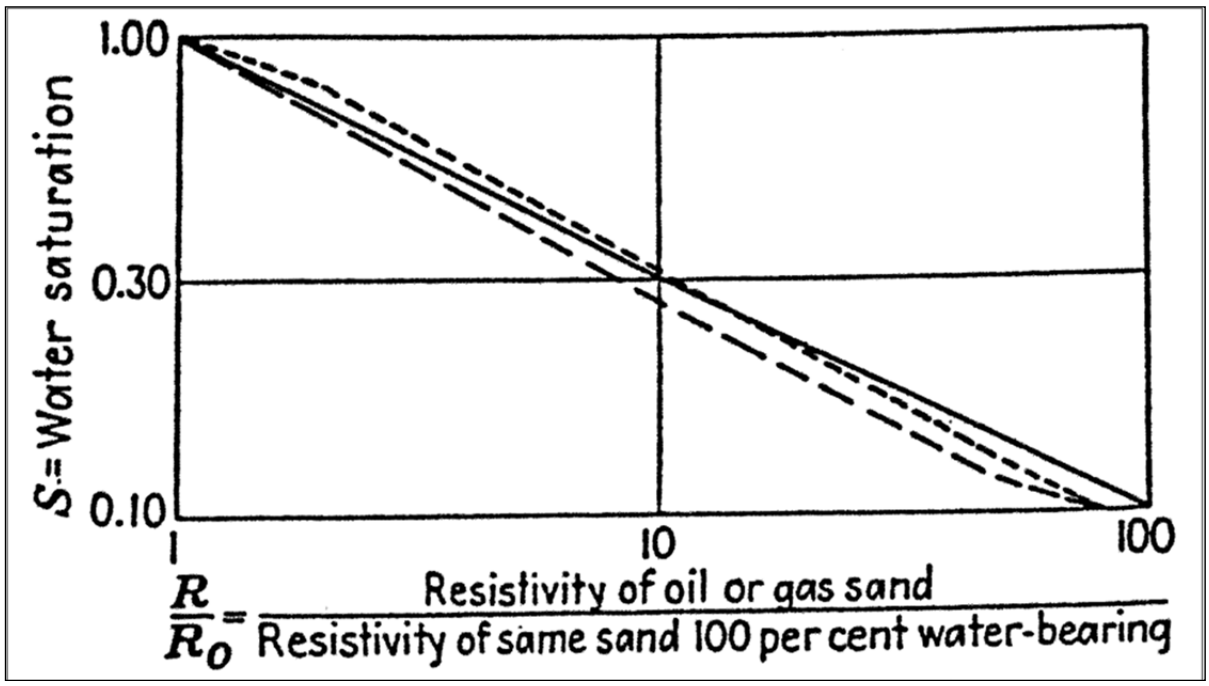

Figure 36: Saturation versus R/R_o (after Archie, 1942). A linear relationship exists between saturation (S) and R/R_o plotted on a logarithmic scale.

The resistivity fraction R/R_o was plotted against saturation for porosities of between 10 and 40%. The linear relationship between R/R_o is shown in Figure 36. It was discovered that for water saturations between 15% and 20% the following relationship exists:

$$S = (R_o/R)^{1/n} \quad \ldots\ldots (4.7)$$

Where,

R = is the resistivity of the non-conducting hydrocarbons

n = saturation exponent

For clean unconsolidated sandstone reservoirs or just clean sands, n is assumed to be 2. Therefore Eq. 4.7 becomes:

$$S = \sqrt{(R_o/R)} \quad \ldots\ldots (4.8)$$

Substituting R_o from Eq. 4.4, the new saturation equation becomes:

$S = \sqrt{(FR_w)/R}$…….. (4.9)

And from Eq. 4.6, Eq. 4.9 becomes:

$S = \sqrt{F.\ \varphi^{-m)}/R}$…….. (4.10)

Archie's equation was later modified to include another constant 'a' for a generalized descriptor of rocks with a range of cementation factors 'm' values. The generalised equation can be written as:

$S_w = [(a*R_w) / (\varphi^m R)]^{(1/n)}$ …….. (4.11)

Resistivity (R) in equation 4.11 is often denoted R_t and it is measured during wireline logging. The resistivity exponents (m) and (n) are usually assumed to be constants as well as the value of "a" and formation water resistivity (R_w). Equation 4.11 can also be written in terms of conductivity as:

$S_w = (C_t/ \varphi^m.C_w)^{1/n}$..... (4.12)

Where,

S_w: Water saturation

C_t: Total conductivity as measured by the resistivity logs = $1/R_t$

φ^m: Total porosity

C_w: Conductivity of the formation water = $1/R_w$

m: Cementation factor

n: Saturation exponent

The following basic information is needed to calculate saturation using Archie's equation:

I. The log-measured bulk resistivity (R_t).
II. The resistivity of brine (R_w) measured from core data as well as water samples collected during drilling of the well.
III. The porosity of the formation. The total porosity (PHIT) and the effective porosity (PHIE) should be measured or calculated.

4.3 Simandoux Water Saturation (S_w) Equation

Since Archie's equation is only applicable to clean (non shaly) sands, several modification of the Archie's equation have been developed in the past to account for shaly formations, one such modification is the Simandoux equation which accounts for the resistivity of the shale in the reservoirs (Simandoux, 1963) given by:

$$[(PHIE)^m x(S_w)^n]/[a.R_w.(1-V_{sh})]+[(V_{sh}.S_w)/R_{sh}]-1/R_t=0 \quad \text{.....(4.13)}$$

Where

a: The coefficient obtained from correlation between cementation factor (m) and porosity using the formation factor (FF) and it has no physical meaning.

R_{sh}: Resistivity of shale

Equation 4.13 can also be simplified and written in terms of conductivity as shown in equation 4.14.

$$C_t = PHIE^m\ S_w^n\ C_w + V_{sh}C_{sh} \quad \text{..... (4.14)}$$

Where,

PHIE: Effective porosity

V_{sh}: Volume of shale

C_{sh}: Conductivity of shale

Equation 4.14 basically introduces another conductivity term arising from shale but since clay is the most prevalent form of shale in Mozambique basin, the author argues that in order for the equation to be more relevant for the J- and K-Reservoirs then it should be re-written as:

$$C_t = PHIE^m\ S_w^n\ C_w + V_{cl}C_{cl} \quad \text{..... (4.15)}$$

Where:

$V_{cl:}$ Volume of clay

$C_{cl:}$ Conductivity of clay

4.4 Faust Equation: Velocity-Resistivity Transform (VRT)

The resistivity response within the hydrocarbon-bearing zone can be modelled using the sonic log according to the relationship between velocity and resistivity described by Faust equation (1953) in equation 4.16 which is only valid for highly consolidated sandstones. However, core data analysis from the J- and K-Reservoirs wells indicates that these reservoirs are poorly consolidated i.e. not well cemented reservoirs (see section 5.2) and therefore, another transform based on Hacikoylu et al. (2006) which represents poorly consolidated reservoirs was used instead.

The main objective for using the velocity-resistivity transform (VRT) was to see if the resistivity derived from the velocity (sonic log) would yield a resistivity response that is more representative of gas-bearing reservoirs than the log-measured resistivity. This section reviews the derivation of an empirical relationship between sonic (velocity) and resistivity which was put forward as early as 1953 by Faust as follows:

$$V_p = Y\,(ZF)^{1/6} \quad \text{..... (4.16)}$$

Where:
V_p: Acoustic or p-wave velocity (km/s)
Y: Constant = 2.2888
Z: Depth (km)
F: R_t/R_w = Formation Factor

Since both resistivity and velocity are empirically related to lithology and they are both dependent on total porosity, the relationship between the two parameters can be justified (Rudman et al., 1976; Hacikoylu et al., 2006). Since equation 4.16 is only applicable to well cemented, highly consolidated sands, Hacikoylu et al. (2006) modified the Faust equation for use in unconsolidated sandstone and sand-shaly formations as defined by equation 4.17 below:

$$V_p = (R_t/R_w)/[0.9 + c(R_t/R_w)],\ 0.27<c<0.32 \quad \text{..... (4.17)}$$

Where:
V_p: Velocity from sonic log
C: mathematical constant

Equation 4.17 was used to transform the velocity as measured from the sonic log to resistivity in the J- and K- Reservoirs. The justification for the above hypothesis is that, if factors that cause the low-resistivity phenomena in these reservoirs do not affect the velocity (sonic) response, then the modelled resistivity will be more representative of the gas prone reservoir than the measured resistivity and therefore the modelled resistivity will be used to calculate the water resistivity within the reservoir section. The results of the calculated water saturation will then be compared to NMR-calculated results to determine the effectiveness of this new method compared to the conventional methods in calculating water saturation in low-resistivity pay zones.

4.5 Possible Causes of Low-resistivity Pay in Mozambique Basin

The following section reviews some of the causes of the low-resistivity phenomena in sedimentary basins around the world and will be evaluated using well log and core data from the J- and K-Reservoirs to determine whether they contribute to the low-resistivity pay phenomena in these reservoirs.

4.5.1 Clay-bound Water

Clay is the most prevalent form of shale in Mozambique Basin. The presence of clay minerals in the reservoir formation could be the primary cause of low-resistivity phenomena. Clay minerals are characterised by a high negative surface charge that causes the log resistivity values to be reduced significantly. This negative surface charge is caused by a substitution of atoms in the clay lattice with lower positive valence, i.e. it attracts cations such as Na^+ and K^+ when the clay is dry (Fig. 37). When water is introduced to the clay, the cations from the clay are released into the water and as a result, the conductivity of the water is increased (Boyd et al., 1995).

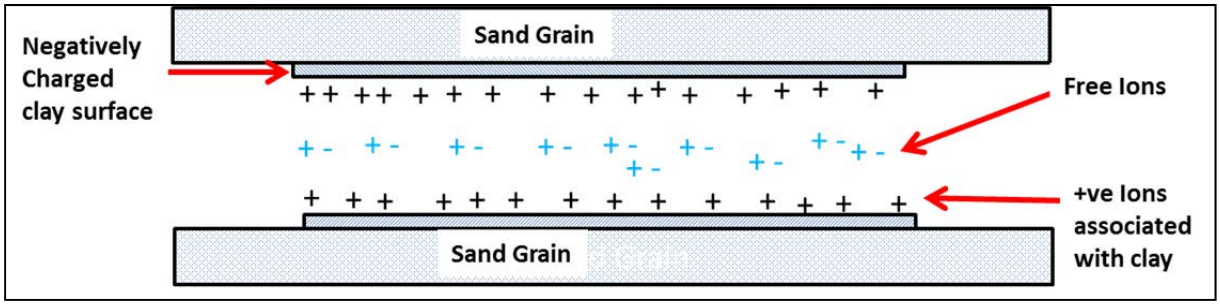

Figure 37: Capillary Exchange Capacity (CEC), the ability to release cations from clay to water in a clay-sand formation. The clay surface area is negatively charged and attracts positively charged ions along its surface.

The ability to release cations from clay to water as described above is called the Cation Exchange Capacity (CEC). The easier it is for cations to be released, the higher the CEC and clays with a higher CEC will have a greater effect on lowering resistivity than those with low CEC.

4.5.2 Silt (Capillary) Bound Water

The increased surface area associated with finer sediment grains holds more irreducible water and, as with clay-coated grains, increasing water saturation by reducing resistivity readings (Boyd et al., 1995). In Figure 38, (irreducible) immovable water is bound by the surface of clay minerals as described above and capillary water is trapped in between the pore spaces and also immovable. Resistivity logs respond to the total water present i.e. free and bound irreducible water. Therefore, calculated water saturations can be higher but water free hydrocarbons can still be produced (Zemanek et al., 1989).

Non-connectivity (poor permeability) of the pores also plays a role in trapping the water in the pores, causing it to be immobile (Taha, 2011). Water can also coat the minerals or grains in water-wet reservoirs, this irreducible water cannot be produced during a typical hydrocarbon production and it occurs in the majority of sandstone reservoirs. The presence of silt can also manifest itself as a clay effect according to Worthington et al. (2000). Core and log data from the J- and K-Reservoirs have shown that these reservoirs exhibit a certain amount of silt, which might affect the overall resistivity of the reservoirs.

4.5.3 The Laminated Sand/Shale Sequences

The general definition of a laminated bed adopted in this study is any bed that is less than 15cm in thickness (Worthington, 2000). Low-resistivity pay can arise due to the logging tool's inability to resolve thin laminated beds as described in the logging review section 4.1. In this case, the overall formation resistivity value recorded by the logging tool is dominated by the resistivity of fresh water formation and not by the high resistivity within the thin hydrocarbon-bearing bed. The ability of the log to calculate the true parametric value of that bed is called resolution (Worthington, 2000).

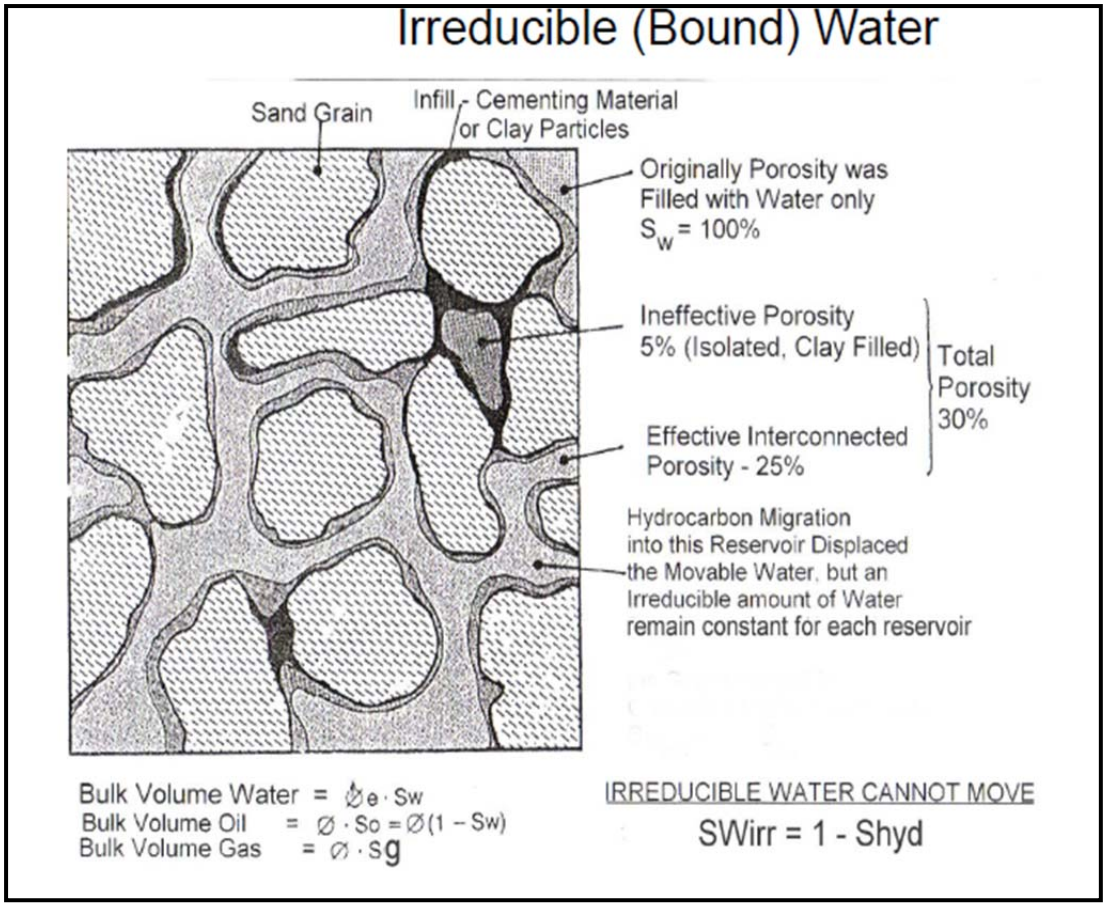

Figure 38: Clay versus capillary bound water in the formation causing irreducible bound water (Taha, 2011). Clay-filled, ineffective and effective pore spaces are shown.

4.5.4 Fresh Formation Water (R_w)

The low-resistivity contrast generally occurs when the formation waters are fresh, i.e., of low salinity. In this situation, the cause of low-resistivity phenomena is due to very low-resistivity contrast between the low salinity formation water and the oil zones (Boyd et al., 1995). In other words, the presence of brine causes the resistivity of the pay zone to be indistinguishable from that of non-pay. In addition, fresh water formations can take logging tools out of the range of salinities that they were designed for (Worthington, 2000) and corrections to the resistivity log is normally required for salinities less than 60 000 ppm of NaCl in order to give optimum results (Zemanek et al., 1989).

4.5.5 Matrix Microporosity

According to Swanson, (1985), micro-pores can be defined as pores whose dimensions are significantly smaller than those contributing to the rock's permeability or any pore space of less than one-micron in diameter (Worthington, 2000) and they tend to retain water and keep

that water from flowing when the reservoir is being produced (Petricola et al., 1995), and thus contributing to the low-resistivity phenomena in the reservoir pay zone. Another contributing factor to the low-resistivity pay is the bimodal particle size distribution where one of the particle size distributions is significantly smaller than the other (Worthington, 2000). X-Ray Diffraction (XRD) and Laser Grain Size Analysis (LGSA) methods are commonly used to determine the grain size distribution in the reservoir. The scanning electron microscope (SEM) is also an effective tool in evaluating micro-porosity, in addition to grain size studies, and the alteration of sediments. SEM can also be used to study microfossils for biostratigraphic dating (Kieke et al., 1974). However, the limitation to the SEM is that only the surface of the sample can be investigated, but no clues are given on its interior. Therefore, more advanced tools such as 3D Computer Tomography (CT) can be used to determine microporosity, down to 1µm scale. This tool was not utilised in the analysis of the data used in this study.

4.5.6 Superficial Microporosity

Diagenetic clays sometimes coat the grains and reduce the pore throat diameter and give rise to superficial microporosity. Smectites or Montmorillonite have high Cation Exchange Capacity (CEC) of 80-150 meq/100g compared to other clays such as kaolinite with a CEC range of 3-5meq/100g (Boyd et al., 1995; Watfa, 2012).

4.5.7 Conductive Minerals

Pyrite is one of the highly conductive minerals found in some sandstone formations and its presence can result in anomalously low-resistive response in the reservoir formations. According to Boyd et al., (1995), sands with more than 7% volume of pyrite with a conductivity of greater than or equal to that of formation water, would produce low-resistivity readings. X-Ray Diffraction (XRD) was used to analyse the mineral composition in the J-Reservoir and K-Reservoir core samples and no such high contents of pyrite (always under detection limits) were found.

.

4.5.8 Glauconitic Sandstones

Another possible cause for low-resistivity pay is the presence of glauconite in the reservoir. Glauconite is an iron-rich clay mineral formed during diagenesis, and can be found as pellets, composite grains or inter-granular cement (Diaz et al., 2003). The highly conductive Fe+ in the mineral could lower the overall resistivity of the reservoir.

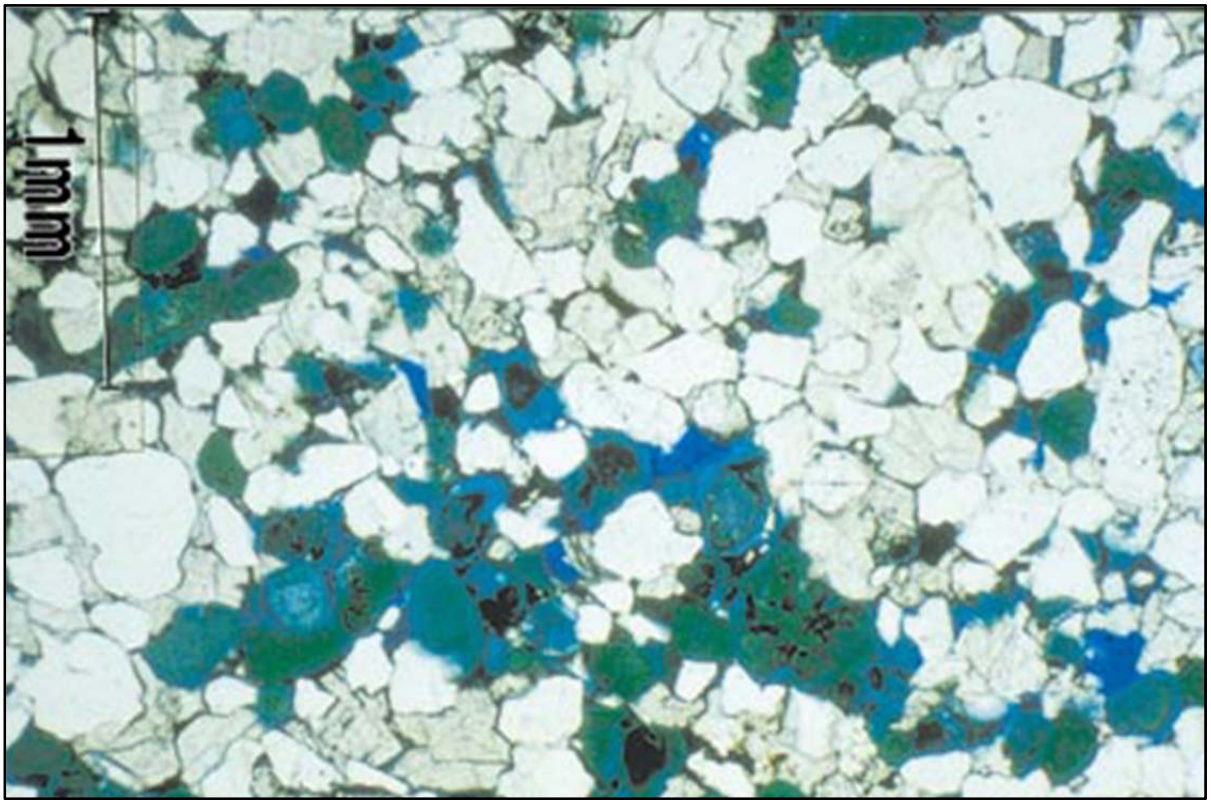

Figure 39: A thin section from the Cretaceous Napo and Hollin Formations of the Oriente basin in Ecuador where the glauconitic, laminated and burrowed sandstones are common (White et al., 1995)

The presence of glauconite is generally used to identify depositional environment and to construct stratigraphic succession of those environments. For instance, glauconite generally occurs in sedimentary rock deposited in Fe-rich conditions in shelf environments where upwelling is common, whereby glauconite forms part of the rock matrix. The Fe^{+} in glauconite can increase the conductivity of the reservoir formation and when it occurs as cement, it can reduce the quality of the reservoir by occluding the original primary porosity. A thin section from the Cretaceous Napo and Hollin Formations of the Oriente basin in Ecuador where the glauconitic, laminated and burrowed sandstones are common is shown in Figure 39 below (White et al., 1995). Another example of glauconitic sandstone can be found in the Palaeocene Greensands sandstone of the North Sea, which exhibits the low-resistivity phenomena due to the presence of porous glauconite (Hossain et al., 2011). This is attributed to the large amount of bound water in the glauconite cement.

4.6 Well Log Character of the J- and K-Reservoirs

The gamma ray (GR) log response in column 2 of Figure 40 shows a coarsening-upward sequence for the J-Reservoir. This is a typical response of the gamma ray log for all the wells that intersected the J-Reservoir. The resistivity response for both the shallow reading resistivity (M2R2) and the deep reading resistivity (M2RX) is also shown (column 3) and the curves generally show a decrease in the resistivity towards the lower part of the reservoir. The top part of the reservoir is characterised by an increase in resistivity associated with the presence of hydrocarbons but the resistivity decreases towards the lower part (low-resistivity response) even though there are hydrocarbons in that part of the reservoir. The effect of this low-resistivity on the calculated water saturation (S_w) is shown in column 4 where water saturation calculated using Archie's equation indicates 100% water saturation and NMR-calculated water saturation indicates the presence of hydrocarbons all the way to the bottom of the reservoir at 1168m (MD or 1121mss.

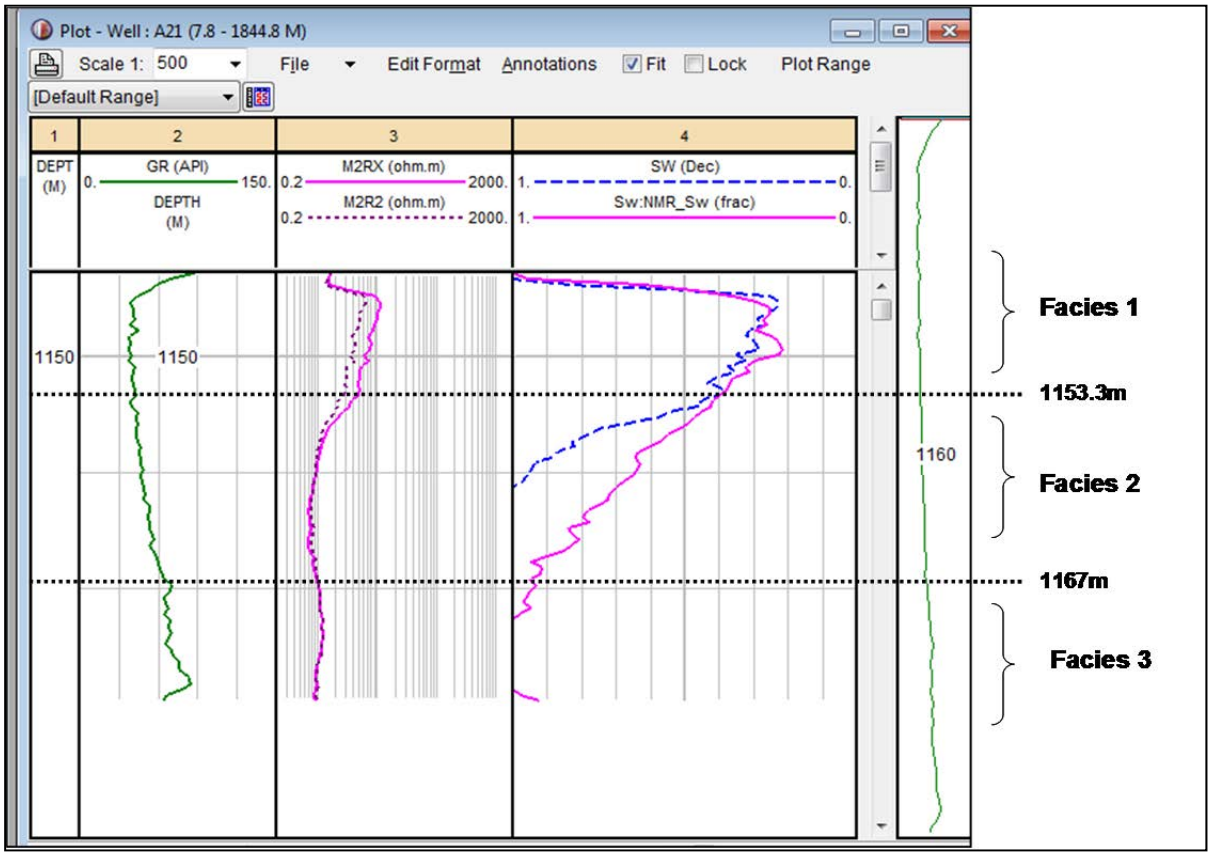

Figure 40: The gamma ray (GR) log in column shows an upward coarsening sequence typical of the J-Reservoir sands. Shallow-resistivity (M2R2) and deep resistivity (M2RX) response for well A21 of the J-Reservoir and the associated water saturation calculated using Archie's equation and NMR in column 4.

The resistivity log profile can be further divided into different *electro-facies* i.e. the variation in electrical conductivity of the formation due physiochemical changes within the formation as shown in Figure 40 and Figure 41 for the J- and K- Reservoirs, respectively. “Electro-facies 1” represents the coarser grained section of the reservoir and shows relatively higher resistivity response whereas “electro-facies 2” represents finer grained sandstone. The lower section of the reservoir is represented by “facies 3” where a moderate increase in resistivity is observed towards the bottom of the reservoir, this could be due to change in facies from silt to the shaly bottom part of the reservoir.

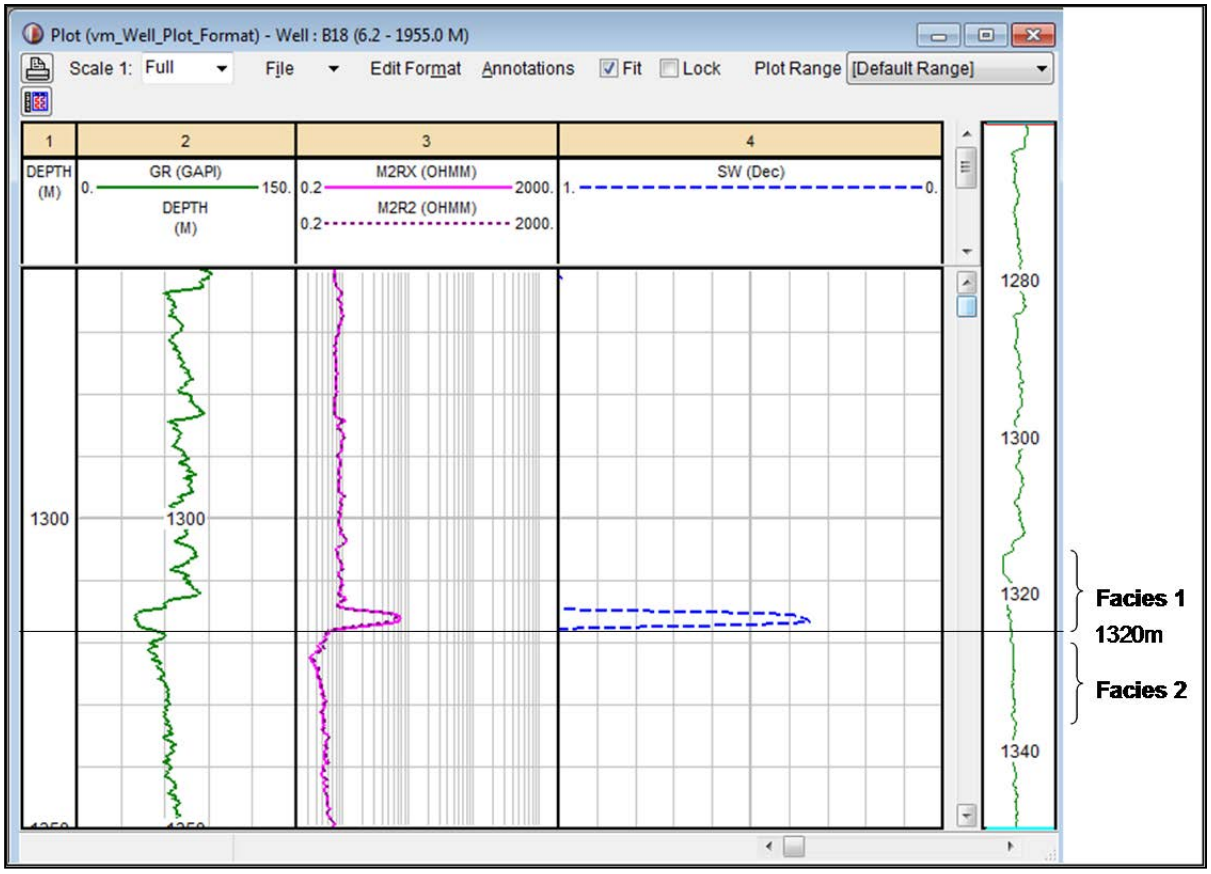

Figure 41: The gamma ray (GR) log in column 2 does not show upward coarsening sequence similar to that of the J-Reservoir sands. Shallow-resistivity (M2R2) and deep (M2RX) resistivity responses for well B18 of the J-Reservoir are shown in column 3 while the associated water saturation is shown in column 4.

The low-resistivity phenomenon in the K-Reservoir (Fig. 41) is not as pronounced as in the J-Reservoir (Fig.40). This is due to the differences in the depositional environment of the two reservoirs which results in different gamma ray log response. The effect of these differences on the water saturation calculation will be demonstrated in section 5.3.

CHAPTER 5: RESEARCH METHODOLOGY

The research approach is outlined in section 3.4. The comprehensive analytical methods, workflow and the results will be discussed in the next section. Analytical methods used in this research, involved mainly integrated data from different sources to investigate empirical relationships between various reservoir properties. These relationships were established mainly from the well logs and core data. Core images from the core data acquired in the some of the wells and published literature were used to describe depositional systems of the J-Reservoir and the K-Reservoir where the low (dual) resistivity profiles are observed. The seismic data were mapped and interpreted to define the reservoir extend and the log data was correlated to investigate the variation in the thickness of the reservoirs from well to well as well as to establish a depositional dip.

The author developed a new approach (algorithm) to calculate water saturation (S_w) calculation and the results were compared to the already existing industry practices such as conventional Archie's and Simandoux equations. All the water saturation results from these methods were compared to NMR-calculated water saturation (S_w). The results of the water saturation calculated using different algorithms including the new method will be discussed in chapter 5.3.

5.1 LOG ANALYSIS

Analytical methods used in this research involved the integration of data from different sources in order to investigate the empirical relationships between reservoir properties such as, fabric and texture, grain size variability, clay content and distribution, porosity and permeability. Interactive Petrophysics (IP) is one of the commonly used software packages, to calculate reservoir properties and water saturation (S_w) in the reservoir formation. However, the author had limited access to the software license and therefore used Excel spreadsheets instead to program the relevant algorithms used in IP to evaluate reservoir properties and to calculate water saturation. Petrophysics (IP) was then used to quality-check the results and also used in cases where the algorithms were too complex to be programmed in an Excel spreadsheet. A workflow was developed to improve the accuracy of the calculated water saturation (S_w) and this will be discussed in detail in chapter 5.2. This section covers the data analysis workflow as well as the outcome, or results of the analysis.

5.1.1 QC of Logs and Depth Calibration

A first pass quality check was done on the logs to edit any noise (spikes) associated with poor quality data. Any additional system errors can be identified once the logs have been normalised and then corrected accordingly. The next step was the depth calibration of the wire-line log data to make sure it matches the depth from the core data since the data were acquired independently of each other during separate down-hole surveys. The recorded data may not be on depth with each other due to various factors ranging from cable stretch during logging operations to poor surface depth registration. The most common procedure used to achieve this is to match the gamma ray measured from the core sample (CGR) to the wireline measured gamma ray (GR). This process is called the gamma ray depth calibration since the depth on the wireline log is often shifted to match the core gamma ray depth.

- **Results: Core Depth Calibration (Well A15).**

Figure 42 shows a core depth calibration for the gamma ray (GR) log in well A15 of the J-Reservoir. In this well, there is a good depth match between the core gamma ray (CGR) shown in red and the wireline gamma ray (GR) is shown in green in column 2, therefore it was deemed not necessary to apply the depth shift. Since well A15 is the only well with core gamma ray (CGR) information within the J-Reservoir, no other CGR data were available to depth match the well log data within the J-Reservoir.

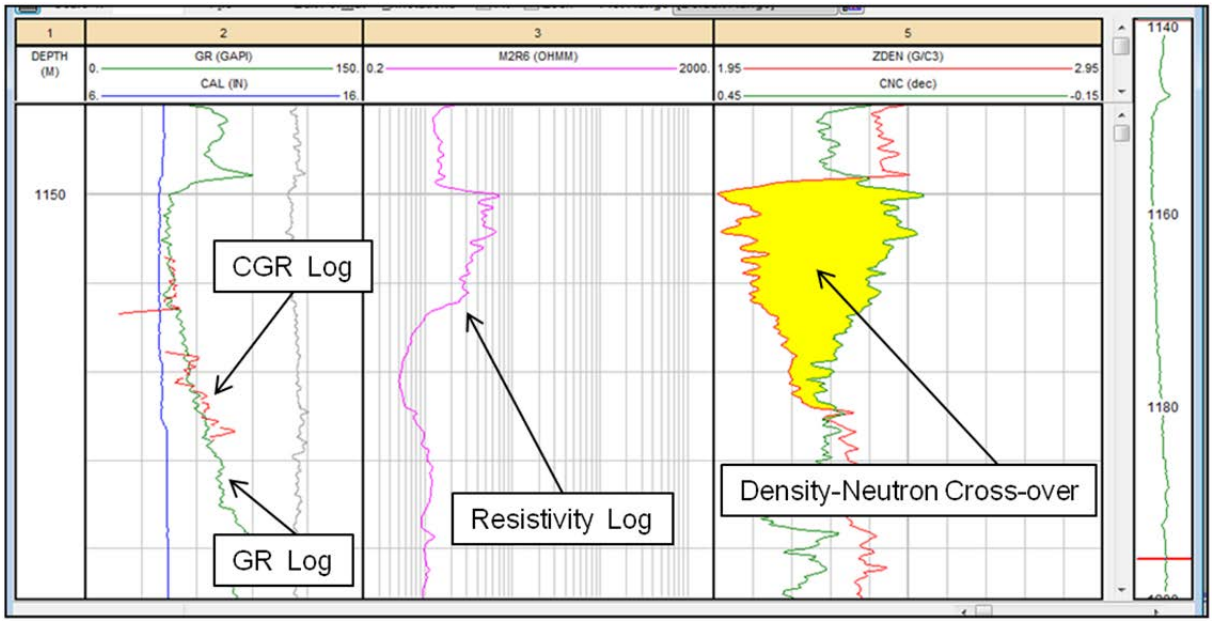

Figure 42 : Core gamma ray (CGR) log versus wireline gamma ray (GR) for well A15 showing the core gamma ray (CGR) in red and the wireline measured gamma ray (GR) log in green in Column 2. The CGR matches the GR and no depth shift was necessary to match the two curves.

- **Results: Core Depth Calibration (Well B12).**

Figure 43 shows a core depth calibration for the gamma ray (GR) log in well B12 of the K-Reservoir. The difference in core gamma curve (CGR) depth and the wireline gamma ray log (GR) depth is 0.5m. Therefore, a 0.5m depth shift was applied to the wireline gamma ray log to align the two independently measured gamma ray logs.

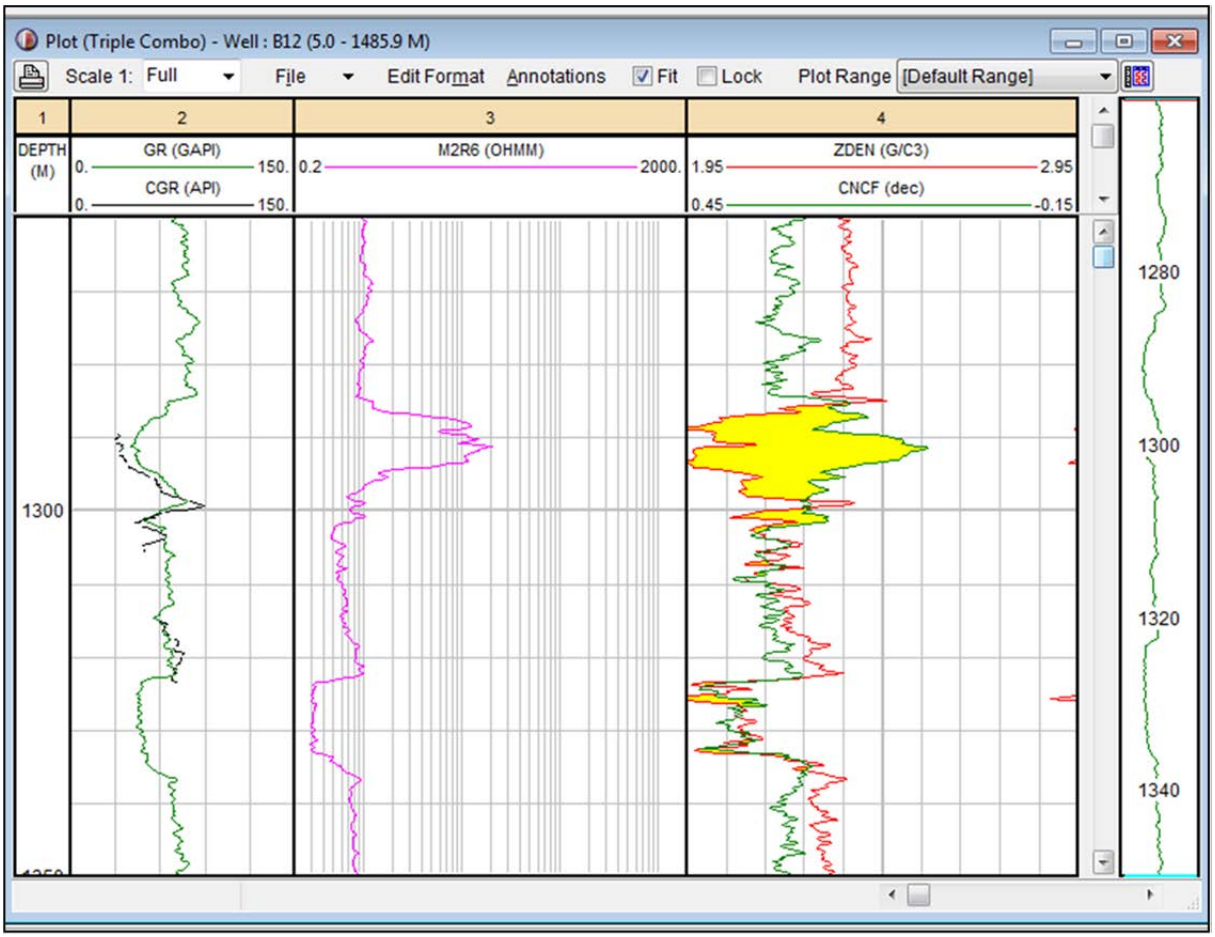

Figure 43: Core gamma ray (CGR) log versus wireline gamma ray (GR) for well B12 showing the core gamma ray (CGR) in black and the wireline measured gamma ray (GR) log in green (Column 2). The CGR matches the CGR and no depth shift was necessary to match the two curves. A depth shift of 0.5m was applied to the GR log to match the CGR's depth.

5.1.2 Well Log Normalization

The well log response within a stratigraphic unit may vary from well to well especially if the data were acquired in different drilling campaigns using different brands or generation of logging tools and instrument calibration errors, different borehole environment, tool design and tool malfunction. In order to obtain standardised and comparable reservoir evaluation results, it is necessary to normalize the log response across different wells. In so doing,

systematic logging errors can be identified and removed from the actual log data (Shier, 2004). The data used in this study comprise wells drilled by different companies using different tools, from 1961 to 2010 (e.g. Baker Hughes and Schlumberger). Therefore it was necessary to carefully check the quality of the data and normalise the log response for the logs used in this study. The normalization workflow was based the publication by Shier (2004), using an Excel spreadsheet to program the following algorithm:

$$V_{norm} = R_{min} + (R_{max} - R_{min})(V_{log} - W_{min})/ (W_{max} - W_{min}) \quad \text{.....(5.1)}$$

Where;

V_{norm}: Normalized values of the curve

R_{min} and R_{max}: Regional best estimates for two lithologies

V_{log}: non-normalized log curve

W_{min}: Value of specific lithology in each well

W_{max}: Value of a different lithology in each well

Based on the initial screening of the entire log data used in the study, it was decided that only the gamma ray (GR) and density (RHOB) logs need to be normalised, because these are the main logs used to calculate key reservoir properties such as silt and clay content, as well as fluids properties such as the water saturation (S_w). Resistivity and neutron logs also looked consistent from well to well and therefore it was deemed not necessary to normalise these logs.

- **Results: Well Normalization for the J-Reservoir**

Separate log trend analyses were generated for the J- and K-Reservoirs to determine the statistical distribution of the gamma ray (GR) and density (ZDNC) log values. A total of nine wells were analysed for the J-Reservoir and the gamma ray distribution (spread) shown in Figures 44 and 46 as multiwall histograms were generated for the J-Reservoir and the K-Reservoir, respectively. The regional best estimates, R_{min} and R_{max} for the two reservoirs were defined form these distributions. Figure 44 below is a multi-well histogram of GR data with a bimodal distribution of GR values. The two modes are labelled Distr 1 and Distr 2.

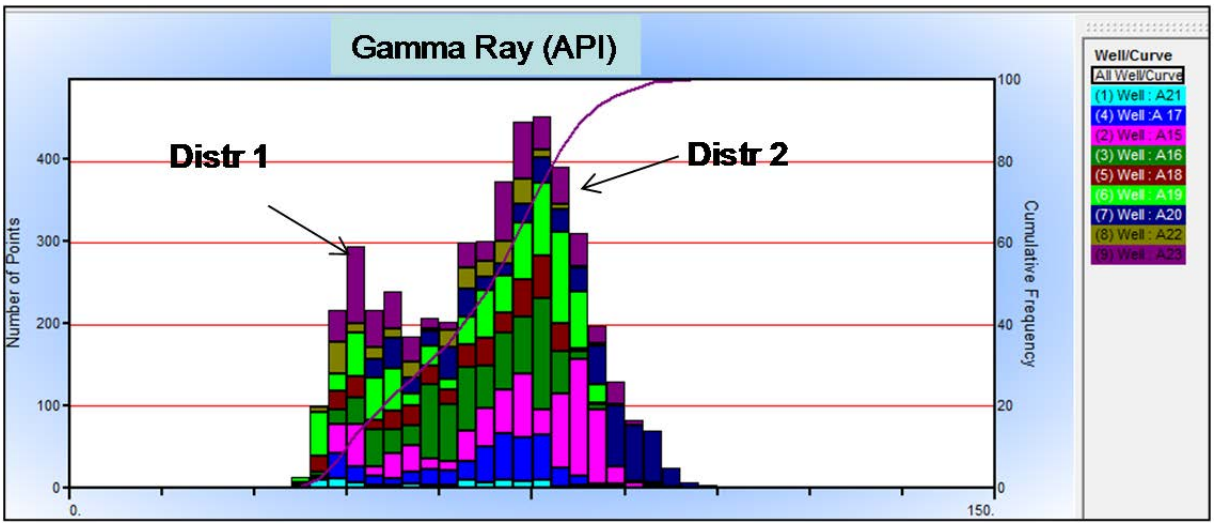

Figure 44: Multi-well histogram of gamma ray (GR) values for J-Reservoir. The histogram represents gamma ray values for all the 9 wells used to generate the regional statistical log distribution.

The data used to generate the gamma ray (GR) distributions in Figure 44 are listed in Table 3 below. The regional minimum (R_{min}) and maximum (R_{max}) gamma ray (GR) values from the distribution are 37.4^{o} API and 106^{o} API, respectively. Figure 45 shows the original gamma ray log (red) and the normalised gamma ray log (blue) for well A21 of the J-Reservoir. There is clearly a shift in the gamma ray values between the original and the normalised log with the latter generally having lower values than the former.

Curve	Well	Top	Bottom	Min	Max	Std Dev	Mean	Mode	P10	P50	P90
GR	Well : A21	1140 M	1190 M	38.138	87.398	14.104	59.582	43.5	40.859	60.994	77.222
GR	Well :A 17	1140 M	1200 M	41.478	93.781	11.61	66.021	70.5	45.615	69.195	78.054
GR	Well : A15	1130 M	1250 M	40.827	96.125	13.615	71.402	82.5	46.833	74.52	84.852
GR	Well : A16	1140 M	1200 M	40.783	86.006	10.512	65.543	76.5	49.412	66.208	77.577
GR	Well : A18	1140 M	1200 M	38.027	94.782	12.793	63.508	76.5	44.236	66.09	78.111
GR	Well : A19	1140 M	1200 M	37.455	86.897	14.25	65.753	79.5	44.841	69.988	81.466
GR	Well : A20	1138 M	1250 M	48.136	106.37	14.961	78.155	88.5	53.88	82.532	94.362
GR	Well : A22	1150 M	1200 M	41.394	88.91	12.037	61.034	43.5	43.678	63.024	74.876
GR	Well : A23	1150 M	1200 M	41.764	91.062	14.353	64.725	46.5	45.85	68.748	83.406
Overall				**37.455**	**106.37**	**14.119**	**67.512**	**76.5**	**46.415**	**69.847**	**84.455**

Table 3: Log data from nine wells (J-Reservoir) used to generate the histogram in Figure 43. The regional minimum (R_{min}) gamma ray (GR) from the data distribution is 37^{o} API with a regional maximum (R_{max}) of 106^{o} API.

A similar regional statistical distribution was also generated for the density log and the R_{min} and R_{max} for the density logs were 2.2 gm/cc and 2.8 gm/cc, respectively. All the well logs used in the study were normalised and the results are shown in Appendices 3-11.

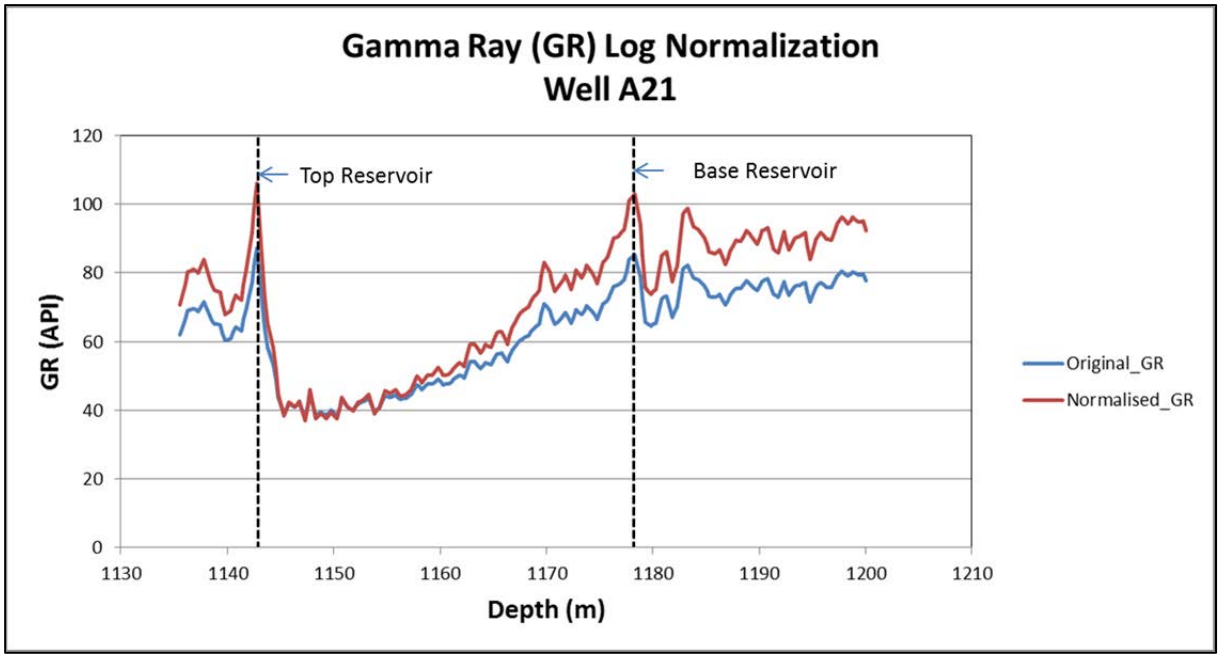

Figure 45: The original gamma ray log (red) and the normalised gamma ray log (blue) for well A21 of the J-Reservoir. The values for the normalised log are lower than those of the original log.

- **Results: Well Normalization for the K-Reservoir**

The statistical log distribution for the K-Reservoir is shown as a multi-well histogram in Figure 46 below. The seventeen well log data are listed in Table 4. The regional minimum (R_{min}) and maximum (R_{max}) gamma ray (GR) values from the distribution are 35^{o} API and 149^{o} API, respectively. Figure 47 shows the original gamma ray log (red) and the normalised gamma ray log (blue) for well B12 of the K-Reservoir. As in well A21, there a shift in the gamma ray values between the original and the normalised log with the latter generally having lower values than the former. The regional minimum (R_{min}) and maximum (R_{max}) density (RHOB) values calculated from the regional density distribution were 1.6 gm/cc and 2.6 gm/cc, respectively.

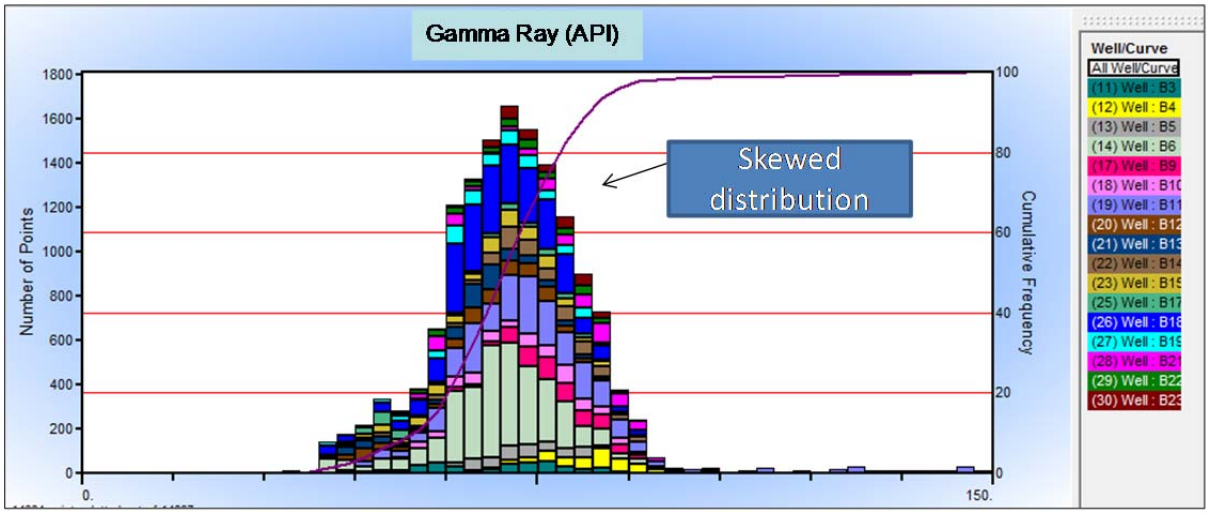

Figure 46: Multi-well histogram of GR values for the K-Reservoir showing a slightly skewed distribution of gamma ray (GR) values for all the 17 wells

Curve	Well	Top	Bottom	Min	Max	Std Dev	Mean	Mode	P10	P50	P90
GR	Well : B3	1260 M	1320 M	43.005	88.015	11.11	68.238	76.5	54.815	70.544	82.017
GR	Well : B4	1260 M	1320 M	68.255	103.86	6.7467	83.878	85.5	74.662	84.525	91.788
GR	Well : B5	1260 M	1320 M	50.809	86.898	7.0816	72.553	70.5	63.513	72.29	82.234
GR	Well : B6	1260 M	1380 M	35.09	91.751	9.8449	68.05	67.5	56.136	68.813	79.048
GR	Well : B9	1260 M	1350 M	59.762	95.127	6.9549	77.948	76.5	69.834	77.651	87.761
GR	Well : B10	1260 M	1350 M	53.414	140.46	12.019	74.128	79.5	59.602	74.464	87.64
GR	Well : B11	1260 M	1350 M	45.106	149.26	19.561	77.85	73.5	59.364	74.063	100.46
GR	Well : B12	1260 M	1350 M	40.509	85.967	11.327	64.95	64.5	46.621	66.898	77.985
GR	Well : B13	1260 M	1350 M	38.257	87.089	10.747	63.8	67.5	46.482	65.67	76.589
GR	Well : B14	1260 M	1350 M	45.172	93.243	10.12	74.013	70.5	60.25	74.142	86.266
GR	Well : B15	1260 M	1350 M	43.005	88.015	10.752	66.504	70.5	50.211	68.129	80.051
GR	Well : B17	1300 M	1350 M	43.519	108.37	14.436	63.139	49.5	47.165	61.988	81.463
GR	Well : B18	1260 M	1350 M	40.025	91.751	9.5432	68.182	61.5	57.249	68.146	79.514
GR	Well : B19	1260 M	1350 M	38.746	86.898	10.728	67.004	61.5	52.065	67.438	80.861
GR	Well : B21	1260 M	1350 M	54.261	103.86	12.182	76.906	85.5	58.685	79.933	90.633
GR	Well : B22	1260 M	1350 M	52.522	97.547	10.156	71.842	73.5	57.47	72.674	84.46
GR	Well : B23	1260 M	1350 M	51.574	90.551	8.1402	74.45	70.5	64.422	74.714	84.195
Overall				**35.09**	**149.26**	**13.052**	**71.077**	**70.5**	**56.323**	**70.745**	**84.744**

Table 4: Log data from seventeen wells used to generate the histogram in Figure 46. The regional minimum (R_{min}) gamma ray (GR) from the data distribution is 35^o API with a regional maximum (R_{max}) of 149^o API.

A slightly skewed distribution is observed in the multi-well histogram of gamma ray logs in Figure 46 above. This pattern, according to Shier (2004), represents an overlapping mix of rock types and minimum and maximum values should be picked on the shoulders of the distribution and not on the tail ends. Figure 47 shows a significantly large difference between the original and the normalised gamma ray log outside of the reservoir section but the two curves are closer to each other within the reservoir section for well B12.

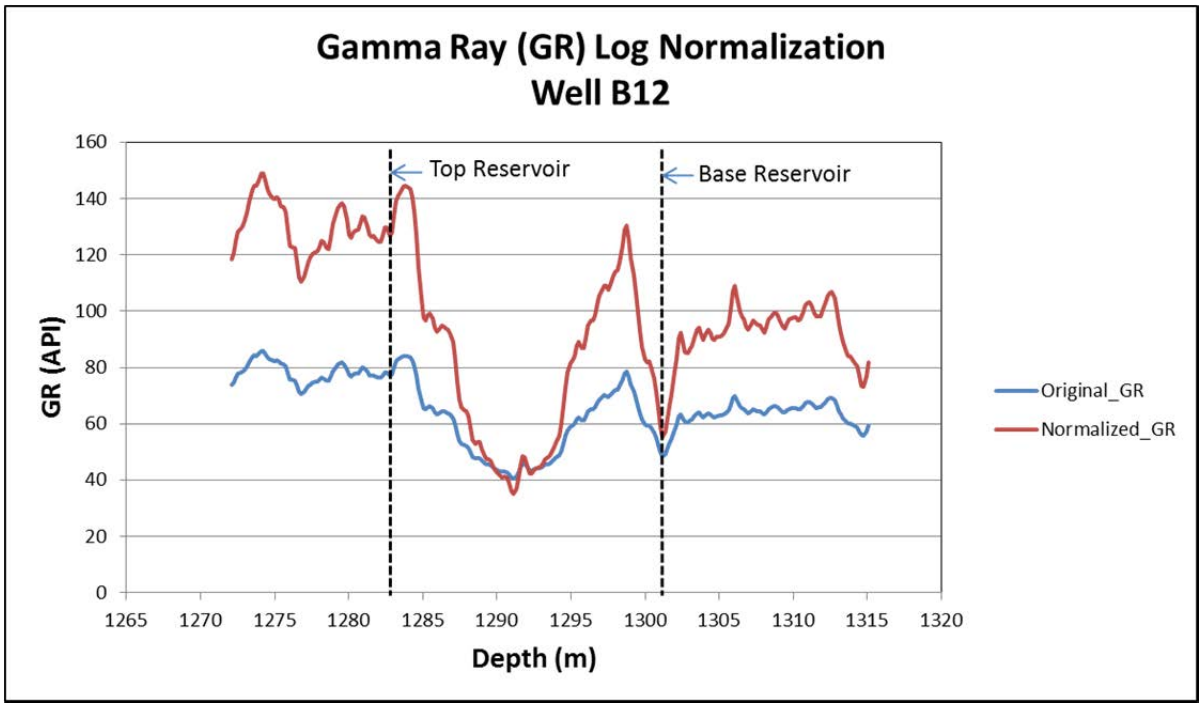

Figure 47: The original gamma ray log (red) and the normalised gamma ray log (blue) for well B12 of the K-Reservoir. The deviation between the two curves is more pronounced outside than within the reservoir section.

5.1.3 Porosity Calculation

Porosity was defined in section 4.1.1 as the ratio of the volume of all pores in a material to the total volume, between 0 and 1, or as a percentage between 0 and 100%, within a reservoir rock. It is one of the key input parameters that control the water saturation (S_w) in the reservoir. In this study, porosity was calculated using equation 4.3 where the input parameters are matrix density, which is measured from the core data, density of the fluid, which is measured in the laboratory and is different for oil, gas and water and the bulk density measured from the wireline density log. Total porosity is given by equation 4.3 in section 4.1.1.2. Effective porosity, which is defined by the connected pore space in the reservoir, was calculated by subtracting the volume of shale (V_{shale}) from the calculated total porosity (PHIT) as shown in equation 5.3.

Effective porosity (PHIE) = PHIT*(1-V_{sh})..... (5.2)

Where,

PHIE: Effective porosity

V_{sh}: Volume of shale

- **Grain Density Measurements**

The average grain density used in equation 4.3 was measured from core data of the A11, A12 and A13 wells to be 2.64 gm/cc for the J-Reservoirs on humidity-dried core and 2.66 gm/cc on vacuum dried core. Similarly, the grain densities from wells B13 and B12 were averaged to calculate the grain density for the K-Reservoir of 2.64 gm/cc on humidity-dried core and 2.69 gm/cc on the vacuum dried core. The J- and J-Reservoirs comprise predominantly of quartz (Table 6) and the grain density of quartz sandstone in the Gulf of Mexico usually varies from 2.65 gm/cc to 2.68 gm/cc (Tixier et al, 1968) and the grain densities in the J- and K-Reservoirs compare well to these values.

- **Results: Porosity for the J-Reservoir**

Figure 48 shows the log calculated porosity using an Excel spreadsheet compared to porosity calculated using Interactive Petrophysics Software (IP) for quality check and validation of Excel based calculations. There is a good correlation between the two calculations. The log calculated average porosity from wells A21 and A15 of the J-Reservoir was 26% based and 28%, respectively and these results compared very well to core measured porosity from well A15 where porosity ranged from 28.7% to 29 % for a humidity- and vacuum-dried core, respectively. No core porosity was measured in well A21 due to the relatively poor quality of the core plugs.

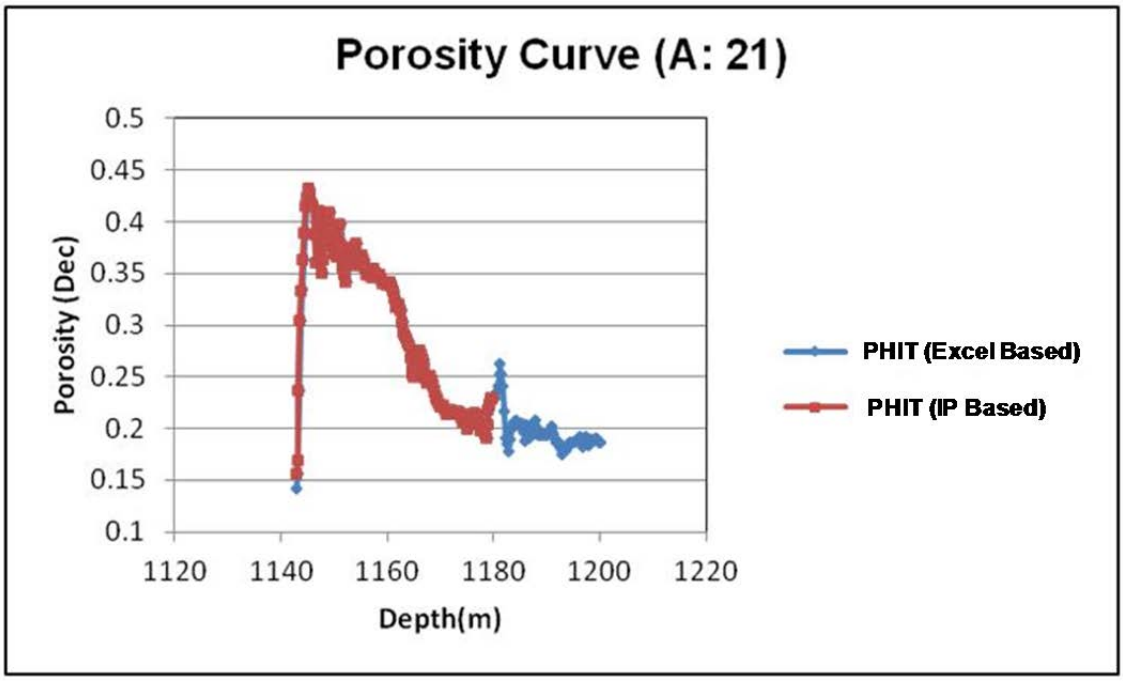

Figure 48: Porosity calculated using the Interactive Petrophysics (IP) Software (red) and the Excel spreadsheet (blue). There is a good correlation between the two curves, which indicates the robustness of using Excel spreadsheet to calculate the reservoir parameters. The blue line overlaps with the red line in the 1140 to 1180m depth.

- **Results: Porosity Calculation for the K-Reservoir**

As in well A21 of the J-Reservoir, Figure 49 shows the log calculated porosity using an Excel spreadsheet compared to porosity calculated using Interactive Petrophysics Software (IP) for well B18 of the K-Reservoir. The calculated porosity log (using Excel spreadsheet) shows more noisy spikes than the porosity log calculated using IP. This could be due to poor quality of the original input logs caused by bad borehole quality such as washouts. This is supported by the caliper log which measures the borehole diameter (Fig.50). The caliper log indicates changes in the borehole diameter of approximately 0.6 inches within the reservoir section. This could have led to poor coupling of the logging tools against the borehole wall, leading to poor quality of the recorded logs. The log calculated average porosity from well B12 of the K-Reservoir was 25.8% compared to core calculated porosity of 26.7%. No core porosity was measured in well B18 due to the relatively poor quality of the core plugs.

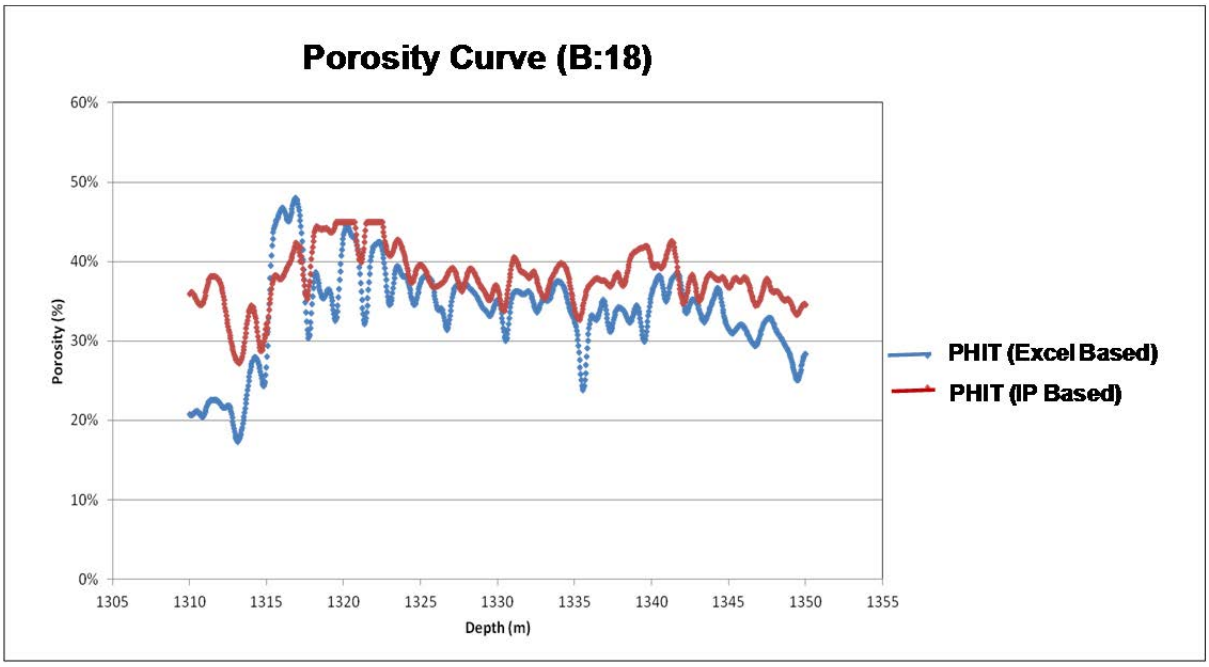

Figure 49: Porosity calculated using the Interactive Petrophysics (IP) Software (red) and the Excel spreadsheet results in blue). The calculated porosity log (Excel based) shows more noisy spikes than the porosity log calculated using IP.

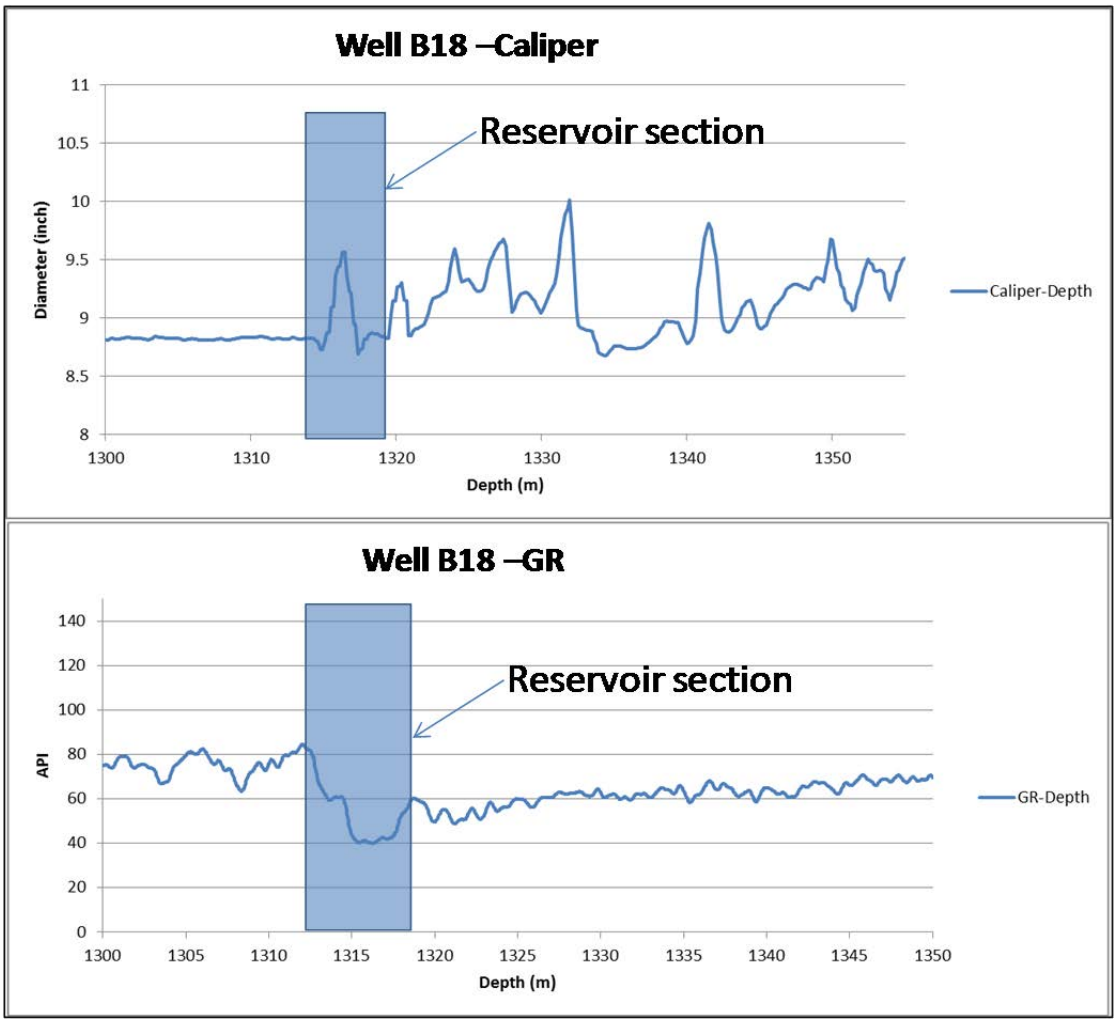

Figure 50: The caliper log in well B18 showing a change in borehole diameter of approximately 0.6 inches within the reservoir section. This could have led to poor coupling of the logging tools against the borehole wall which resulted in the poor quality of the logs, as seen in Figure 49.

- **Porosity Ranges from Density-Neutron Cross-Plots**

A graphical method to estimate the porosity, volume of shale versus sand in the reservoir using the density and the neutron porosity logs as inputs is the density-neutron (D-N) cross-plots shown in Figures 51, 52, 53 and 54. These plots can also be used to identify complex mixtures of sandstone and limestone from porosity logs as described in section 4.1.1. In this study, the D-N lithology plots were modified using an Excel spreadsheet to differentiate between sandstone and shale as shown below.

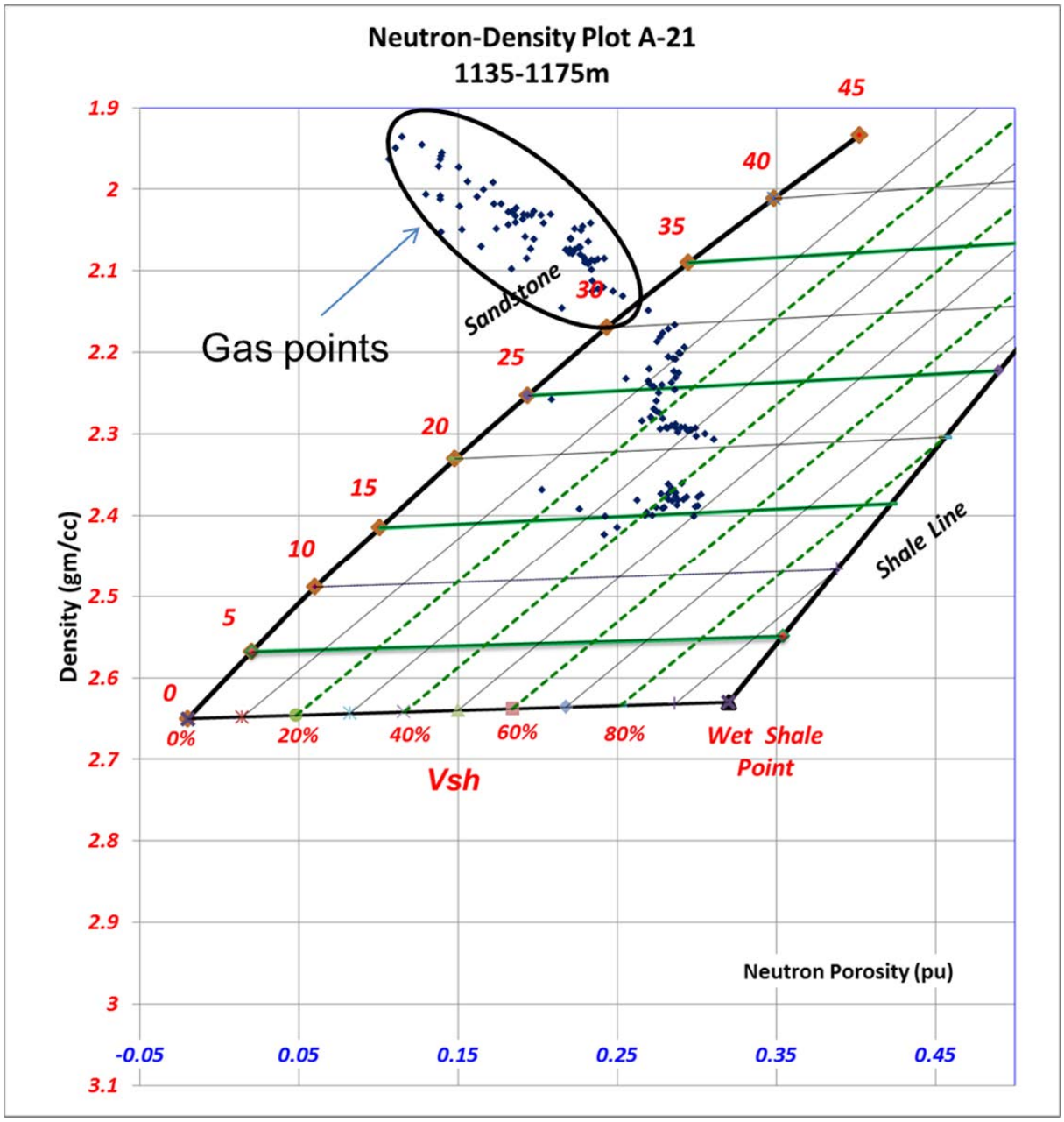

Figure 51: Neutron-Density plot for Well A21 showing porosity ranges from approximately 14-33% and the volume of shale ranges from 0-45%. The gas effect points are shown outside the sandstone boundary line.

Figure 51 and 52 shows porosity ranges from approximately 14% to more than 33% and the volume of shale ranges from 0 to 45% in wells A21 and A16. The points outside of the clean sandstone-shale line are caused by the presence of gas in the reservoir which causes the density log to measure anomalously low density values.

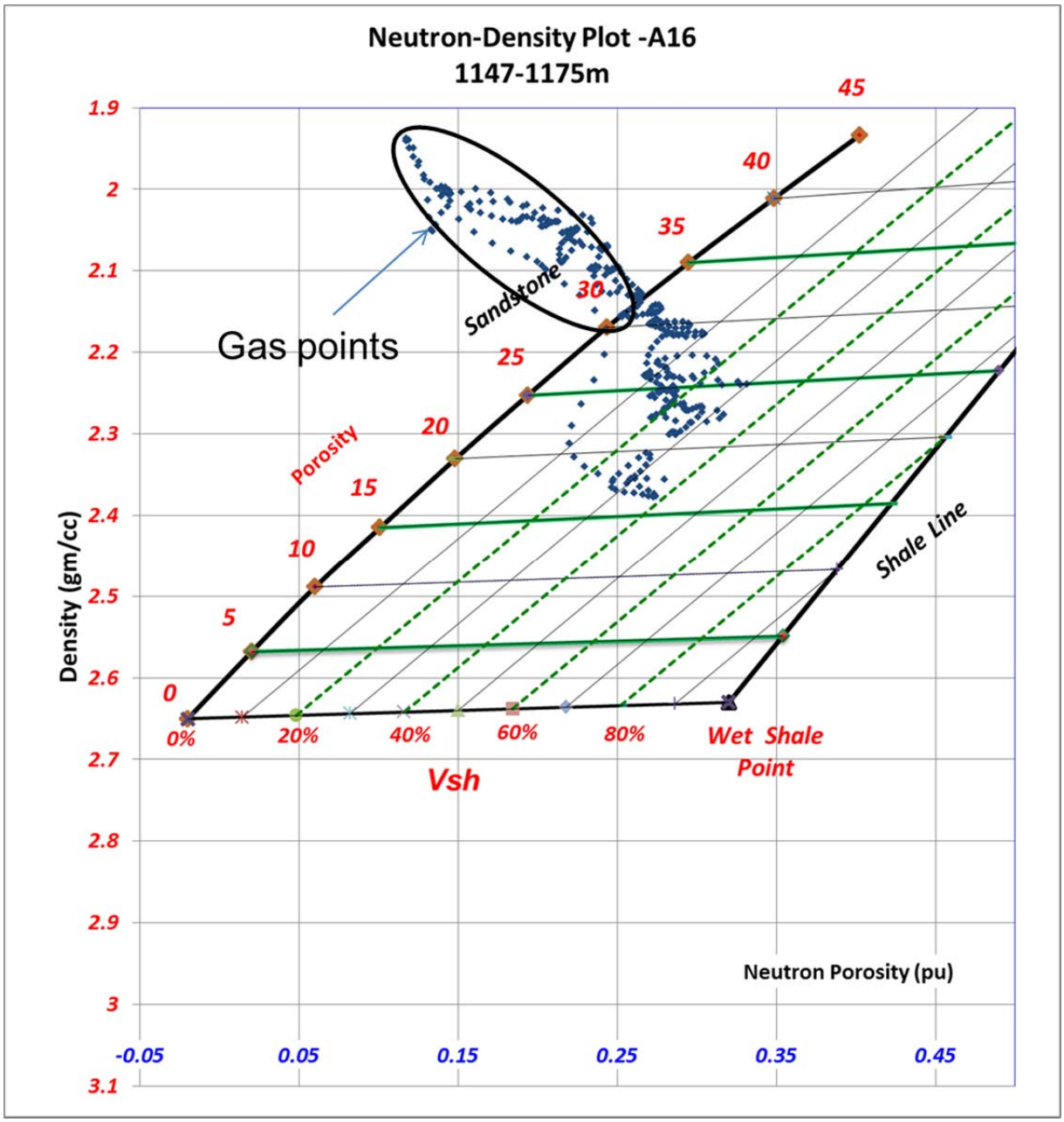

Figure 52: Neutron-Density plot for Well A16 showing porosity ranges from approximately 16-33% and the volume of shale ranges from 0-40%. The gas effect points are shown outside the sandstone boundary line.

In the K-Reservoir, a similar trend is observed, where the porosity ranges of between 16-34% and 19-30% for wells B12 and B13, respectively. The volume of shale ranges from 0-38% and 0-16% for wells B12 and B13, respectively. Again, the points outside of the clean sandstone-shale line are caused by the presence of gas in the reservoir.

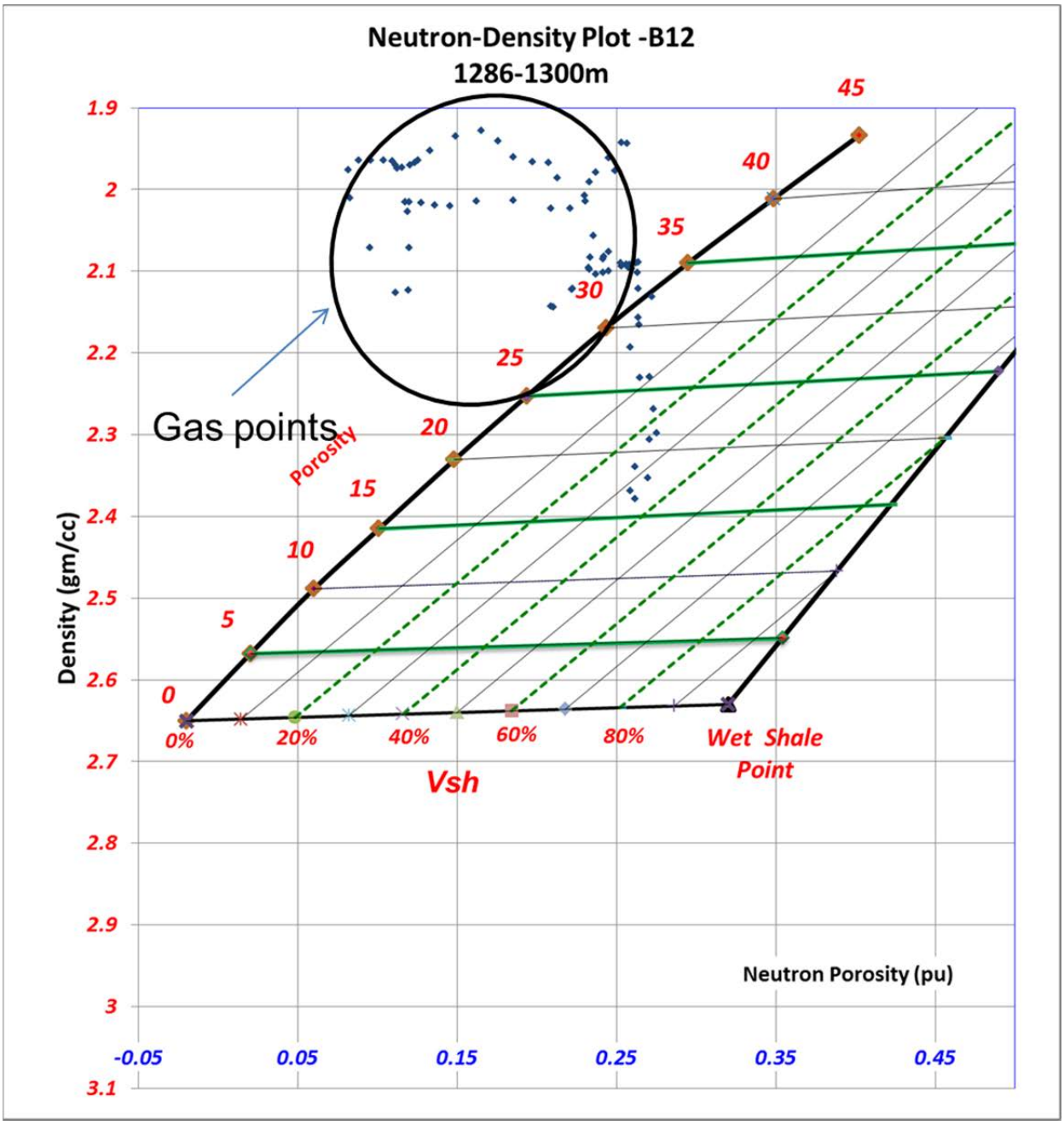

Figure 53: Neutron-Density plot for Well B12 showing porosity ranges from approximately 16-34% and the volume of shale ranges from 0-38%. The gas effect points are shown outside the sandstone boundary line.

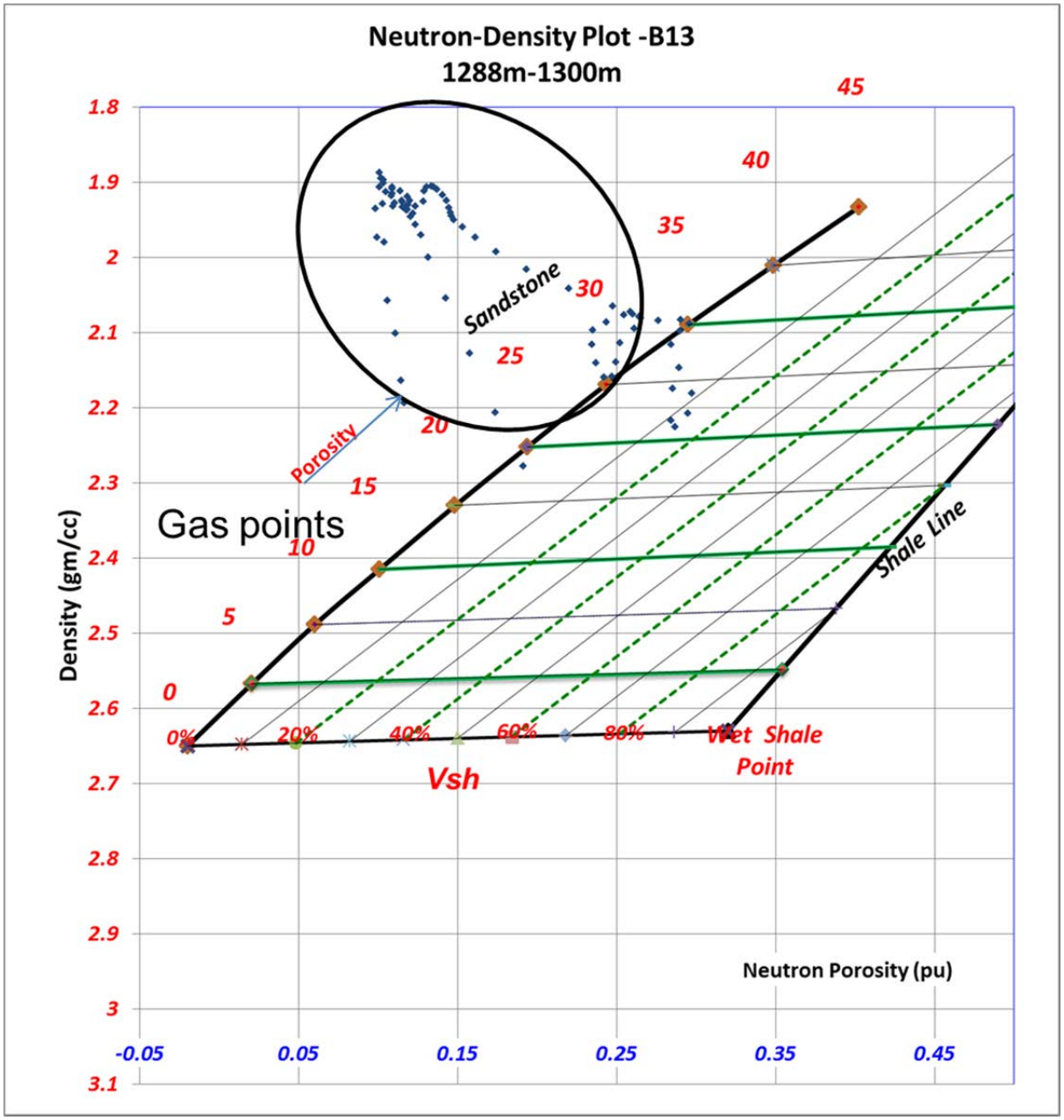

Figure 54: Neutron-Density plot for Well B12 showing porosity ranges from approximately 19-30% and the volume of shale ranges from 0-16%. The gas effect points are shown outside the sandstone boundary line.

5.1.4 Reservoir Thickness Analysis

The reservoir thickness was calculated using the top and the base of the reservoir as defined in the well log data, particularly the gamma ray (GR) in each well. The thickness data points from each well were then gridded to generate the reservoir thickness map shown in Figure 55 and Figure 56 for the J-Reservoir and the K-Reservoir, respectively. The reservoir thickness away from the well control depends on the gridding algorithm used and cannot be verified or calculated with a high level of confidence. The seismic data were not used to calculate the reservoir thickness due to the poor resolution and the large average spacing of approximately 6km between the lines whereas the top and base of the reservoir were easily resolvable on the well log data to calculate the reservoir thickness.

- **Results: Thickness Analysis for the J-Reservoir**

The isopach map of the J-Reservoir in Figure 55 shows that the reservoir thickness increases from 18m to 40m in the east to west direction. This is indicative of a deltaic prograding sequence with sediment input from the west or north-west and is supported by core data and evidence paleontological evidence. The map also suggests that the reservoir pinches out to the west of the block which forms the up-dip stratigraphic trap for the K-Reservoir.

- **Results: Thickness Analysis for the K-Reservoir**

The isopach map of the K-Reservoir in Figure 56 shows that the reservoir thickness increases to the south and east with the thinnest part in the north-west direction. However, there is very little well control in the south-east of the block to accurately calculate the reservoir thickness with a high level of confidence. The minimum and maximum thickness calibrated to the well is 8 and 14m, respectively.

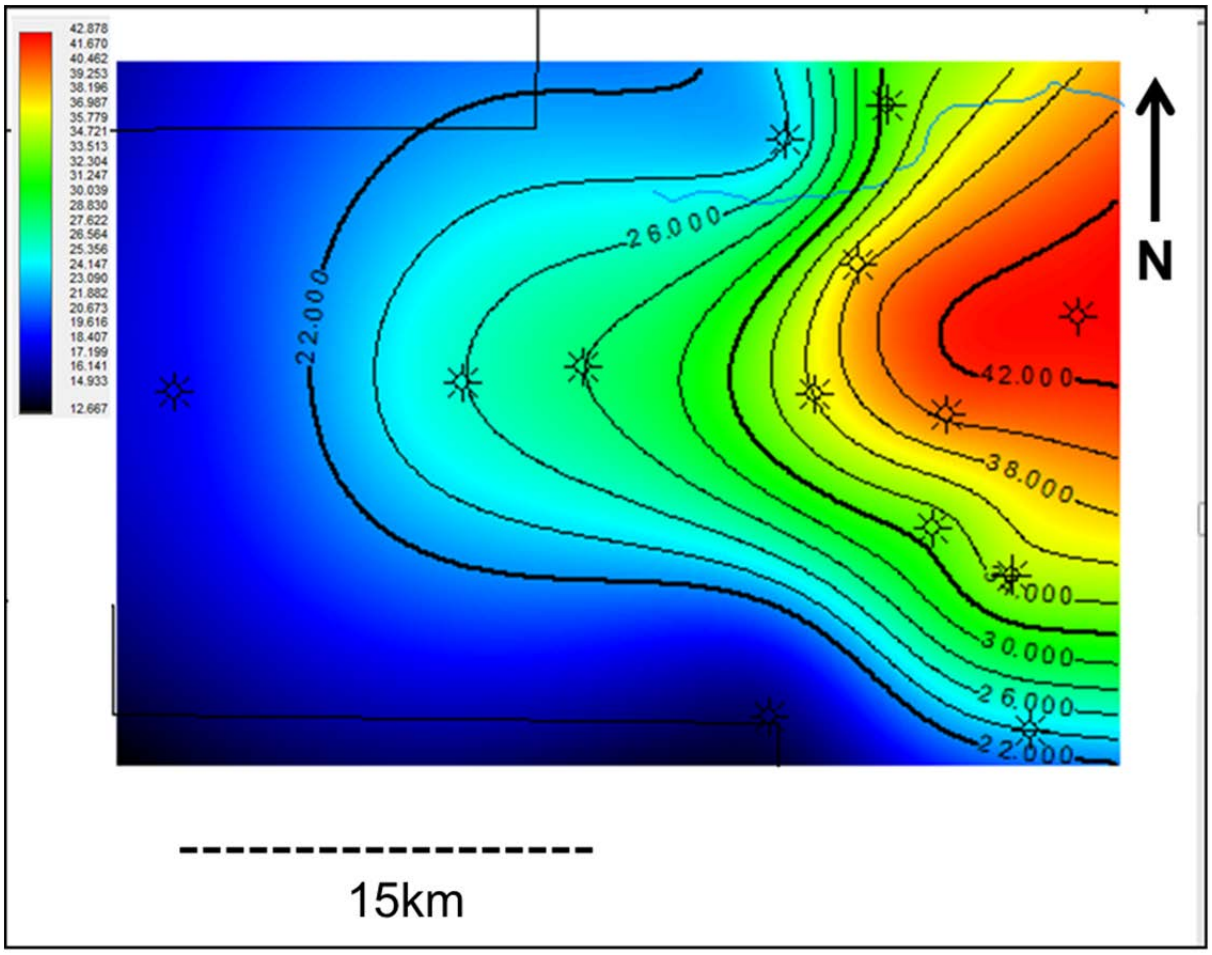

Figure 55: The isopach (thickness) map for the J-Reservoir generated from well formation tops shows the thickest part of the reservoir towards the eastern part of the field and thinning to the west and to the south.

5.1.5 Reservoir Lamination Analysis

The lamination analysis was based on the description of core images from the two reservoirs. The inability of the seismic data to resolve very thin, laminae-scale beds due to inherent low resolution in the available 2D seismic lines meant that the seismic data could not be used for reservoir lamination analysis. As mentioned in sections 4.1 and 4.5, one of the probable causes of low-resistivity pay reservoirs are thin beds that cannot be resolved by the logging tool.

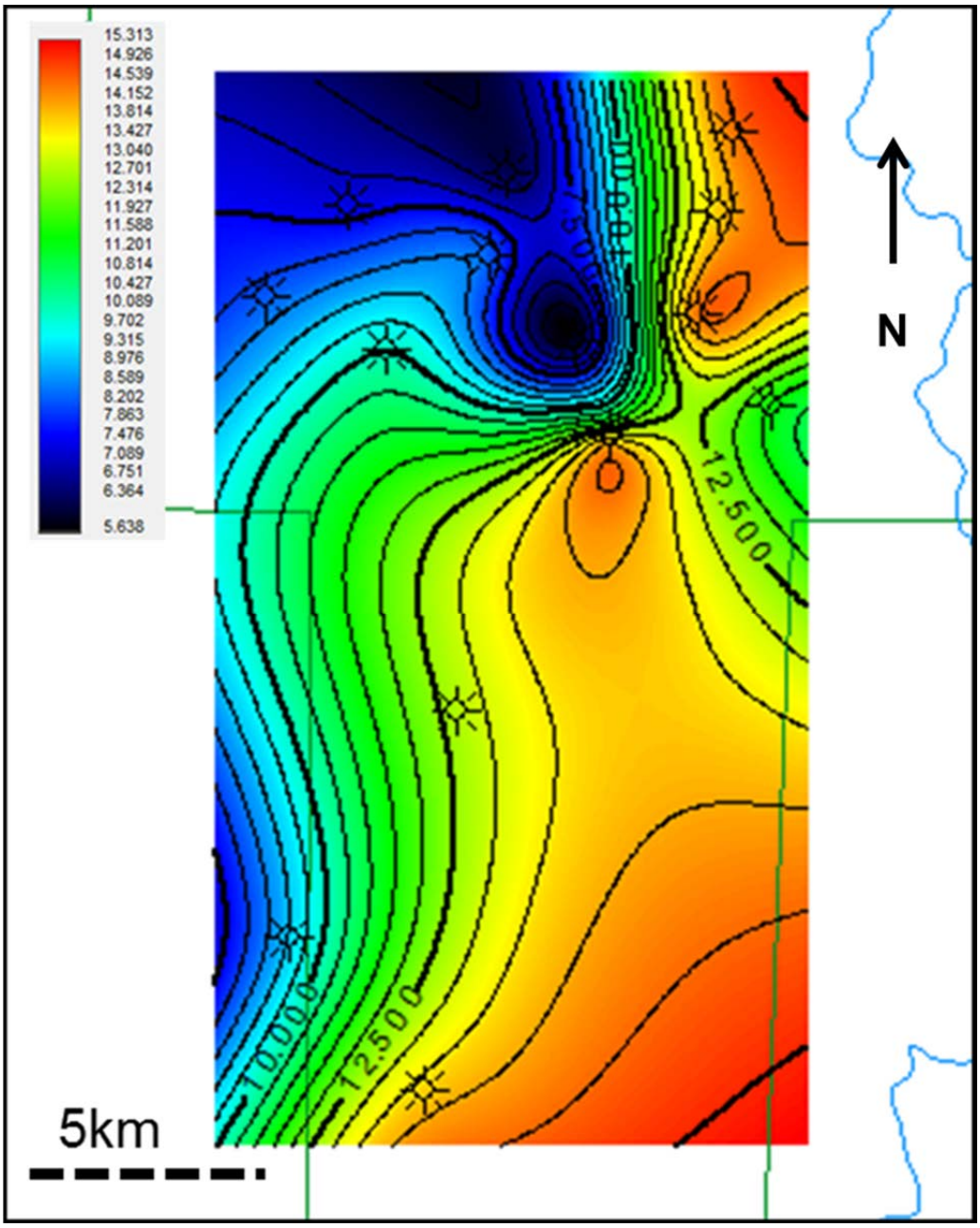

Figure 56: Isopach (thickness) map for the K-Reservoir generated from well formation tops show the increase in reservoir thickness to the south and to the east.

- **Results: Reservoir Lamination Analysis**

The core description of well A15 of the J-Reservoir shown in Figure 11 of section 2.3.3.1 indicates the presence of shale lamination, which cannot be resolved from seismic data. However, the gross reservoir thickness of between 19m and 43m, calculated for the J-Reservoir, can be resolved by most logging tools and thus the lamination shown in the core data becomes insignificant relatively to the gross thickness of the reservoir. The same argument also holds for the K-Reservoir where the reservoir thickness calculated using the

reservoir top and base calculated from the wells is between 9m and 15m, and is resolvable by most if not all the logging tools shown in Figure 24. The true parametric values of the reservoirs were therefore measured by the logging tools.

5.1.6 Modelling the Resistivity Log from the Sonic Log (VRT)

The method used to transform velocity measured from sonic log to resistivity was fully described in section 4.4.

- **Results: Modelling the Resistivity Log from the Sonic Log**

In Figure 57, a comparison between the measured resistivity (R_t_measured) and the velocity-derived resistivity (R_t_modelled) show that the resistivity modelled from the sonic log is lower than the measured resistivity within the reservoir section. This is caused by the fact that the sonic log slows down within the reservoir section due to the presence of less dense hydrocarbons (gas) in the reservoir and therefore lowers the modelled resistivity. Based on these results, the modelled resistivity cannot be used to accurately calculate the water saturation since the resistivity is expected to increase in the hydrocarbon-bearing reservoir.

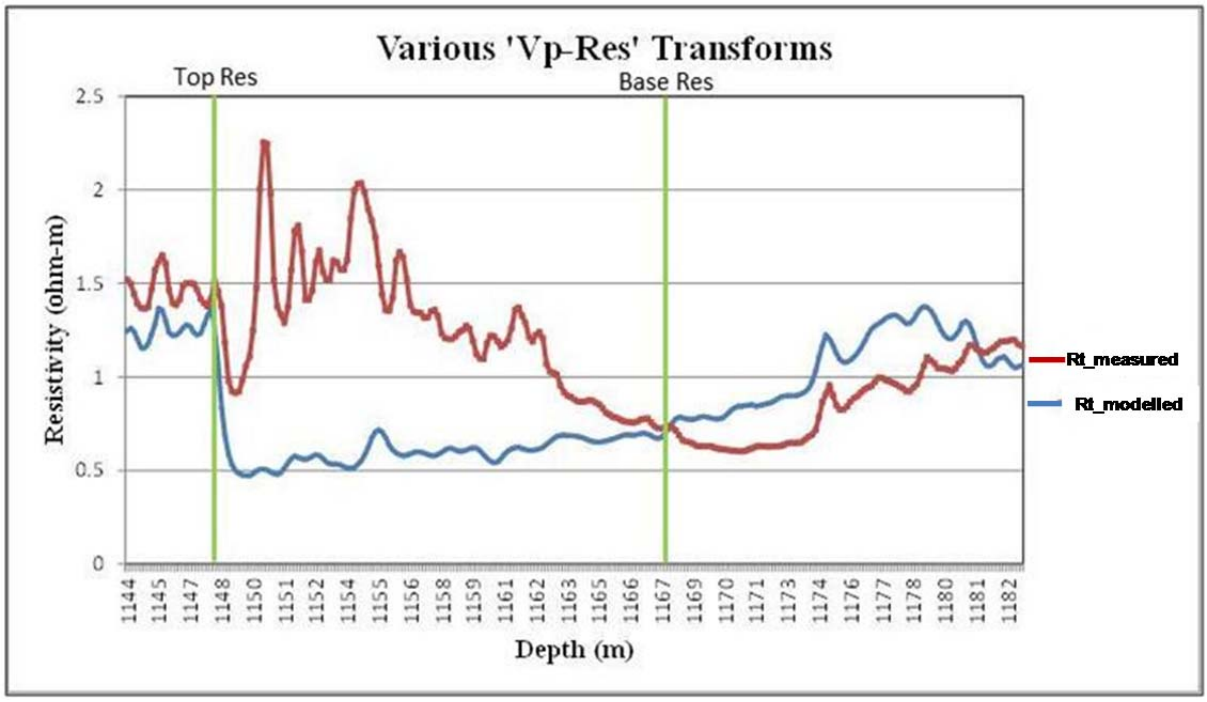

Figure 57: Log-measured resistivity (R_t_measured) compared to the modelled resistivity (R_t_modelled) derived from the velocity-resistivity transform for well A21. The presence of gas in the reservoir lowers the velocity and this result in the lower, modelled resistivity shown in blue.

5.1.7 Nuclear Magnetic Resonance (NMR) Analysis

The Nuclear Magnetic Resonance (NMR) tool is a highly specialised logging tool and therefore, no in-depth analysis of the tool was done for this project. However, the NMR-derived water saturation (S_w) was available for use as a benchmark to evaluate the efficacy of the algorithms used to calculate water saturation (S_w). The NMR-derived water saturation in this study includes free clay- and capillary- bound water.

5.1.8 Reservoir Shale, Clay and Silt Analysis

- **Volume of Shale (V_{sh}) from Neutron-Density Logs**

Shale refers to a broad spectrum of grain sizes 0.001 – 0.063mm and according to Williams et al. (2011); silt has grain size range of 0.004-0.0063mm whereas clay has grain size range of 0.001-0.004. This grain size classes comprise clay and silt. The volume of shale in this study is considered to be the sum of the volume of silt (V_{silt}) and the volume of clay (V_{clay}) as defined by:

$$V_{sh} = V_{clay} + V_{silt} \quad (5.3)$$

The neutron-density log separation was used to estimate the volume of shale (V_{sh}) in the reservoirs. The rationale behind using the density-neutron (D-N) separation is that both clay and silt bind water – although they do so to different degrees. Clay has more bound water than silt because of its smaller grain size. The bound water contains hydrogen in the form of H_2O and therefore the neutron log as discussed in section 4.1.1.3 measures the amount of hydrogen in both silt and clay-bound water. The fine grains of different grain size classes that make up shale, have relatively high surface area and they behave like capillary tubes of different but relatively narrow diameters. This capillary tube effect accounts for the bound water that is higher for clay (smaller diameter capillary tube) in comparison to silt.

The density log on the other hand, responds to the minerals in the formation. The separation between the density- and neutron-porosity logs therefore becomes larger with the increase in shale-bound water in the formation and therefore can be used to estimate the combined volume of silt and clay (V_{sh}) in the reservoir. This assumption will tested using well log data and data from X-Ray Diffraction (XRD) and Laser Grain Size Analysis (LGSA). The volume of shale (V_{sh}) is therefore given by:

$V_{sh} = (DN - DN_{sand})/ (DN_{shale} - DN_{sand})$…….…….....…… (5.4)

Where,

DN: Density-Neutron separation

DN_{sand}: Density-Neutron for the clean sands

DN_{shale}: Density-Neutron for the clean shale

- **Volume of Clay (V_{cl}) Calculated Using Gamma Ray (GR)**

Most clay is rich in potassium minerals that lead to an enhanced gamma ray (GR) response and therefore the GR response is indicative of the volume of clay in the formation. The amount of clay in the reservoir was estimated using the Steiber (1970) equation that states:

$V_{clay} = 0.5* I_{GR}/ (1-1.5*I_{GR})$..... (5.5)

Where,

I_{GR}: Gamma Ray Index which indicates the amount of shale in the formation calculated as:

$I_{GR} = GR-GR_{min}/(GR_{max}-GR_{min})$…….(5.6)

GR_{min}: API reading of 0% volume of shale in the formation.

GR_{max}: API reading of 100% volume of shale in the formation.

The basic workflow for determining the volume of clay (V_{cl}) using gamma ray (GR) logs is shown in Figure 58.

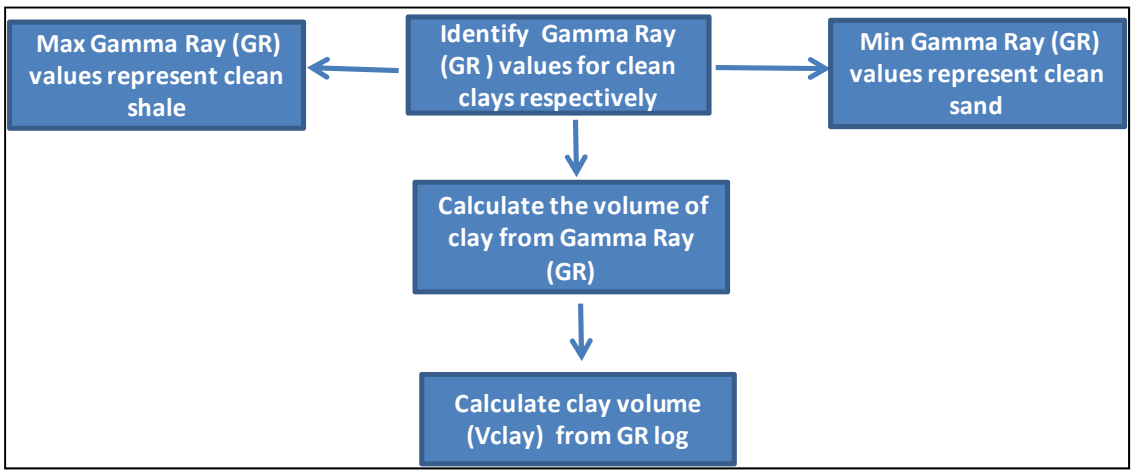

Figure 58: The basic workflow for determining the volume of clay (V_{cl}) using gamma ray (GR) logs.

Once the volume of shale (V_{sh}) and the volume of clay (V_{cl}) have been calculated, the volume of silt (V_{silt}) can be calculated from re-arranging equation 5.3 as:

Volume of silt (V_{silt}) = volume of shale (V_{sh}) – volume of clay (V_{cl})…. (5.7)

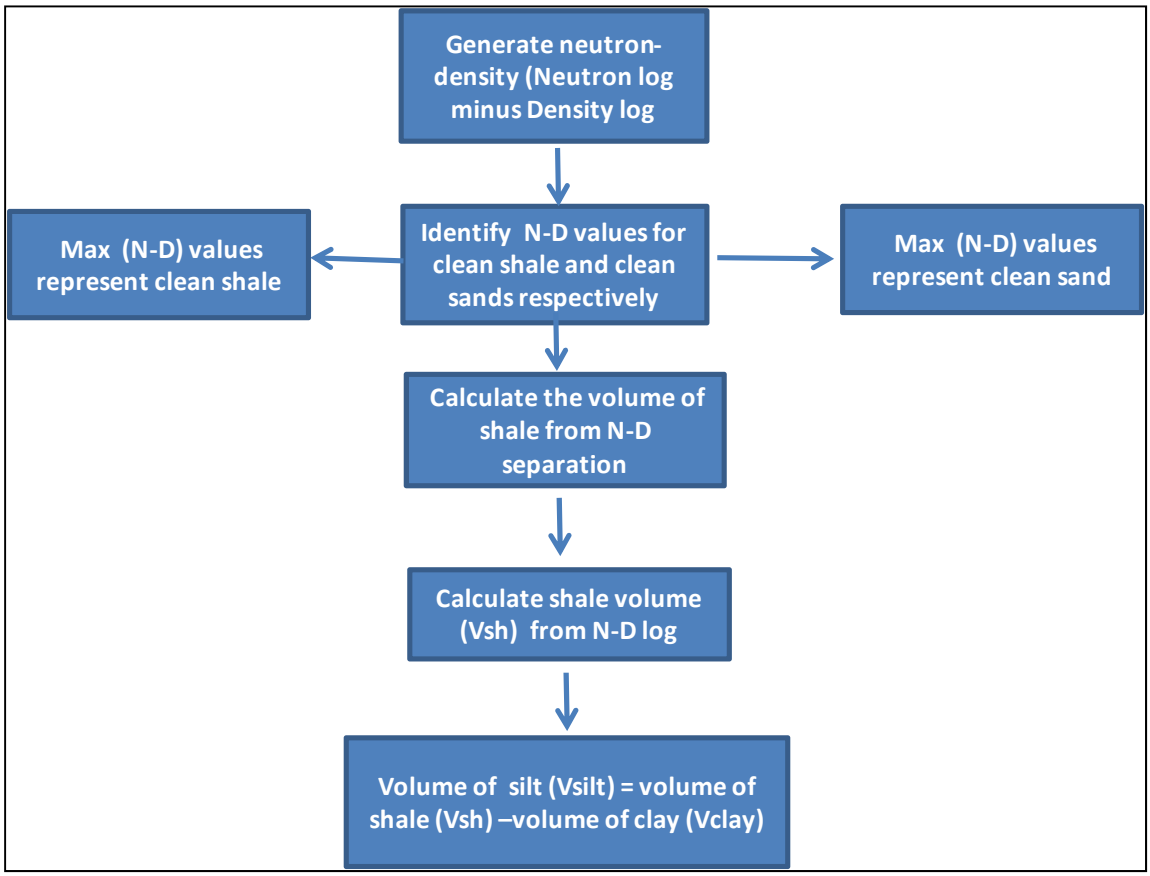

Figure 59: The workflow to calculate the amount of silt in the reservoir. The log calculated volume of silt was compared to core measured volume of silt in the subsequent sections.

- **Results: Volume of Clay for the J-Reservoir**

The volumes of clay and silt of the J-Reservoir calculated using the equations 5.5 and 5.7 are shown in Figures 60 and 61 for wells A15 and A23, respectively. The volume of clay within the reservoir section ranges from approximately 2% at the top of the reservoir to about 9% towards the bottom of the reservoir for well A15 and 9% to 30% for well A23. The volume of clay calculated from the core data using Laser Grain Size Analysis (LGSA) is also plotted in Figure 60 and Figure 61 and shows a high degree of correlation with the volume of clay calculated from gamma ray log (GR). This validates the use of gamma ray log and Steiber's equation to accurately calculate the volume of clay in the J-Reservoir.

- **Results: Volume of Shale and Silt for the J-Reservoir**

The calculated volume of shale and silt seems to give inaccurate results in both A15 and A23 wells as shown in Figure 60 and Figure 61. The volume of clay and silt seem to be higher at the top of the reservoir and decreases towards the bottom. This trend contradicts the coarsening-upwards sequence nature of the J-Reservoir as described in section 2.3.3 and 4.6 and also contradicts the measured volume of both silt and shale from well A15 core data. Table 5 shows the combined volume to silt and clay measured from core data with a range of 16% at the top of the reservoir to 39% towards the bottom of the reservoir. It is therefore concluded that the neutron- density log separation cannot be used to determine the volume of shale i.e. a combination of silt and clay in the J-Reservoir. The core data in well A21 only covered the very top of the reservoir and therefore could not be used to validate the calculated volume of silt and clay in that well.

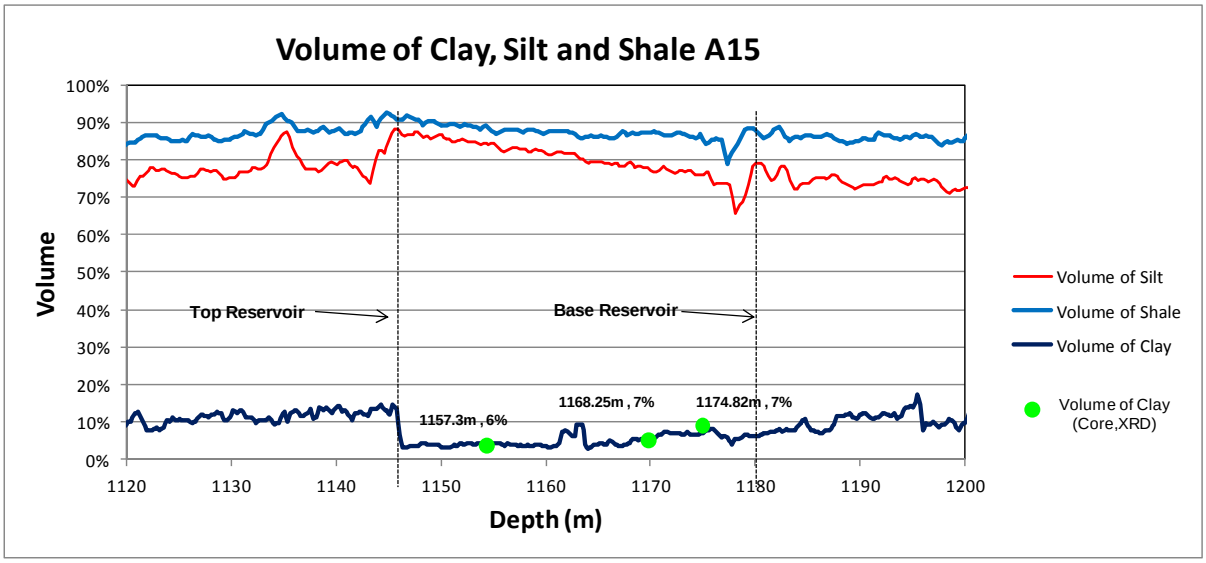

Figure 60: The volume of silt, shale and clay for well A15. The log calculated volume of clay increases towards the lower part of the reservoir, which is consistent with the volume of clay measured from XRD and LGSA while the log calculated volume of silt and shale is inconsistent with the XRD and LGSA results.

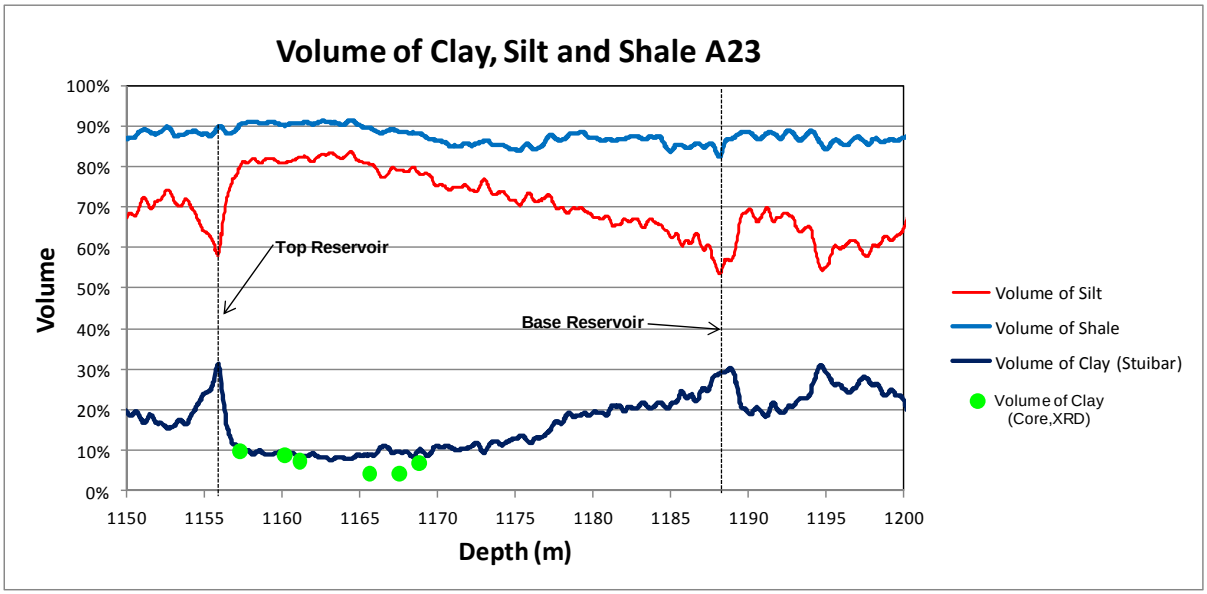

Figure 61: The volume of silt, shale and clay in well A23. The log calculated volume of clay increases towards the lower part of the reservoir, which is consistent with the volume of clay measured from XRD and LGSA while the log calculated volume of silt and shale is inconsistent with the XRD and LGSA results.

- **Results: Volumes of Shale, Clay and Silt for the K-Reservoir**

The volumes of clay and silt of the K-Reservoir are shown in Figures 62 and 63 for wells B12 and B18, respectively. In well B12, the log calculated volume of clay within the reservoir section ranges from approximately 5% to about 16%, towards the bottom of the reservoir for well B12. The clay volume calculated from XRD Analysis was also plotted in Figure 62 and they are in agreement with the log-measured volume of clay. Figure 62 also shows some volume of clay outside the reservoir section in the deeper KB and KC Reservoirs.

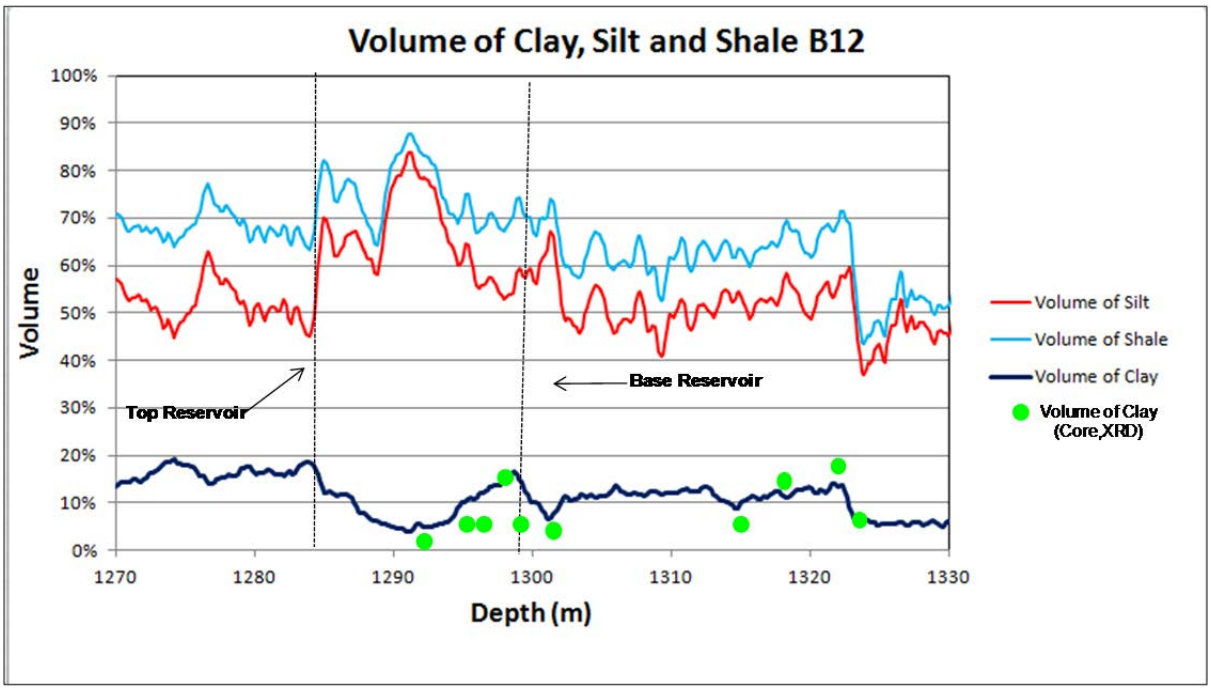

Figure 62: The volume of silt, shale and clay for well B12. The log calculated volume of clay increases towards the lower part of the reservoir, which is consistent with the volume of clay measured from XRD and LGSA while the log calculated volume of silt and shale is inconsistent with the XRD and LGSA results.

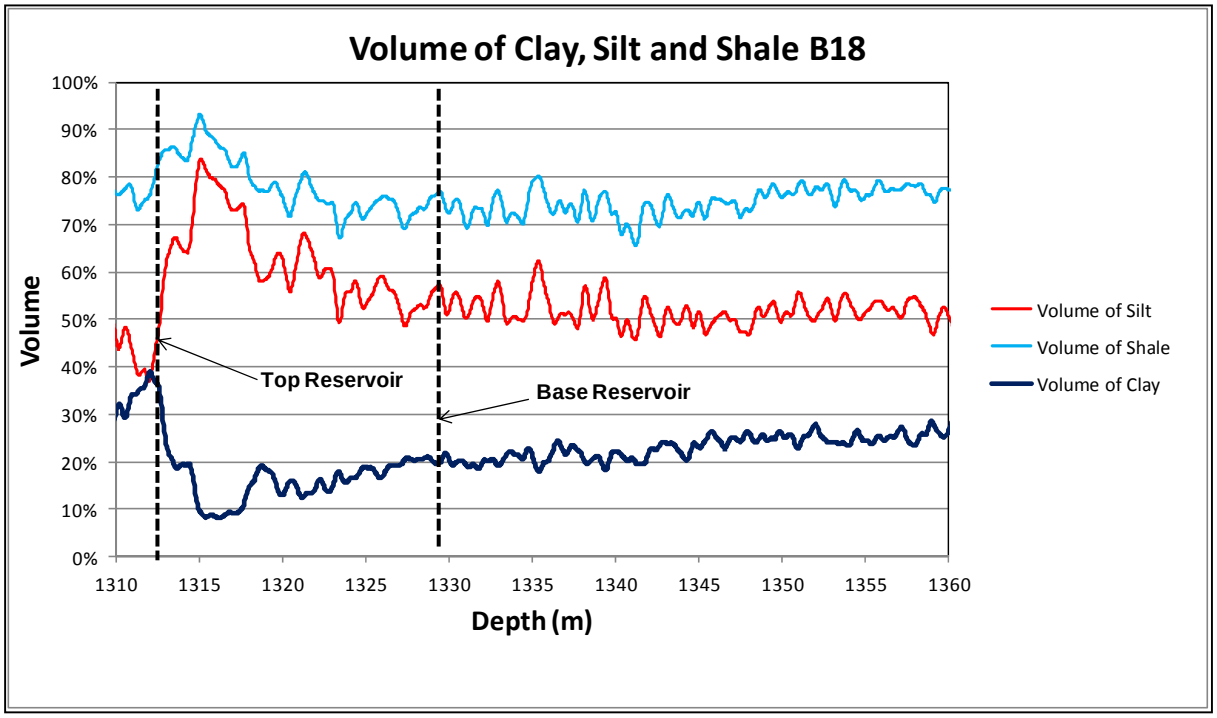

Figure 63: The volume of silt, shale and clay for well B18. The log calculated volume of clay increases towards the lower part of the reservoir. No core data were available in B18 to compare the calculated and the measured volume of clay.

As in the J-Reservoir, the silt and shale trend also contradicts the measured volume of both silt and shale measured from well B12 core data. No core data were available in well B18 to compare the calculated and the measured volume of clay.

5.2 CORE ANALYSIS

5.2.1 Petrology Studies: Thin Sections, LGSA and XRD Analysis

Petrological analyses were based on data from well A15 and B12 for the J-Reservoir and the K-Reservoir, respectively and comprised thin sections, X-Ray Diffraction (XRD) and Laser Grain Size Analysis (LGSA) that were conducted by OMNI Laboratories in 2005 to describe the textural fabric of the reservoir, grain size, grain distribution, mineralogy, and the relative abundance of minerals and clays within the J- and K-Reservoirs.

5.2.1.1 Petrology Studies for the J-Reservoir (Well A15)

Figure 64 is a micrograph of a plane polarised thin section prepared from a sample from well A15, taken towards the top of the reservoir, at depth of 1157.30m. The grains are moderate to well sorted, but angular to very angular. The rock was classified as immature lithic arkoses cemented by calcite (2%) and analcime (3%). The analcime cements, which are relatively low in abundance, generally occur in larger patches that encompass several grains (H3). The calcite cement, which has a reddish stain (alizarin) and occurs in very small patches within isolated pores (E2, B7, C7.5) is shown in Figure 64. The very low rounding degree indicates that the grains have not been reworked extensively, and possibly are from a first depositional cycle, just downstream of a deltaic system**.** Yellowish grains are potassium feldspar stained with sodium cobaltinitrite, a yellow crystalline salt often used as a selective staining of K-feldspar and plagioclase in thin sections (Bailey et al., 1960). The enlarged pores are probably the result of leaching of framework grains (F-G6.5, G-H7.7, H8, and F9.5). The grain density and average porosity are 2.642 gm/cc and 28.7% respectively.

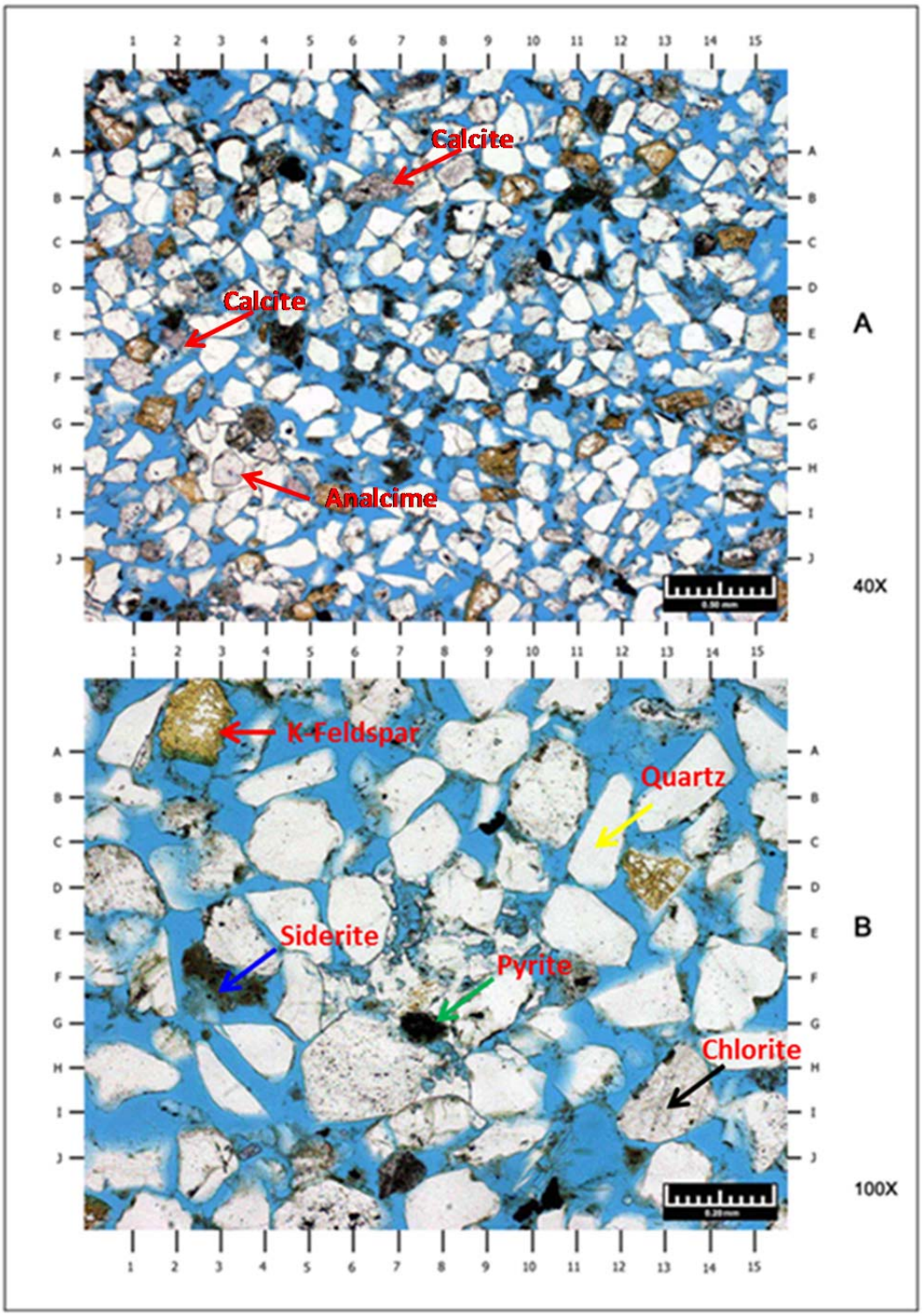

Figure 64: A plane polarised thin section from well A15 sample taken towards the top of the reservoir at depth of 1157.30m, magnified to 40X and 100X in (A) and (B), respectively. The scale bars are 0.5mm in A and 0.1 mm in B.

- **Mineral Composition: J-Reservoir**

The framework grain type consists mainly of mono-crystalline quartz with plagioclase and potassium feldspar as the second most common minerals. Modal analysis indicate that the quartz content ranges from 59% - 78%. K-feldspar content ranges from 14%-19% in this well A15. The lithic fragments content range from 6% to 10%, metamorphic rock fragments are the most common (1-5%) followed by the plutonic rock fragments (1-3%). Volcanic and sedimentary rock fragments are also common from trace level to 3% (OMNI, 2005).

- **Clay and Silt Content: J-Reservoir**

The amount of clay- and capillary-bound water is controlled by the reservoir's mineral composition, texture and grain size. There is a relationship between the decreasing of the grain size and the amount of clay and capillary bound water (Worthington, 2000). The smectites, commonly known as swelling clays, have been detected in most of the cores from Mozambique Basin. These clays commonly occur as mixed layers of smectites and illites and are known to expand to 95% of the original size when they come into contact with water. Due to the high Cation Exchange Capacity (CEC) of smectites, discussed in 4.5.6, more ions are dissolved from the clay when it comes into contact with water, thereby increasing the conductivity of the water. The amount of bound water is further increased by the presence of carbonate cement in this reservoir. The combined volume of silt and clay was calculated from Laser Grain Size Analysis (LGSA) and the separate clay volume was calculated from X-Ray Diffraction (XRD). The difference between the combined clay and silt volume (LGSA) and the clay volume (XRD) is shown as silt, in Figure 65 below, and was calculated from equation 5.7. The results show that both the silt and shale increase sharply with depth but clay shows a moderate increase from 5-10% with depth.

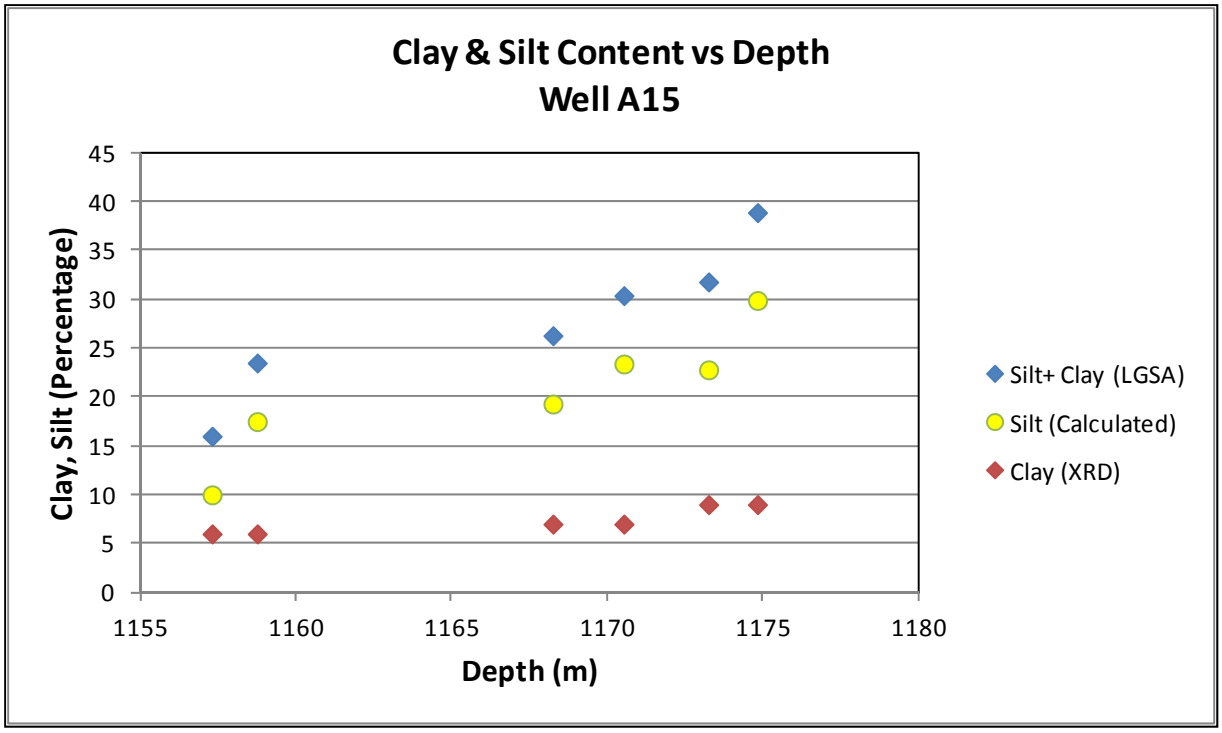

Figure 65: Clay and silt volumes in well A15 show an increase with depth. The volume of clay shows a moderate increase with depth whereas the volume of silt shows a sharp increase with depth.

Well A15 Petrological Analysis					
Sample Depth (m)	LGSA Silt+Clay %	XRD Clay (% weight)	Calculated Silt	Porosity at NCS 1050 psi	Permeability (mD)
1157.3	16	6	10	31.9	400
1158.75	23.5	6	17.5	31.2	447
1168.25	26.3	7	19.3	30.1	144
1170.53	30.4	7	23.4	28.6	58.8
1173.25	31.8	9	22.8	28.7	35
1174.82	38.9	9	29.9	26.1	11.1

Table 5: Petrology results from the core analysis in well A15 plotted in Figure 64.

- **Cement and Authigenic Clay Minerals**

The total cement volumes range from 6% to 9% by weight including authigenic clays, which are diagenetic clays, generated where they are found rather than been transported from their source of origin and deposited (detrital clays). The low weight percentage volume of total cement is indicative of reservoir sandstone that is not well lithified. The most common cements are quartz overgrowth which occurs in weight percentage of between 1% and 8%

(OMNI report, 2005) and the calcite cement which is present in isolated patches that appear to been partially dissolved. The increase in these two cements in the reservoir reduces the reservoirs porosity and permeability and thus the reservoir quality.

- **Clay Mineralogy and Content: J-Reservoir**

X-Ray Diffraction (XRD) analysis on well A15 core samples indicates that the distribution of clay mineral suite is consistent for all depths (Table 6).

Sample	CLAYS				CARBONATES			OTHER MINERALS				
Depth (m)	Chlorite	Kaolinite	Illite	Mx I/S*	Calcite	Fe-Dol	Siderite	Quartz	K-spar	Plag.	Pyrite	Clays
1157.30	3	Tr	2	1	1	Tr	Tr	77	4	12	Tr	6
1158.75	3	Tr	2	1	2	Tr	0	78	4	10	Tr	6
1168.25	3	Tr	2	2	1	1	0	72	6	13	Tr	7
1170.53	3	Tr	2	2	3	Tr	Tr	66	8	16	Tr	7
1173.25	3	Tr	3	3	3	Tr	Tr	66	7	14	1	9
1174.82	3	Tr	3	3	5	Tr	0	59	9	17	1	9
1176.85	2	Tr	3	Tr	8	Tr	Tr	66	5	15	1	5
AVERAGE	3	Tr	2	2	3	Tr	Tr	70	6	14	Tr	7

Table 6: Clay and mineral composition of the J-Reservoirs (weight percentage) as determined from LGSA and XRD from well A15.

The clay minerals consist of chlorite (2% to 3%), illite (2% to 3%), mixed-layer illite/smectite (trace to 3%) and kaolinite at trace level. The smectites occur as pure smectites and as a stratified mix layer of smectites and illites. Carbonate minerals such as calcite and siderite were found in average concentrations of 1-8 weight % and 0% to trace level, respectively.

- **Conductive Minerals: K-Reservoir**

One of the conductive minerals, pyrite, is found in small quantities of between trace level and 1 weight % on average, between the two reservoirs. The pyrite content is dependent on the oxygenation during diagenesis, the content of organic matter in the sediments and on water circulation. High clay content can inhibit the water circulation. Good circulation of oxygenated water in the reservoir will reduce the volume of pyrite through oxygenation. The presence of glauconite, which was initially thought to be a possible contributor to the resistivity of the reservoirs, was not revealed by X-Ray Diffraction (XRD) analysis from the core data and also not detected in thin sections in any significant quantity.

5.2.1.2 Petrology Studies for the K-Reservoir (Well B12)

The sandstones within the cored sequence of well B12 vary from friable to well-cemented. Figure 66 is a plane polarized thin section of a sample taken towards the top of the reservoir at depth 1291m, The scale bars are 0.5mm in A and 0.1 mm in B. The poorly to moderate and angular grains in this sample consist of quartz, feldspars, lithic fragments, rare detrital mica and constitute either immature arkoses or lithic arkoses. Figure 66a shows a sparsely distributed analcime (C-D5, A125) which occurs in moderate volumes of 0-1% and calcite cements (E-F3.5, D6.5) that replaces a grain and fills an inter-granular pore in Figure 66b (H14). Quartz overgrowth cement is also present and well developed at E7 in Figure 66b, where it also is partially dissolved showing resorption embayments. The large mineral, just above the scale bar in B, is a later, post quartz-cement poikilotopic calcite cement crystallite. The dark to black elongated grain at the upper left top of B is an altered biotitic mica (clay mineral) grain.

Other cements include zeolite cement which appears to be partially dissolved and is shown as “swiss-cheese” like appearance in Figure 68b. Yellow grains are potassium feldspar, stained with sodium cobaltinitrite. The grains are sub-angular angular, which indicates that they have not been reworked extensively, and possibly indicate a first depositional cycle in a shallow-marine depositional system. Pyrite is present as particle replacement in Figure 68b, where it replaces mica at B3. The grain density and average porosity are 2.64 gm/cc and 26.7%, respectively. The majority of the porosity is inter-granular with some fraction of that due to the leaching of the inter-granular analcime cements (OMNI, 2005).

- **Mineral Composition: K-Reservoir**

The dominant grain constituent of the K-Reservoir is quartz (12-79%), but there is a wide range of other constituents such as lithic fragments which consists of volcanic rock fragments (trace to 9%) and both, plutonic and metamorphic rock fragments (trace to 3%), based on modal analysis. There is an increase in the lithic fragments from the upper K-Reservoir to the deeper KC-Reservoir (OMNI, 2005).

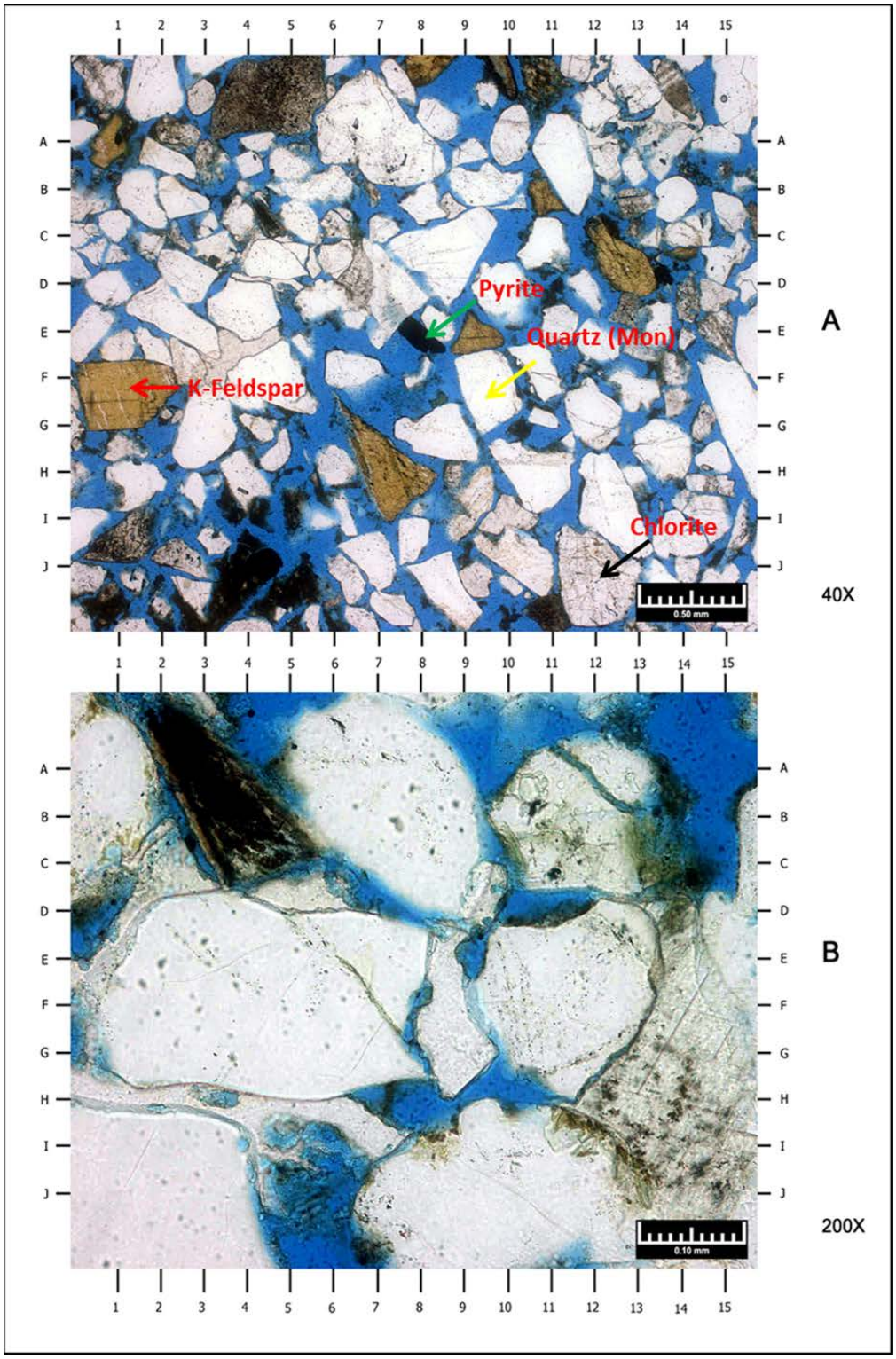

Figure 66: A plane polarised thin section from well B12 sample taken towards the top of the reservoir at depth of 1291m, scale bars are 0.5 mm in A and 0.1 mm in B. In B, quartz cement overgrowth on angular quartz grains and its later partial dissolution at the resorption embayment and holes are visible.

- **Clay and Silt Content: K-Reservoir**

In well B12, the silt volume was measured using Laser Grain Size Analysis (LGSA) and the clay volume was measured using X-Ray Diffraction as shown in Figure 67 and Table 7 below. Both clay and silt volumes show an increase with depth, with clay volume increase from 2-18% and silt volume from 9 to 52%. The amount of clay in the K-Reservoir compares very well with the clay volume calculated using gamma ray log shown in Figure 62.

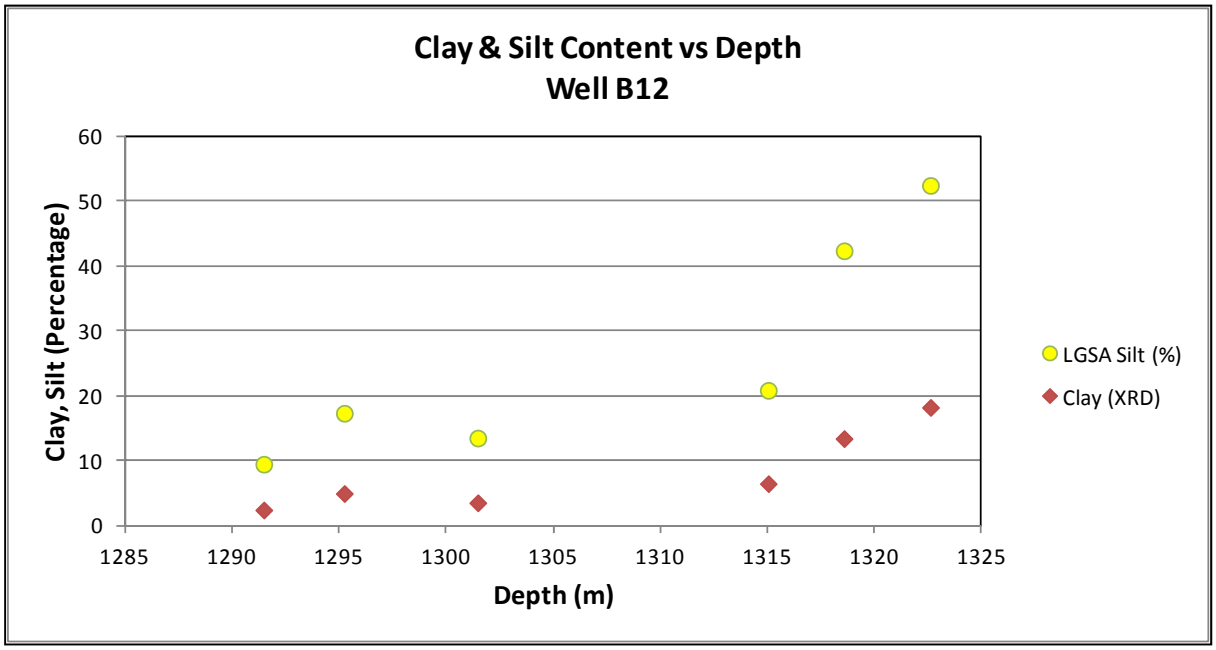

Figure 67: Clay and silt volumes in well B12 show an increase of the volume of silt and clay with depth. The clay content shows a moderate increase whereas the silt volume shows a sharp increase with depth.

Well B12 Petrological Analysis				
Sample Depth (m)	LGSA Silt (%)	XRD Clay %	Porosity at NCS 1200 psi	Permeability (mD)
1291.48	9.4563	2.387097	0.267	1520
1295.24	17.317204	4.930567	1140	0.317
1301.47	13.485391	3.499456	4.56	0.267
1315.03	20.855189	6.454746	31.5	0.265
1318.57	42.381145	13.4109	0.162	0.246
1322.6	52.462898	18.219661	0.032	0.098

Table 7 : Petrology results from the core analysis in well B12 show an increase in silt and clay volume with depth. The increase in silt and clay with depth also causes a decrease in porosity and permeability, as shown in the table.

- **Cement and authigenic clay minerals : K-Reservoir**

The sandstones within the cored sequence of well B12 vary from friable to well consolidated (cemented) with total cement volumes, including authigenic clays, ranging from 3% to 18% (Table 8). Modal thin section analysis of these samples indicates that within reservoir unit, authigenic clay comprises about 2% of the sample volume versus detrital clay, which comprises about 3%. Sparsely distributed calcite, due to partial dissolution of the mineral, and pyrite are the most common cements present. Pyrite is present as particle replacement and as cement from trace level to 2% (weight). Another form of cement is quartz overgrowth which exists in variable amounts from trace to 2% in all the samples analysed (OMNI, 2005).

- **Clay Mineralogy and Content : K-Reservoir**

The clay minerals present with the K-Reservoir of well B12 are chlorite (trace to 4%), kaolinite (trace to 1%), illite (trace to 5%) and mixed-layer illite/smectite (1-15%) for a total average content of approximately 9% by weight. Carbonate minerals such calcite (1-68%) and siderite (trace-0%) are also present (OMNI, 2005). Similar mineral compositions were observed in core samples from other wells.

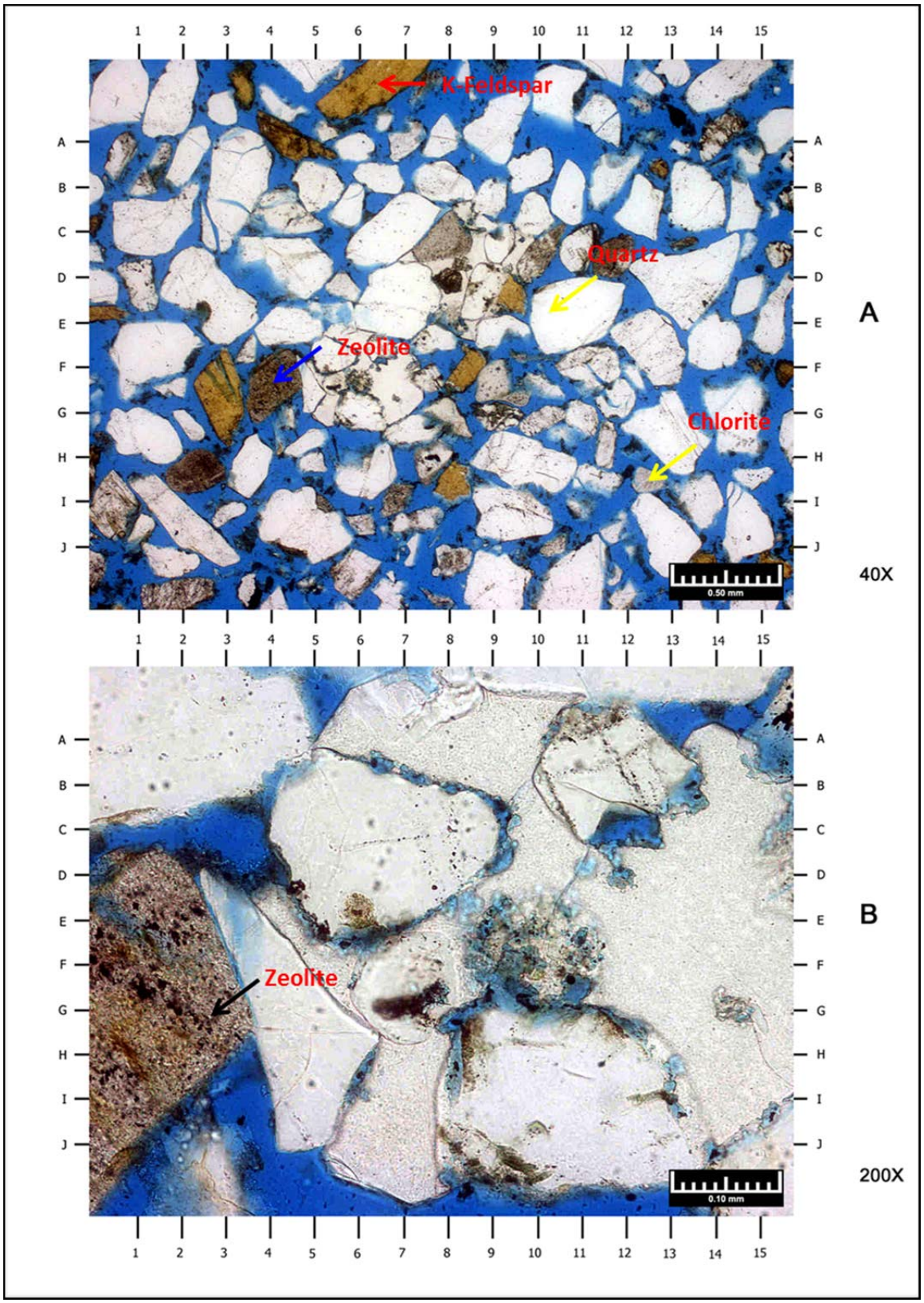

Figure 68: A plane polarised thin section from well B12 core sample taken towards the top of the K-Reservoir at depth 1290m, scale bar in A is 0.5 mm and in B 0.1 mm. In B angular grains of quartz and dissolution of quartz cement and of zeolite are visible from holes in the minerals and from irregular embayment in the cement and grain boundaries.

WELL B12 : MINERAL COMPOSTION														
Sample	CLAYS				CARBONATES			OTHER MINERALS				TOTALS		
Depth (m)	Chlorite	Kaolinite	Illite	Mx I/S	Calcite[1]	Fe-Dol	Siderite	Quartz	K-spar	Plag.	Pyrite	Clays	Carb.	Other
1290.24	Tr	Tr	2	1	1	Tr	Tr	79	5	12	Tr	3	1	96
1291.48	Tr	Tr	2	1	6	Tr	0	72	5	14	Tr	3	6	91
1291.90	1	Tr	2	1	2	Tr	Tr	76	5	13	Tr	4	2	94
1293.03	1	Tr	1	2	3	1	1	71	8	12	Tr	4	5	91
1295.24	1	Tr	2	2	5	1	Tr	62	7	20	Tr	5	6	89
1297.91	1	1	2	3	3	1	Tr	55	5	28	1	7	4	89
1299.24	4	1	5	7	7	1	Tr	39	9	26	1	17	8	75
1299.90	1	Tr	2	1	68	Tr	Tr	12	6	8	2	4	68	28
1300.83	1	Tr	1	10	2	1	Tr	46	10	29	Tr	12	3	85
1301.10	1	Tr	1	9	10	Tr	Tr	43	10	25	1	11	10	79
1301.47	Tr	Tr	Tr	3	2	1	Tr	67	9	18	Tr	3	3	94
1302.24	1	Tr	Tr	8	1	Tr	0	54	8	27	Tr	10	1	89
1303.50	1	Tr	1	6	4	Tr	Tr	47	15	25	1	8	4	88
1315.03	1	Tr	2	8	10	1	Tr	47	9	21	1	11	11	78
1316.46	1	Tr	2	10	5	Tr	0	38	12	30	1	14	5	81
1318.57	1	Tr	2	15	3	1	Tr	43	8	26	1	18	4	78
1319.20	3	Tr	4	11	4	Tr	0	41	14	22	1	18	4	78
1322.60	1	Tr	2	13	43	0	0	19	9	11	2	16	43	41
1323.30	1	Tr	2	8	1	Tr	Tr	58	7	22	1	11	1	88
AVERAGE	1	Tr	2	6	9	Tr	Tr	51	9	21	1	9	9	82

Table 8: Clay and mineral composition of the K-Reservoir (weight percentage) as determined from LGSA and XRD on the B12 well core sample.

5.2.1.3 Clay Distribution Using the Thomas-Stieber Model

In the preceding section, the volume of clay calculated using the gamma ray log was compared to the clay volume calculated using X-Ray Diffraction (XRD). Quantifying the volume of clay is a very important step in estimating the volume of bound, irreducible water in the reservoir and its contribution to the low resistivity phenomena of the J- and K-Reservoirs. The extent to which the presence of clay in the reservoir affects the reservoir quality i.e. porosity and permeability, is dependent on its distribution within the reservoir. The clay distribution is controlled by the conditions that prevail during deposition as wells the post-depositional diagenetic conditions. Therefore, understanding the clay distribution is equally important as quantifying its volume in the reservoir. The volume of shale (V_{sh}) and the volume of clay (V_{cl}) will be used inter-changeably in this section and should be assumed to mean the same thing since the most dominant form of shale in Mozambique Basin is clay.

The clay distribution analysis was based on the Thomas-Stieber (1975) clay distribution model, which looks at the relationship between total porosity and the volume of shale (V_{sh}) to classify the distribution as laminated, dispersed, structural or any combination of these three configurations. Each of the above clay configurations represents a certain response on a gamma ray log (Thomas and Stieber, 1975). Figure 69 shows the clay distribution in well A21. Clay is deposited or settles as lamina (shale layers in between sand layers) if it is distributed during the reservoir deposition, i.e., syn-depositional (Boyd et al., 1995). Dispersed clays are normally deposited caused by diagenetic process such as alteration of feldspar as well as burrowing and they are distributed randomly within the formation. Structural clays occur as grains in the formation matrix and do not alter the reservoir properties (Boyd et al., 1995). Figures 69 and 70 are based on the Thomas-Stieber model and show the clay volume that is dominated by laminated clay distribution with some dispersed clay within the J-Reservoir in wells A21 and A15. The small amount of dispersed clay causes a decrease in porosity with the increase in the volume of clay observed in Figure 71. Laminated clays have very little to no secondary effect on the porosity and permeability of the reservoir.

- **Results: Clay Distribution for the J-Reservoir**

Laminated clay distribution is common in sediments that are not very matured compositionally and deposited under normal sedimentary conditions, probably under slightly turbulent or laminar flow. During diagenesis, the clay is compressed with other grains and usually moves towards pores and fills the pore space and pore throats. It can also grow from other minerals during diagenetic and post-diagenetic alteration, even at low temperatures.

- **Results: Clay Distribution for the K-Reservoir**

The K-Reservoir's clay content for well B12 was calculated using logs and calibrated to core data (section 5.1.8). However, clay distribution in K-Reservoir is laminated (Fig. 71) with a small fraction and not dispersed and therefore, should have little impact on the reservoir quality, i.e. the porosity and permeability.

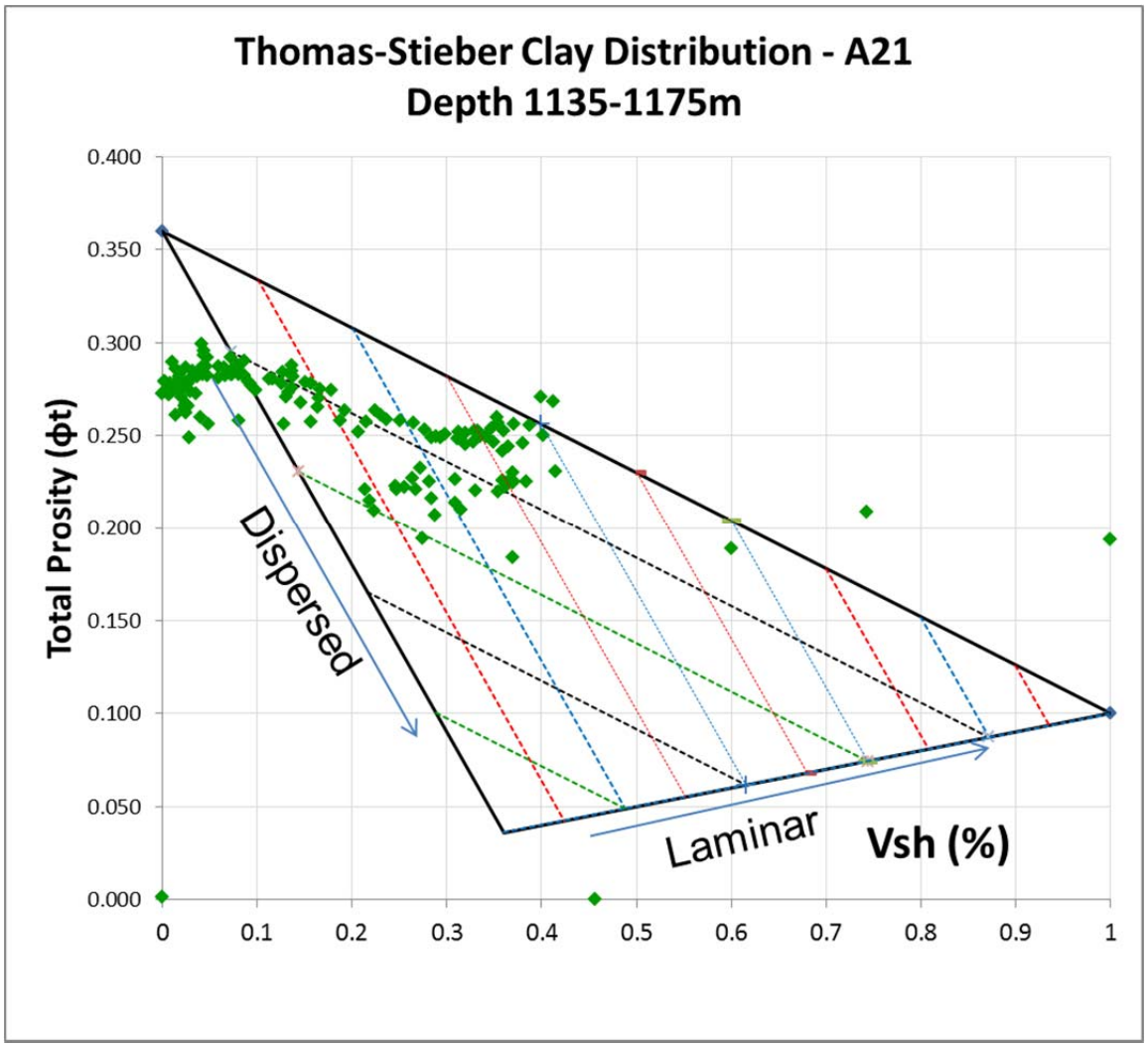

Figure 69: Thomas-Stieber Plot: Well A21 from depth 1135-1175m is dominated by laminated clay based on the observed clay distribution. There is small fraction of dispersed clay as indicated by the points along the dispersed clay axis.

5.2.1.4 Effect of Clay on the Reservoir Pore System

In the previous section, the effect of clay distribution on the reservoirs pore system was discussed and it was demonstrated that the clay distribution in both the J- and K-Reservoirs are dominated by laminated shales with a small fraction of clay dispersed within the reservoir sections. In the following sections, the effect of clay on pore system (porosity and permeability) of the two reservoirs will be further investigated.

- **Results: Effect of Clay on the Pore System of the J-Reservoir**

In Figure 71, a plot of porosity versus clay content shows a log- relationship between porosity and clay content for well A15. An increase in clay content result in a decrease in

porosity and according to the Thomas-Stieber model, the small fraction of dispersed clay should be responsible for the reduction in porosity since most of the clay in the J-Reservoir is laminated.

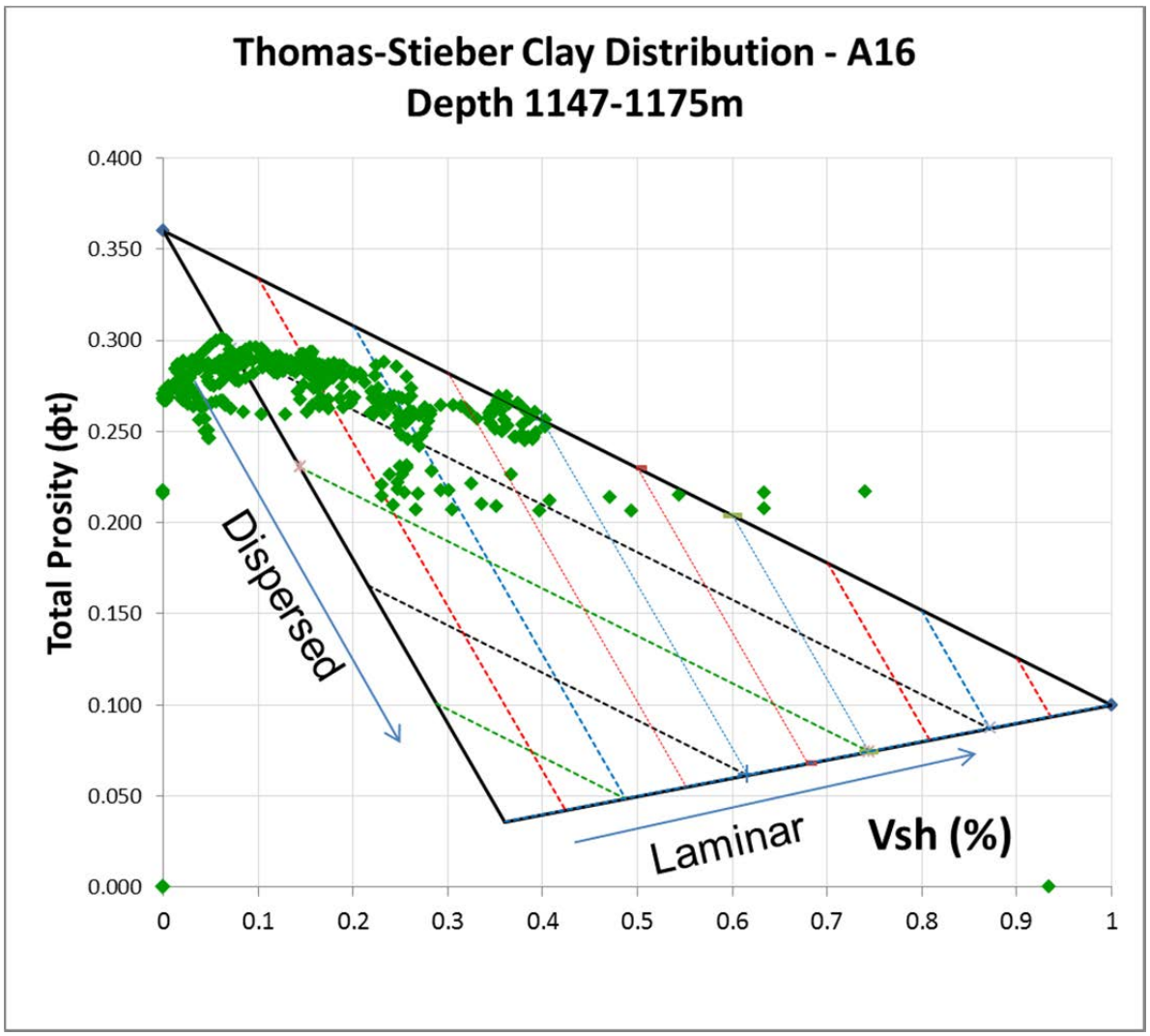

Figure 70: The Thomas-Stieber Plot for well A16 from depth 1147-1175m shows laminated shale distribution similar to the shale distribution in well A21 with a small percentage of dispersed clay.

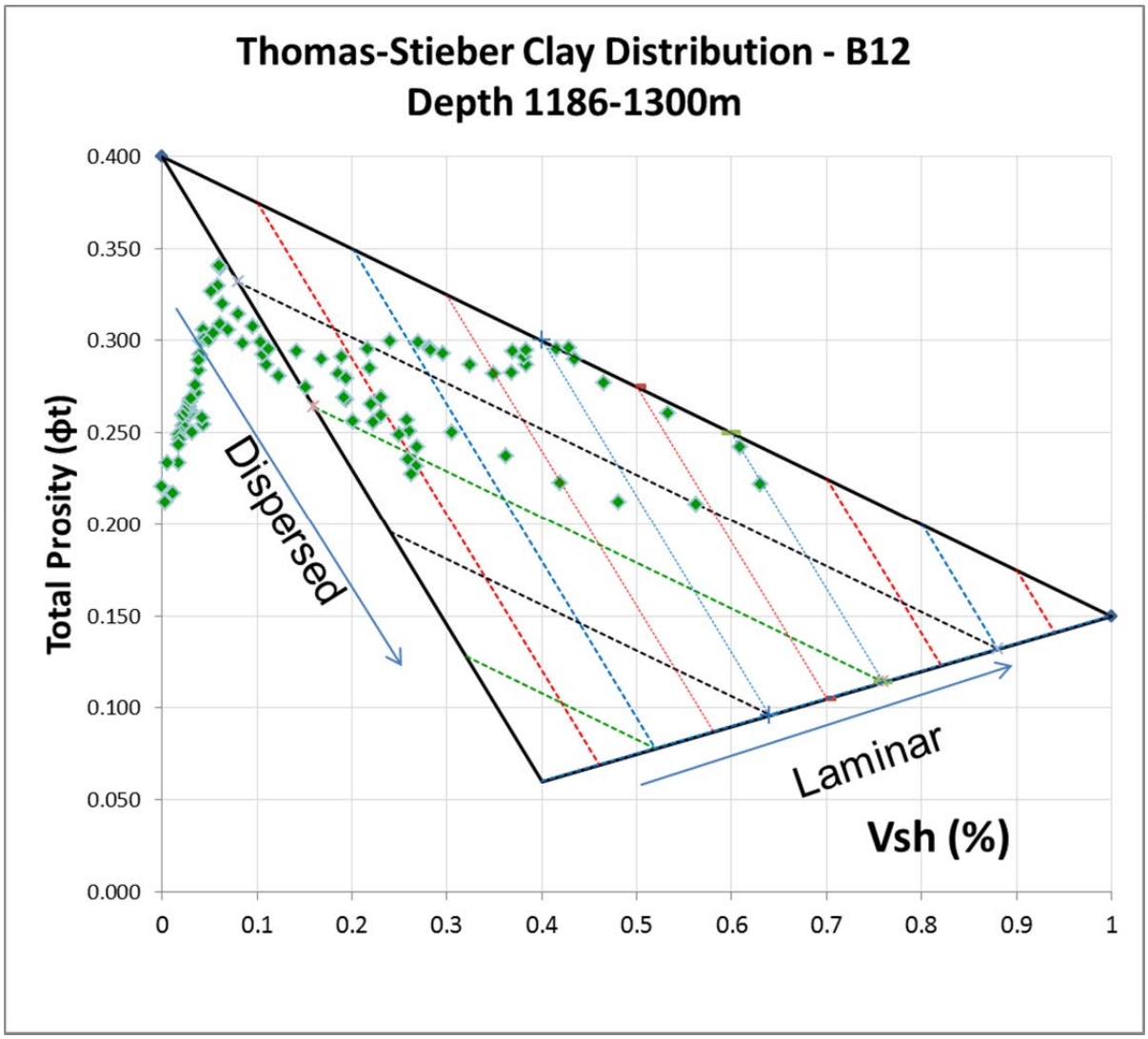

Figure 71: The Thomas-Stieber Plot for well B12 from depth 1186-1300m shows laminated shale distribution similar to the shale distribution in well A15 and A16 with a small percentage of dispersed clay.

- **Results: Effect of Clay on Permeability**

Permeability was calculated using laboratory hydrocarbon injection at suitable rates at reservoir net confining stress until an equilibrium differential pressure was observed. Effective permeability to hydrocarbons at initial water saturation was determined at 2 injection rates. The sample was then subjected to Dean Stark toluene extraction and dried to a constant weight in a vacuum oven at 140°F (OMNI, 2005). Figure 72 shows a relationship between permeability and the clay volume for well A15 of the J-Reservoir. The plot shows a decrease in permeability due to an increase in, mainly, dispersed clay content.

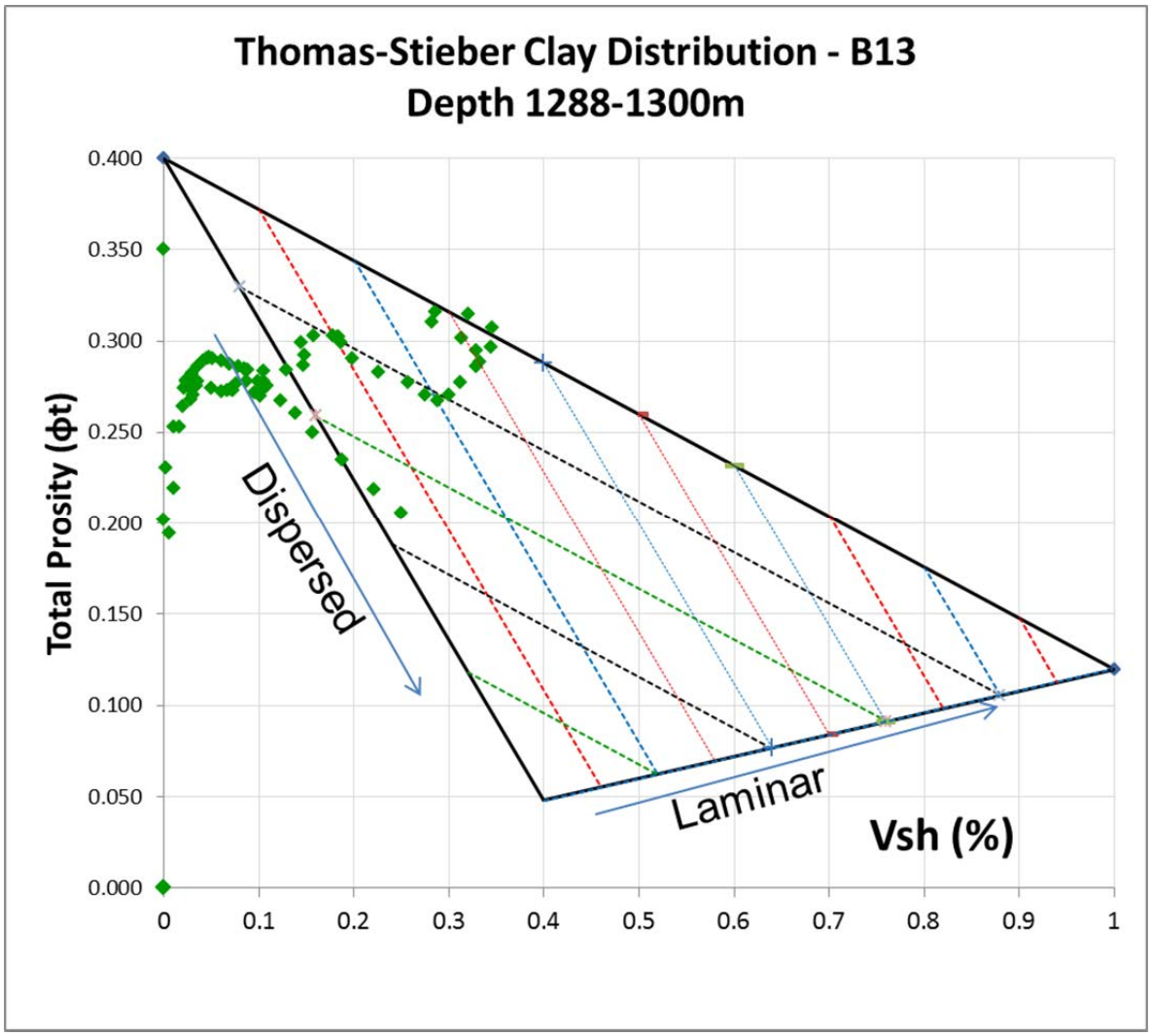

Figure 70: The Thomas-Stieber Plot for well B13 from depth 1288-1300m shows laminated shale distribution but the distribution does not show consistent change in shale volume with porosity similar to the shale distribution in well A15 and A16.

The presence of clay in the reservoir can have an impact on the ability of fluids, in particular hydrocarbons, to flow from the reservoir during production. The ability of fluids including hydrocarbons to flow in a reservoir reflects the permeability of the reservoir and when dispersed clay fills the pore throats, the permeability of the reservoir is reduced as shown in Figure 72.

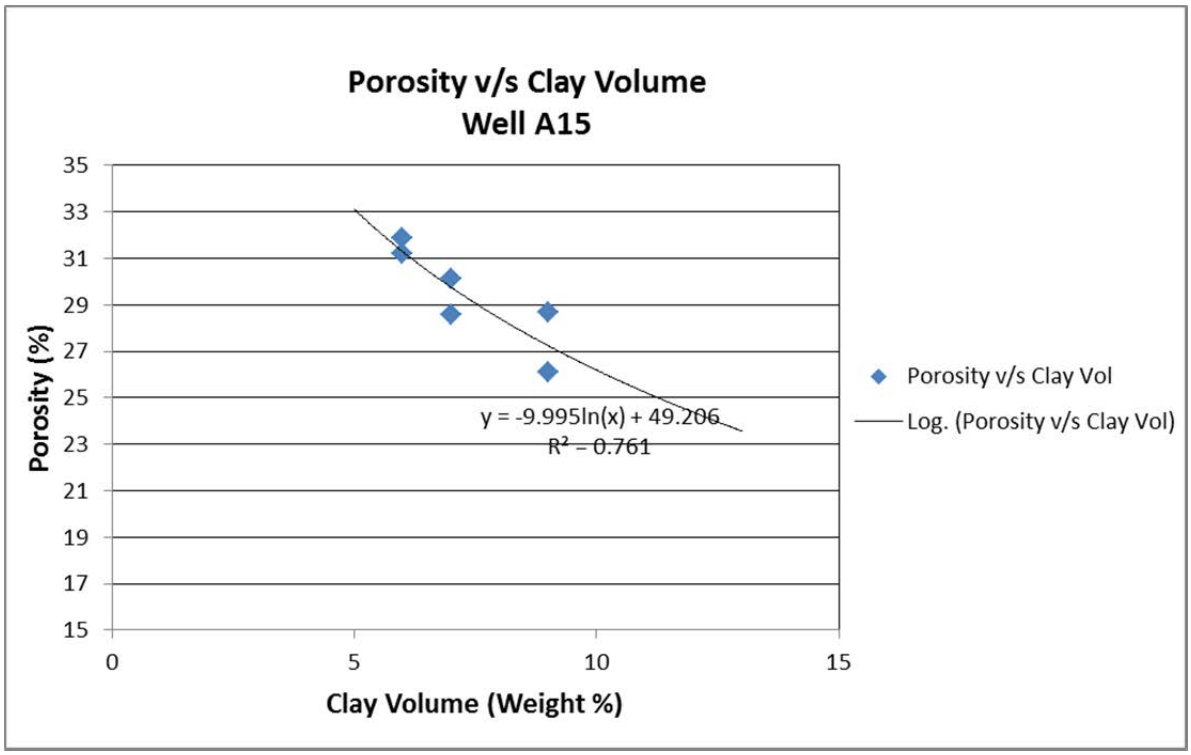

Figure 71: Porosity versus clay content for well A15 shows an almost linear relationship between porosity and the volume of clay.

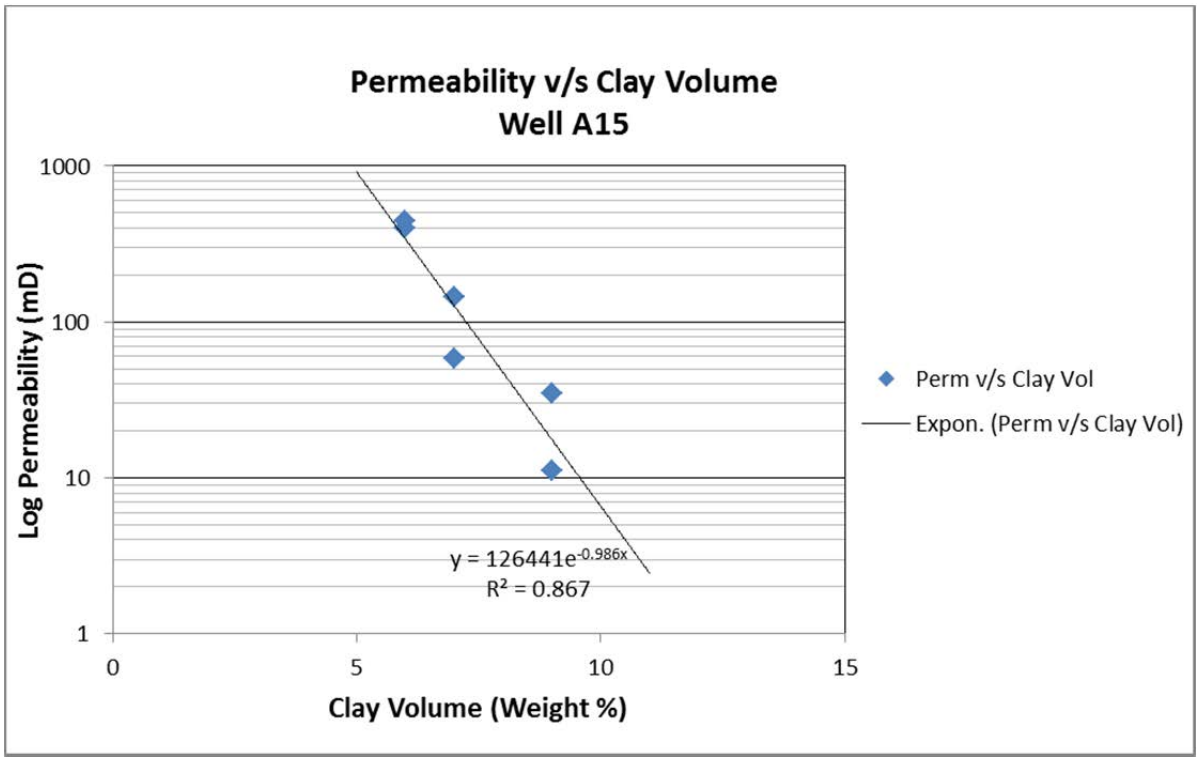

Figure 72: Log (Permeability) versus clay content for well A15 indicates a decrease in permeability with an increase in clay content as measured by XRD. The small percentage of dispersed clay fills the pore throats and reduces the reservoir permeability.

- **Results: Effect of Grain Size on Irreducible Water Saturation (S_{wirr})**

The mineral grain size of sandstone is one of the factors that control the amount of capillary bound water as described in section 4.5. As shown in Figure 73, a decrease in grain size causes an increase in irreducible water saturation in the B12 well. The relationship seems to level out at the grain size of about 0.2mm diameter, where a further decrease in grain size has little effect on irreducible water saturation (S_{wiir}). No information on irreducible water saturation (S_{wirr}) was available from any of the core data in the J-Reservoir and hence the relationship between grain size and irreducible water saturation (S_{wirr}) was not investigated.

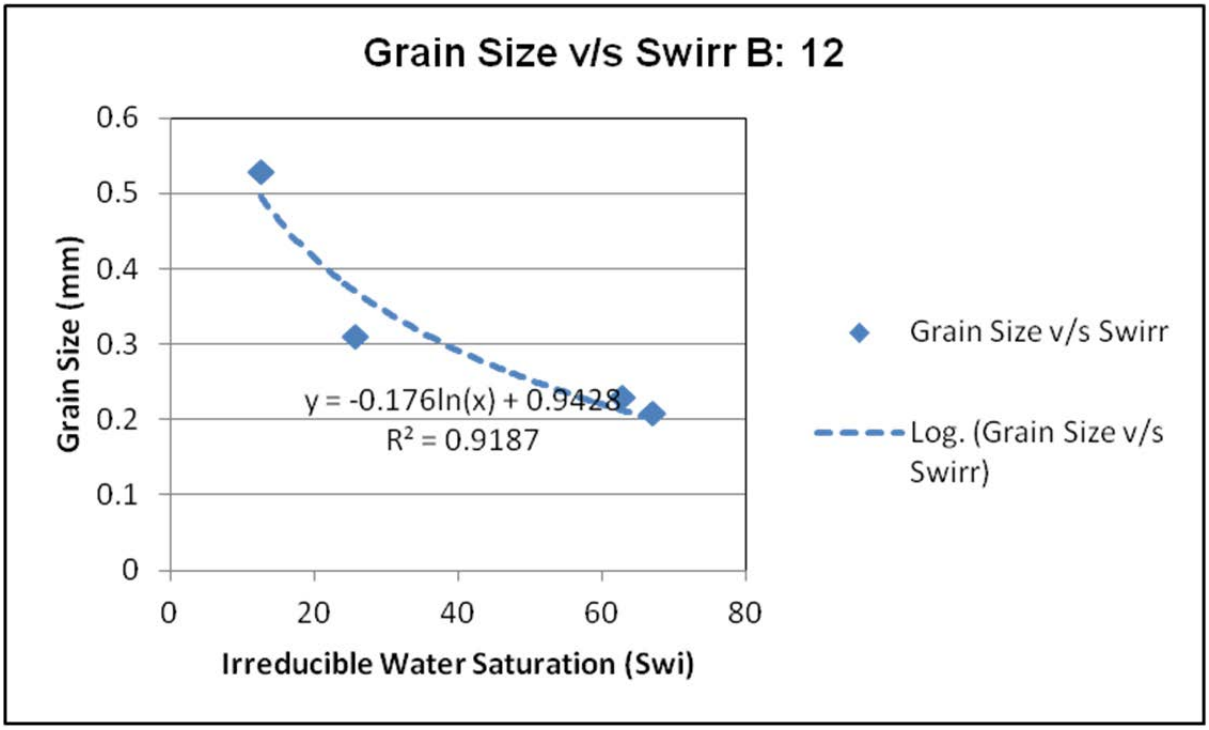

Figure 73: Grain size versus irreducible water saturation (S_{wirr}). A decrease in grain size results in an increase in irreducible water saturation for B12.

5.3 WATER SATURATION (S_w) CALCULATION

The following section describes the workflow used to calculate the water saturation on the J- and K-Reservoirs. The section will focus on Archie's equation and its modified version (variable m), Simandoux equations and the new algorithm developed by the author to calculate water saturation. The use of variable (m), Simandoux equation and the new method were employed to investigate possible improvements in the accuracy of the water saturation results. Such improvements are necessary because conventional water saturation

gives inaccurate results when used in the low-resistivity pays of the Mozambique basin. The following workflow was adopted:

1. Determination of the reservoir temperature for the J- and K-Reservoirs.
2. Determination of the water resistivity (R_w).
3. Estimation of water salinity, a possible cause of low-resistivity pay and not a direct input into any of the water saturation equations.
4. Calculation of water saturation (S_w) using Archie's equation with constant (m) and (n).
5. Calculation of water saturation using Archie's equation with variable cementation factor (m).
6. Calculation of water saturation (S_w) using Simandoux equation.
7. Calculation of water saturation (S_w) using the new equation developed by the author.
8. Compare results to calculated water saturation calculated from Nuclear Magnetic Resonance (NMR).
9. Comparison of the results to Drill Stem Test (DST) and the production data.

5.3.1 Reservoir Formation Temperature

Water saturation (S_w) calculations depend on the formation water resistivity (R_w) which is a function of formation temperature, therefore it is important to know the formation temperature to accurately calculate the water resistivity. Two main factors that affect the conductivity of the formation are the salinity and the temperature. Higher temperature results in low formation resistivity due to an increase in the mobility of ions. An increase in the dissolved solutes (salinity), results in an increase in the conductivity (decrease of resistivity) of the solution. Two approaches were employed to determine the formation temperature, the first was to calculate the temperature gradient for each of the well in the study area, using the surface temperature and measured temperature at the well's total depth (TD) as follows:

$$\text{Temp Gradient} = \Delta T^{o} / \Delta \text{ Depth} \quad (5.8)$$

Where

$\Delta T^{o} = T^{o}(TD) - T^{o}(Surface)$

$T^{o}(TD)$: Temperature at the well's Δ total depth (TD)

T^{o} (Surface): Temperature at surface, assumed to be 21^{o}

Δ Depth: Change in depth from surface to TD

The second approach was to generate reservoir temperature versus depth plot for the wells in J- and K-Reservoirs and then fit a straight line through the points and the average, regional temperature gradient. The temperature value at any depth can then be read off from the linear fit of the data.

- **Results: Temperature Gradient for the J-Reservoir and the K-Reservoir**

The plot of temperature versus depth is shown in Figure 74 below and it based on the temperature from all the wells used in the study. A gradient is then established by fitting a straight to the data.

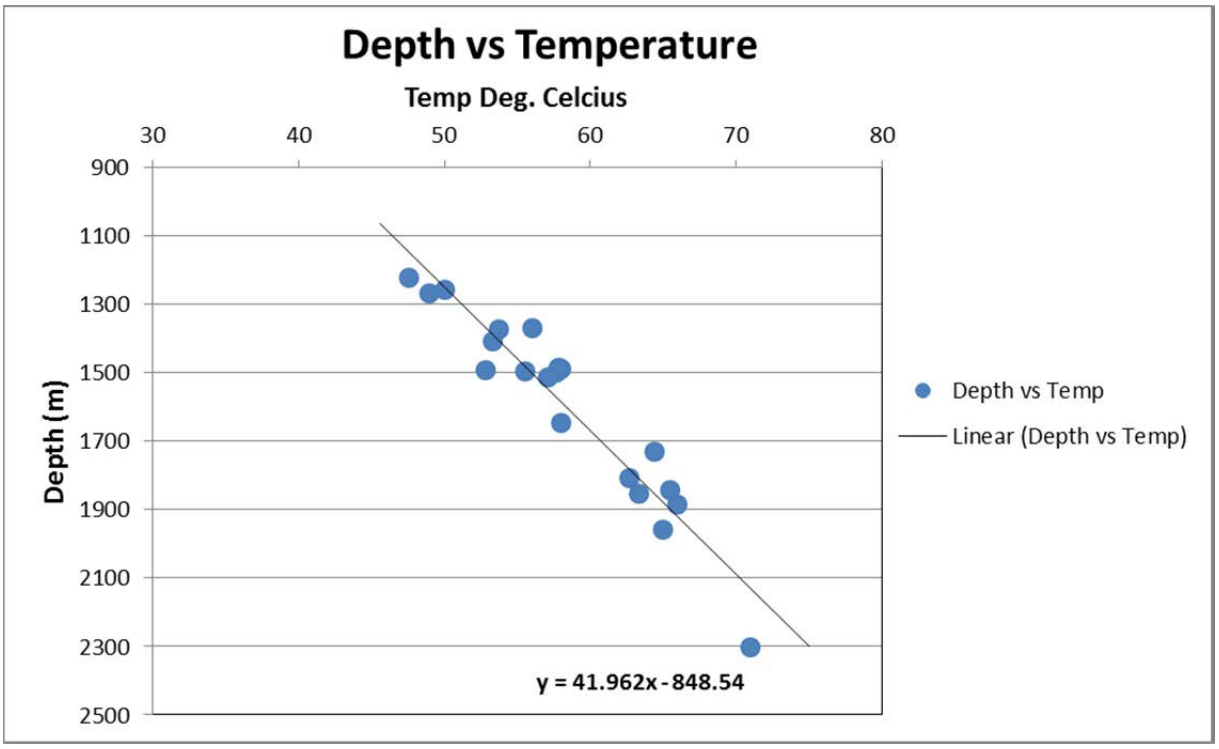

Figure 74: Average temperature gradient for J- and K-Reservoirs. The line gradient is approximately 43^{o}C/m, being the average reservoir temperature gradient for the J- and K-Reservoirs.

Once the temperature gradient is established, temperature values can be read off from any depth along the borehole without having physical temperature measurement at that point. The calculated average reservoir temperature for J- and K-Reservoirs is between 45^{o}C and 60^{o}C. The hydrocarbons were generated at higher burial depths and higher temperatures before migrating into the shallower reservoirs depths of 1140 – 1320m.

5.3.2 Formation Water Resistivity (R_w) from Pickett Plot

In the absence of reliable water sample resistivity measurements, the Pickett Plot was used to calculate the water resistivity (R_w) of the formation. Well A21 was used to derive a Pickett Plot as shown in Figure 75. It is important that the analysis is done in a water-wet section of the reservoir, in order to get more reliable water resistivity results; in this case the depth range used was from 1122m to 1160m, above the J-Reservoir, where the average temperature was 45^{o}C. Since the top of the J-Reservoir in well A21 is approximately 1143m, the chosen depth range for water resistivity (R_w) analysis includes the top section of the gas bearing reservoir i.e. 17m of the gas section was included in the analysis. The gas points from this section are shown in Figure 75 and they plot away from the 100% water-saturated line.

The plot in Figure 75 is essentially a graphical solution to Archie's saturation equation given by re-arranging the equation as follows:

$$\text{Log } \varphi = (-1/m) \log (R_t) - n (\log (S_w) + \log (a.R_w)) \quad (5.9)$$

Plotting resistivity against porosity on a log-log scale yields:

Log φ = Y-axis
Log (R_t) =X-axis and,
Log ($a*R_w$) = Y-Intercept.

- **Results: Formation Water Resistivity from Pickett Plot**

Several parameters can also be estimated from the linear fit through the water point (red line). For instance, the slope of the linear fit gives an estimate of cementation factor (m) and the water resistivity (R_w) is given by the intersection of the red and the y-axis as shown in Figure 75 where the intersection equates to $a*R_w$. This is how the water resistivity (R_w) is estimated from the Pickett Plot. In this case the estimated (R_w)=0.0947 ohm-m. The values of cementation factor, m=1.46 and saturation factor, n=2 are calculated and a=1. The value of m suggests, according to Archie (1941), that the J-Reservoir is moderately cemented.

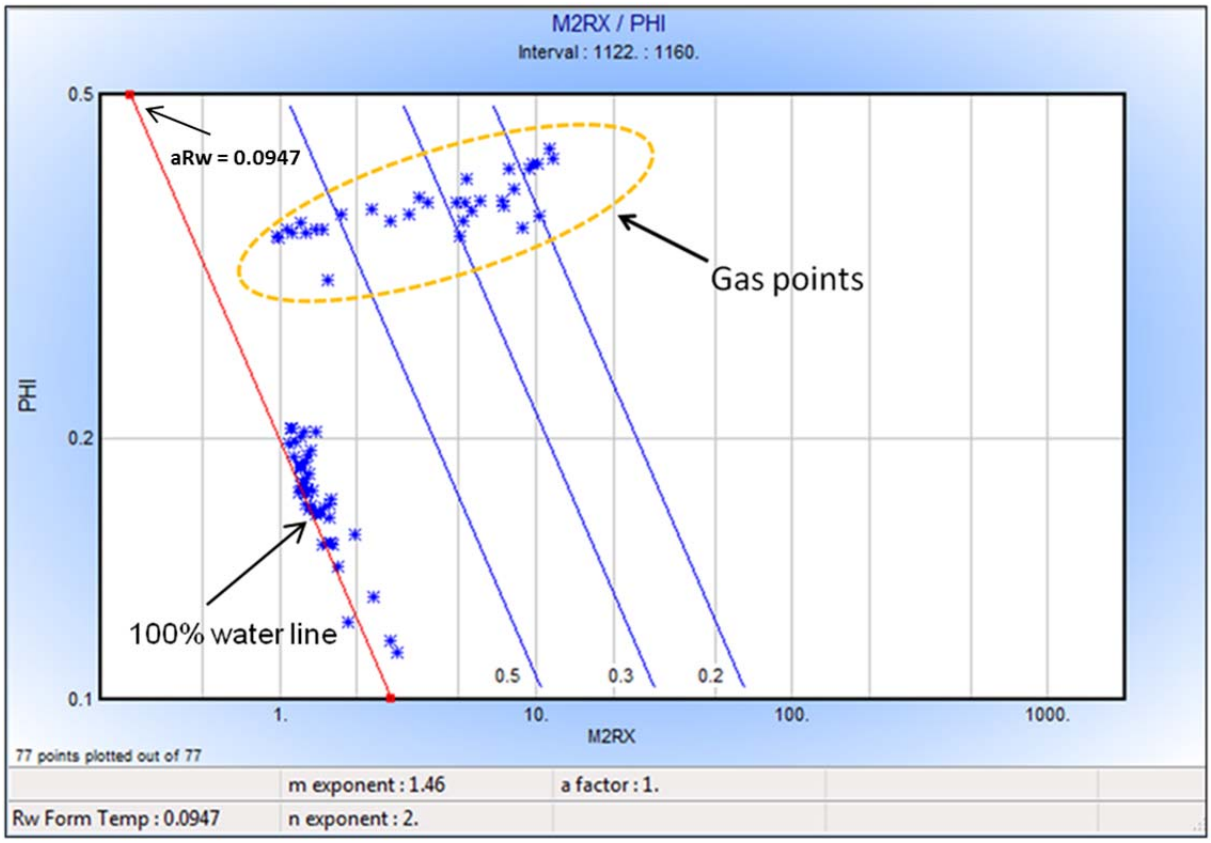

Figure 75: Pickett Plot results for well A21. The red line represents 100% water line with every point that falls to the right of it representing hydrocarbons (gas).

5.3.3 Estimation of Formation Water Salinities

The resistivity of the formation water (R_w) also depends on the salinity and since no reliable water samples were available for this study, calculated water resistivity (R_w) and temperature (T) were used to estimate the salinity of the formation water, using an empirical chart in Figure 76. The water salinity at reservoir temperature of about 45^{o}C is approximately 120000ppm NaCl.

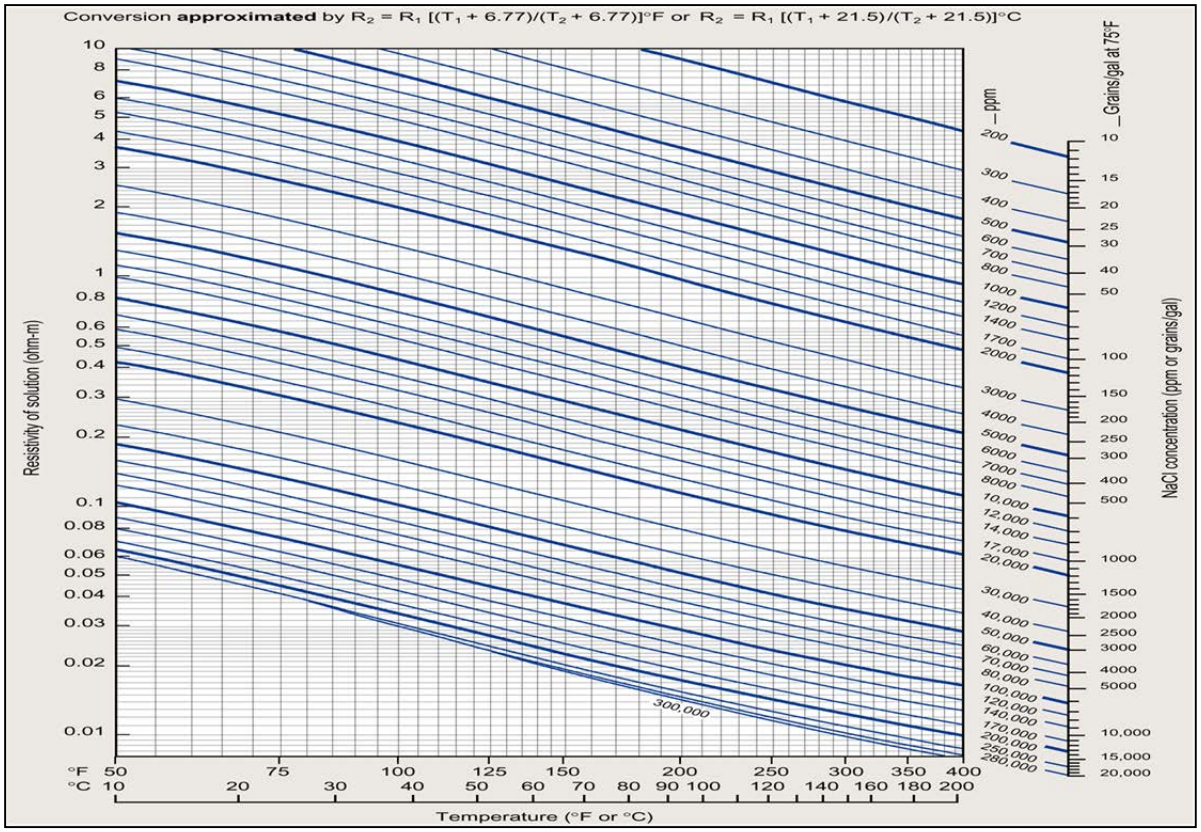

Figure 76: Salinity chart (Schlumberger, 2009). If water resistivity (R_w) and formation temperature are known, salinities can be read off from the chart.

5.3.4 Water Saturation (S_w) -Archie's Equation (constant m and n)

The conventional approach to calculating water saturation (S_w) uses the parameters (m, n, R_w) as single value inputs into Archie's equation. These input parameters were calculated in the previous section as m=1.46, n=2 and R_w=0.0947 Ohm-m (see Table 9). This section presents the results of water saturation calculation, using Archie's equation in wells that intersected the J-and K-Reservoirs.

The results of the calculated water saturation (S_w) for wells A21 and A23 of the J-Reservoir are shown in Figure 77 and Figure 78. In both cases, the calculated water saturation overestimates the amount of water in the reservoir formation, as measured by NMR, particularly towards the bottom of the reservoir. In well A21, the saturation curve suggests that the J-Reservoir is water wet below 1164m MD (measured depth), although the gas water contact is known to exist at depth of 1182m MD (1121mbmsl), below which, the reservoir is assumed to be 100% water-saturated. The presence of gas between 1164m and 1182m is further supported by other data, such as fluid gradient measured from Modular

Dynamics Tester (MDT) as shown in Appendix 12. Similar results are shown in well A23, where the water saturation results from Archie's equation overestimate the water saturation compared to the NMR-calculated results.

- **Water Saturation: Archie (constant m), Wells A21 & A23**

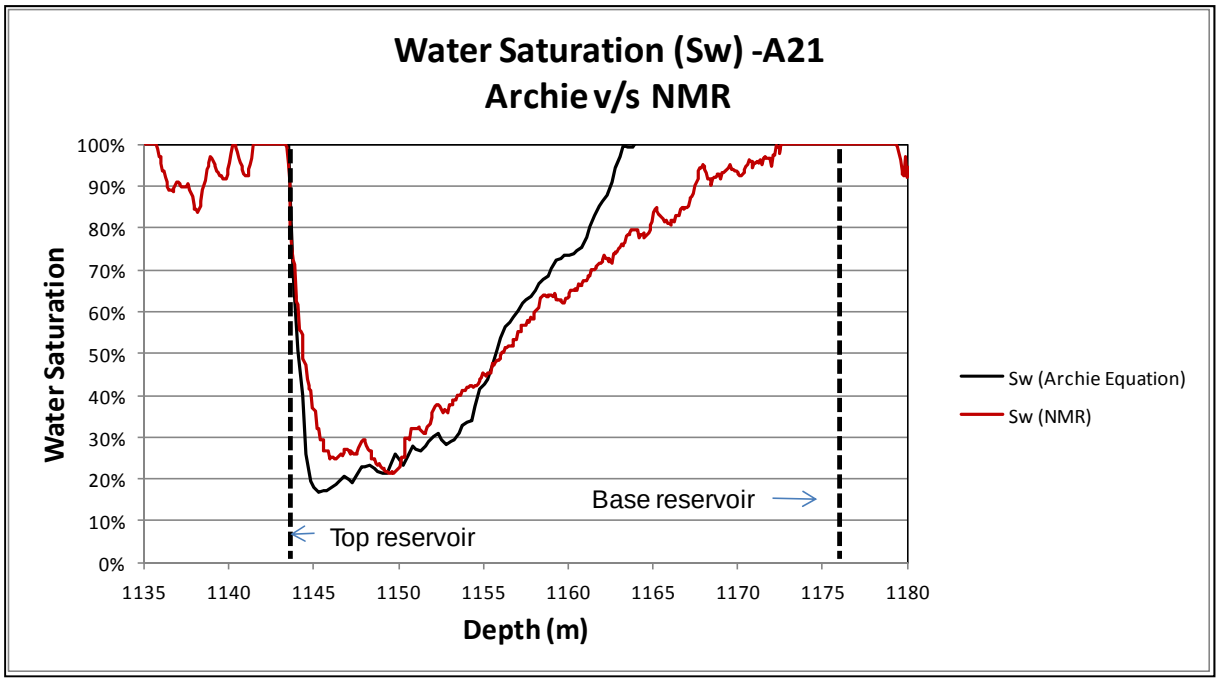

Figure 77: Water Saturation (S_w) calculated using Archie's equation compared to water saturation calculated using Nuclear Magnetic Resonance (NMR), well A21.

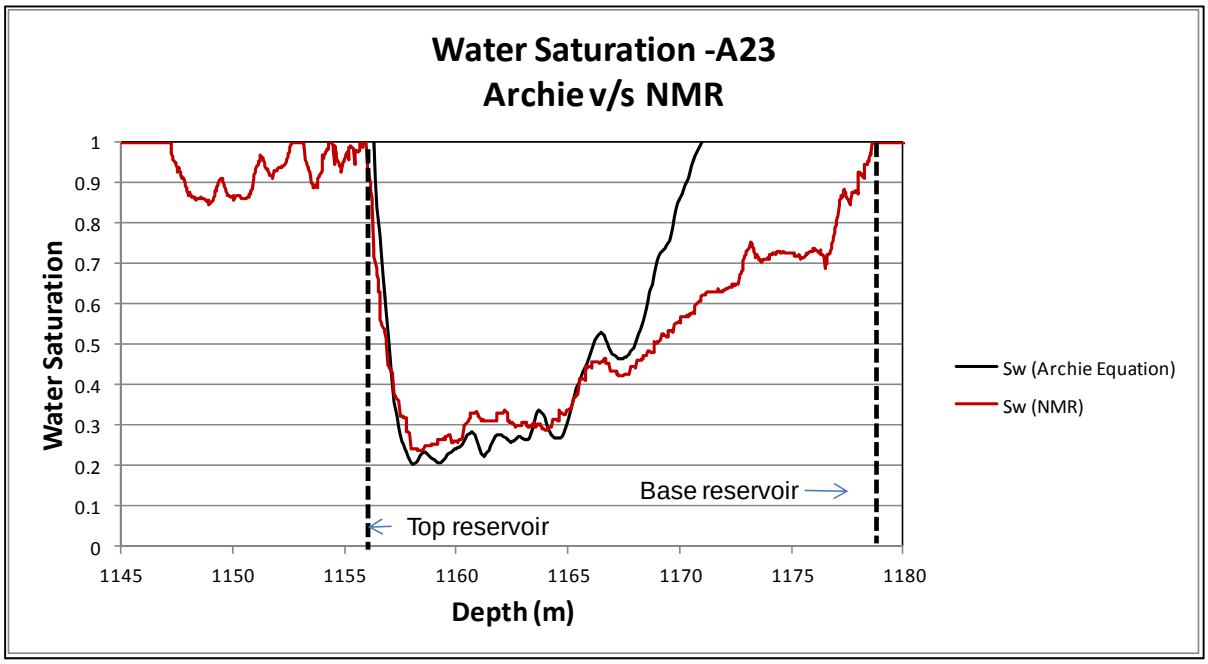

Figure 78: Water Saturation (S_w) calculated using Archie's equation compared to water saturation calculated using Nuclear Magnetic Resonance (NMR), well A23.

Results from B12 and B18 wells of the K-Reservoir shown in 79 and Figure 80, respectively, also show some inconsistencies between the water saturation calculated using Archie's equation and the NMR-calculated water saturation. In well B12, the inconsistencies between the water saturation calculated using Archie's equation and the NMR-calculated water saturation occur throughout the reservoir section whereas in well B18, the water saturation results are similar to that of well A21 where Archie's equation overestimates the water saturation more towards the bottom of the reservoir compared to the top of the reservoir.

- **Water Saturation: Archie (constant m), Wells B12 & B18**

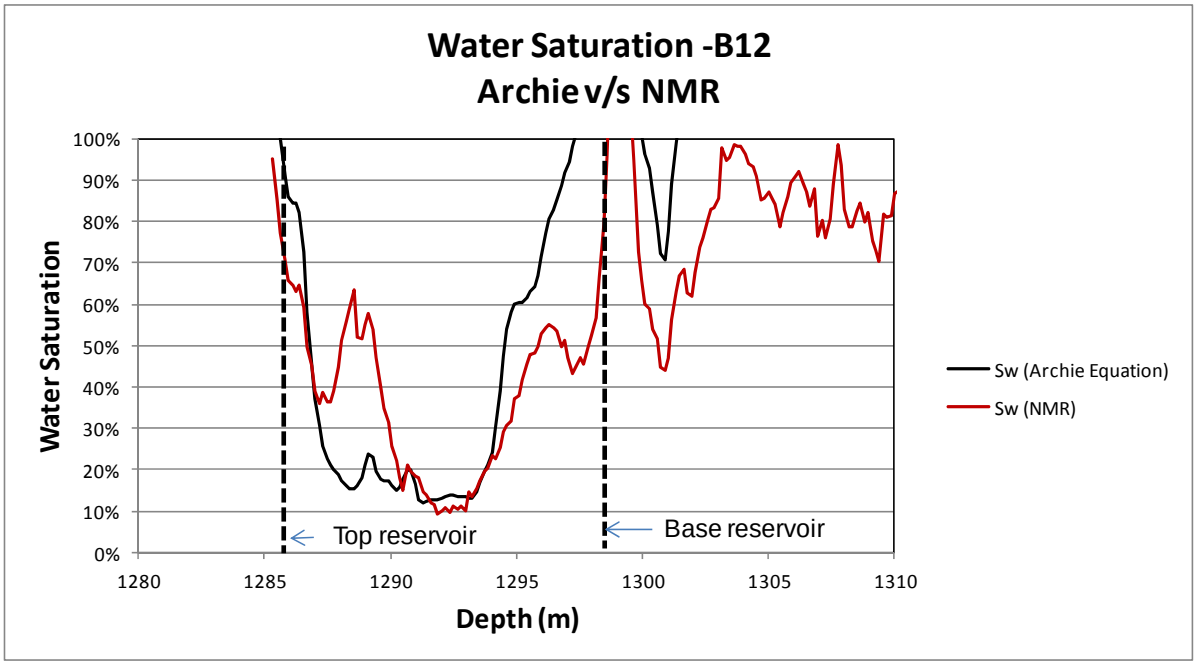

Figure 79: Water Saturation (S_w) calculated using Archie's equation compared to water saturation calculated using Nuclear Magnetic Resonance (NMR), well B12.

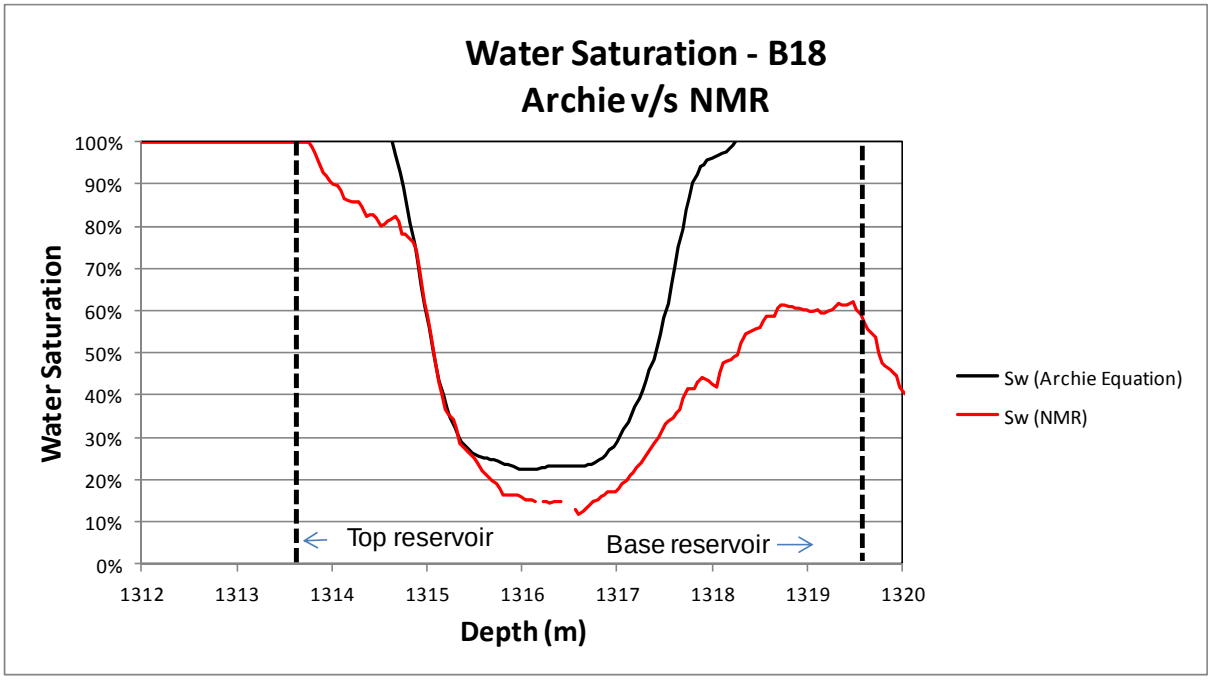

Figure 80: Water Saturation (S_w) calculated using Archie's equation compared to water saturation calculated using Nuclear Magnetic Resonance (NMR), well B18.

The input parameters used in calculating the water saturation are shown in Table 9 below.

Water Saturation Inputs (Archie's Equation)				
Rw (Ohm-m)	**m**	**n**	**a**	**Effective Porosity (PHIE)**
0.0947	1.46	2	1	PHIT*(1-Vsh)

Table 9: Inputs into Archie's equation using constant cementation factor (m) and saturation factor (n).

5.3.5 Water Saturation (S_w) -Archie's Equation (variable m)

The Formation Factor (FF), which is defined as the ratio of the resistivity of the brine filled formation to the resistivity of the brine was plotted against porosity (φ) on a log scale and an empirical relationship was established, based on the equation described in section 4.2 i.e. $FF = a/(\varphi)^m$. This relationship was used to vary the resistivity exponent (m) with porosity since the factor is implicitly related to porosity and FF. The values of FF and (m) were measured from core data in the following wells from the J- and K-Reservoirs, A11, A12 and

A15 and B12. Different empirical relationships were also investigated such as the one in Appendix 1, which shows the following relationship between FF and porosity:

$$FF=-0.0006\varphi^3+0.0462\varphi^2-1.1252\varphi+10.845 \quad (5.10)$$

This relationship was not pursued any further due to yielding extremely poor results when used to calculate water saturation (S_w). In the following section, plots of the formation factor (FF) against porosity on a log-log scale are used to derive the relationship between porosity and the cementation factor (m).

- **Results: Variable Cementation Factor (m)**

The relationship between the cementation factor (m) and porosity in well A11, as derived from the plot in Figure 81, is given by the following equation:

$$FF=1.2495(\varphi)\exp(-1.524) \quad (5.11)$$

Where
a=1.2495
m=1.524
φ=porosity

Equation 5.12 is the best fit between the porosity values and formation factor (FF) which is defined as the ratio of the resistivity of the brine (water-saturated formation) to the resistivity of the brine. The cementation factor (m) implies that the J-Reservoir at well A11 is only moderately consolidated.

A different relationship between FF and porosity exists for well A12 as shown in Figure 82, where the relation is given by:

$$FF=0.9284(\varphi)\exp(-1.968) \quad (5.12)$$

Where,
a = 0.9284 and,
m = 1.968.

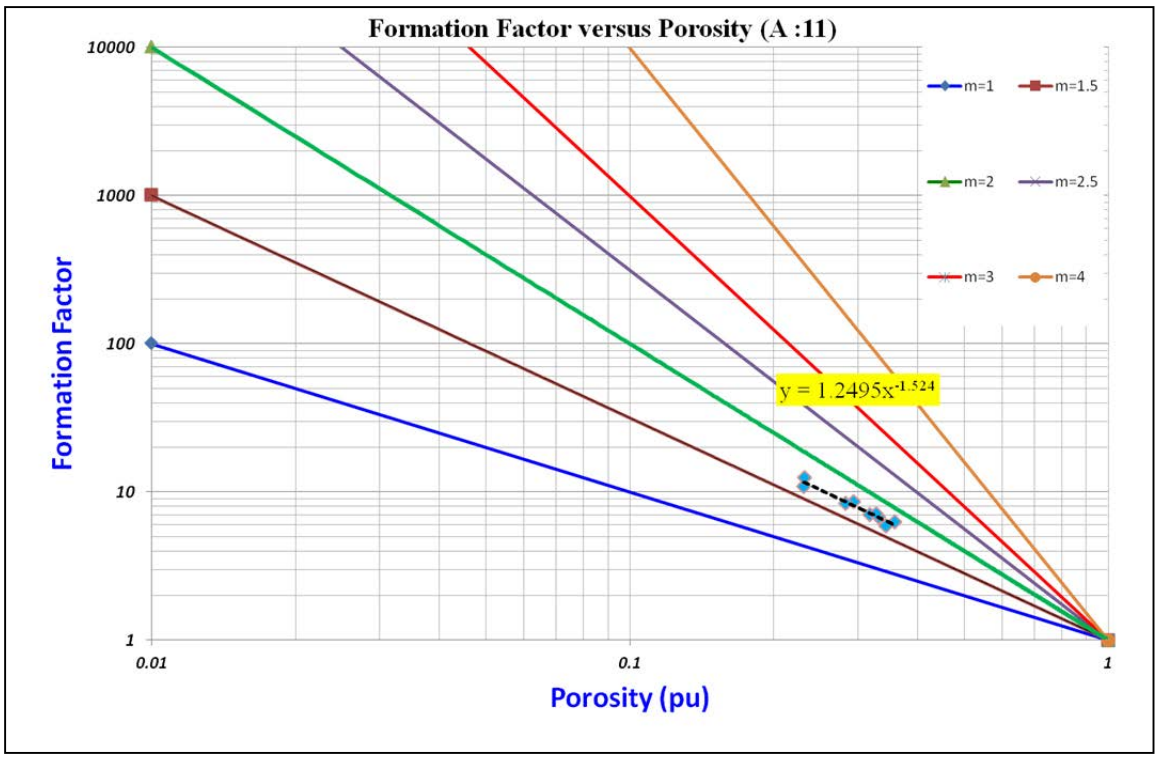

Figure 81: Formation factor (FF) versus porosity for well A11, plotted on the log-log scale. The six lines represent lines of constant cementation factor (m) values and the formation factor (FF) versus porosity pairs lie between m=1.5 and m=2.

The value of the cementation factor (m) implies that the J-Reservoir at well A12 is more consolidated than at well A11. The amount of consolidation or compaction in the reservoir affects the porosity of the reservoir and in turn, the water saturation (S_w). The results show that within the J-Reservoir, the sand consolidation can be variable and therefore using a constant cementation factor (m) for water saturation (S_w) calculation is a simplistic approach and hence a justification to use a variable cementation factor that captures the variability of the cementation with porosity.

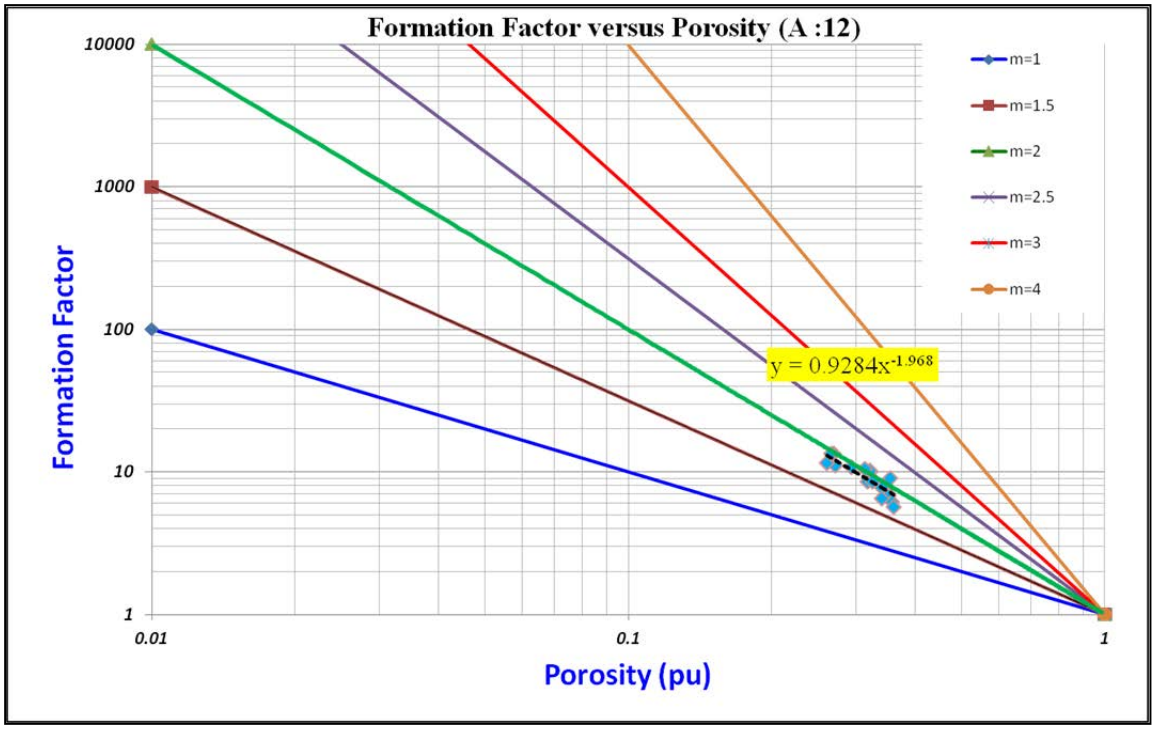

Figure 82: Formation Factor (FF) versus porosity for well A12 plotted on the log-log scale. The six lines represent lines of constant (m) values and the FF-Porosity pairs fall between m=1.5 and m=2.

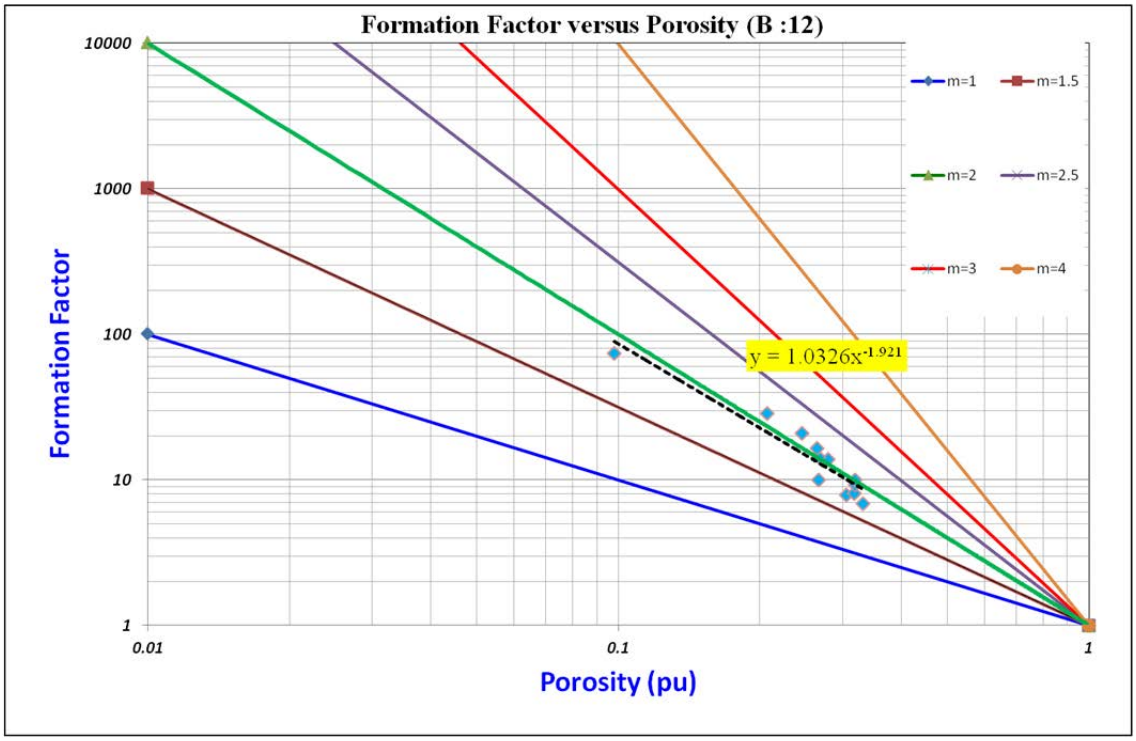

Figure 83: Formation factor (FF) versus porosity (B12) plotted on the log-log scale. The six lines represent lines of constant (m) values and the FF-Porosity pairs for well B12 fall approximately on the m=2 line.

Figure 83 revealed the following relationship between the formation factor (FF) and porosity for well B12 of the K-Reservoir:

$$FF=1.032(\varphi) \exp(-1.921) \quad (5.13)$$

The value of cementation factor (m) in well B12 suggests a consolidated K-Reservoir with a tortuosity factor (a), that is very close to the constant value of 1 normally used in the industry as an input to Archie's equation to calculate water saturation.

- **Water Saturation: Archie (variable m), Well A21**

The relationship between porosity and the cementation factor demonstrated in the preceding section was used to vary the value of (m) in Archie's equation instead of using a constant value that was estimated using a Pickett plot in Figure 75. The result of the calculated water saturation is shown in Figure 84. Both the constant and variable cementation factor (m) approach yield comparable results and the two methods over-estimate the amount of water in the reservoir compared to the NMR-calculated water saturations.

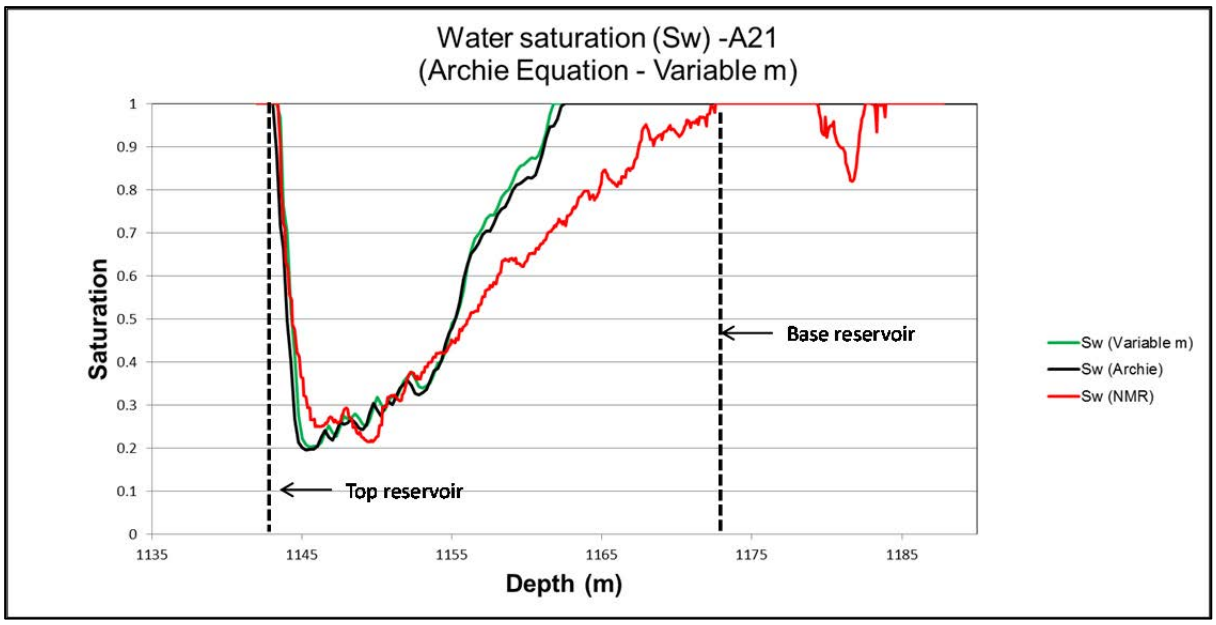

Figure 84: Water saturation from Archie and variable (m) compared to NMR-calculated water saturation (S_w) for well A21. The water saturation (S_w) calculated from the variable (m) is not consistent with the water saturation (S_w) calculated from NMR.

The calculated water saturation for the K-Reservoir is shown in Figure 85 for well B12, the water saturation (S_w) calculated from the variable (m) is also not consistent with the water

saturation (S_w) calculated from NMR. The input parameters used in calculating the water saturation are shown in Table 10.

- **Water Saturation: Archie (variable m), Well B12**

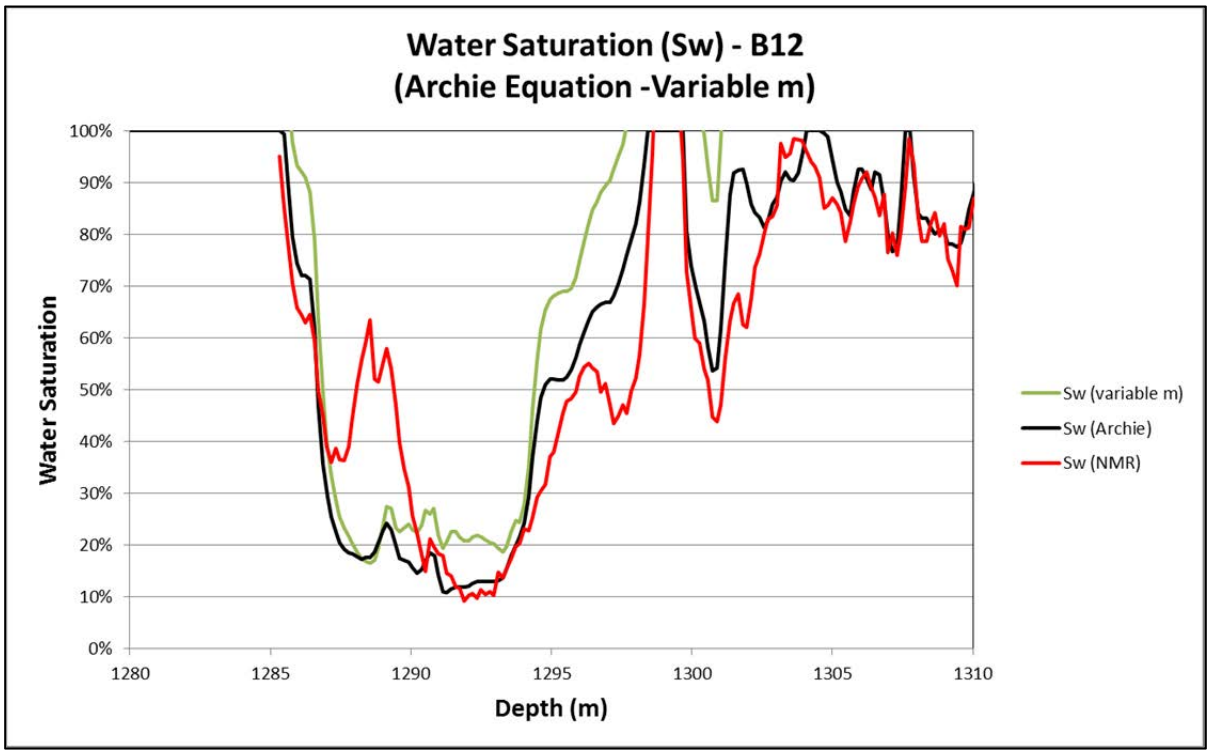

Figure 85: Water saturation from Archie and variable (m) compared to NMR-calculated water saturation (S_w) for well B12. The water saturation (S_w) calculated from the variable (m) is not consistent with the water saturation (S_w) calculated from NMR.

Water Saturation Inputs (Archie's Equation)				
Rw (Ohm-m)	**m**	**n**	**a**	**Effective Porosity (PHIE)**
0.0947	1.46	2	1	PHIT*(1-Vsh)

Table 10: The input parameters into Archie's equation using variable cementation factor (m) and saturation factor (n).

5.3.6 Variable (n) Method

The relationship between the saturation factor (n) and the porosity was investigated from available core data such as in wells A15 and B12 and no empirical trends could be

established between the two parameters. The saturation factor (n) appears to be independent of porosity, as shown in Appendix 2.

5.3.7 Water Saturation (S_w) – Simandoux Equation

The Simandoux equation was described in detail in section 4.3. The equation is essentially applied for shaly reservoir as opposed to Archie's equation which works better in clean, non-shaly reservoirs. The water saturation was calculated using the Simandoux equation for the J-Reservoir and the K-Reservoir, as shown in Figures 86, 87, 88 and 89.

- **Water Saturation: Simandoux (Wells A21 & A23)**

Figures 86 and 87 display the water saturation results for wells A21 and A23 of the J-Reservoirs. In both cases the results show an improvement in the water saturation calculated using Simandoux equation compared to Archie's equation, more so in well A21 than in well A23. In well A21, the water saturation results compare well to the NMR-calculated water saturation. Similar results were observed in wells B12 and B18 of the K-Reservoir where water saturation calculated using Simandoux equation yield better results compared to water saturation derived from Archie's equation.

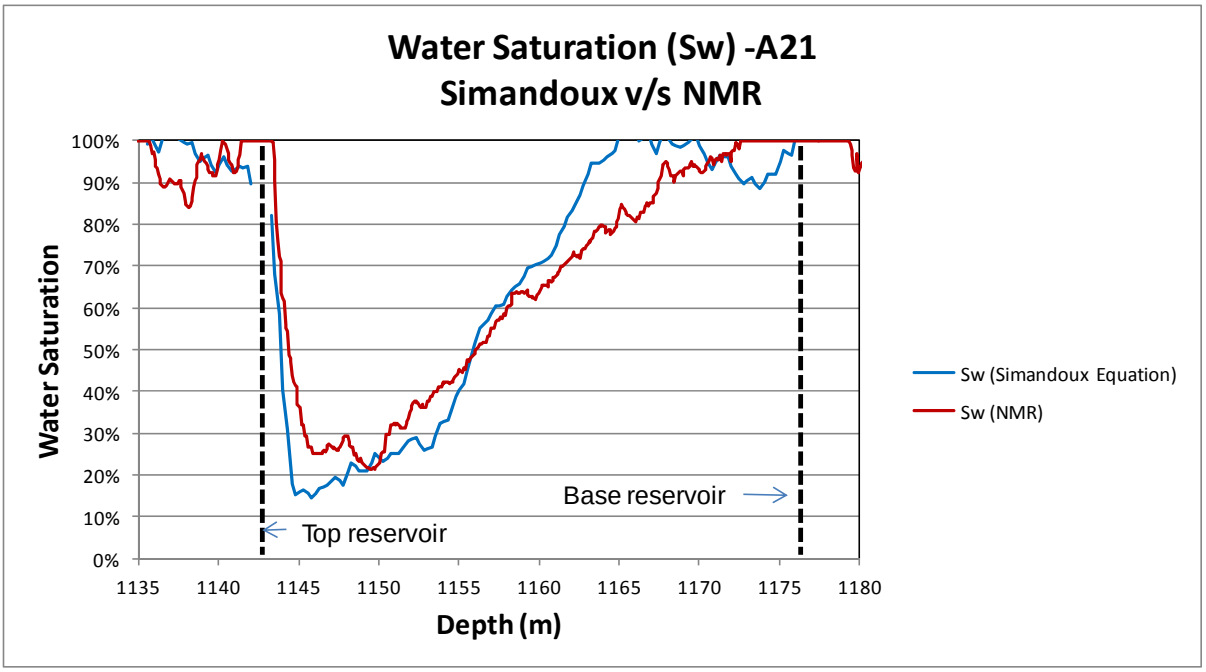

Figure 86: Water saturation from Simandoux equation compared to NMR-calculated water saturation (S_w) in well A21 (Field A). The results show an improvement in the water saturation calculated from the Simandoux equation.

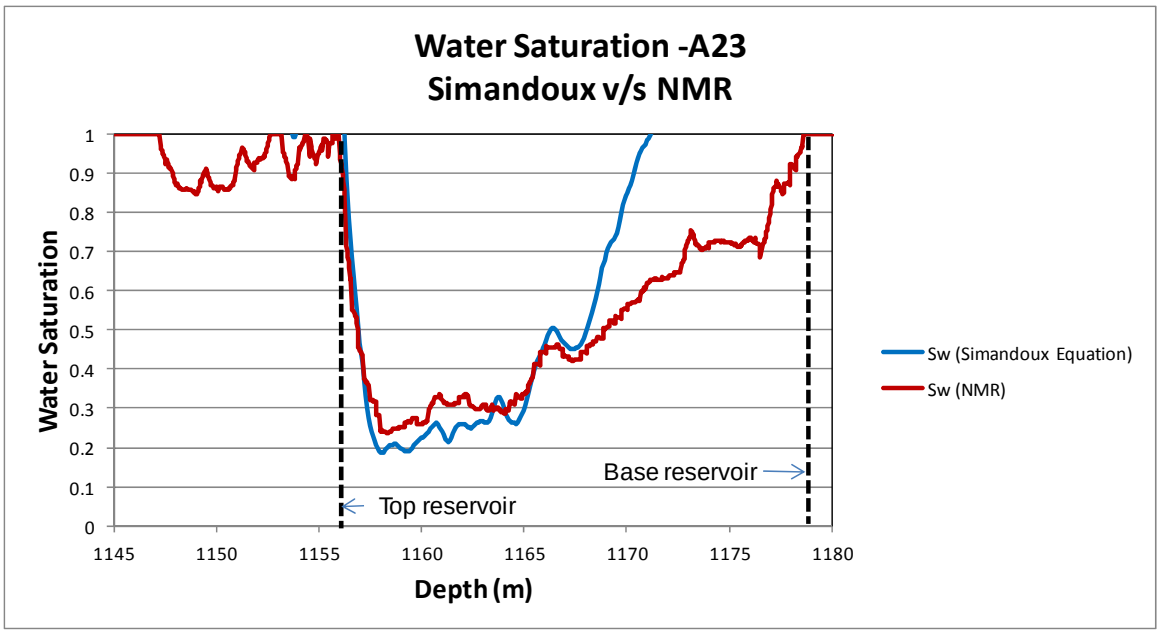

Figure 87: Water saturation from Simandoux equation compared to NMR-calculated water saturation (S_w) in well A23 (Field A). The results show an improvement in the water saturation calculated using Simandoux equation, especially in the shallower section of the reservoir.

- **Water Saturation: Simandoux (Wells B12 & B18)**

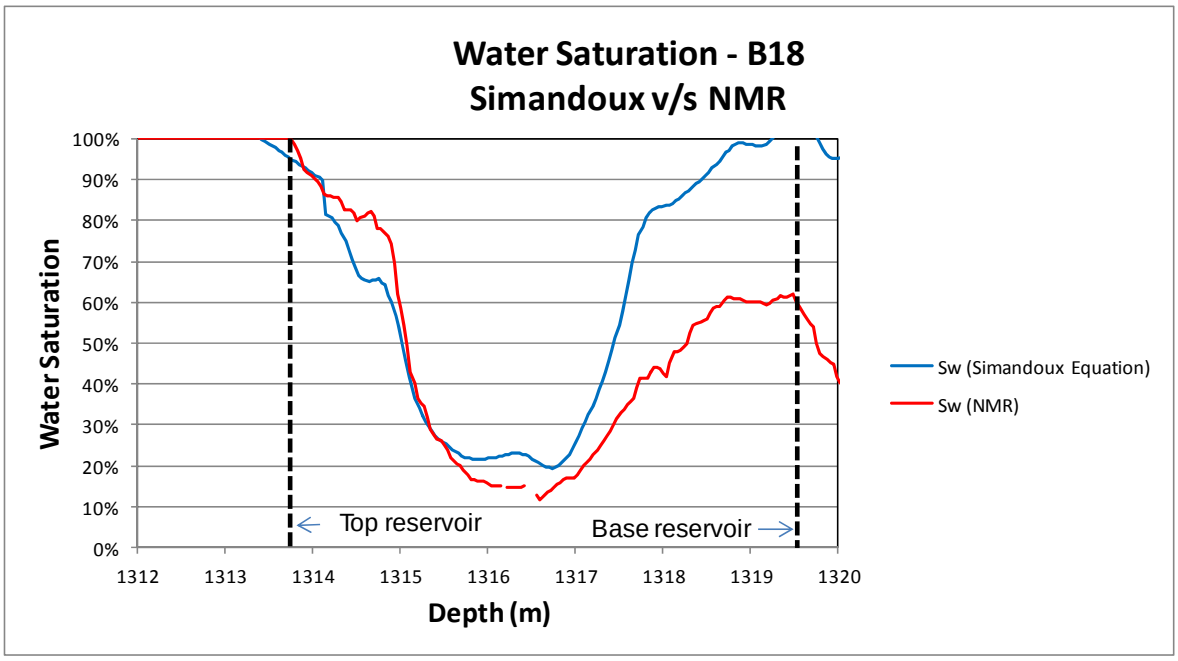

Figure 88: Water saturation derived from Simandoux equation compared to NMR-calculated water saturation (S_w) in well B18 (Field B). The Simandoux equation overestimates the water saturation, especially towards the bottom part of the reservoir.

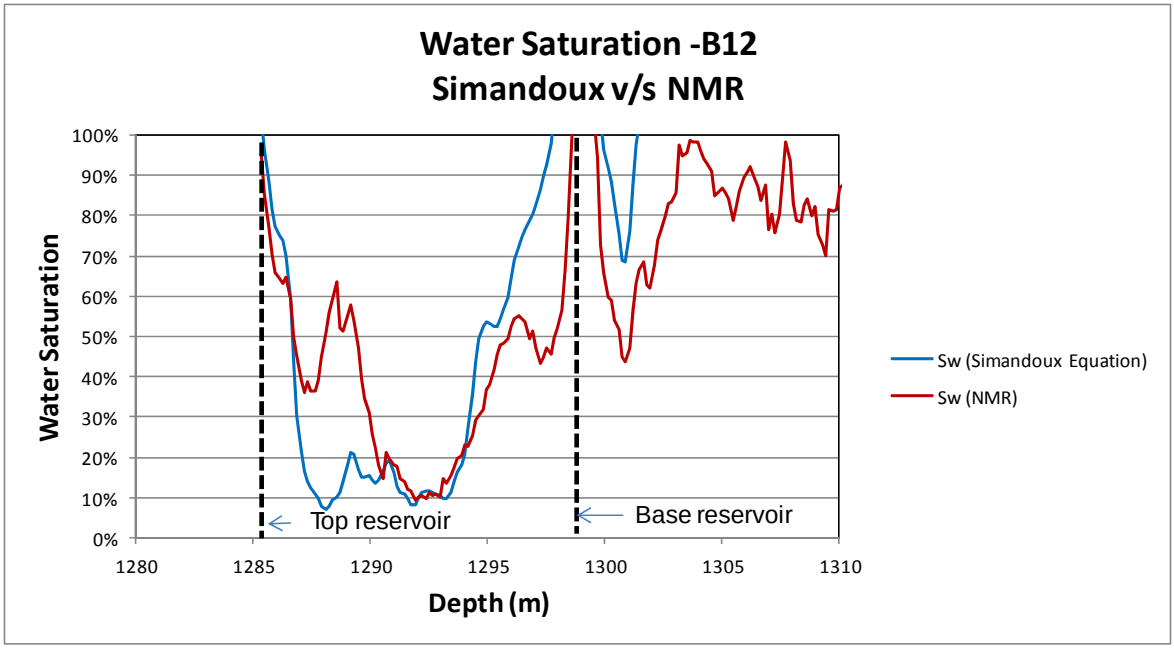

Figure 89: Water saturation derived through the Simandoux equation compared to NMR-calculated water saturation (S_w), in well B12 (Field B). The water saturation (S_w) calculated from the Simandoux is inconsistent with water saturation calculated using NMR for most part of the reservoir.

The input parameters used in calculating the water saturation (Simandoux equation) are shown in Table 11. The resistivity of shale (R_{sh}) was read off from the resistivity of log shown in Appendices 13-17.

Water Saturation Inputs (Simandoux Equation)						
Rw (Ohm-m)	**m**	**n**	**a**	**Rsh (Ohm-m)**	**Effective Porosity (PHIE)**	**Vclay**
0.0947	1.46	2	1	0.9-5	PHIT*(1-Vsh)	Calculated

Table 11: Input parameters used in Simandoux equation to calculate water saturation (S_w).

5.3.8 Water Saturation (S_w) –Sensitivities in R_w and (m)

One of the contributing factors to the inconsistencies in the water saturation calculated using the Archie and Simandoux equations seems to be the water resistivity (R_w), estimated using the Pickett Plots (see section 5.2.3). In order to match the water saturation calculated from conventional logs, the water resistivity should be lowered from the estimated 0.094 ohm-m to 0.05 ohm-m. Figures 89, 90 and 91 show the water saturation results based on the lower,

0.05 ohm-m water resistivity for wells A21, A23 and B12. Using this lower resistivity in matches the water saturation calculated using NMR, more so in the reservoirs that exhibit an upward coarsening, sequence where more irreducible water exists in the finer, bottom part of the reservoir. (0.05Ohm corresponds to unrealistic salinity of over 280 000ppm (not encountered in Mozambique) and off the scale of Schlumberger salinity charts.

- **Water Saturation: Wells A21 & B18**

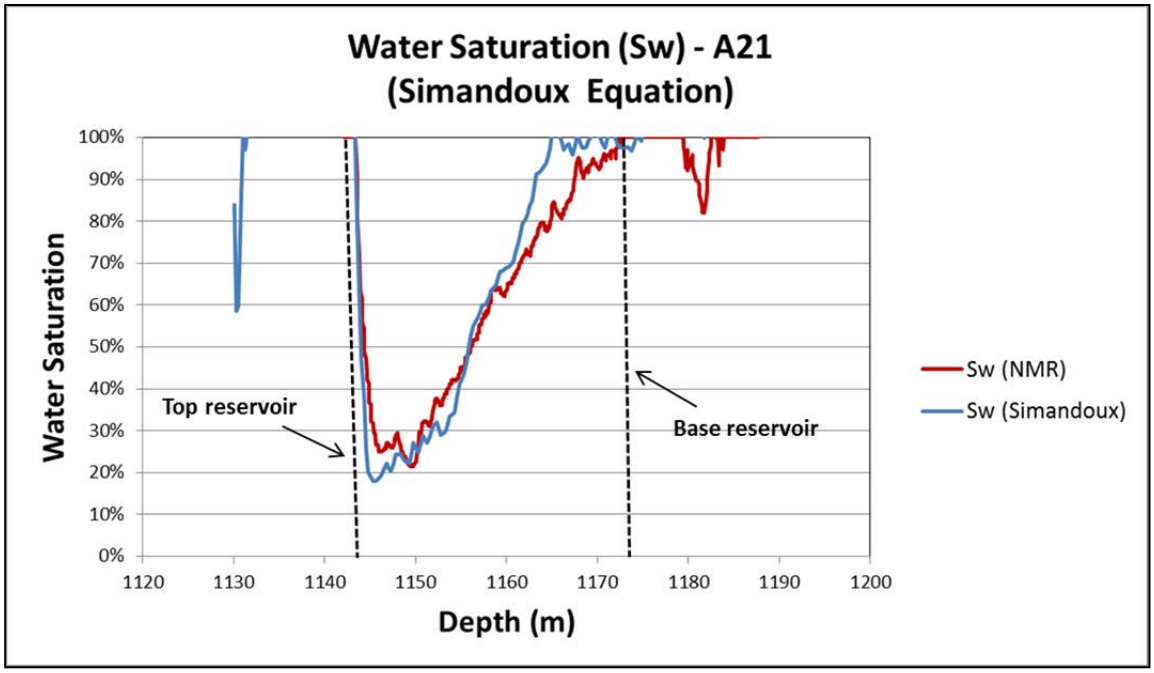

Figure 90: Water resistivity of 0.05 Ohm-m matches the water saturation values derived from the Simandoux equation to NMR-calculated water saturation, well A21 (Field A).

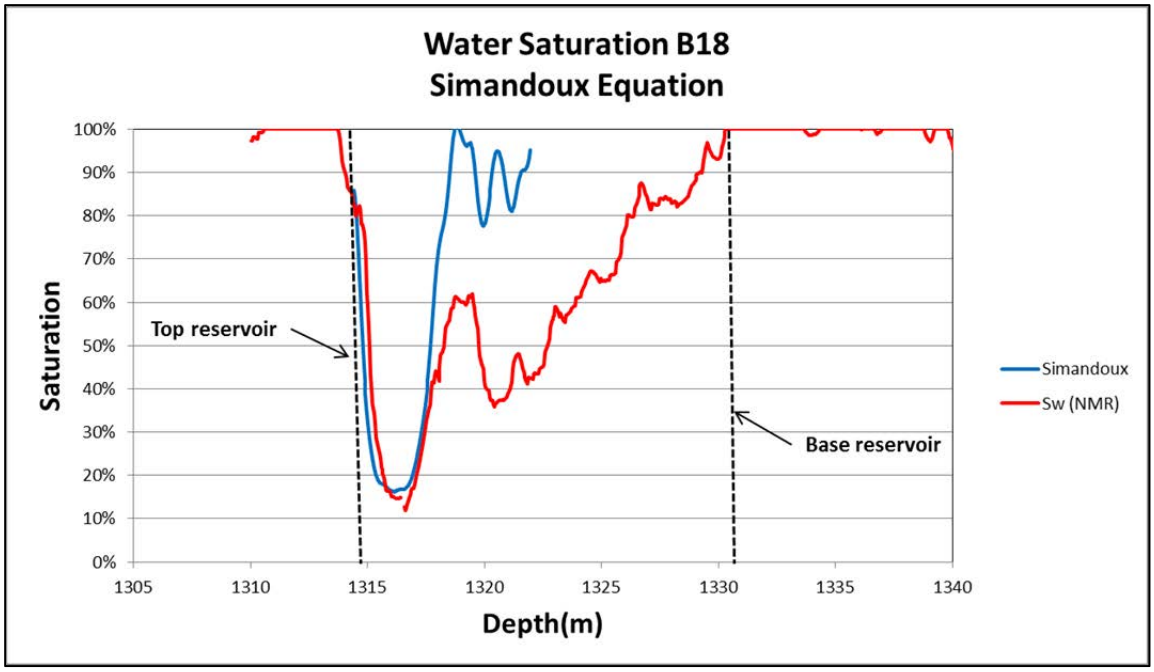

Figure 91: Water resistivity of 0.02 Ohm-m matches the water saturation calculated using the Simandoux equation to NMR-calculated water saturation, well B18 (Field B).

CHAPTER 6: NEW EQUATION FOR WATER SATURATION (S_w) CALCULATION

The basis of Archie's equation was that the conductivity of the formation arises from the conductivity of the water in the pore space and therefore the equation can be written in terms of conductivity as:

$C_t = PhiT^m S_w^n C_w$..... (6.1)

Where,

C_t: Total conductivity as measured by the resistivity logs = $1/R_t$

PhiT: Total porosity

C_w: Conductivity of the formation water = $1/R_w$

m: Cementation factor

n: Saturation exponent

S_w: Water saturation

This equation is applicable to clean non-shaly sands, however for formations with extra source of conductivity such as shale, defined by the Simandoux equation (1963):

$C_t = PhiE^m\ S_w^n\ C_w + S_wV_{sh}C_{sh}$……………………….……………… (6.2)

Where,
PHIE: Effective porosity
V_{sh}: Volume of shale
C_{sh}: Conductivity of shale

Equation 6.2 basically introduces another conductivity term arising from shale but since clay is the most prevalent form of shale in Mozambique basin, the author argues that in order for the equation to be more relevant for the J- and K-Reservoirs then it should be re-written as:

$C_t = PhiE^m\ S_w^n\ C_w + S_wV_{cl}C_{cl}$………………..…………………..…….... (6.3)

Where:
V_{cl}: Volume of clay
$C_{cl:}$ Conductivity of clay

But silt is also present in the shale, in other words, shale in the J- and K-Reservoirs occurs as a sum of clay and silt, therefore, the author suggests that volume of silt and its associated conductivity be taken into account and equation 6.3 can be re-written as follows:

$C_t = C_w *(S_w)^n \text{ x } (PHIE)^m + V_{cl}*C_{cl}*S_w + V_{silt}*C_{silt}S_w$ ....(6.4)

Where,
V_{silt} = Volume of silt
C_{silt} = Conductivity of silt bound water
To solve for S_w in equation 6.4, one has to assume that n=2 and re-write the equation as follows:

$(S_w)^2 *(C_w)*(PHIE)^m + S_w*(V_{cl})*(C_{cl}) + (S_w)*(V_{silt})*(C_{silt})* - C_{total} = 0$…... (6.5)

Equation 6.5 is now a quadratic equation similar to equation 6.3 below

$0 = -ax^2 + bx + c$……………………...…………………………………......... (6.6)

Where;

$a = (C_{w}) \times (PHIE)^{m}$

$b = V_{cl}*C_{cl} + V_{silt}*C_{silt}$ (factors in equation 6.2 associated with S_w)

$c = -C_{total}$

The solution to equation 6.6 is given by the quadratic equation:

$x = \frac{-b \pm \sqrt{b^2-4ac}}{2a}$…………………………………………………...................... (6.7)

Substituting a, b and c in equation 6.7, the solution (x) for water saturation is given by equation (6.8):

$S_w = \{[-(V_{cl}*C_{cl} + V_{silt}*C_{silt}) \pm ((V_{cl}*C_{cl} + V_{silt}*C_{silt})^{2} - 4*(C_w* PHIE^{m})*(-C_t))^{1/2}]/(2*C_w \times PHIE^{m})\} + F_{corr}$ ....(6.8)

Where,

F_{corr}: Correction factor to account for using a constant n=2. This factor shift the saturation curve up or down by a constant match the NMR-calculated water saturation. There was no shift applied to water saturation results calculated using the new algorithm.

Equation 6.8 is the full water saturation equation for the J- and K-Reservoirs of Mozambique Basin.

- **Calculation of silt volume (V_{silt})**

Since the volume of silt calculated using neutron-density separation was not consistent with the volume of silt calculated using Laser Grain Size Analysis (LGSA), another method was employed to calculate the amount of silt in the J- and K-Reservoirs. The volume of silt and porosity was measured from well A15 and B12 cores. The relationship between porosity and silt for the J- and K-Reservoirs as defined by linear fit in Figures 92 and 93 is given by the following equations:

Silt Volume (J-Reservoir) = -3.0662*Porosity + 1.1073………..……. (6.9)

Silt Volume (K-Reservoir) = -3.0662*Porosity + 1.1073…… (6.10)

The relationship above was used to model the volume of silt in sections of the reservoir where core data does not exist and the results are shown in Appendices 13-18. These volumes of silt profiles were as inputs in equation 6.8 to calculated water saturation. The conductivity of the silt bound water was also estimated from the resistivity curves shown in Appendix 13-18 where, the average resistivity corresponding to the high volume of silt is taken to represent the resistivity of the silt bound water. The input parameters used in equation 6.8 are shown in Table 12 below. The conductivity ($1/R_{sh}$) of the shale (R_{sh}) was read off from the resistivity log in the shaly, top section of the reservoir (Appendices 13-17). The resistivity of the silt-bound water ranged from 0.9-1 Ohm-m, this was read off from the resistivity log in the more silt section of the reservoir.

Water Saturation Inputs (New Equation)							
Rw (Ohm-m)	**m**	**n**	**a**	**Rsh (Ohm-m)**	**Rsilt (Ohm-m)**	**Vclay**	**Vsilt**
0.0947	1.46	2	1	0.9-5	0.9-1	calculated	Modelled

Table 12: Input parameters used in the new equation to calculate water saturation (S_w).

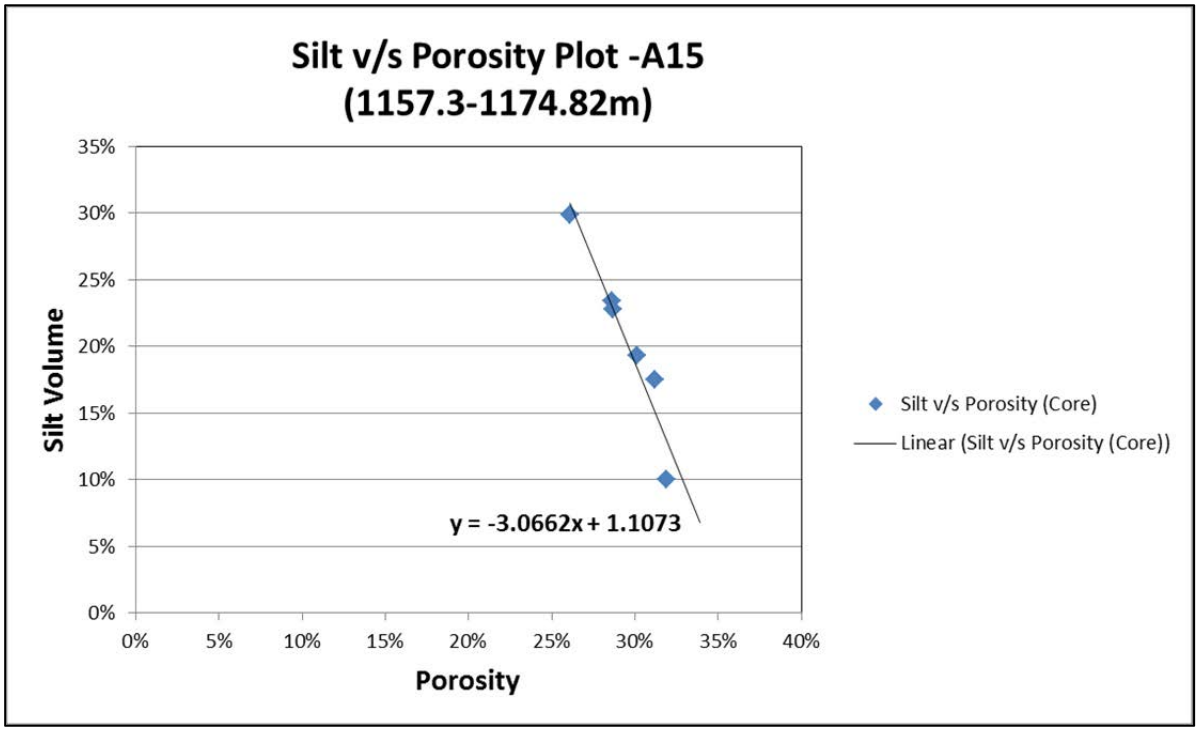

Figure 92: The volume of silt from Laser Grain Size Analysis (LGSA) plotted against core measured porosity for well A15. The linear fit to the data was used to define the relationship between porosity and the volume of silt and then used to model the volume of silt in the entire section of the J-Reservoir.

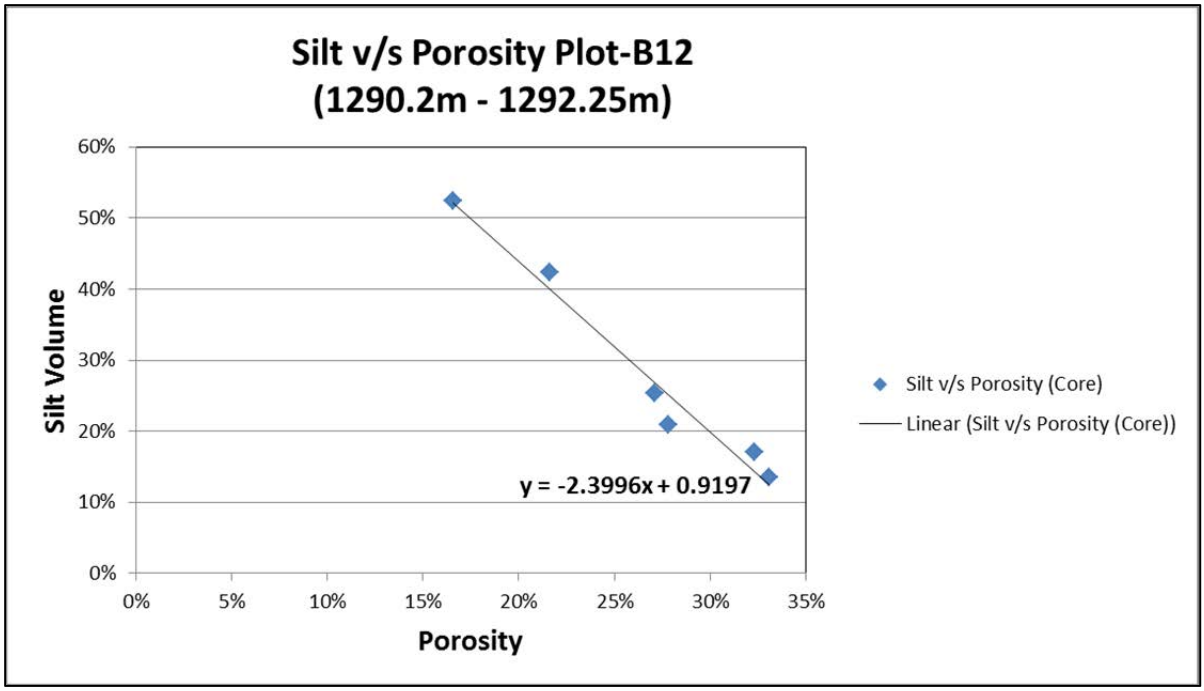

Figure 93: The volume of silt from Laser Grain Size Analysis (LGSA) plotted against core measured porosity for well A15. The linear fit to the data was used to define the relationship between porosity and the volume of silt.

- **Results: Water Saturation (S_w) Calculated from the New Equation**
-

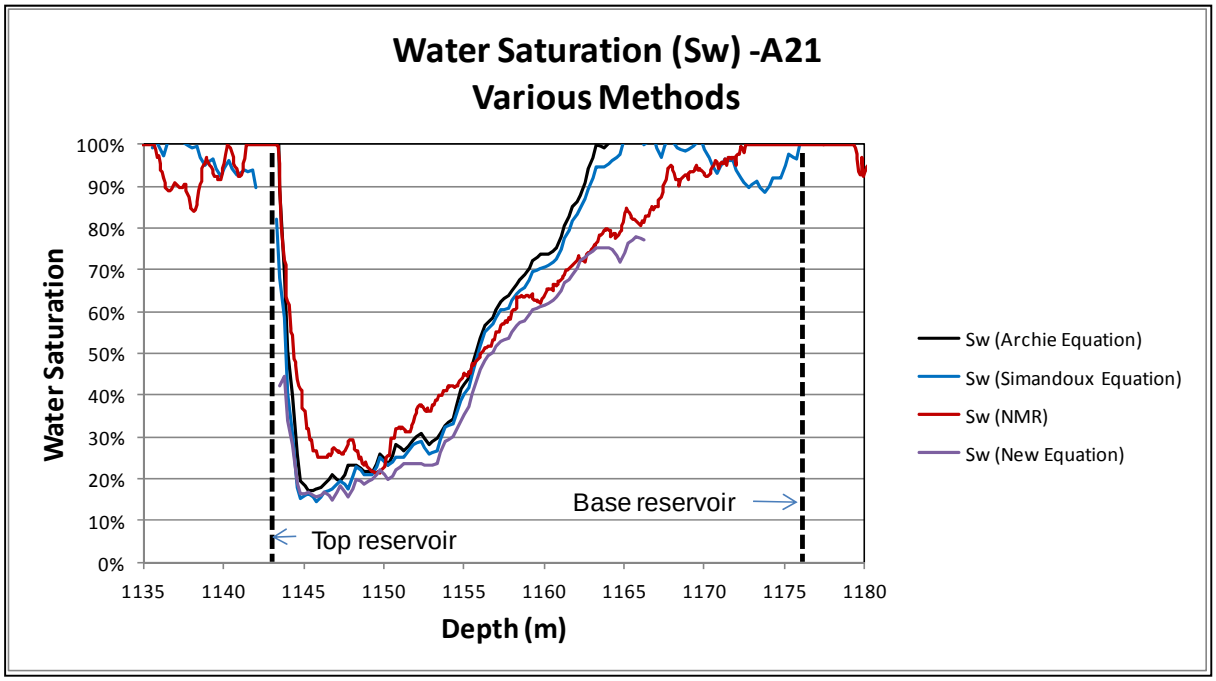

Figure 94: Water Saturation (S_w) calculated using the new method (algorithm) compared to other Archie, Simandoux and NMR-calculated water saturation, well A21 (Field A).

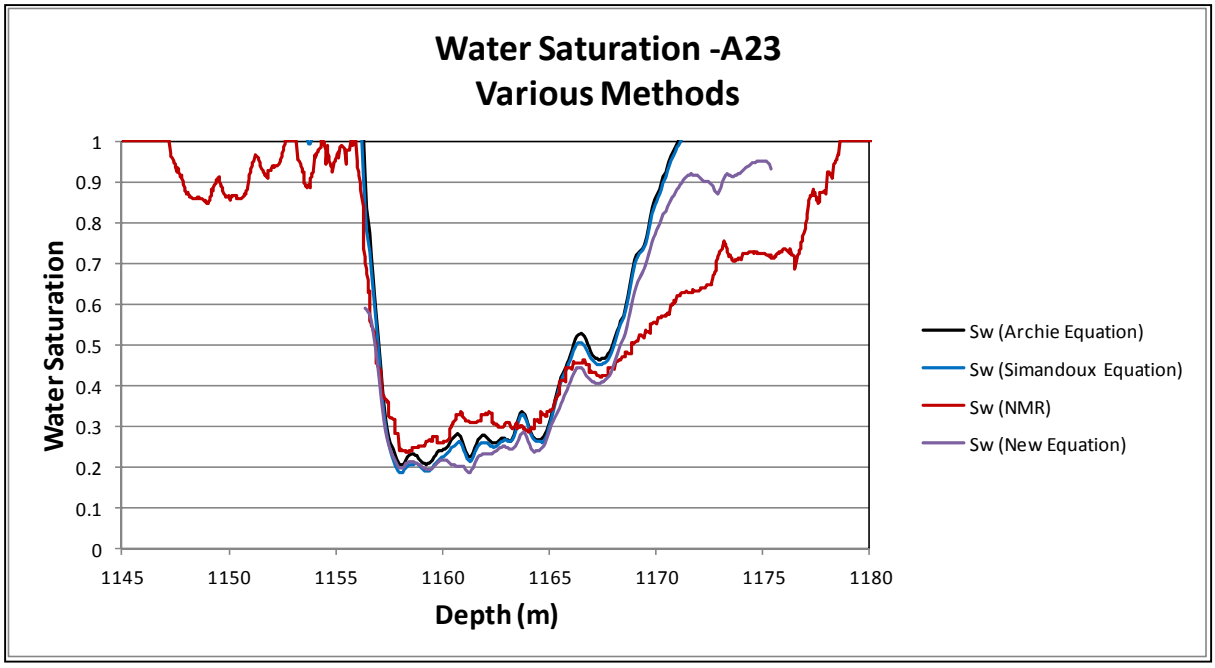

Figure 95: Water Saturation (S_w) calculated using the new method (algorithm) compared to other Archie, Simandoux and NMR-calculated water saturation, well A23 (Field A).

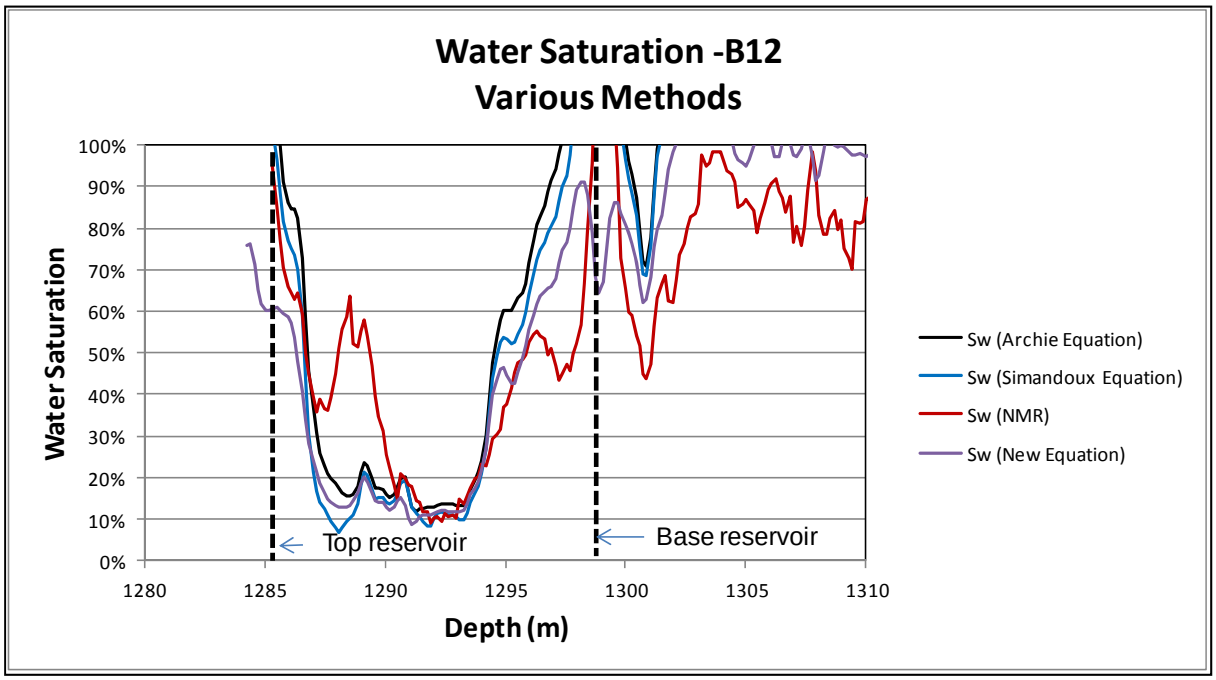

Figure 96: Water Saturation (S_w) calculated using the new method (algorithm) compared to other Archie, Simandoux and NMR-calculated water saturation, well B12 (Field B).

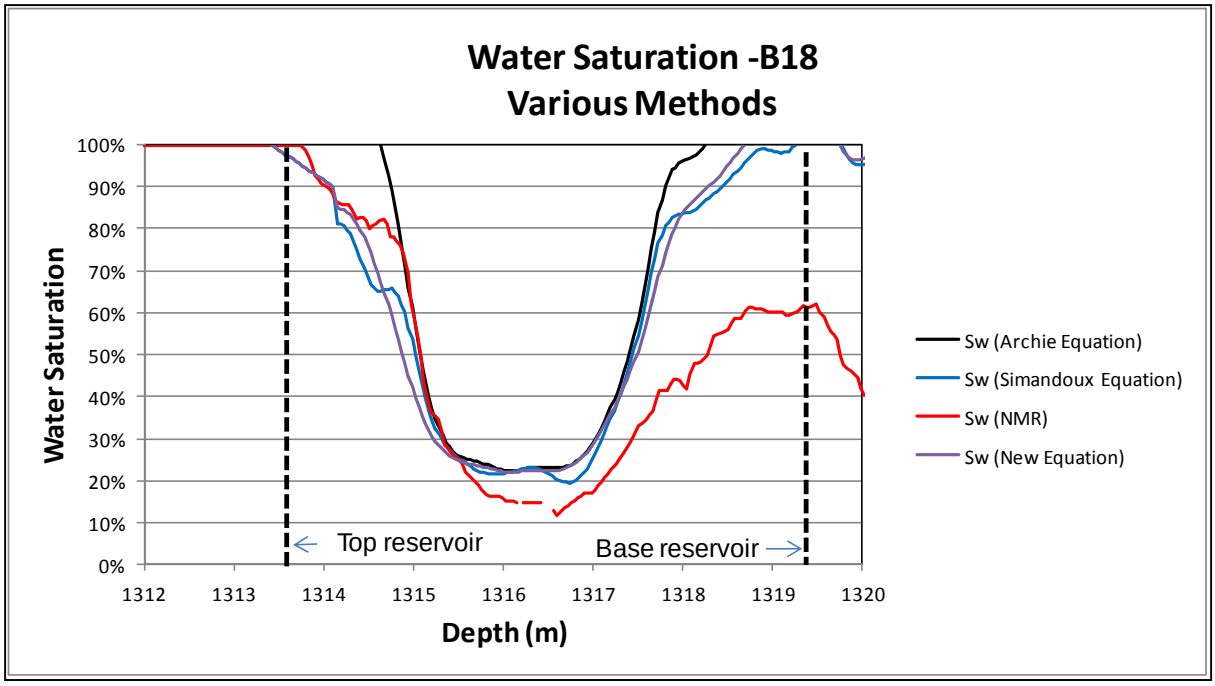

Figure 97: Water Saturation (S_w) calculated using new method (algorithm) compared to other Archie, Simandoux and NMR-calculated water saturation, well B18 (Field B).

The following shortcomings of the algorithm have been identified:

I. The algorithm becomes unstable when the effective porosity is zero, since equation 6.8 is non- divisible by zero.

II. A correction factor (F_{corr}) may have to be applied to the water saturation (S_w) to correct for the assumption that n=2 in order to solve for the quadratic equation 6.5. The correction factor shift the saturation curve up or down to match the NMR-calculated water saturation, no shift was applied to any of the water saturation results calculated using the new algorithm.

III. The volume of silt should be measured during core analysis and the relationship between core measured porosity and silt content must be established. Core samples are normally sparse and seldom cover the entire reservoir section and therefore modelling of silt content based on the relationship between silt volume and porosity has to be done.

The advantages of using the algorithm

I. The water saturation (S_w) calculated using the new algorithm yields more improved results compared to water saturation (S_w) calculated using conventional Archie and Simandoux equation.

II. The new algorithm can also be applied for more reliable and accurate water saturation (S_w) results in wells where NMR data was not acquired.

CHAPTER 7: SUMMARY OF WATER SATURATION (S_w) RESULTS

Water resistivity of the clay- and silt-bound water seems to be the major contributing factor in the inconsistencies of the water saturation calculated from conventional logs. Based on XRD and LGSA analysis, the amount of clay and silt increases towards the bottom of the J- and K-Reservoirs, this in turn, causes an increase in the amount of bound water towards the bottom of the reservoir.

Several approaches to water saturation calculation were undertaken, namely, Archie's equation, Simandoux equation and the new algorithm developed by the author. The former, which is widely used in the industry to calculate water saturation in clean, non-shaly sands, tends to overestimate the water saturation in the J- and K-Reservoirs. This method was slightly modified by using a variable cementation factor (m) instead of a constant value of (m) and the results did not show any improvements in calculating the water saturation, when compared to the results derived from a constant cementation factor (m).
The second approach was to use the Simandoux equation to calculate water saturation. This approach is applicable to shaly reservoirs and takes into account the contribution of the shale in the overall resistivity or conductivity of the reservoir. The water saturation using this equation generally yielded improved results in most wells when compared to the results derived via Archie's equation. Only one well (A23) yielded comparable results between Archie and Simandoux equations.

The third approach was to use a new algorithm developed by the author to account for the silt-bound water in addition to the clay-bound water accounted for in the Simandoux equation. This approach generally showed improved water saturation results compared to Archie and Simandoux equations, only in one well (B18) were the water saturation results from using Simandoux and the new equation were comparable. In well A21, the water saturation calculated results using the new equation were very close to the NMR-calculated water saturation.

7.1 Well Test and Gas Production

Well tests in the form of Drill Stem Tests (DST) are used in the oil and gas industry to measure the productivity or flow capability of the reservoir. Reduced to essentials, the tool measures the amount of different fluids produced in the reservoir namely gas, oil and water.

DST results from well A21 were used to analyse the amount of hydrocarbons versus water that were produced from this well during the test. Figure 98 below, displays a change in gas production over a period of time (test period) indicating that very little to no water was produced during the tests. This confirms that the water saturation as calculated using various approaches and NMR is mostly irreducible water that is bound by the grain surface area in clay and therefore cannot be produced during hydrocarbon production. Gas production data over a 24 month period also indicate very little to no water production during that period.

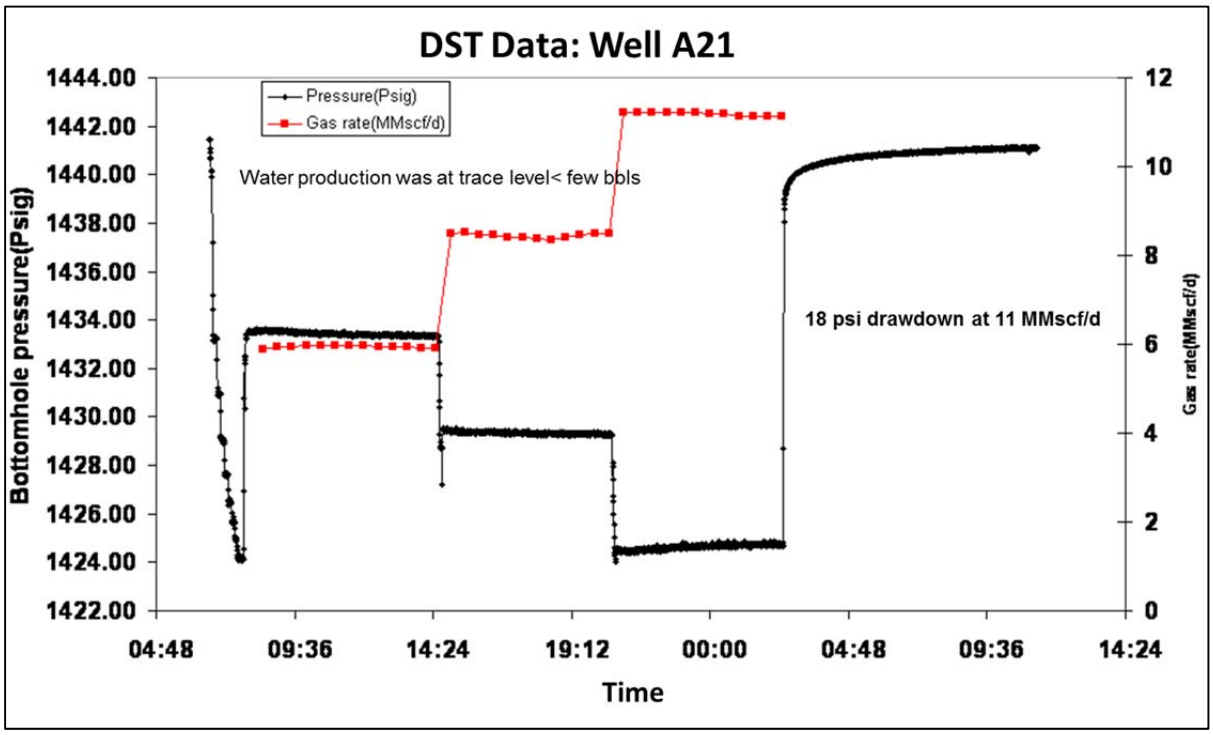

Figure 98: Drill Stem Test (DST) results from well A21. The amount of gas produced (tested) over certain time intervals is shown with water production at trace levels, i.e. less than a few barrels over the entire test.

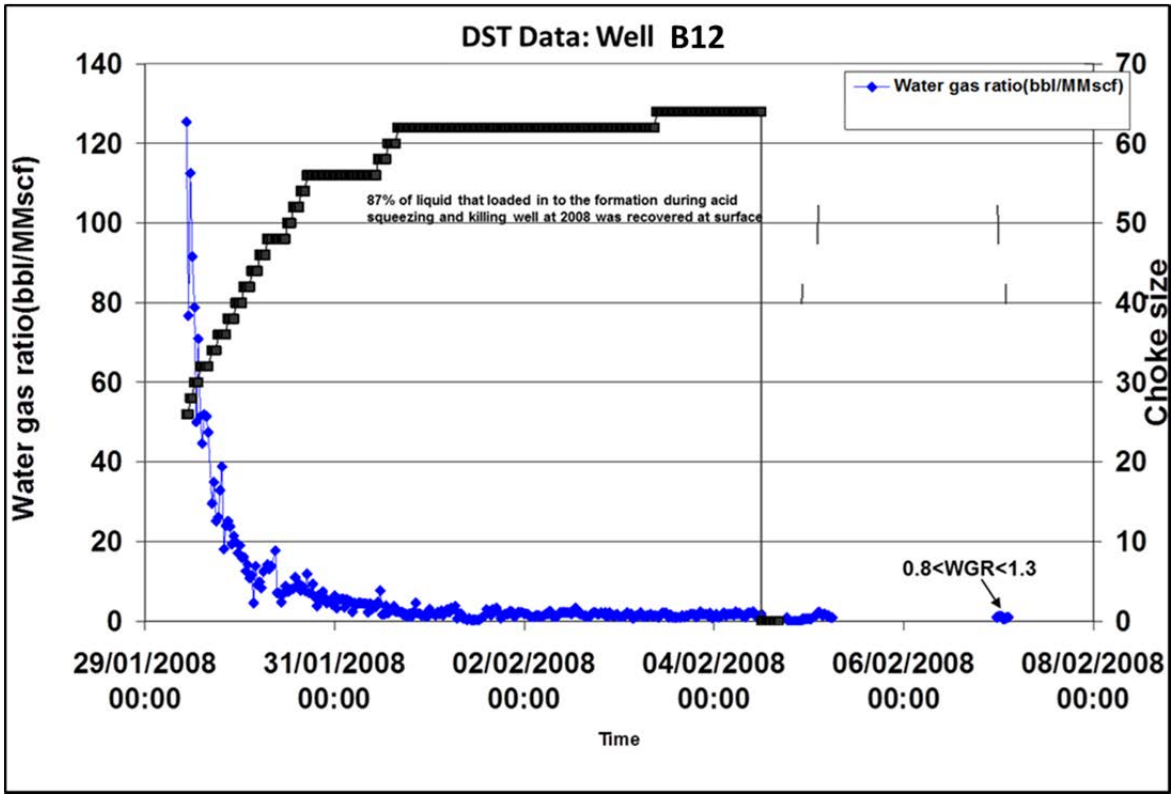

Figure 99: Drill Stem Test (DST) results from well B12. The amount of gas produced (tested) over certain time intervals is shown with water production at trace levels, i.e. less than a few barrels over the entire test.

CHAPTER 8: STUDY SUMMARY

Understanding of the cause of low-resistivity phenomena in the Mozambique Basin is very important for current and future exploration for hydrocarbons in the basin and also for better predictability of reservoir performance and the ultimate hydrocarbon recovery in the low-resistivity J - and K-Reservoirs. The possible causes of low-resistivity pay zones vary from basin to basin and are unique to each basin. In Mozambique, the reservoirs show low-resistivity phenomena and when conventional methods are used to estimate water saturations in the J- and K- Reservoirs, they give inaccurate results and the low-resistivity at the lower part of the reservoir gives high apparent water saturations (water is less resistive than oil and gas). As a result, the overall water saturation of the reservoir formation is over-estimated. These reservoirs produced only a few barrels of water during gas production based on the 24 months cumulative production data that the author has analysed. Due to

confidentiality reasons, the production data could not be presented in this study. The causes of low-resistivity in these reservoirs were investigated using available data from the study area. The data comprised static data which included seismic data, well logs and core data while dynamic data comprised production and well test data (DST).

- **Seismic data**

2D Seismic data were used mainly to map and define the outline of the two reservoirs in the case study, using amplitude extraction at the top of each reservoir. The other two data sets i.e. core and well data were empirically analysed to test the hypotheses put forward in this research.

- **Well data**

Well data were depth calibrated to core data, using the core gamma ray (GR) and the wireline log gamma ray (GR). The logs were also normalised based on the regional trends, to ensure that the outcome of the analysis is standardised across the study area. The data were then used as input to water saturation equation.

- **Core data**

Core Analysis was available in some wells and the data were used to investigate amongst other things, the relationship between cementation factor and porosity. This relationship was in turn, used to vary the cementation factor (m), which was used as an input into Archie's equation to estimate water saturation (S_w) to determine whether there would be an improvement in the accuracy of the calculated water saturation. The core data were also used to determine the depositional setting of the two reservoirs and to estimate the volume of clay and silt in these reservoirs. Thin sections were analysed to describe the textural fabric of the reservoir, grain size, grain distribution, mineralogy, and the relative abundance of minerals and clays.

- **Dynamic data**

The dynamic data comprised mainly well test data (DST) and were used to test the conclusions made from the static data analysis. For example, water saturation calculated using the Archie and Simandoux equations resulted in a significantly overestimated amount of water calculated in the formation, especially towards the base of the J-Reservoirs,

whereas production and test data indicated that the amount of water produced by these reservoirs was actually negligible.

- **Water Salinity**

In the absence of reliable water sample analysis for this study, the accurate prediction of water salinity was based on published charts. Knowing the salinity of the formation water is important since the salinity, together with the temperature affects the overall water resistivity (R_w).

- **Water Saturation (S_w) Calculations**

The following methods were used to calculate water saturation (S_w) and the results were tested against water saturations (S_w) calculated using nuclear magnetic resonance (NMR):

I. The Archie and Simandoux equations. The former is more suitable for clean non-shaly sandstones whereas the latter is more applicable to shaly reservoir sandstones. The water saturation calculated using Simandoux equation produced improved result compared to Archie's equation. However, results from both methods failed to match the water saturation derived via the NMR.

II. Using the variable cementation factor (m) into Archie's equation instead of using a constant value of (m), as is commonly the practice yielded better results. Even though this technique has been used elsewhere, in other basins, the empirical relationship between porosity and cementation factor developed in this research study is unique to the J and K-Reservoirs of Mozambique Basin. The results for water saturation using this method (variable m) were generally less accurate than the saturation calculated using the constant cementation factor (m) in Archie's equation.

III. Since the relationship between the saturation factor (n) and any of the reservoir parameters could not be established, the utilisation of the variable (n) to calculate water saturation was not pursued further.

IV. Modelling the resistivity log from the sonic log was based on the fact that both, the sonic and the resistivity logs, are depended on lithology and on total porosity. The author argued that if the sonic log is not affected by the same factors that cause low resistivity values in the acquired resistivity log, then the resistivity modelled from the sonic log would yield values that are representative and consistent with resistivity values in the "normal-resistivity"

reservoirs. The modelling yielded poor results within the reservoir section and the method was not pursued further.

V. The new method developed by the author to calculate water saturation in the J- and K-Reservoirs, generally yielded improved results compared to Archie and Simandoux equation. In some wells, the results from the new method were comparable to the results from Simandoux equation.

CHAPTER 9: CONCLUSIONS AND SCIENTIFIC CONTRIBUTIONS OF THE STUDY

A significant scientific contribution has been made by the present study towards the understanding of the low-resistivity gas reservoirs of the Mozambique Basin. The below section summarises the conclusions and contributions of the study:

- **The cause(s) of low-resistivity pay zones**
  - I. The reservoir texture and grain size, as well as its mineral composition, control the amount of bound water in the reservoir. The relationship between decreasing grain size and an increase in the amount of irreducible water saturation S_{wirr} has been demonstrated for the J- and K-Reservoirs of the Mozambique Basin in this thesis.
  - II. The type of clay minerals present in both the J- and the K-Reservoirs, which includes mixed layers of smectites and illites that are known to expand to about 95% of their original volume, contributes to an increase in clay-bound water within these reservoirs. Conductive minerals such as pyrites were present only in small quantities in both reservoirs and do not have any measurable effect on the conductivity of the reservoir.
  - III. The presence of cements such as carbonates and the alteration of feldspar grains to clay increase the microporosity and thus, the amount of bound water in the reservoir, further influencing the conductivity through increased amount of irreducible water.
  - IV. Small quantities of chlorite contribute to moderate increase in surface area of clay minerals and thus to the amount of bound water.

- **The calculation of Water Saturation (S_w)**

I. The use of the resistivity log, as modelled from the sonic log, has been shown not to represent the true resistivity of the reservoir formation and cannot be applied as an alternative to the log acquired resistivity data, to improve water saturation calculations.

II. The Simandoux equation, which takes into account the resistivity of the shale- bound water, gives better water saturation results than Archie's equation which is more suitable to clean non-shaly sands.

III. The new equation, which separates the contribution of the clay-bound and the silt-bound water to the overall resistivity of the resistivity of the reservoir, gives better water saturation results than Archie's equation which is more suitable to clean non-shaly sands. The equation generally yield improved results compared to Simandoux although in some wells, the results from the two methods are comparable.

IV. The calculated water saturation using all the different is mostly bound, irreducible water saturation that cannot be produced during gas production as demonstrated by the results of the drill stem test (DST) in the J- and K-Reservoirs.

REFERENCES

Publications and Reports

Archie, G.E., 1942. The electrical resistivity log as an aid in determining some reservoir characteristics. Trans AIME 146, pp. 54-62.

Armitage, S.J., Botha, G.A., Duller, G.A.T., Wintle, A.G., Rebelo, L.P., and Momade, F.J., 2006.The formation and evolution of the barrier islands of Inhaca and Barazuto, Mozambique. Geomorphology 82, pp 295-308.

Bahr, E.M., Patchett, J.G., Wiley, R., 1993. Modelling the effects of glauconite on some open-hole logs from the Lower Senonian in Egypt. Society of Petrophysicists and Well log Analysts. SPWLA 34, Annual Logging Symposium.

Bailey, E.H., Stevens, R.E., 1960. Selective staining of K-feldspar and plagioclase on rock slabs and thin sections. American Mineralogist 45, pp 1020 -1025.

Bassiouni, Z., 1994. Theory, measurement and interpretation of well Logs. SPE Textbook Series Vol.1.

Bergh, H.W., 1977. Mesozoic sea-floor off Dronning Maud Land, Antarctica. Nature 269, pp 686-68.

Bernard, A., Munschy, M., Rotstein, Y., Sauter, D., 2005. Refined spreading history at the Southwest Indian Ridge for the last 96 Ma, with the aid of satellite gravity data. Geophysical Journal International 162, pp 765–778.

Boyd, A., Darling, H., Tabanou, J., Davis, B., Lyon, B., Flaum, C., Klein, J., Sneider RM., Sibbit, A., and Singer, J., 1995. The low down on low-resistivity pay. Oilfield Review.

Coates, G.R., Xiao, L., and Prammer, G.M., 1999. NMR logging principles and applications. Halliburton Energy Services.

Coster, P.W., Lawrence, R., and Fortes, G., 1989. Mozambique: A new framework for hydrocarbon Exploration. Journal of Petroleum Geology 12, 2, pp 205-230.

Courtillot, V., Jaupart, C., Manighetti, I., Tapponnier, P., Besse, J., 1999. On causal links between flood basalts and continental breakup. Earth and Planetary Science Letters 166, pp 177-195.

Cox, K.G., 1992. Karoo igneous activity, and the early stages of the break-up of Gondwana. In: Storey, B.C., Alabaster, T., and Pankhurst, R.J. (Eds), magmatism and the causes of continental break-up. Spec. Publication, Geological Society Special Publication, 68, pp 137-148.

Cox, K.G., 1970. Tectonic and volcanism of the Karoo period and their bearing on the postulated fragmentation of Gondwanaland. African Magmatism and Tectonics. Oliver and Boyd, Edinburgh, pp 211 – 235.

Cox, K.G., and Bristow, J.W., 1984. The Sabie River basalt formation of the Lebombo Monocline and Southeast Zimbabwe. Geological Society of South Africa 13, pp 125-147.

Daly, M.C., Chorowicz, J., and Fairhead, J.D., 1996. Rift basin evolution in Africa: The Influence of reactivated steep basement shear zones. Journal of African Earth Sciences 23, 1, pp 3-15.

Diaz, E., Prasad, M., Mavko, G., and Dvorkin, J., 2003. Effect of glauconite on elastic properties, porosity and permeability of reservoir rocks. The Leading Edge 22, pp 42-45.

Ditzhuijzen, P., 1994. Petrophysics: In touch with the reservoir. Shell International Petroleum Company.

Duncan, R.A., Hooper, P.R., Rehacek, J., Marsh, J.S., Duncan, A.R., 1997. The timing and duration of the Karoo igneous event, Southern Gondwana. Journal of Geophysical Research Issue 102 (B8), 18, 138, pp 127-18.

Du Toit, A.L., 1937. Our wondering continents. Oliver & Boyd, Edinburgh.

ENH-ECL., 2000. The petroleum geology and hydrocarbon prospectivity of Mozambique Open Report, Vols. 1 and 2.

Faust, L.Y., 1953. A velocity function including lithological variation: Geophysics, 18, 2, pp 271-288.

Filbrandt, J.B., Smith, R., 1990. Assessment of hydrocarbon potential, Cretaceous plays, SW Onshore Mozambique. Shell International Petroleum Maatschappij. The Hague,EP 90-2270.

Fitch, F.J., and Miller, J.A., 1984. Dating Karoo igneous rocks by conventional K-Ar and 40Ar/39Ar age spectrum methods in petrogenesis of the volcanic rocks of the Karoo Province. Ed.A.J. Erlank Spec.Publ. Geol. Soc 13, pp 247-266.

Flores, G., 1970. Suggested origins of Mozambique Channel. Transactions of Geological Society of South Africa, issue 73, pp 1-16.

Flores, G., 1973. The Cretaceous and Tertiary sedimentary basins of Mozambique and Zululand, Sedimentary basins of the African coasts. Association of African Geological Surveys, Paris, pp 81-11.

Gerard, J. and Bromley, R., 2008. Ichnofabric in clastic sediments 1st Edition. Jean R.F. Gerard.

Goudie, A.S., 2005. The drainage of Africa since the Cretaceous. ScienceDirect, Geomorphology 67, pp 437-456.

Grantham, G.H., Groenewald, P.B. and Hunter, D.R., 1988. Geology of the northern H.U. Sverdrupfjella, western Dronning Maud Land and implications for Gondwana reconstructions. South African Journal of Antarctic Research 18, pp 2-10.

Gwavava, O., Swain, C.J., Podmore, F., and Fairhead, J.D., 1992. Evidence of crustal thinning beneath the Limpopo Belt and Lebombo Monocline of Southern Africa based on regional gravity studies and implications for the reconstruction of Gondwana. Tectonophysics, 212, pp 1-20.

Hacikoylu, P., Dvorkin, J., and Mavko, G., 2006. Resistivity-velocity transform revisited. The Leading Edge, pp 1006-1009.

Haddon, I.G., McCarthy, T.S., 2005. The Mesozoic–Cenozoic interior sag basins of Central Africa: The Late-Cretaceous–Cenozoic Kalahari and Okavango basins. Journal of African Earth Sciences 43 pp 316–333.

Hales, A.L., 1960. Research at the Bernard Price Institute of Geophysical Research, University of Witwatersrand, Johannesburg, Proceedings of the Royal Society of London, Series A, Mathematical and Physical Sciences, 258, 1292, pp 1-26.

Hamada, G.M., Al-Blehed., and Al-Awad M.N.J., 2000. Nuclear Magnetic Resonance log evaluation of low-resistivity sandstone reservoirs bypassed by conventional logging analysis. SPE Asia Pacific Oil and Gas Conference and Exhibition, Brisbane Australia SPE 64406.

Hamada, G.M., and Al-Awad, M.N.J., 2002. Evaluation of low-resistivity beds using nuclear magnetic resonance log. Engineering Science 14, pp 47-61.

Heirtzler, T.R., Burroughs, R.W., 1971. Madagascar's palaeo-position: New data from Mozambique Channel. Science, 174, pp 488-490.

Howard, J.D. and Reineck, H.E., 1981. Depositional facies of high-energy beach-to-offshore sequence: comparison with low-energy sequence: Am. Assoc. Petroleum Geologists Bull 65, pp 807-830.

Hossain, Z., Mukerji, T., Dvorkin, J., and Fabricius I.L., 2011. Rock physics model of glauconite greensand from the North Sea. Geophysics 76, 6, pp 199-209.

International Finance Corporation (IFC)., 2012. The Future of Natural Gas in Mozambique: Towards a Gas Master plan. IFC International, 9300 Lee Highway, Fairfax, VA 22031. Interactive Petrophysics (IP) Interpretation Software (version3.5). Synergyworld Inc.

James, D.E., Niu, F., and Rokosky, J., 2003. Crustal structure of the Kaapvaal Craton and its significance for early crustal evolution. Lithos 71, pp 413-429.

Johnson, M.R., Van Vuuren, C.J., Hegenberger, W.F., Key, R., and Show, U., 1996. Stratigraphy of the Karoo Super-group in Southern Africa: An Overview. Jour. African Earth Sci 23, pp 2-15.

Kieke, E. M., and Hartman, D.J., 1974. Detecting microporosity to improve formation evaluation. Journal of Petroleum Technology 26, 10, pp 1080-1086.

Kingston, D.R., Dishroon, C.P., and Williams, P.A., 1983. Global basin classification. Am. Assoc. Petroleum Geologists Bull 67, 12, pp 2175-2193.

Klein, J. D., 1993. Induction log anisotropy corrections. The Log Analyst 34, pp 18–27.
Klein, J. D., Martin, P. R., and Allen, D. F., 1997. The Petrophysics of Electrically Anisotropic Reservoirs. The Log Analyst, 38, pp 25–36.
KPMG report, 2013. Oil and gas in Africa: Africa's reserves, potential and prospects. KPMG Africa Limited, a Cayman islands company.
König, M., Jokat, W., 2006. The Mesozoic breakup of the Weddell Sea. Journal of Geophysical Research 111, B12102.
König, M., Jokat, W., 2010. Advanced insights into magmatism and volcanism of the Mozambique Ridge and Mozambique Basin in the view of new potential field data. Geophysical Journal International 180, 1, pp 158-180.
Lawver, L., Gahagan, L.M., Dalziel, I.W.D., 1991. Continental break-up and tectonic evolution. Nato Advanced Study Institute, 'Dynamic Modelling and Flow in The Earth and Planets', Alaska, Abstracts volume 1991a.
Lawver, L., Royer, J.Y., Sandwell, D.T., Scotese, C.R., 1991. Evolution of the Antarctic continental margins. In: Thomson, M.R.A., Crame, J.A., Thomson, J.W. (Eds.), Geological Evolution of Antarctica. Cambridge University Press, New York, pp 533-540.
Leinweber, V.T., Jokat, W., 2011. Is there continental crust underneath the Northern Natal Valley and the Mozambique Coastal Plains?. Geophysical Research Letters 38, L14303.
Leinweber, V.T., Jokat, W., 2012. The Jurassic history of the Africa–Antarctica corridor: new constraints from magnetic data on the conjugate continental margins. Tectonophysics, pp 530-531.
Log Interpretation Charts, 2009. Schlumberger well services, Houston.
Mahumane, G., Mulder, P and Naudad, D., 2012. Energy Outlook for Mozambique 2012. 2030 LEAP based scenarios for energy demand and power generation. Instituto de Estudos Sociais economicos (IESE) Conference.
Mahanjane, E.S., 2012. A geotectonic history of the northern Mozambique basin including the Beira high- A contribution for the understanding of its development. Marine and Petroleum Geology 36, pp 1-12.
Martin, A.K., 2007. Gondwana Breakup via double-saloon-door rifting and sea-floor spreading in a back-arc basin during subduction rollback. ScienceDirect. Tectonophysics 445, pp 245-272.
Matthews, A., Lawrence, S.R., Mamad, A.V., Fortes, G., 2001. Mozambique basin may have a bright future under new geological Interpretation. Oil and Gas Journal, 99, 27, pp 70-75.
Moore, A.E., Larkin, P.A., 2001. Drainage Evolution in South-Central Africa since breakup of Gondwana. South African Journal of Geology 104, 1, pp 47-68.
Omni Laboratories, Inc., 2007. Mozambique, well report Volume 1, Houston, TX Omni File No.: H-30691.
Pemberton, G.S., 2001. Using trace fossils in reservoir characterization: Ichnogenera and Ichnofacies and their influence on permeability fabrics and reservoir performance. AAPG Annual Meeting Program with abstracts.
Petricola, M.J.C., and Watfa, M., 1995. Effect of microporosity in carbonates: Introduction of a versatile saturation equation. Society of Petroleum Engineers.
Reeves, C., De Wit, M., 2000. Making ends meet in Gondwana: retracing the transforms of the Indian Ocean and reconnecting continental shear zones. Terra Nova 12, pp 272–280.
Rudman, A.J., Whaley, J.F., Blakely, R.F., and Biggs, M.E., 1976. Transformation of resistivity to pseudo-velocity logs. Log Analyst.
Salman, G., and Abdula, I., 1995. Development of the Mozambique and Ruvuma Sedimentary basins, offshore Mozambique. Sedimentary Geology 96, Elsevier Science BV 96, pp 7-41.
Schlumberger Limited, 1991. Log interpretation principles and applications. Schlumberger Educational Services, Technology and & Mining.
Schon, J. H.,Yu, L., Georgi,D. T., and Fanini,O., 2000. Aspects of multi-component
resistivity data and macroscopic resistivity anisotropy. Ann. Tech. Conf., Soc. Petr. Eng., Proceedings, paper SPE 62909.

Shier, D.E., 2004. Well log normalization: methods and guidelines. Petrophysics, 45, pp 268-280.
Simandoux, P., 1963. Dielectric measurements on porous media: Application to the measurements of water saturations: Study of the behaviour of argillaceous formations. Revue de I' Institut Francais du Petrole 18, Supplementary issue, pp 193-215 (Translated text in Shaly Sand Reprint Volume, SPWLA, Houston, pp 97-124).
Simpson, E.S.W., Sclater, J.G., Parsons, B., Norton, I., Meinke, L., 1979. Mesozoic magnetic lineation in the Mozambique Basin. Earth and Planetary Science Letters 43 (1919), 260-264. Elsevier Scientific Publishing Company, Amsterdam.
Swanson, B.F., 1985. Microporosity in reservoir rocks: Its measurements and Influence on electrical resistivity. The Log Analyst.
Thomas, E.C., and Stieber, S.J., 1975. The distribution of shale in sandstones and its effect upon Porosity. SPWLA, 16th Annual Logging Symposium Transactions.
Thomas, D.S.G., Shaw, P., 1991. The Kalahari environment. Cambridge University Press, Cambridge.
Tiab, D., and Donaldson, E.C., 2004. Petrophysics 2nd Edition, Theory and practice of measuring reservoir rocks and fluid transport properties. Gulf Professional Publishing.
Tixier, M.P., Morris, R.L., and Cornell, J.G., 1968. Log evaluation of low-resistivity pay sands in the Gulf coast. The Log Analyst 9, pp 3-20.
Walford, H.L., White., N.J., Sydow, J.C., 2005. Solid sediment load of the Zambezi. Earth and Planetary Science Letters, pp 49-63.
Wellington, J.H., 1955. Southern Africa : A geopgraphic study. Physical geography. Cambridge University Pres, UK 1, pp 528.
Williams, J., Arsenault, M.A., Buczkowski, B.J., Reid, J.A., Flocks, J.G., Kulp., M.A., Penland, S., Jenkins, C., 2011. Superficial sediment character of the Louisiana offshore continental shelf region. Wentworth grain size chart from United States Geological Survey Open-file report 2006-1195.
Worthington, P.F.,2000. Recognition and evaluation of low-resistivity pay. Petroleum Geoscience 6, pp 77-92.
White, H. J., R. A. Skopec, F. A. Ramirez, J. A. Rodas, and G. Bonilla., 1995. Reservoir characteristics of the Hollin and Napo formations, western Oriente basin, Ecuador, *in* A. J. Tankard, R. Suárez S., and H. J. Welsink, Petroleum basins of South America: AAPG Memoir 62, pp 573–596.
Wyllie, M.R.J., Gregory, A.R., and Gardner, L.W., 1956. Elastic wave velocities in heterogeneous and porous media. Geophysics 21, pp 41-70.
Zemanek, J., 1989. Low-resistivity hydrocarbon-bearing sand reservoirs. SPE Formation Evaluation 4, pp 515-521.

Courses and websites

Baker Hughes Oil Services presentation (2007, 2012): www.bakerhughes.com
Department of Energy of South Africa, www.energy.gov.za
Department Geology, University of Wyoming: www.gg.uwyo.edu
Instituto de estudos sociiasis e economicos (IESE) study (2012): www.iese.ac.mz
Petrophysics Lecture Notes: www.petrophysics.net
Sasol: www.sasol.com
Stocks, A.: Well Log Interpretation Short Course, ECL, Cape Town, May 2003
Taha, A.: Basics of Petrophysical Analysis Short Course, RPS, Johannesburg, South Africa, February 2010
United Nations Development Programme (UNDP): www.undp.org
Watfa, M.: Advanced Formation Evaluation Short Course, Schlumberger, Cape Town, South Africa, 2012
Weatherford open-hole logging tools: www.weatherford.com

APPENDIX

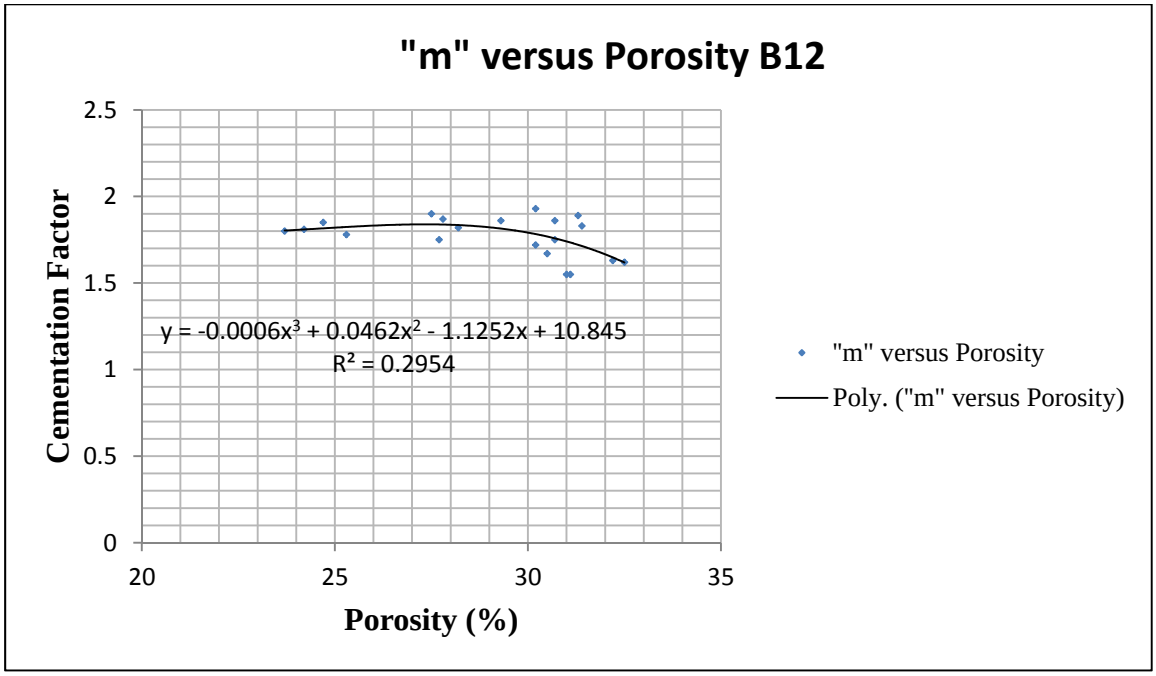

Appendix 1: Cementation factor (m) versus porosity for well B12 on a non-logarithmic scale. The empirical relationship yields poor results for saturation estimates.

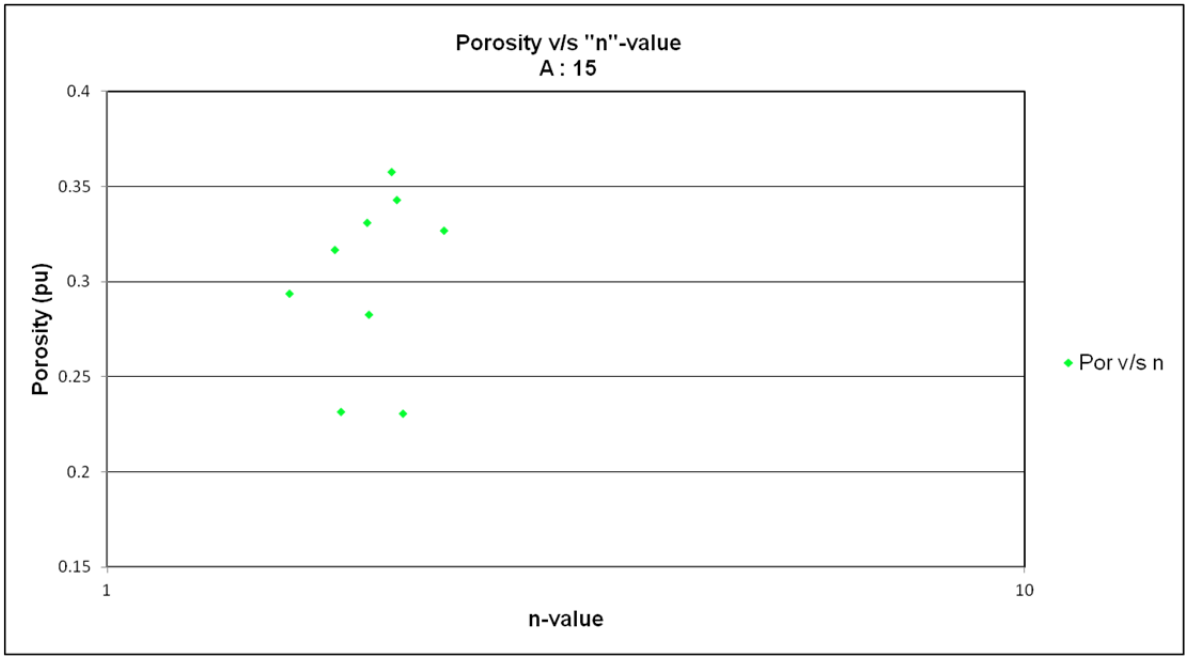

Appendix 2: Porosity versus n-value for well A15. No apparent relationship between the porosity and saturation factor (n).

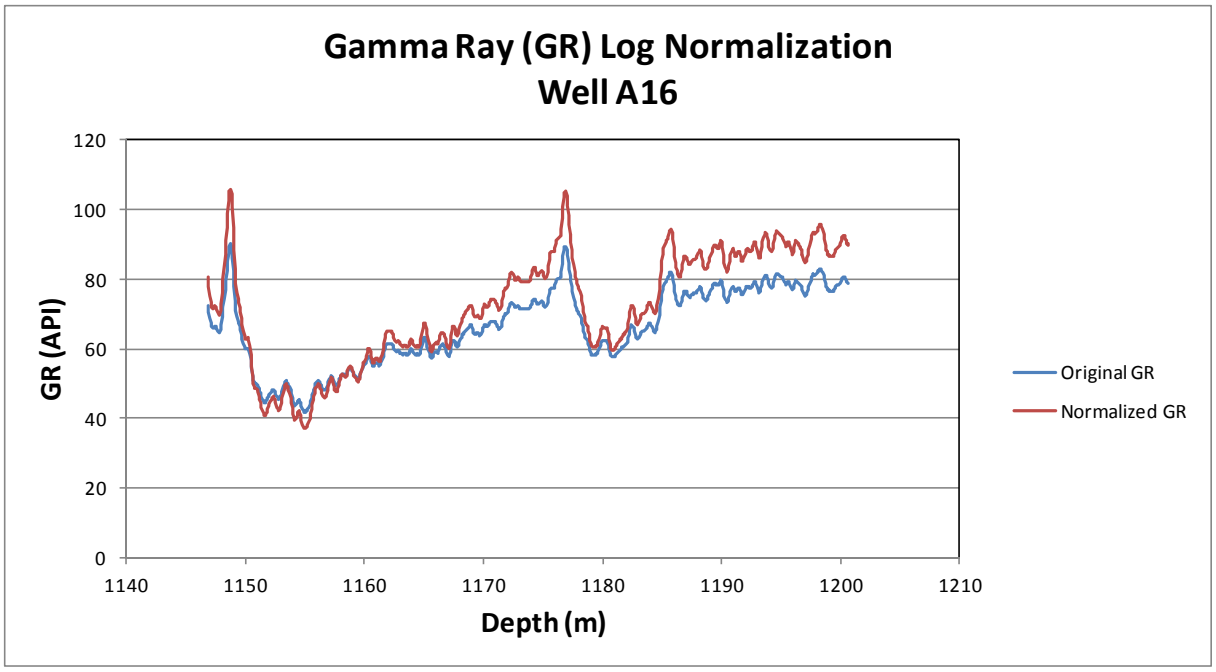

Appendix 3: Gamma ray log normalization for well A16 of the J-Reservoir (Field A).

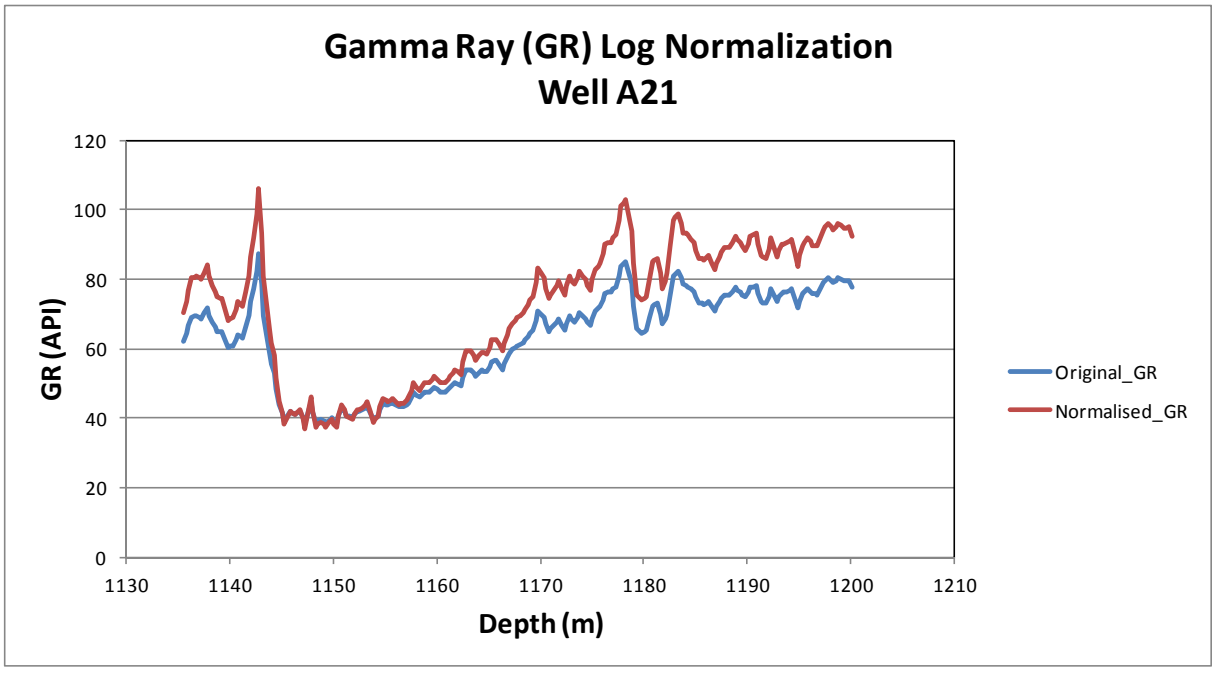

Appendix 4: Gamma ray log normalization for well A21 of the J-Reservoir (Field A).

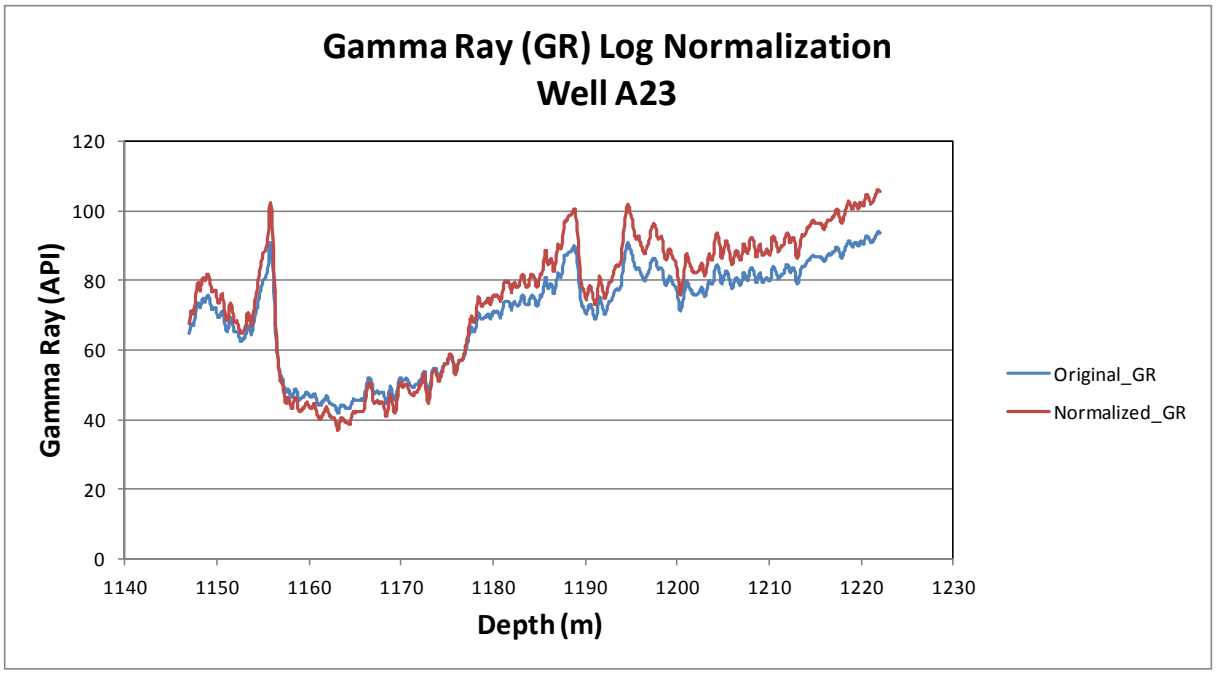

Appendix 5: Gamma ray log normalization for well A23 of the J-Reservoir (Field A).

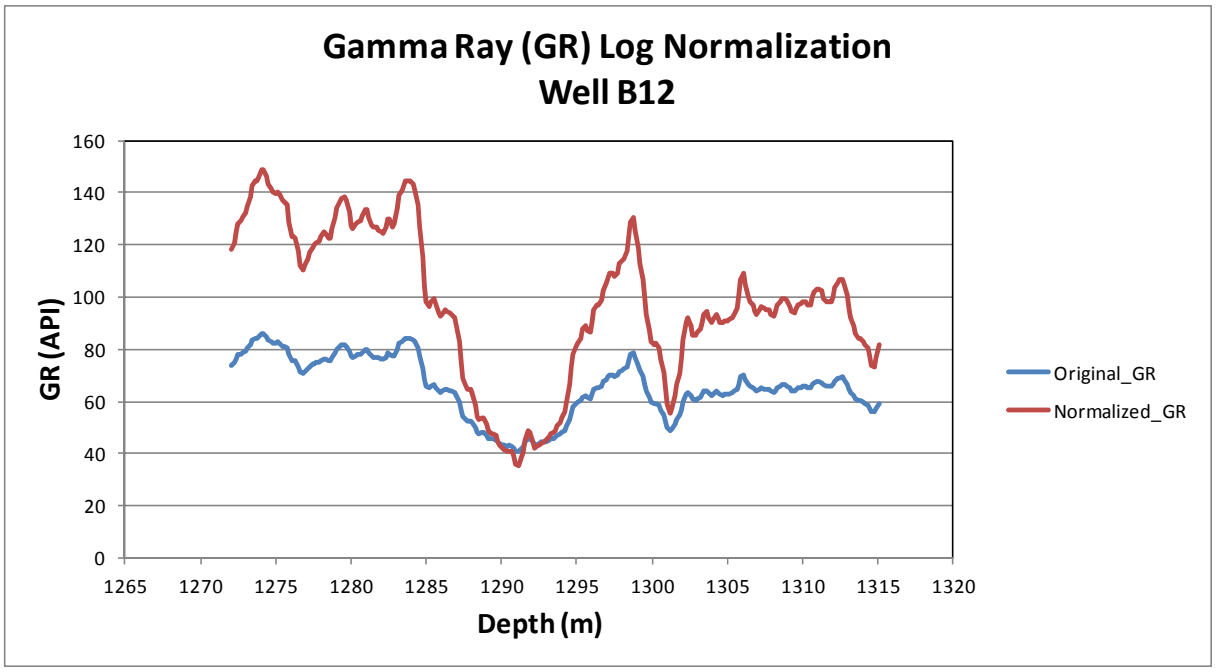

Appendix 6: Gamma ray log normalization for well B12 of the K-Reservoir (Field B).

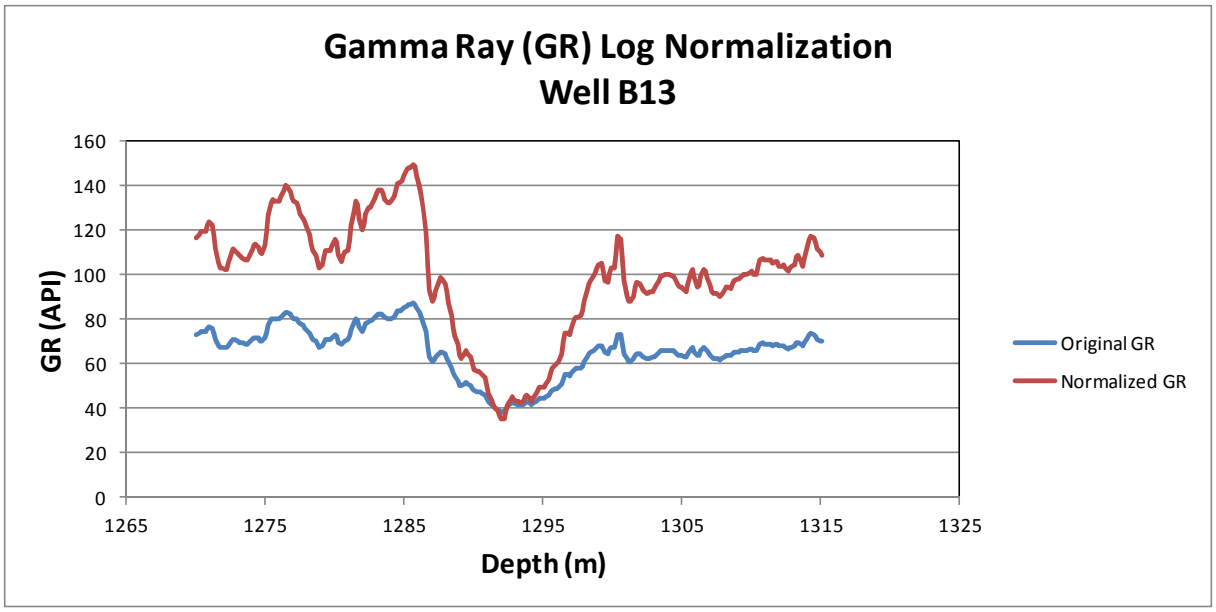

Appendix 7: Gamma ray log normalization for well B13 of the K-Reservoir (Field B).

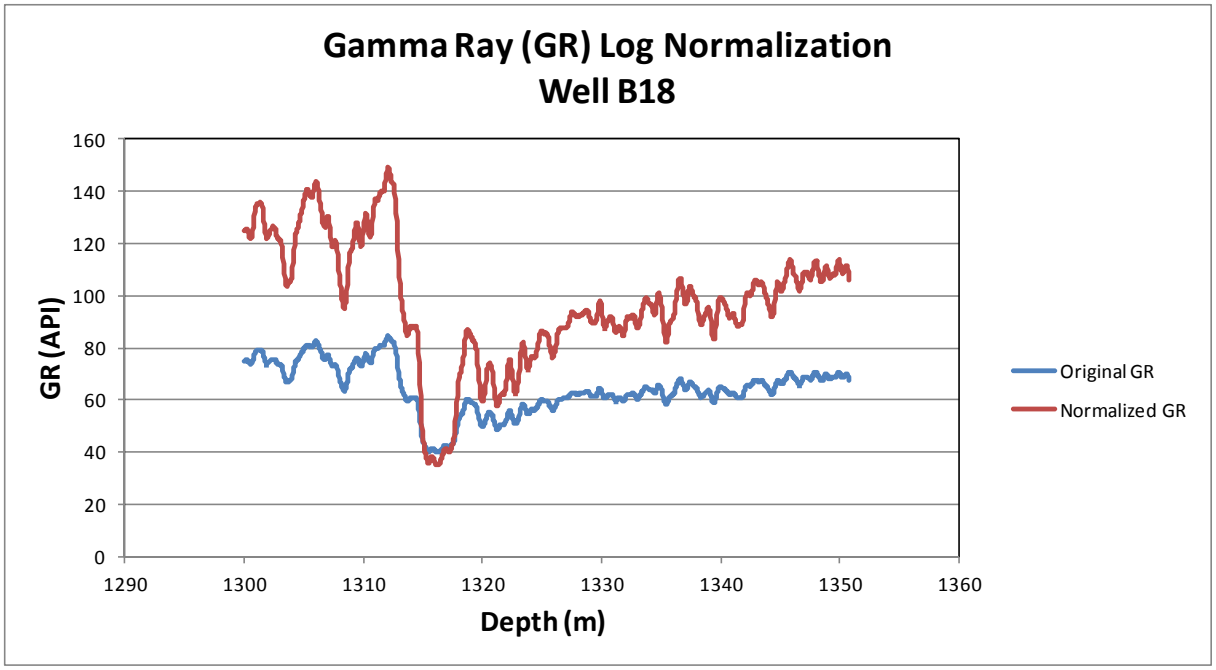

Appendix 8: Gamma ray log normalization for well B18 of the K-Reservoir (Field B).

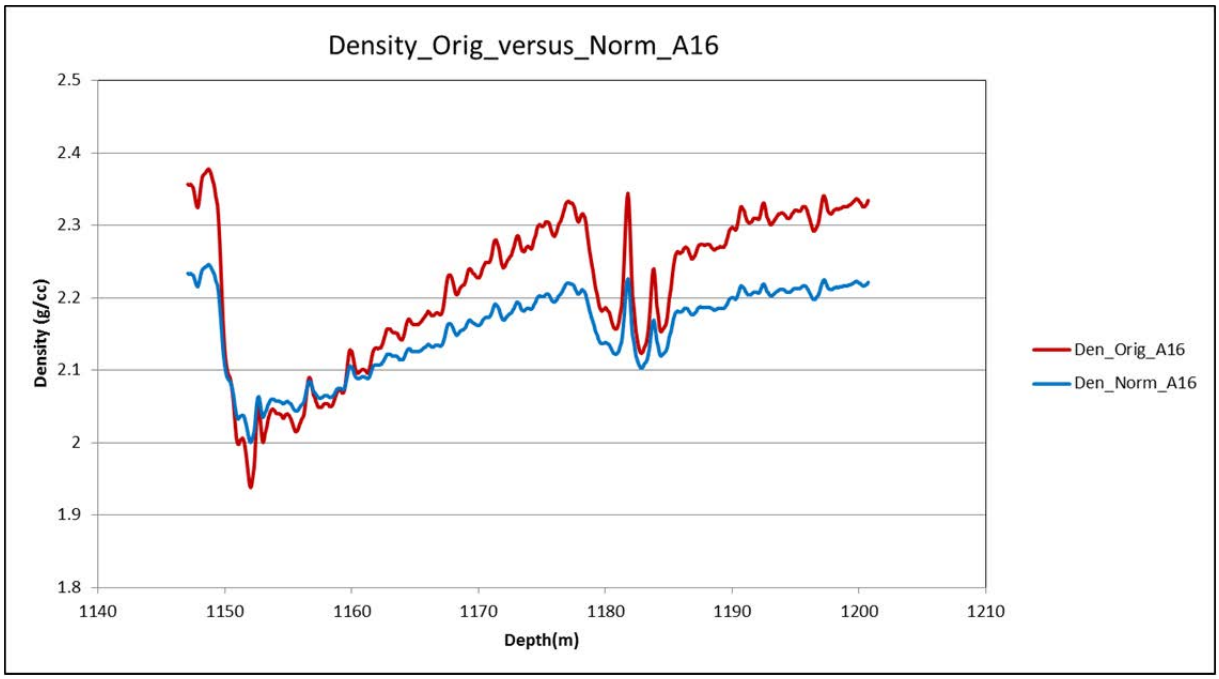

Appendix 9: Density log normalization for well A16 of the J-Reservoir (Field A).

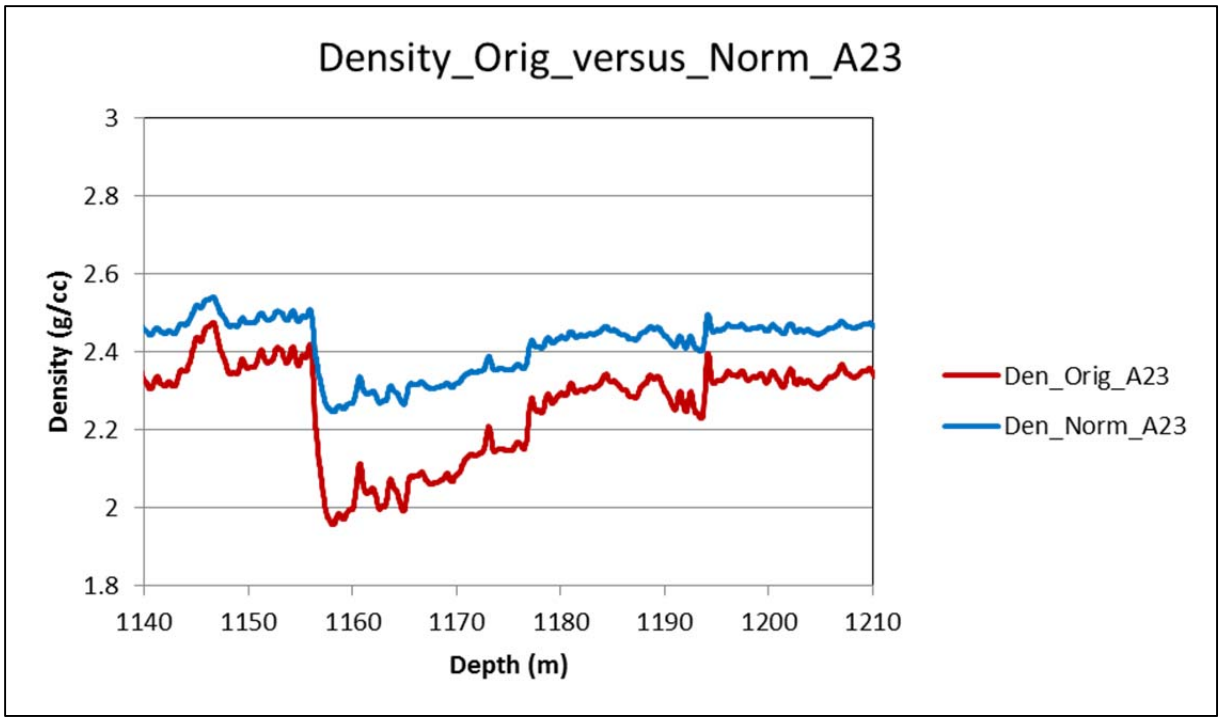

Appendix 10: Density log normalization for well A23 of the J-Reservoir (Field A).

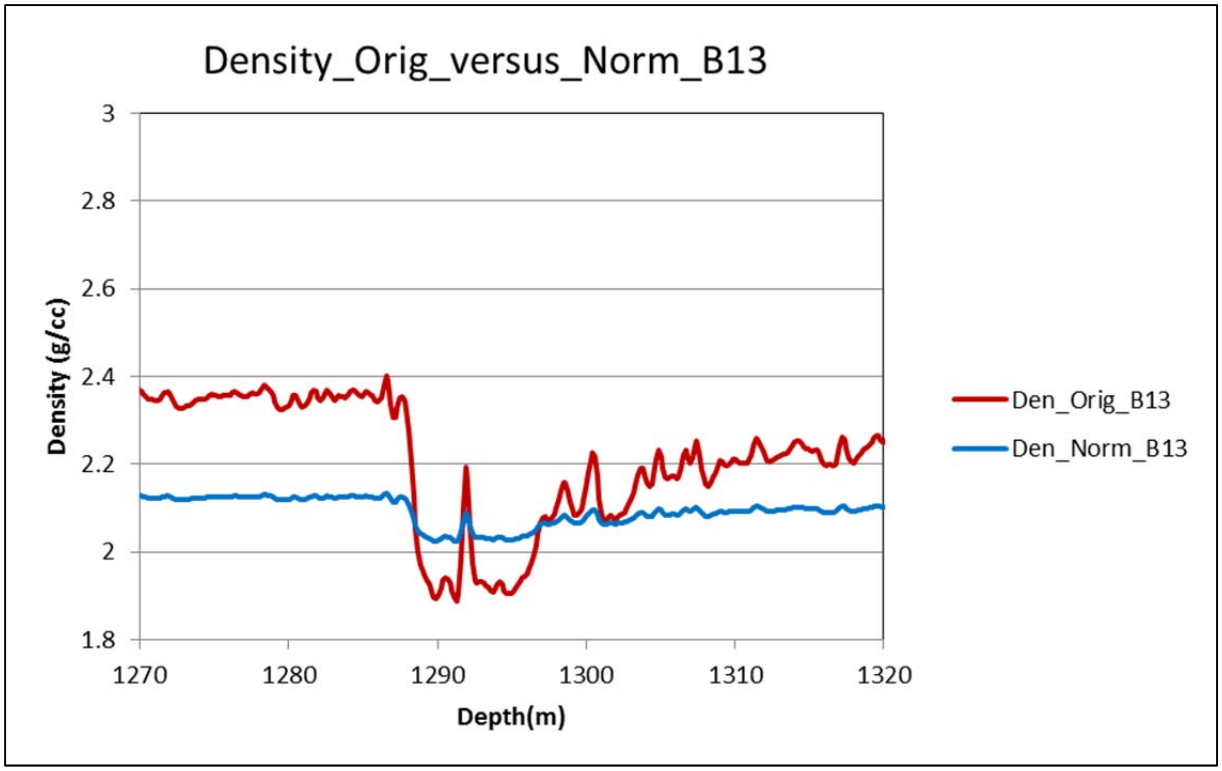

Appendix 11: Density log normalization for well B13 of the K-Reservoir (Field B).

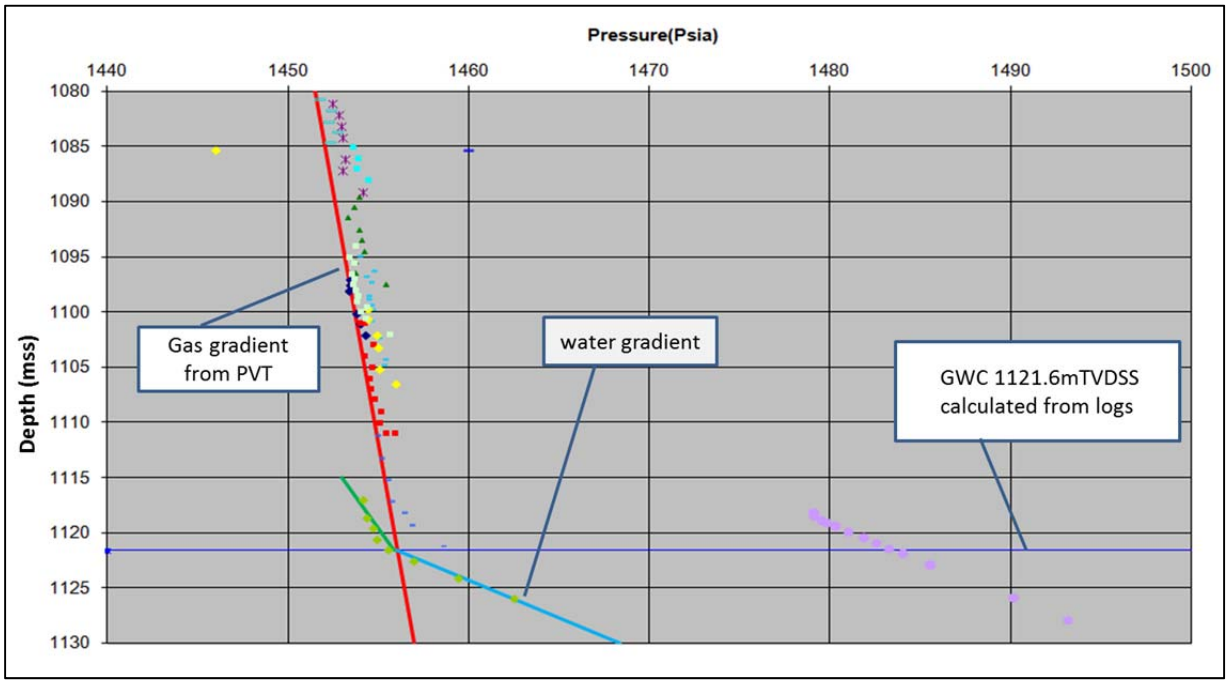

Appendix 12: Pressure data from the wells in Field A. The gas water contact (GWC) is shown at 1121m below mean sea level (bmsl).

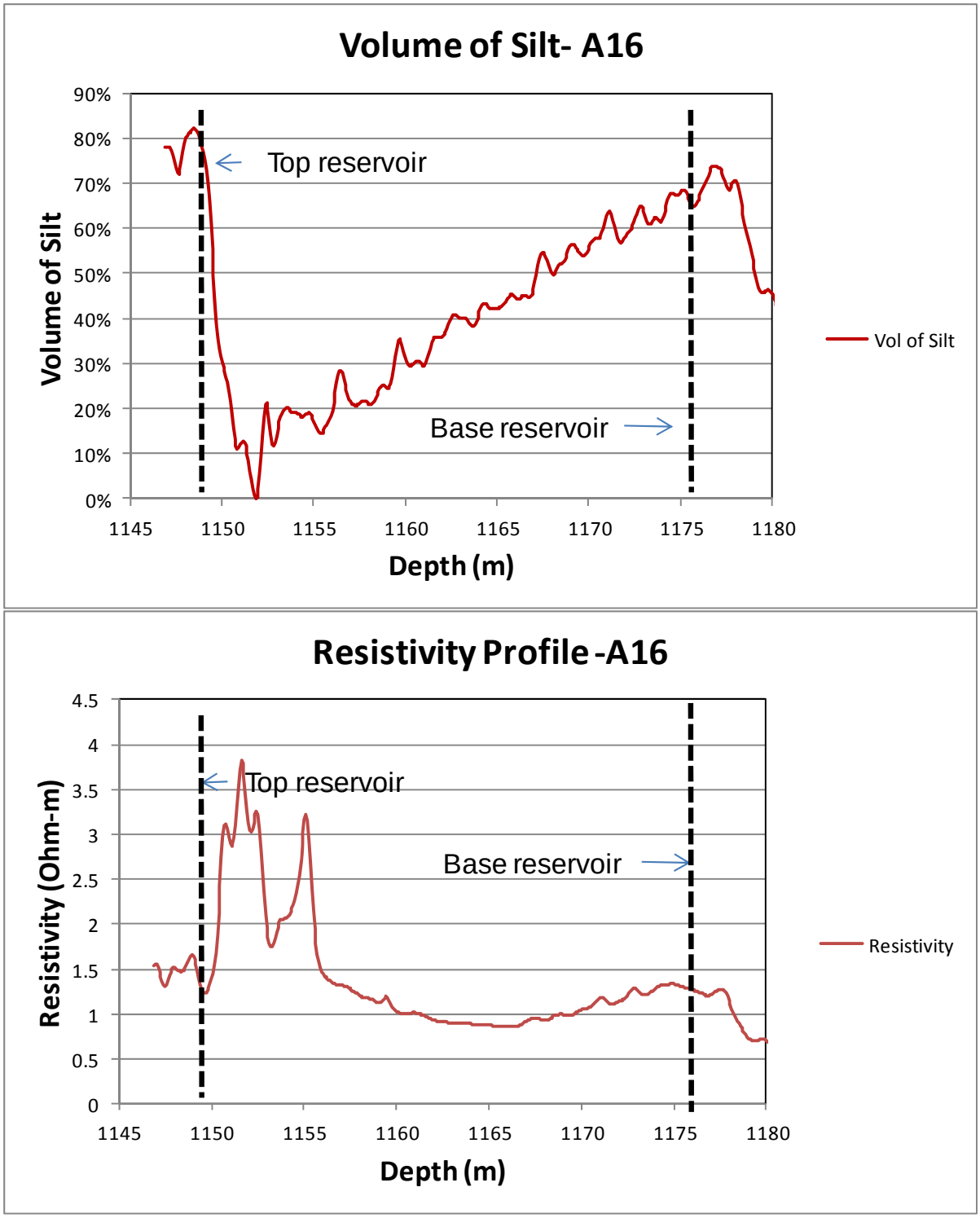

Appendix 13: Volume of silt versus depth (top) and the resistivity profile in well A16 of the J-Reservoir.

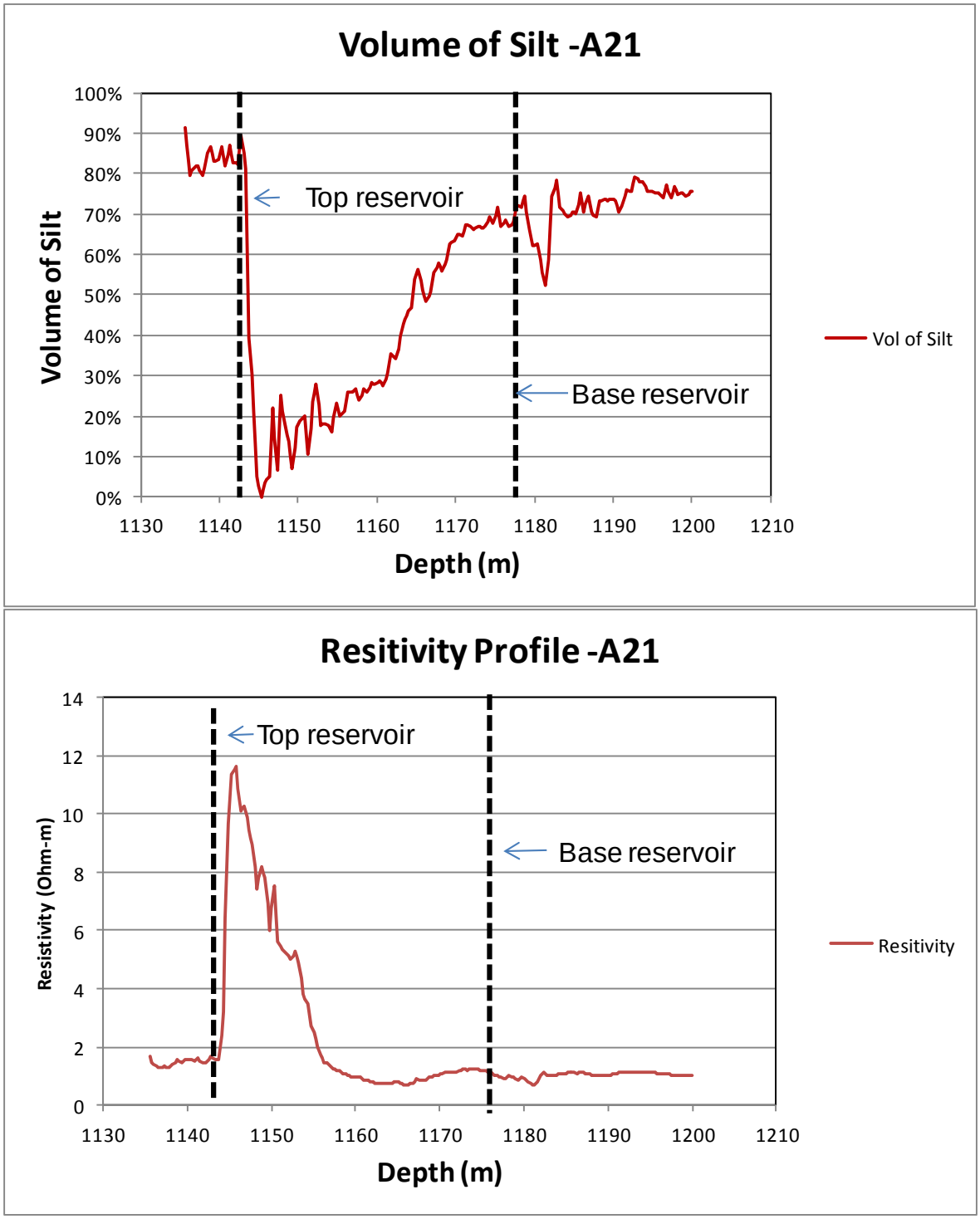

Appendix 14: Volume of silt versus depth (top) and the resistivity profile (bottom) in well A21 of the J-Reservoir.

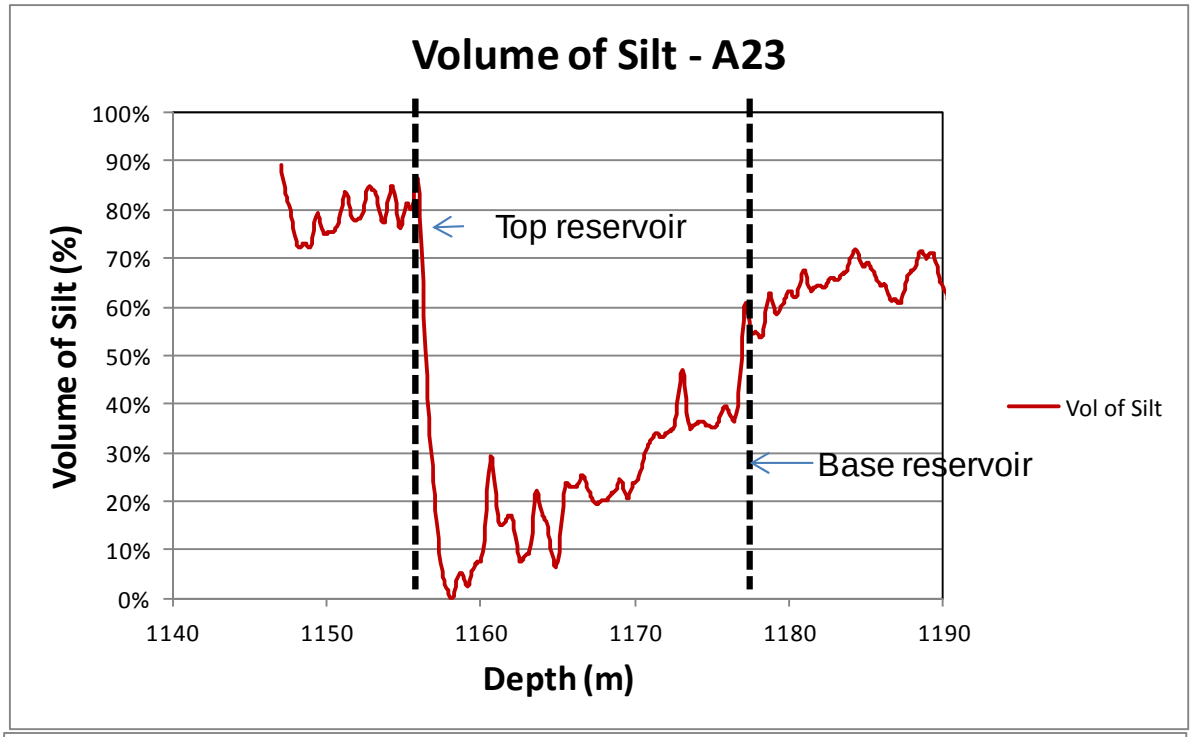

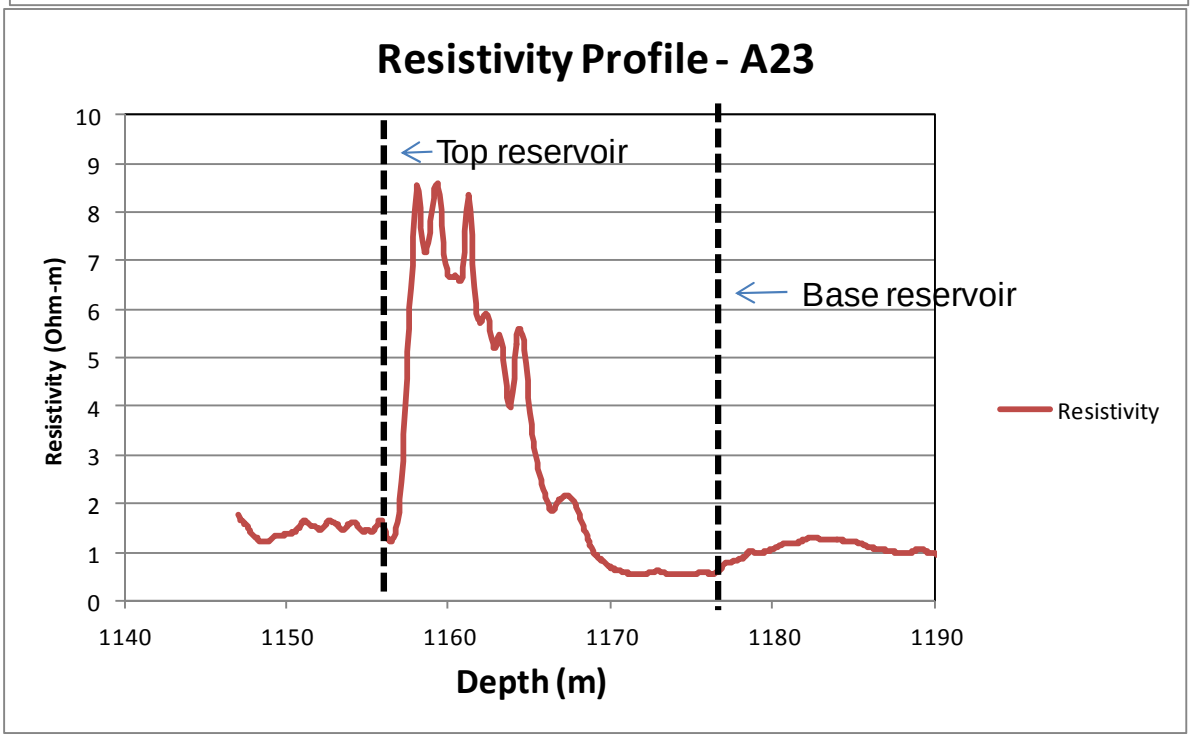

Appendix 15: Volume of silt versus depth (top) and the resistivity profile (bottom) in well A23 of the J-Reservoir.

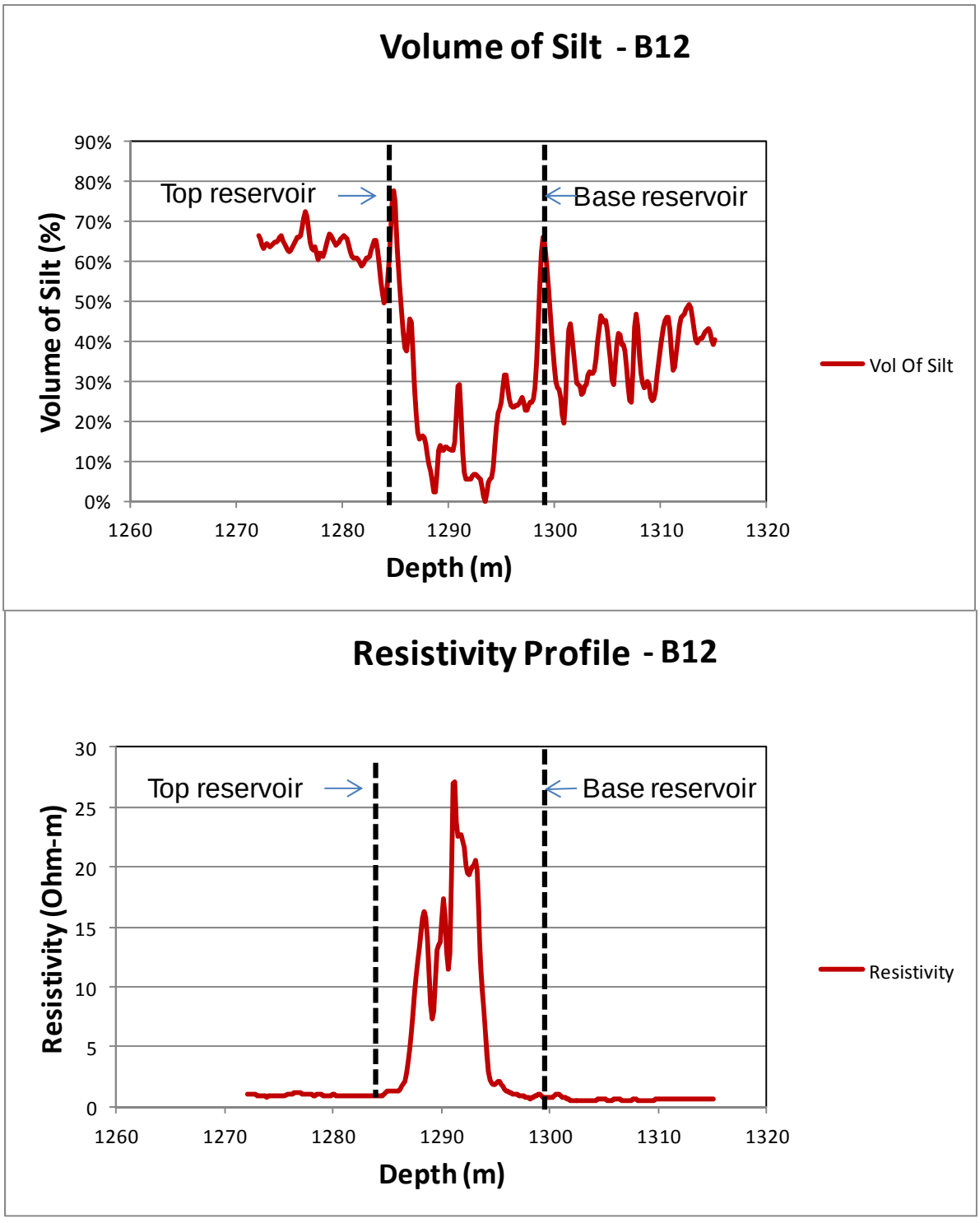

Appendix 16: Volume of silt versus depth (top) and the resistivity profile (bottom) in well B12 of the K-Reservoir.

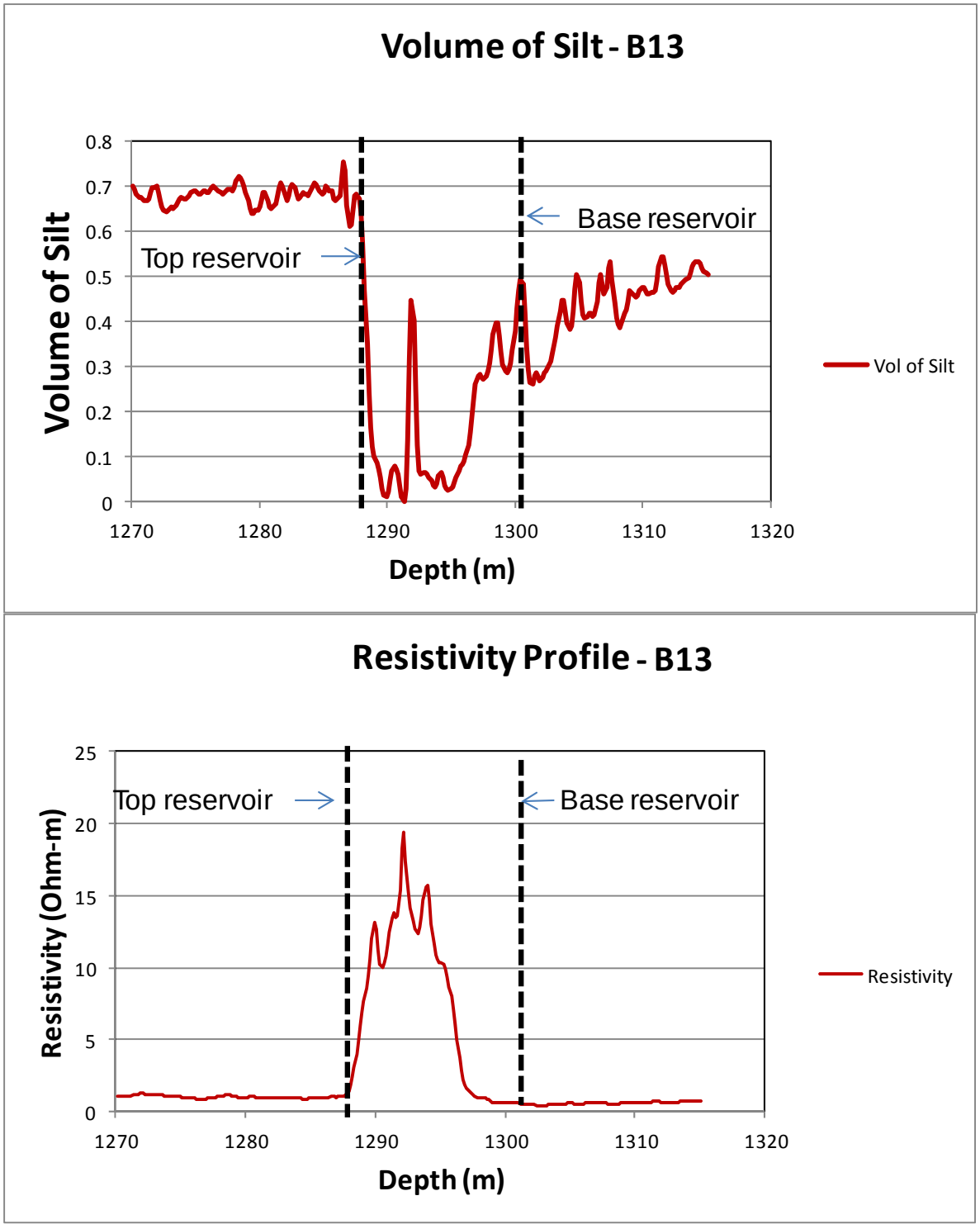

Appendix 17: Volume of silt versus depth (top) and the resistivity profile (bottom) in well B13 of the K-Reservoir.

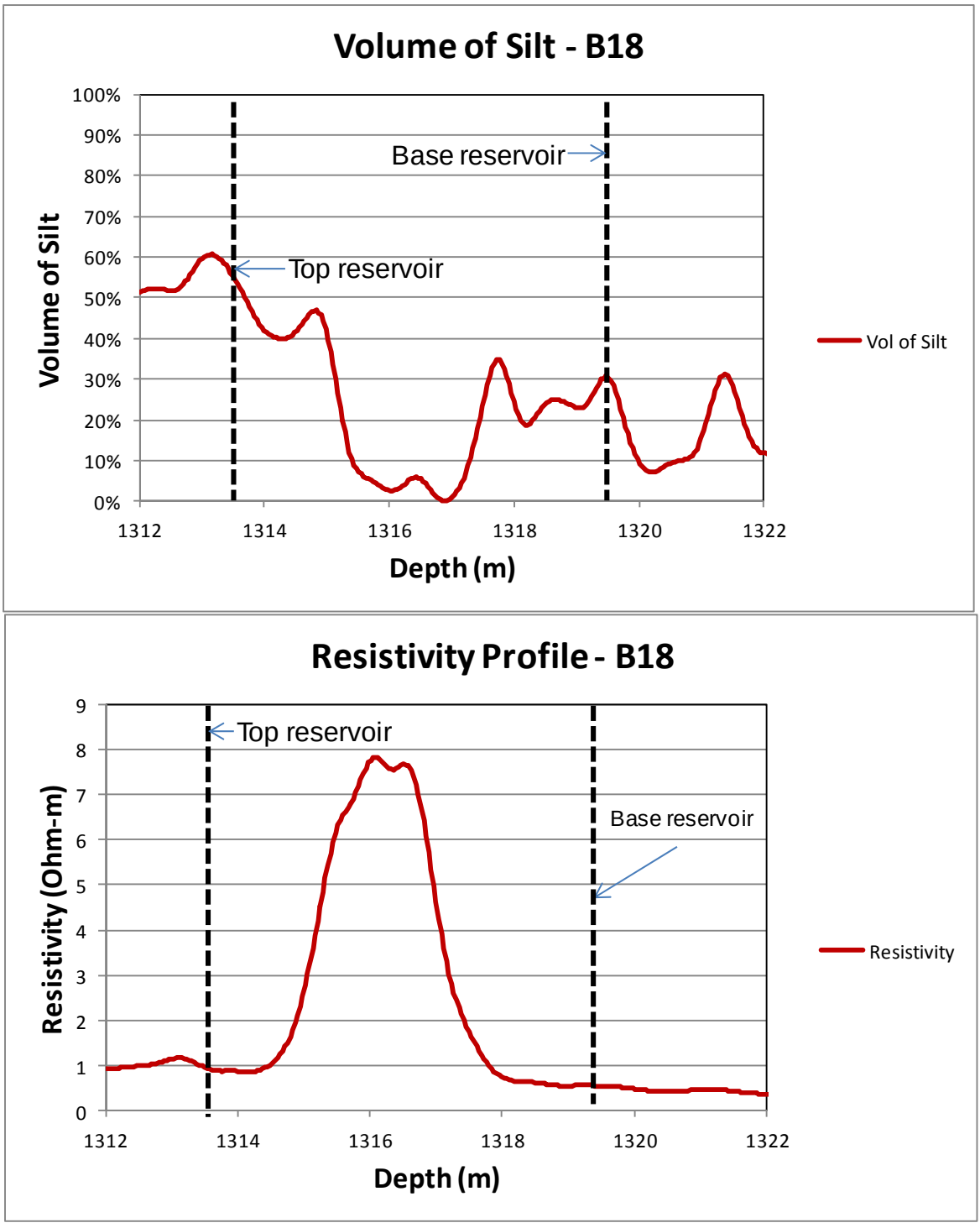

Appendix 18: Volume of silt versus depth (top) and the resistivity profile (bottom) in well B18 of the K-Reservoir.